

PL-TR-97-2137

INTEGRATED EFFORTS FOR ANALYSIS OF GEOPHYSICAL MEASUREMENTS AND MODELS

S. M. Ayer
J. N. Bass
K. H. Bhavnani
K. H. Bounar
R. G. Caton
J. M. Griffin

C. A. Hein
M. J. Kendra
A. G. Ling
A. R. Long
W. J. McNeil
D. S. Reynolds

G. P. Seeley
A. A. Setayesh
M. F. Tautz
R. P. Vancour
J. E. Wise

Radex, Inc.
Three Preston Court
Bedford, MA 01730

September 26, 1997

Final Report
February 1993 to August 1997

Approved for public release; distribution unlimited



PHILLIPS LABORATORY
Directorate of Geophysics
AIR FORCE MATERIEL COMMAND
HANSCOM AIR FORCE BASE, MA 01731-3010

DTIC QUALITY INSPECTED 8

19980608 173

REPRODUCTION QUALITY NOTICE

This document is the best quality available. The copy furnished to DTIC contained pages that may have the following quality problems:

- **Pages smaller or larger than normal.**
- **Pages with background color or light colored printing.**
- **Pages with small type or poor printing; and or**
- **Pages with continuous tone material or color photographs.**

Due to various output media available these conditions may or may not cause poor legibility in the microfiche or hardcopy output you receive.



If this block is checked, the copy furnished to DTIC contained pages with color printing, that when reproduced in Black and White, may change detail of the original copy.

This Technical Report has been reviewed and is approved for publication"



JOHN CIPAR
Contract Manager



LT COL FRANK ZAWADA
Branch Chief

This report has been reviewed by the ESC Public Affairs Office (PA) and is releasable to the National Technical Information Service (NTIS).

Qualified requestors may obtain additional copies from the Defense Technical Information Center (DTIC). All others should apply to the National Technical Information Service (NTIS).

If your address has changed, if you wish to be removed from the mailing list, or if the address is no longer employed by your organization, please notify PL/IM, 29 Randolph Road, Hanscom AFB, MA 01731-3010. This will assist us in maintaining a current mailing list.

Do not return copies of this report unless contractual obligations or notices on a specific document require that it be returned.

REPORT DOCUMENTATION PAGE			Form Approved OMB No. 0704-0188	
Public reporting burden for this collection of information is estimated to average 1 hour per response, including the time for reviewing instructions, searching existing data sources, gathering and maintaining the data needed, and completing and reviewing the collection of information. Send comments regarding this burden estimate or any other aspect of this collection of information, including suggestions for reducing this burden, to Washington Headquarters Services, Directorate for Information Operations and Reports, 1215 Jefferson Davis Highway, Suite 1204, Arlington, VA 22202-4302, and to the Office of Management and Budget, Paperwork Reduction Project (0704-0188), Washington, DC 20503.				
1. AGENCY USE ONLY (Leave Blank)		2. REPORT DATE 26 September 1997		3. REPORT TYPE AND DATES COVERED Final Report (February 1993 to August 1997)
4. TITLE AND SUBTITLE Integrated Efforts for Analysis of Geophysical Measurements and Models			5. FUNDING NUMBERS PE 62101F PR 7659 TA GY WU AA Contract F19628-93-C-0023	
6. AUTHORS S. M. Ayer K. H. Bounar C. A. Hein A. R. Long G. P. Seeley R. P. Vancour J. N. Bass R. G. Caton M. J. Kendra W. J. McNeil A. A. Setayesh J. E. Wise K. H. Bhavnani J. M. Griffin A. G. Ling D. S. Reynolds M. F. Tautz				
7. PERFORMING ORGANIZATION NAME(S) AND ADDRESS(ES) Radex, Inc 3 Preston Court Bedford, MA 01730			8. PERFORMING ORGANIZATION REPORT NUMBER RXR-971002	
9. SPONSORING / MONITORING AGENCY NAME(S) AND ADDRESS(ES) Phillips Laboratory 29 Randolph Road Hanscom AFB, MA 01731-3010 Contract Manager: John Cipar/GPD			10. SPONSORING / MONITORING AGENCY REPORT NUMBER PL-TR-97-2137	
11. SUPPLEMENTARY NOTES				
12a. DISTRIBUTION / AVAILABILITY STATEMENT Approved for public release; Distribution unlimited			12b. DISTRIBUTION CODE	
13. ABSTRACT (Maximum 200 words) This contract supported investigations of integrated applications of physics, ephemerides, and mathematics of the atmosphere and near space. Projects undertaken and reported include spacecraft, ionospheric, atmospheric, and astronomical circumstances; data based studies of air combat targeting; meteorology including cloud scene simulation and ITASCA expert system; ionospheric scintillations; atmospheric metal deposition; auroral particle and electric field modeling, magnetic field studies for CRRES; atmospheric density models, databases and drag; PL-GEOSpace code for 3D visualization studies; DMSP magnetic field studies: ephemerides; comparison of LOKANGL and SPACETRACK codes for orbital prediction, and software development for most of these fields of study.				
14. SUBJECT TERMS Targeting, Cloud simulation, Scintillation, Bubble model, Visualization, GEOSpace, Orbital lifetime, Metal deposition, Ablation, Solar wind, Radiation, Dosage, Electron, Proton, Atmospheric density, Drag, APEX, LOKANGL, MSTI II, DMSP, Archival system, Models library, SSJ4/5, Ephemerides			15. NUMBER OF PAGES 232	
			16. PRICE CODE	
17. SECURITY CLASSIFICATION OF REPORT Unclassified	18. SECURITY CLASSIFICATION OF THIS PAGE Unclassified	19. SECURITY CLASSIFICATION OF ABSTRACT Unclassified	20. LIMITATION OF ABSTRACT Unlimited	

TABLE OF CONTENTS

<u>Section</u>	<u>Page</u>
1. AIR COMBAT TARGETING AND METEOROLOGICAL STUDIES	1
1.1 INFRARED TARGET SCENE SIMULATION (IRTSS)	1
1.1.1 Web Technology	3
1.2 CLOUD SIMULATION	4
1.2.1 SERCAA Algorithms	4
1.2.2 SERCAA Output Products	5
1.2.3 Integration of MM5 and CSSM	5
1.2.4 PL Virtualskies	5
1.3 DATA IMPROVEMENT	7
1.4 THE ITASCA EXPERT SYSTEM	11
1.4.1 Evaluation Process	12
1.4.2 The Evaluation Results and Analysis	12
1.4.3 Summary and Conclusion	13
2. SCINTILLATION NETWORK DECISION AID (SCINDA)	15
2.1 PL-SCINDA	15
2.2 GEOMETRY OF OBSERVING STATIONS	17
2.3 THE BUBBLE MODEL	18
2.3.1 Bubble Recognition	19
2.3.2 Bubble Propagation	20
2.4 ALL-SKY DEPLETION REGIONS AND GPS DATA VALIDATIONS	20
2.5 PL-SCINDA: VISUALIZATION AND ANALYSIS TECHNIQUES	22
2.5.1 View Controls	23
2.5.2 Map Selection Capabilities	23
2.5.3 Threshold Selection Capabilities	23
2.5.4 Printing Capabilities	24
2.5.5 Communication Links Program (Comlinks)	24
2.5.6 Data Plotting Program (DataPlot)	25
2.5.7 Outage Map Products	25
2.6 SUPPORT OF PL-SCINDA INSTALLATION AT FALCON AFB	26
3. THE PL-GEOSPACE CODE	26
3.1 DEVELOPMENT OF PL-GEOSPACE	27
3.2 THE CRRESPRO MODULE	28
3.2.1 The CRRESPRO Science Module	29
3.2.2 The CRRESPRO Application Module	29

Table of Contents (Cont'd)

<u>Section</u>	<u>Page</u>
3.3 THE HIGH ENERGY ELECTRON MONITOR (HEEM) DATA	
MODULE	30
3.3.1 HEEM Module Inputs	31
3.3.2 Plot Options	32
3.3.3 HEEM Module Outputs	32
3.4 GRAPHICAL OBJECT MODULE STARS	32
3.4.1 Stars Inputs	33
3.5 DETECTOR OBJECT GRAPHICS MODULE	34
3.5.1 Coordinate Transformation to the Earth Centered System	35
3.5.2 User Interface to PL-GEOSpace	36
3.6 VISUALIZATION/REAL TIME MAGNETOSPHERE	39
3.6.1 VMS and LINUX System Administration	39
3.7 CONCLUSION	40
 4. ATMOSPHERIC METAL DEPOSITION	 40
4.1 COSMIC DUST DEPOSITION	41
4.2 DIFFERENTIAL ABLATION	42
4.3 CHEMISTRY AND DIFFUSION	44
4.4 RESULTS	44
4.5 CONCLUSION	45
 5. SOLAR WIND ACTIVITY	 46
5.1 THE 22-YEAR CYCLE OF GEOMAGNETIC AND SOLAR WIND	
ACTIVITY	46
5.1.1 Analysis	46
5.1.2 Conclusion	54
5.2 THE SOLAR WIND FROM L1 THROUGH THE MAGNETOPAUSE	55
5.2.1 Interplanetary Shock Detection Algorithm	56
5.2.2 Performance of the Algorithm Using the ISEE-3 Database	57
5.2.3 Conclusion	59
5.3 A PREDICTION OF THE PEAK SUNSPOT NUMBER FOR SOLAR	
CYCLE 23	59
5.3.1 Analysis	59
5.4 THE SOLAR WIND DURING THE MAUNDER MINIMUM	62
 6. CRRES SATELLITE RESULTS	 65
6.1 PROTEL	65
6.1.1 Methodology	66
6.1.2 Results	68

Table of Contents (Cont'd)

<u>Section</u>	<u>Page</u>
6.2 DOSAGE PREDICTION AND OBSERVATION COMPARISON	72
6.2.1 Modified $\text{Sin}^N \alpha$ Pitch Angle Distributions and their Properties	73
6.2.2 Modified $\text{Sin}^N \alpha$ Fits of the Protel Active and Quiet Model Data	74
6.2.3 Rothwell-Yates Proton Dose Computation	74
6.2.4 Spin Averaged Modified $\text{Sin}^N \alpha$ Pitch Angle Path Length Distribution Calculations	75
6.2.5 Results	76
6.3 NUMERICAL COMPUTATION OF OMNIDIRECTIONAL FLUX.1	85
6.4 PROTON SPECTRAL AND PITCH ANGLE DISTRIBUTION UTILITY	89
6.4.1 User's Guide	89
6.4.2 Program Flow and Mathematical Description	94
6.5 DERIVATION OF NEAR-EARTH MAGNETOSPHERIC PLASMA MOMENTS FROM LEPA MEASUREMENTS	101
6.5.1 Overview of Moments Computation	102
6.5.2 Methodology	104
6.5.3 Error Analysis	109
7. VERTICAL CLOUD STRUCTURE	113
7.1 RADIATIVE TRANSFER MODELING	113
7.1.1 Attenuation	113
7.1.2 Emissivity	115
7.1.3 RADTRAN	116
7.1.4 FASE	131
7.2 SUMMARY	132
8. ATMOSPHERIC DENSITY MODELS FOR ORBIT DETERMINATION	132
8.1 EVALUATION OF FIRST PRINCIPLES DENSITY MODELS	132
8.1.1 Comparison of Models with Data	133
8.2 DATABASE MIGRATION	139
8.2.1 Description of the Cyber-based Database	139
8.2.2 Migration to Sun Workstations	142
8.2.3 Exabyte Database Organization	142
8.2.4 File Formats	145
8.3 REENTRY BY DRAG VS REENTRY BY RETROBURN	147
8.3.1 Retrofire Fuel Consumption	147
8.4 DRAG-INDUCED ORBITAL LIFETIME STUDIES	152
8.4.1 Single-Satellite Case Study	154
8.4.2 Controlled Drag-Induced Reentry Study	160
8.5 SPACECOM ORBIT DETERMINATION SUPPORT	163
8.5.1 Extension of SBIR Work	164

Table of Contents (Cont'd)

<u>Section</u>	<u>Page</u>
8.5.2 New Results	165
8.5.3 Recommendations	171
9. APEX - MSTI-II	172
9.1 ATTITUDE AND EPHEMERIS FOR THE APEX AND MSTI-I SATELLITES	172
9.1.1 Preliminary Investigations and Documentation	173
9.2 THE APEX SATELLITE	174
9.3 THE MSTI-II SATELLITE	179
10. DMSP MAGNETOMETER	183
10.1 BRIEF DESCRIPTION OF THE APHB CODE	183
10.1.1 History	183
10.1.2 Basic Operation of the F12 and Beyond Instruments	184
10.1.3 SSM Data Input at PL/GP	184
10.1.4 Converting from Telemetry Data to Magnetic Field Measurement ...	184
10.1.5 Measured Minus Model Geomagnetic Field	185
10.1.6 Jump Removal	185
10.1.7 Noise Removal	185
10.1.8 Output	186
10.1.9 Program Control	186
10.2 PROBLEMS AND MODIFICATIONS REQUIRED FOR DMSP F12, F13 AND BEYOND	186
10.2.1 False Large Jumps	186
10.2.2 Slow Small Jumps	187
10.2.3 Calibration Problem	187
10.2.4 Tweaking the Small Jump Logic	190
10.2.5 Model Magnetic Field	190
11. EPHEMERIDES	190
11.1 SATELLITE ELEMENT ARCHIVAL SYSTEM	190
11.1.1 Original Satellite Element Processing Procedure	191
11.1.2 Processing Procedure Development	191
11.2 GEOPHYSICAL MODELS LIBRARY	192
11.3 SSM4/5	192
11.4 COMPARISON OF LOKANGL AND SPACETRACK CODES FOR ORBIT PREDICTION	196
12. REFERENCES	204

LIST OF FIGURES

<u>Figure</u>	<u>Page</u>
1. IRTSS client server architecture	1
2. IRTSS sensor pointing web page	2
3. IRTSS scene prediction sample 1	3
4. IRTSS scene prediction sample 2	3
5. Virtual Skies cloud parameter web page interface	6
6. A good example of banding due to FLIR sensor defects	8
7. The full-frame color classification of the test-target scene	9
8. A column slice of the test-target scene vs. time, before registration	10
9. The same column slice vs. time as in Figure 8, after registration	11
10. 12 hours observation and forecast temperature profiles, January 3, 1990, Parksburg, WV, at 12:00GMT with 9 hours of weather history	14
11. 12 hours observation and forecast average wind speed difference, selected days in January, 1990, Des Moines, IA	14
12. SCINDA system concept	16
13. Schematic diagram of receiver locations and ionospheric penetration points for the current configuration	17
14. Sample scintillation data from the four links comprising the current scintillation bubble model	18
15. Edited and averaged S_4 data along with the bubbles generated from the night shown in Figure 14	19
16. Depletion Regions of October 1, 1994	21
17. Depletions regions, longitudinal extent versus time	21
18. PL-SCINDA 3D Main View	23
19. 3D main view display showing communications links	24
20. Outage map display	25
21. GEOSpace 2-D and 3-D windows	38
22. The deposition rates for the three metals assuming an entry velocity of 15 km/s	43
23. Mesospheric neutral metal layers as calculated in the 15 km/s model	45
24. (a) Yearly averages of the geomagnetic aa index, 1844-1994. Vertical dashed lines indicate the 11-year geomagnetic minima. (b) Yearly averages of the sunspot number (SSN), 1844-1994. The sunspot cycles are numbered at the top of the panel	47
25. (a) Composite weighted annual averages of aa for the six even-numbered and six odd-numbered solar cycles that made up complete Hale (22-year)cycles since 1844	48
26. (a) <i>Sargent's</i> [1985] recurrence index (RI) for 150 years of aa data. The dashed vertical lines indicate 11-year minima in the aa indices and the shaded rectangles at the bottom of the panel indicate the "2 nd half" periods used to obtain the average RIs plotted in (b)	49

List of Figures (Cont'd)

<u>Figure</u>	<u>Page</u>
27. (a) Composite FFT spectra of aa for the declining phase (2 nd half) of even-numbered solar cycles since 1855. (b) Averaged FFT spectra of aa for the "2 nd half" of odd-numbered solar cycles since 1855	52
28. The simulated aa time series	53
29. The FFT spectra of simulated aa for the declining phase of even- and odd- numbered solar cycles	54
30. An ideal case with a correlation coefficient of 0.98 at the discontinuity	56
31. Example of a shock detection. This particular shock on 09 March 1979 resulted in a SSC 40 minutes later [<i>Gonzalez and Ts uratani</i> , 1989]	58
32. (a) Correlation coefficients (C.C.) for the aa-SSN relationship as a function of various averaging times for aa. The solid line is for time periods that end at the smoothed minimum at the end of a sunspot cycle and begin at a point corresponding to the indicated percentage of a cycle, measured backward from the minimum. For the dot-dash line, the end point of the time range corresponds to 10% of the way through the following cycle, measured forward from the same sunspot minimum. Same as (a) for the standard error of estimate (S.E.) of SSN_{max}	60
33. Regression line for peak SSN of a cycle vs. aa averaged over the last 30% (measured backward from the smoothed sunspot minimum) of the previous cycle. The filled square indicates the prediction (161) for cycle 23	61
34. Correlation between 11-yr averages of aa and SSN	63
35. Correlation between the ratio of the minimum annual average of aa during an 11-year cycle (aa_{min}) to the average aa value during that cycle ($\langle aa \rangle_{11}$) and the average sunspot number ($\langle SSN_{11} \rangle$) over the cycle. The length of the cycle corresponds roughly to the interval between consecutive sunspot maxima	63
36. Computed equatorial flux at $\alpha = 90^\circ$ (incorporating the effects of the PROTEL HEH aperture and rotation), as a function of L for modified $\sin^N \alpha$ distributions for $N = 4, 5, 6$, and 8	69
37. The computed distributions (incorporating the effects of aperture and rotation) have been fitted to a single modified $\sin^N \alpha$ distribution	70
38. Ratio of equatorial omnidirectional flux (from fits of the computed pitch angle distribution to a single modified $\sin^N \alpha$ distribution) to that of the original modified $\sin^N \alpha$ distribution is plotted as a function of L for $N = 4, 5, 6$, and 8	70
39. Ratio of equatorial omnidirectional flux (from fits of the computed pitch angle distribution to the sum of two modified $\sin^N \alpha$ distributions) to that of the original modified $\sin^N \alpha$ distribution is plotted as a function of L for original $N = 4, 5, 6$, and 8	71
40. Sample comparison ($N = 4$, $\alpha_c = 47.5$, $L = 1.25$) of the computed pitch angle distribution with the original modified $\sin^N \alpha$ pitch angle distribution	71

List of Figures (Cont'd)

<u>Figure</u>	<u>Page</u>
41. Computed and measured dose of the Quiet Model, dosimeter HILET data, channel #1	77
42. Computed and measured dose of the Quiet Model, dosimeter HILET data, channel #2	78
43. Computed and measured dose of the Quiet Model, dosimeter HILET data, channel #3	79
44. Computed and measured dose of the Quiet Model, dosimeter HILET data, channel #4	80
45. Computed and measured dose of the Active Model, dosimeter HILET data, channel #1	81
46. Computed and measured dose of the Active Model, dosimeter HILET data, channel #2	82
47. Computed and measured dose of the Active Model, dosimeter HILET data, channel #3	83
48. Computed and measured dose of the Active Model, dosimeter HILET data, channel #4	84
49. Attenuation rate by cloud liquid water as a function of microwave frequency at the indicated temperatures and a cloud water concentration of 1g/m^2	114
50. Temperature and dew point temperature profiles for seven Atlantic stratocumulus profiles, each having a different cloud thickness	116
51. Brightness temperature in horizontal polarization as a function of the amount of total cloud liquid water for an Atlantic stratocumulus atmosphere as calculated by RADTRAN	117
52. Same as Figure 51, but with cloud thickness as the abscissa	117
53. Brightness temperature in horizontal polarization for an Atlantic stratocumulus atmosphere as calculated by RADTRAN showing the contours of cloud thickness and cloud water content	118
54. The relative combination of the surface, direct, reflected, and space terms of the radiative transfer equation to the brightness temperature as calculated with RADTRAN	122
55. Channel bar chart for the terms of the radiative transfer equation as explained in the text	123
56. Cloud water, temperature, and dew-point temperature profiles for a typical mid-latitude summer atmosphere used as input into RADTRAN	125
57. Brightness temperature in the horizontal polarization as calculated with RADTRAN for a set of mid-latitude summer atmosphere profiles as a function of cloud base altitude	125
58. Same as Figure 57, but with the difference between the surface brightness temperature and the cloud base temperature plotted	126

List of Figures (Cont'd)

<u>Figure</u>	<u>Page</u>
59. Same as for Figure 57, but with the abscissa as the difference between the brightness temperature at the cloud base altitude for a cloud-free profile and the cloud base temperature	126
60. Brightness temperature in vertical polarization for mid-latitude summer atmosphere containing two clouds as calculated by RADTRAN	127
61. The total atmospheric attenuation as a function of microwave frequency for a nadir view through a U. S. Standard Atmosphere having a cloud with its top at 6.9km or -30°C	128
62. The difference in brightness temperatures calculated by RADTRAN using the Ray or LHM attenuation models	128
63. Results of simulating the retrieval of the total amount of cloud liquid water from the SSM/I	130
64. Same as Figure 62, but the retrieved results are for an upward-looking ground-based radiometer	130
65. Brightness temperature for a cloudless Atlantic stratocumulus atmosphere as calculated using the modeling codes RADTRAN and FASE	131
66. Standard Deviation of the natural log of measured to model density ratio, for the VSH quiet and storm models, the MSIS90E model, and the Jacchia-70 model, for SETA-2 data, June, 1982, for three geomagnetic activity (K_p) levels	134
67. Comparison of standard deviations of log of the ratios of data to model for the VSH storm, Jacchia-70, and MSIS-90E models as functions of latitude-local time, for the same period as in Figure 66	135
68. Top panel: Overlay showing measured density, MSIS-90E model density, and TFM model density, for orbit 98, day 81 (1979), SETA-1 data	137
69. Same as for Figure 68, except that the VSH storm model is shown instead of the TFM model	137
70. Same as for Figure 68, except that it is for orbit 114	138
71. Same as for Figure 69, except that it is for orbit 114	138
72. Fuel requirement (pounds) to a specified perigee height from a circular orbit as a function of its altitude	149
73. FSW-1 ballistic coefficients derived from fitting over pairs of NORAD element sets with the Jacchia 70E density model using fixed solar fluxes of 85, geomagnetic indices of 7	159
74. FSW-1 ballistic coefficients derived from fitting over pairs of NORAD element sets with the Jacchia 70E density model using actual solar fluxes and geomagnetic indices	160
75. The LDEF ballistic coefficient determined from orbit decay in the period 1988 day 180 - 1989 day 365	166

List of Figures (Cont'd)

<u>Figure</u>	<u>Page</u>
76. The scaled ballistic coefficients, associated with the original Jacchia 1970 model, for the four satellites, for the same period as in Figure 75	166
77. The ratio of the scaled ballistic coefficients of SALYUT 7, and SOLAR MAX to the scaled ballistic coefficient of LDEF, for the same period as Figures 75 and 76	167
78. A scatter plot of corrected exospheric temperature vs daily 10.7 cm solar flux, based on LDEF data	167
79. Bin averaged corrected exospheric temperature vs daily 10.7 cm solar flux	168
80. Scatter plot of corrected exospheric temperature vs 81 day mean 10.7 cm solar flux ...	168
81. Bin averaged corrected exospheric temperature vs 81 day mean 10.7 cm solar flux	169
82. New EUV index ("measured EUV flux") vs time	170
83. Scatter plot of new EUV index vs daily 10.7 cm solar flux	170
84. Comparison of LDEF ballistic coefficients, associated with the Jacchia 1970 model, obtained using the operation solar and geomagnetic indices ("USAF") with those obtained using the standard ("JGR") indices	171
85. Orbital Elements derived from position/velocity vectors for the APEX satellite	175
86. Illustration of the fitting of the anomalistic mean motion to arrive at the period decay ..	176
87. Sample quality control plot from a typical APEX orbit in which there are no eclipses ..	177
88. Sample APEX attitude quality control plot showing pitch and yaw and roll as well as flags for bad telemetry and eclipse conditions	178
89. Sample of the ephemeris and attitude control plot for a MSTI-II stare at Hawaii	180
90. Sample of MSTI-II Q.C. tools for an attempted (and failed) star search	181
91. An example of the tool developed to locate the center point of the MSTI-II camera line of sight on the Earth's surface	182
92. MSTI-II Images (left) of a river and volcano and (right) of a brush fire in Nevada	183
93. Magnetic field line trace from altitude to ground, using the IGRF 1995 model, altitude 850 km	195
94. Magnetic field line trace from altitude to ground using the SFC CONVERT_GEO_COORD routine for 1995	196
95. In-track differences between the predictions of LOKANGL and SGP4 (top) and LOKANGL and SGP (bottom), for DMSP F7 (14506)	199
96. In-track differences between the predictions of LOKANGL and SGP4 (top) and LOKANGL and SGP (bottom), for the Mir satellite (16609)	200
97. In-track differences between the predictions of LOKANGL and SDP4 (top) and LOKANGL and SGP (bottom), for the CRRES satellite (20712)	201
98. In-track prediction accuracy of SGP4 for DMSP F7	202
99. In-track prediction accuracy of SGP4 for Mir	202
100. In-track prediction accuracy of SDP4 for CRRES	203
101. In-track prediction accuracy of SGP4 for CRRES	203

LIST OF TABLES

<u>Table</u>	<u>Page</u>
1. Relative Neutral Abundances	44
2. Calculation of i^2 Statistic for a 27-Day Recurrence Period for Storm Days	51
3. Summary of the Results for Correlation Threshold of 0.8	58
4. Summary of the Results for Correlation Threshold of 0.9	59
5. Omni-directional Flux for $n=10.0$, loss cone edge=30 deg	88
6. PROTEL Energies	93
7. Moments and Associated Parameters	103
8. Sets of Parameter Values Used to Test the <i>Bauer and Grody</i> [1995] Land Surface Emittance Model	115
9. The Results of Applying the Gradient Calculations as Explained in the Text To Atlantic Stratocumulus Contour Plots as Exemplified in Figure 53	120
10. Statistical Summary of Neutral Atmosphere Models Altitude Range 160 - 250 km	136
11. Neutral Atmospheric Density Data Base Characteristics	140
12. Neutral Atmospheric Density Data Base Tape Library	140
13. Density Models	141
14. Satellite Experiment-dependencies Parameters	146
15. Fuel Consumed and Δv Required from an Initial Circular Orbit at 300 km	149
16. Transfer between Circular Orbits	150
17. Fuel Consumed (Pounds) in Orbit Transfer	151
18. A Sample Set of Crash Dates and Final Orbits for Various Ballistic Coefficients	157
19. Summary of the Decay Times	162
20. Relative Orbital Lifetimes for Satellites With and Without Balloon Deployed According to MSISE90	163
21. Satellites in the Snow-Liu Study	164

ACKNOWLEDGMENTS

The work described in this report required the involvement and guidance of numerous individuals at PL, and their interest and encouragement is gratefully acknowledged.

Ed Robinson of the Data Analysis Division initiated and coordinated the activities as Contract Monitor. His contributions are deeply appreciated. John Cipar followed through to completion, and has particularly helped in shaping this final report.

Various investigators were involved throughout the projects, and provided essential support and the opportunity for some challenging studies in their fields:

Al Griffin, Bob McNerney, and Bob Raistrick	Data Analysis Division
---	------------------------

Ed Cliver, Greg Ginet, Sue Gussenhoven, and Gary Mullen	Space Particle Environment Branch
--	-----------------------------------

Fred Rich	Space Plasmas and Fields Branch
-----------	---------------------------------

Shu Lai and Ed Murad	Spacecraft Interactions Branch
----------------------	--------------------------------

Dave Anderson, Santimay Basu, Keith Groves, Frank Marcos	Ionospheric Effects Branch
---	----------------------------

Joel Mozer, Dana Madsen, Rosemary Dyer Alan Lipton	Atmospheric Science Division
--	------------------------------

This report has been compiled and prepared by Susan Cline.

LIST OF ACRONYMS

ACT-EOS	Air Combat Targeting Electro-Optical Simulation
AE	Atmosphere Explorer (Satellite)
AFCCC	Air Force Combat Climatology Center
AFGWC	Air Force Global Weather Central
AFIT	Air Force Institute of Technology
AFITSSSA	A program which displays pitch angle distribution data
AFMSS	Air Force Mission Support System
AIMS	Air Force Interactive Meteorological System
APEX	Advanced Photovoltaic and Electronic Experiment (Satellite)
APHB	DMSP magnetometer code
ARC/INFO	A commercial geographic information package
ASAP	Artificial Satellite Analysis Program
ASc	Atlantic Stratocumulus
ASCII	American Standard Code Information Interchange
AU	Astronomical Unit
AWDS	Automated Weather Distribution System
AWS	Air Weather Squadron
BG	Bauer and Grody Land Surface Emittance Model
CGI	Common Gateway Interface
CGLALO	Corrected Geomagnetic Latitude Longitude
CGM	Corrected Geomagnetic Coordinate System
CIB	A geographic data product
CLWC	Cloud Water Content
COTS GIS	Commercial off-the-shelf Geographic Information System
CRAND	Cosmic Ray Albedo Neutron Decay
CRRES	Combined Release and Radiation Effects Satellite
CRESSELE	CRRES Electron
CRRESPRO	CRRES Proton
CRRESRAD	CRRES Radiation
CRUX	Cosmic Ray Upset Experiment
CSSM	Cloud Scene Simulation Model
CSTC	Combined Space Test Center
DMSP	Defense Meteorological Satellite Program
DSBMOD	Discrete Scintillation Bubble Model
DSC	Double-Solar-Cycle
DTED	Digital Terrain Elevation Data
ECI	Earth-Centered Inertial Frame
ELP82B	A Fortran code, used with PLANETAP, to provide lunar and planetary positions for use in PL-GEOSpace
ESA	Electrostatic Analyzer
ESC	Electronics Systems Center

ESF	Equatorial Spread-F
EUV	Extreme Ultra Violet
FASE	Radiative transfer code
FERRO	Thin-film Ferroelectric Experiment
FFT	Fast Fourier Transform
FLIR	Forward-Looking InfraRed
FSW-1	Chinese Military Payload
GEOS	Geostationary Earth Orbiting Satellite
GIF	Graphics Interchange Format
GIS	Geographic Information System
GLOBALS	An SQL database code to access 3 hr. k_p , a_p , F10.7, and sunspot number for input to PL-GEOSpace.
GPS	Global Positioning System
GSATEL	Satellite element processing program
GSM	Geocentric Solar Magnetospheric
HEEM	High Energy Electron Monitor
HEH	High Energy Head
HILET	Accumulated energy deposited by individual events in the energy loss range of 1-10 MeV
HMW90	Companion wind model for MSIS-90E
HTML	Hyper Text Markup Language
HTTP	Hyper Text Transmission Protocol
IDL	Interactive Data Language
IEEE	Institute of Electrical and Electronic Engineers
IGRF	International Geophysical Reference Field
IMF	Interplanetary Magnetic Field
IRIX	Silicon Graphics UNIX operating system
IRTSS	Infrared Target Scene Simulation
JPL	Jet Propulsion Laboratory
LDEF	Long Duration Exposure Facility
LHM	Liebe, Hufford, and Manabe Attenuation Model
LOKANGL	Ephemeris Calculation Program
LOLET	Accumulated energy deposited by individual events in the energy loss range of 0-1 MeV
LOS	Loss-of-Signal
MLS	Mid-Latitude Summer
MM5	PSU/NCAR Mesoscale Model Version 5
MODVIEW	A program which displays omnidirectional flux
MOTIF	X Windows user interface system
MSIS	Mass Spectrometer and Incoherent Scatter (neutral density model)
MSTI	Miniature Sensor Technology Integration (Satellite)
MWIR	Medium Wave InfraRed

NASA	National Aeronautics and Space Administration
NCSA	National Center for Supercomputer Applications
NGDC	National Geophysical Data Center
NOAA	National Oceanic and Atmospheric Administration
NORAD	North American Aerospace Defense Command
NORAPS	Navy Operational Regional Atmospheric Prediction System
NSSDC	National Space Science Data Center (NASA)
NSWP	National Space Weather Program
OBAFGKM	Stellar Spectral Classification Types
ORBEL	An SQL database code for inputting orbital elements to PL-GEOSpace
ORBITAPP	A PL-GEOSpace module
PASP	Photovoltaic Array Space Power
PGM	Precision Guided Munitions
PIM	Parameterized Ionospheric Model
PLANETAP	A Fortran code, used with ELP82B, to provide lunar and planetary positions for use in PL-GEOSpace
PROTEL	Proton Telescope
RADTRAN	Radiative Transfer Code
RDB/VMS	Receive Data Buffer/Virtual Memory System
RGB	Red-Green-Blue
RI	Recurrence Index
ROPP	Rapid Orbit Prediction Program
SAA	South Atlantic Anomaly
SALYUT 7	Russian Spacecraft
SBIR	Small Business Innovative Research
SCINDA	Scintillation Network Decision Aid
SDP	Satellite element prediction model
SERCAA	Support of Requirements for Cloud Analysis and Archive
SGI	Silicon Graphics
SGP	Satellite element prediction model
SME	Solar Mesospheric Explorer
SNR	Signal-to-Noise Ratio
SPACECOM	Space Command
SPACETRACK	Satellite Orbit Prediction Code
SQL	Structured Query Language
SSM/I	Special Sensor Microwave/Imager
SSN	Sunspot Number
STOA	Shock Time-of-Arrival
SWC	Space Weather Center
SWIR	Short Wave InfraRed
TEC	Total Electron Content
TFM	Thermosphere Forecast Model

TGCM	Thermosphere General Circulation Model
TIGCM	Thermosphere-Ionosphere General Circulation Model
UHF	Ultra-high Frequency
US76	US Standard Reference Atmosphere
UT	Universal Time
VAX	Virtual Address Extension
VMS	Virtual Memory System
VPF	Geographic data product
VSH	Vector Spherical Harmonics
WBMGRID	Data-driven scintillation climatology code
WBMOD	Wideband Scintillation Model
WIDA	AF Weather Impact Decision Aids

1. AIR COMBAT TARGETING AND METEOROLOGICAL STUDIES

Air Combat Targeting Electro-Optical Simulation (ACT/EOS) is a product of the Air Force Weather Impact Decision Aids (WIDA) Program based at Phillips Laboratory, Hanscom AFB, MA. The goal of ACT/EOS is to provide Air Force mission planners with predictions of infrared (IR) target scene radiances to aid in tactical decision making.

1.1 INFRARED TARGET SCENE SIMULATION (IRTSS)

IRTSS is a component of the PL/GPOF ACT-EOS program and provides aircrews with a weather enabled 8-12 micron IR mission preview capability. Figure 1 shows the high level architecture of the system. An OpenGL based high-fidelity terrestrial IR scene rendering capability was constructed that is driven through a web/cgi interface. An important advantage of this design is that the entire capability is driven by standard http protocol, thus, making the system usable on all hardware platforms that support the widely used TCP/IP networking protocol. The design allows users in remote geographic locations on hardware of their choice easy access to the physical modeling and scene generation capabilities.

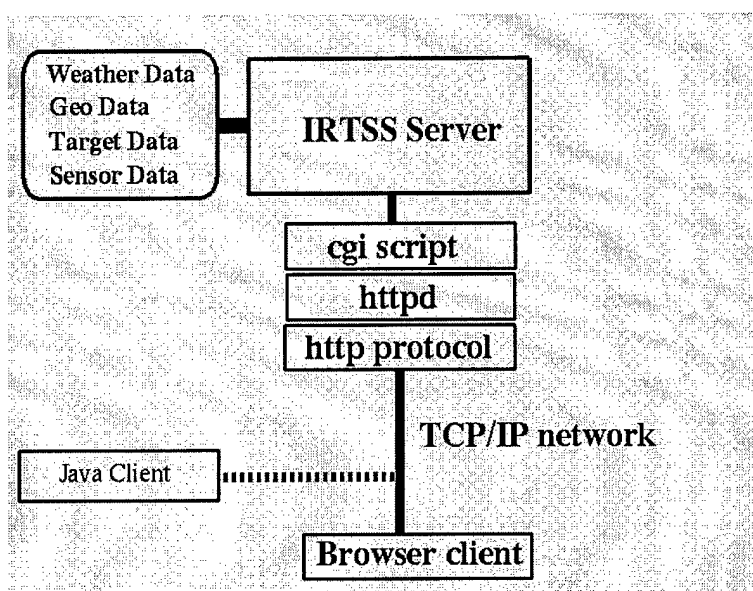


Figure 1. IRTSS client server architecture.

IRTSS was designed to support missions involving Precision Guided Munitions (PGMs). These are standoff weapons that are typically released from aircraft 30 km or more from targets. It is often difficult for aircrews to locate target areas due to lack of thermal contrast in the scene or unfamiliarity with the appearance of geographic features on their cockpit displays. The IRTSS system has the ability to display visible and IR imagery.

The design of IRTSS is also affected by the availability of increasing amounts of remotely sensed data. In order to provide good visual fidelity, IRTSS uses high resolution satellite imagery. Modern imagery of Earth's surface from commercial and military providers has resolutions approaching 1 meter. Since the length of a typical PGM track is of the order of 30 km, hundreds of megabytes of

management and use of the imagery. IRTSS has also used a commercial GIS system to exploit many established and emerging geographic data products such as Digital Terrain Elevation Data (DTED), Vector Product Format (VPF), Controlled Imagery Base (CIB), Landsat, and other satellite and aerial products.

IRTSS appears to the user as a resource available at a known web address (see Figure 2). The user can insert mission factors such as target type, location, planned mission time, weapon system, local meteorology, etc. Meteorology is inserted into the system through a real-time AWDS weather feed. Output is a weapon system specific scene prediction for a given time and location, as shown in Figures 3 and 4. The image appears directly in the client browser. The geographic data does not have to be sent over the net, it stays on the IRTSS server and is used for rendering. This concept has been tested in the context of supporting F-16 test missions at Eglin AFB, FL. IRTSS has received a favorable reaction from the staff meteorologists who are responsible for briefing aircrews on electro-optical weapons system performance. IRTSS is an example of a system that uses hundreds of megabytes of environmental background information and delivers a bottom line system performance prediction to a remote user using commercial internet technology. This shows that the web can be used for more than browsing a static data archive or searching a data base. Here, the web is used to actually carry out physical modeling using real-time data feeds and extensive geographic background information.

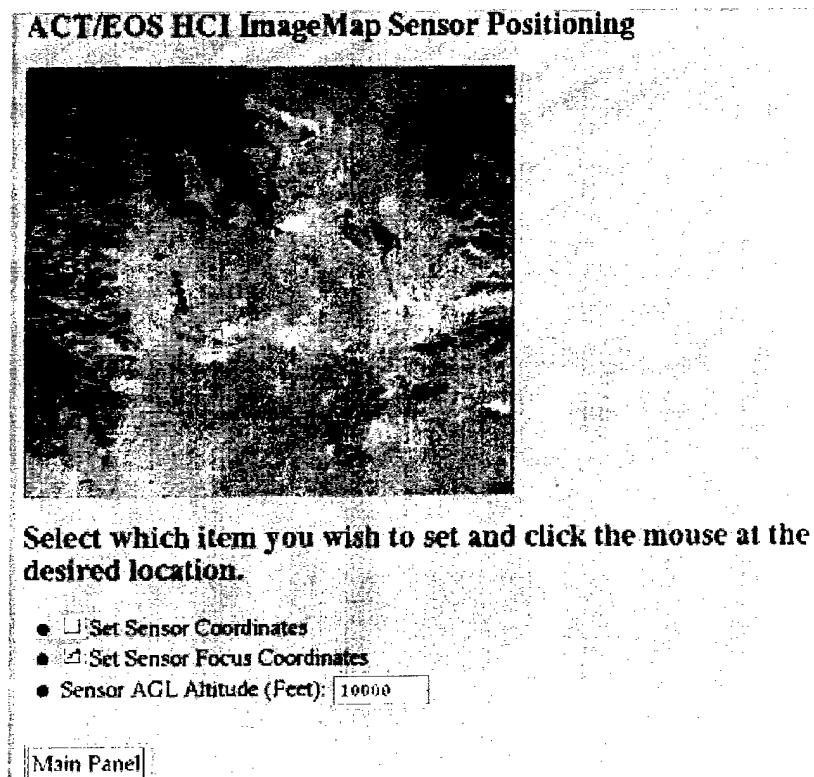


Figure 2. IRTSS sensor pointing web page.

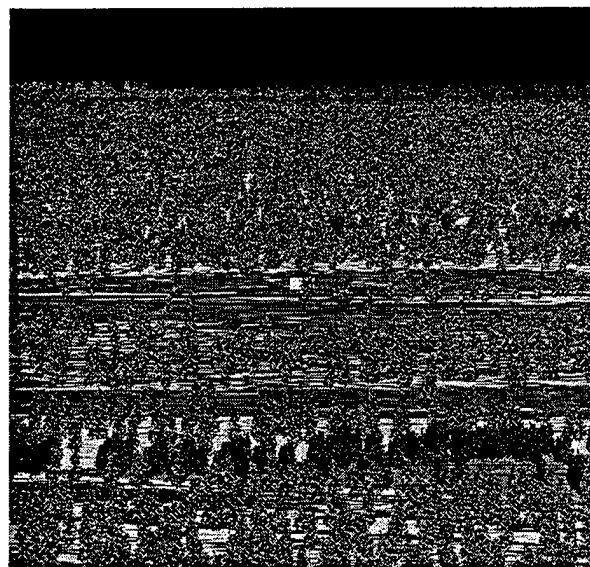
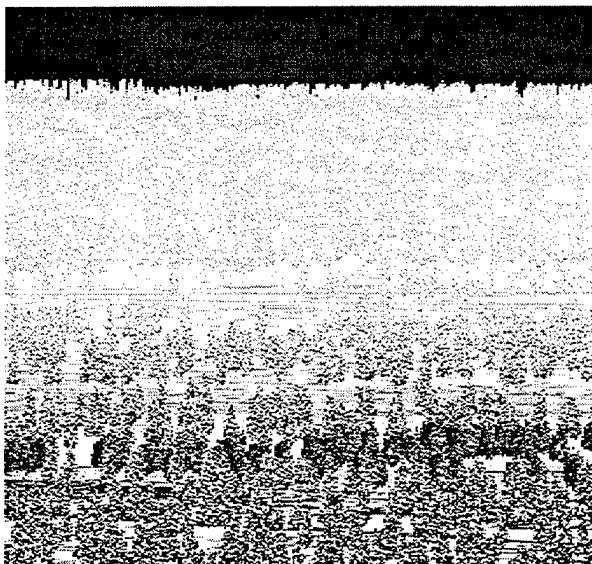


Figure 3. IRTSS scene prediction sample 1. **Figure 4.** IRTSS scene prediction sample 2.

Using a http/CGI interface has also enabled IRTSS functionality to integrate into AFMSS, the Air Force Mission System Support. In cooperation with the MITRE/JMPS architecture team, an http/CGI interface for exporting AFMSS flight route data was established. The interface allows an IRTSS user to query an AFMSS system for what flight routes are on board and to download a selected route. HTTP is the common thread that integrates disparate pieces of software.

1.1.1 Web Technology

Web technology offers many advantages including platform independence and a wide variety of commercial software products designed explicitly for web use. It is realized that the web is an ideal vehicle for disseminating data and explicitly provide environmental background data on the web. Inexpensive commercial browsers continue to provide new capability and are available for all significant computing platforms presently in use. The web-browser interface is a de facto standard for interaction with computers. It has been shown that use of the web has been of great advantage to several PL projects. The standard protocols used by the web such as HyperText Transmission Protocol (HTTP) and Common Gateway Interface (CGI) have provided a robust, flexible paradigm for constructing software systems. HTTP is the protocol that a browser or other software uses to obtain HyperText Markup Language (HTML) documents and imagery. CGI is a mechanism that allows a user to run programs on a remote web server. Constructing a web server allows transparent interaction between commodity Wintel platforms and UNIX workstations. Use of the web has made it possible to exploit large background data sets and efficiently deliver information to the warfighter using existing computer hardware/software infrastructure. IRTSS, as well as the Cloud Scene Simulation activity in the following section, have employed this technology.

1.2 CLOUD SIMULATION

Strategies for dealing with cloud cover have been of concern to the Air Force since its inception. Clouds can adversely affect many types of military missions, from satellite reconnaissance to special operations forces. Satellite imagery has been a very effective tool for predicting and locating cloud cover. Fast, accurate, and automated analysis of satellite images is critical to the management of modern high-throughput live data feeds. The ability to extract information from imagery in near real-time is important to the warfighter.

1.2.1 SERCAA Algorithms

Support of Requirements for Cloud Analysis and Archive (SERCAA) algorithms were developed by AER and were designed to provide multi-layer cloud analysis of geostationary satellite images. The multilayer cloud information can be constructed from live data-feeds.

SERCAA reads a pair of images in Terrascan data format (tdf). The tdf files are the direct output product of the SeaSpace, Inc. downlink hardware located at AIMS. SERCAA requires visible and infrared co-located images that ideally differ in time by one or two hours. With these images, SERCAA performs nephanalysis algorithms to first produce a cloud mask buffer, (called the Mask and Confidence Flag, or mcf buffer), with one byte of information per image pixel. These operations use, at minimum, one long-wave infrared and a visible spectrum data channel, along with short-wave and medium-wave, if available, and with sun angle, geography, and surface temperature data to run temporal differencing and spectral discrepancy tests to determine the location of which pixels contain clouds. At present, surface temperatures are acquired from a coarse-grain database of monthly averages. Geography information is taken from a static database and mapped to a clear-case background brightness for temperature differencing tests. The cloud mask bit-flags in the mcf buffer indicate the presence of cloud; the detection of several cloud category clues like cirrus, low altitude or precipitating, and a confidence bit. The mcf buffer is then passed to another set of algorithms that generate stratified information, using the cloud mask and IR data, about cloudy pixels. Clustering and maximum likelihood classification algorithms categorize up to four cloud layers into stratiform or cumuliform, estimate coverage, and determine mean cloud-top temperature, which can be used to make crude cloud-top altitude approximations through the use of a standard atmosphere. The ability to derive this much information from two satellite passes makes SERCAA a valuable tool.

Radex has gathered the core SERCAA algorithms into one fast, automated software program, giving PL the ability to go from downlinked satellite imagery to analysis product within minutes, once a data subset is selected. This consolidated SERCAA software utilizes new data manipulation algorithms with a streamlined, comprehensive software design. It incorporates the AER-developed analysis routines largely intact, allowing scientists to perform a cloud analysis on a geostationary satellite image in a single action. Actual analysis now completes within 15-120 seconds depending on the size of selected analysis area.

1.2.2 SERCAA Output Products

The SERCAA output products are needed by other cloud modeling efforts and the software has been adapted to work in conjunction with other models. SERCAA provides an excellent starting point in a unified suite of software models and tools to bridge the gap between low-resolution satellite images and high-resolution atmospheric models. The SERCAA software was modified to produce three categories of output:

- 1) Terrascan data format files, easily used to visually validate results directly against the input tdf files;
- 2) ASCII CSSM model input files -- Cloud Scene Simulation Model (CSSM) produces high resolution 4D liquid water content fields that describe clouds. The core of the model is a fractal algorithm whose parameters have been tuned so that the produced fields look like clouds. The model is widely used for synthetic scene generation of cloud scenes. Gathering appropriate input data for CSSM is not a trivial task. SERCAA analysis products provide most of the needed inputs.
- 3) netCDF databases with gridded analysis product for integration with other simulation platforms, such as the PL/GPM weather simulation or IRTSS.


1.2.3 Integration of MM5 and CSSM

A prototype integration of PSU/NCAR Mesoscale Model Version (MM5) and the PL Cloud Scene Simulation Model (CSSM) is described [Setayesh, 1996]. The MM5 is a numerical hydrodynamical model designed to predict mesoscale and regional-scale atmospheric circulation. The CSSM is an empirical model that produces high resolution, multi-layer, four-dimensional cloud liquid water content fields and uses two sets of data for its input, viz., meteorological data and cloud data. CSSM has been using meteorological input data fields from NORAPS to use MM5 output data for CSSM, routines were needed to convert the MM5 data field to NORAPS data field format, as described in the Setayesh [1996].

1.2.4 PL Virtualskies

Another demonstration of coupling data with model software in order to do high-resolution simulation is the PL VirtualSkies jointly with PL/GPOF. The VirtualSkies site offers the user the ability to go from a satellite image to a fine-detail visualized scene through a short series of steps by combining SERCAA, CSSM and a visualization tool, allowing the user to interact with each model's parameters at each phase. The VirtualSkies site displays an actual meteosat image. The user clicks on a pixel whose location is mapped to the geographic location in the image. SERCAA cloud analysis product is then produced for that location, and this is fed to the CSSM in the form of cloud deck parameters. The user can interact with these cloud parameters and then run the CSSM using this input.

The user can generate a scene of the three-dimensional cloud-field that the CSSM has just produced by selecting the image's viewpoint interactively. Along the way, the CSSM's liquid water content and either the starting or finished, simulated images can be down-loaded by the user, as shown in Figure 5.



US Air Force
Phillips Laboratory
Weather Simulation Facility

Here are the clouds parameters at the selected site:

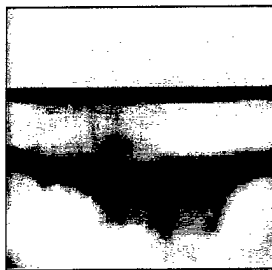
	TYPE	COVER	BASE	TOP
LAYER 1	Cirrostratus —	3/8 —	6 km —	7 km —
LAYER 2	Altostratus —	3/8 —	3 km —	5 km —
LAYER 3	Altostratus —	2/8 —	2 km —	4 km —

Random Number Seed (for fractal algorithm): 1234

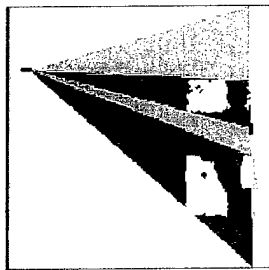
Submit Query
Reset

View Geometry

Altitude: 25000 ft
Azimuth: 45 deg
Range: 15 mi
Time: 35 sec



Cockpit View



10 km. Cloud Cross-Section

Figure 5. Virtual Skies cloud parameter web page interface.

Here, two distinct projects that use large amounts of environmental background data and support users at remote sites has been outlined. In both cases, the use of web technology provides a software infrastructure that is economical and effective.

1.3 DATA IMPROVEMENT

A large database of FLIR (Forward-Looking InfraRed) images exists for validation of the ACT-EOS project's PL Modeling and Visualization software. Raw FLIR imagery has been taken for comparison to the IRTSS scene generation process. Validation of the model depends on comparison of specific areas in the synthetic imagery with the real imagery. The ability to analyze the images depends upon compensating for the FLIR's camera drift, amidst image-processing obstacles such as low signal-to-noise ratio and image distortion, as well as FLIR sensor noise compounded by compression and interlacing artifacts.

The primary goal was to correctly register the large body of movies in a short period of time with a minimum of human interaction, so that statistical analysis of the brightness of specific objects in the scene, from which temperature is easily derived, could be performed. The best of earlier schemes to register the FLIR movies generated unsatisfactory results with all but the cleanest of data-sets and consumed over 5 seconds per frame processed.

The second goal was to develop an implementation that adapted automatically to different scenes. Originally, the test scenes were of a target site that consisted of relatively high-contrast (via cyclical heating) geometrically-shaped objects. Ultimately, registration and analysis must be performed with natural landscape scenes containing irregularly-defined features, such as vegetation and roads.

Due to mismatched gains from the two rows of the FLIR sensors, the FLIR images also appear to be striped. Interlacing enhances this effect, making the stripes two pixel-rows in height. Compressing the images compounds the problem by causing any given dark/dark or light/light pair in a stripe to have identical row sums, making it virtually impossible for the software to "distinguish" individual scan-lines when correlating. Furthermore, a large number of the images in the dark-set also have a column offset of one or two pixels because of a sensor time-delay error, giving edges a saw-tooth appearance (Figure 6).

Image registration requires a modicum of clarity in the reference image. Most methods assume that a noise-free reference is unattainable [Eversole and Nasberg, 1983] and that rectification must be performed on an image prior to registration to correct for different perspectives and resolutions, typically the result of a movie camera, e.g., satellite image processing.

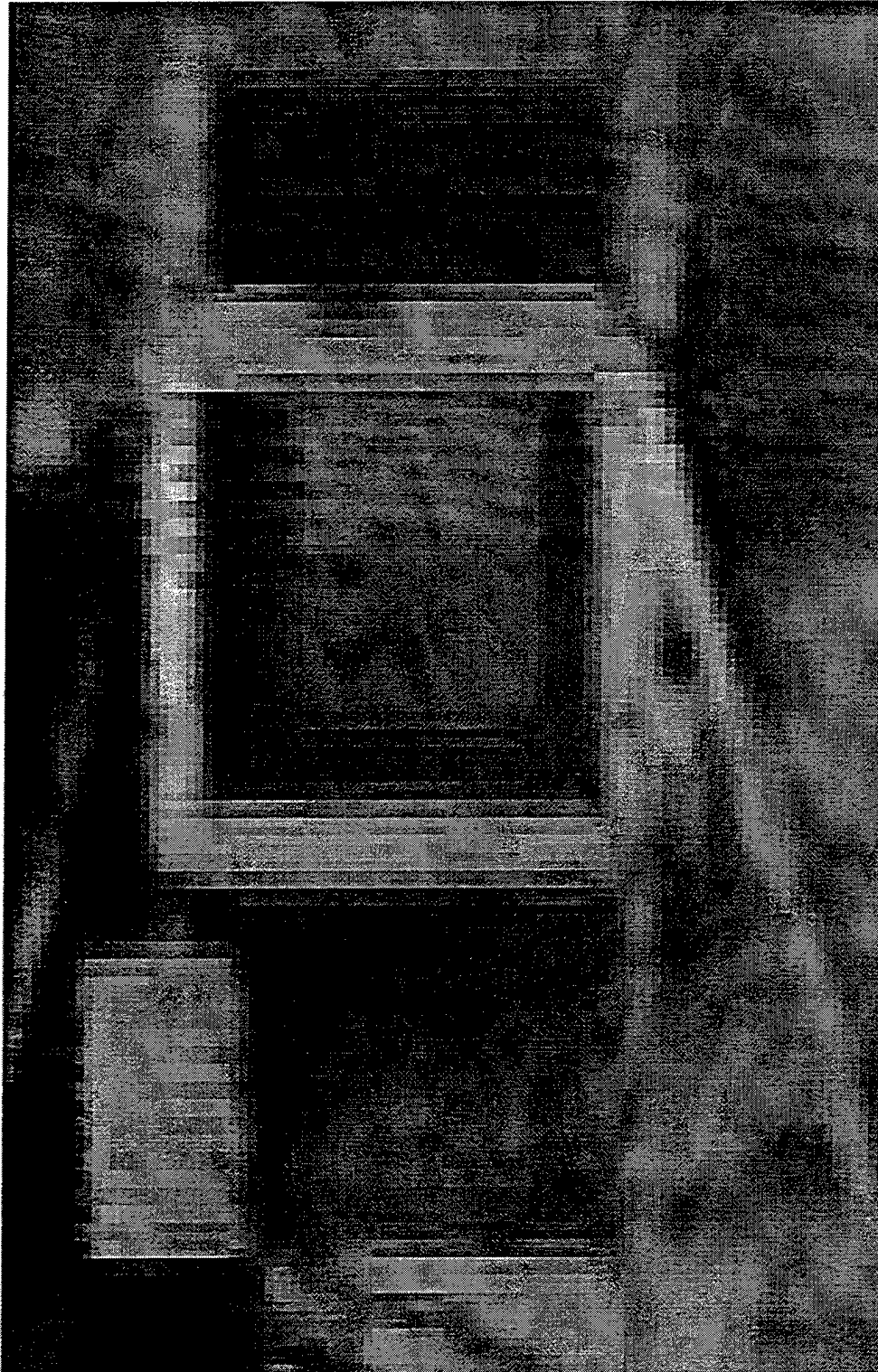


Figure 6. A good example of banding due to FLIR sensor defects. Each stripe is two pixels in height. Note jagged vertical edges.

The basic image registration method employs correlation of a reference image to a filter image [Pratt, 1978] using Fast Fourier Transforms [Schowengerdt, 1983]. Both reference and filter images were used full-frame (640x480 pixels). The reference image is reversed and normalized, and an FFT is performed. Each frame of the movie is used as a filter. An FFT is performed on the filter image, the product of the two is calculated, and then an inverse FFT is run on the result. The maximum of this function represents the registration of the two images, or the number of pixels that the filter image drifted from the canonical position of the reference position.

Initial efforts to register the movies used a “clean”, high-contrast frame directly from the movie being processed as a reference image. This method produced mixed results due to the image’s inherent sensor, interlacing, and compression noise. Thus, success in registering images using a canonical FLIR image as a reference depended heavily upon the filter’s image similarity in contrast signal-to-noise, and banding orientation. To overcome this limitation, two reference images were constructed from the original FLIR references, one for each target scene in the data-set, with a COTS GIS package, ARC/INFO. The scene was classified by hand, with each feature-class mapped to a different color, e.g., grass was mapped to green, target legs were mapped to blue, and the calibration plates were each mapped to a separate shade of gray (Figure 7). This noise-free reference provided sharp edges and eliminated the difficulty of choosing a single good reference from the FLIR images. It made the registration method much stronger by allowing individual correlation of each feature-class in the image.



Figure 7. The full-frame color classification of the test-target scene.

This method produced accurate results even with poor quality filter images, but ran slowly, approximately one minute per frame due to the heavy computational burden of correlating (two 640x480 images) for each feature. The target reference has 11 features and the landscape reference has 20 features. In order to increase speed, the colored reference image, hereafter referred to as the "cartoon", was cropped to include only features that are nearly always visible above the noise in the FLIR images. Each filter image was cropped accordingly for the registration. A rectangular cropped area of roughly 10,000 pixels, including the roughly 60% of the original reference features, proved sufficient to successfully register movies in which the cropped portion was distinguishable in every frame.

The multiple sub-area correlation variation [Lo and Gerson, 1979] provides quick registration with the ability to avoid false fixes by feeding the multiple registration data to a decision-making function that essentially determines which of the data is least aberrant, taking advantage of the fact that the drift in the FLIR movies is smooth on a frame-to-frame basis.

The registration software is effective to within 4 pixels and takes about 1.6 seconds per frame. Figures 8 and 9 show before- and after-registration column slice vs. time images for one experiment, respectively. Overall vertical drift in the uncorrected movie is 18 pixels. The corrected movie drifts a total of 4 pixels, despite visible evidence of image size distortion over the course of the movie, and the signal-to-noise varies widely over the course of the movie. Given this performance, the goal of correctly registering FLIR images quickly with little human interaction was achieved.

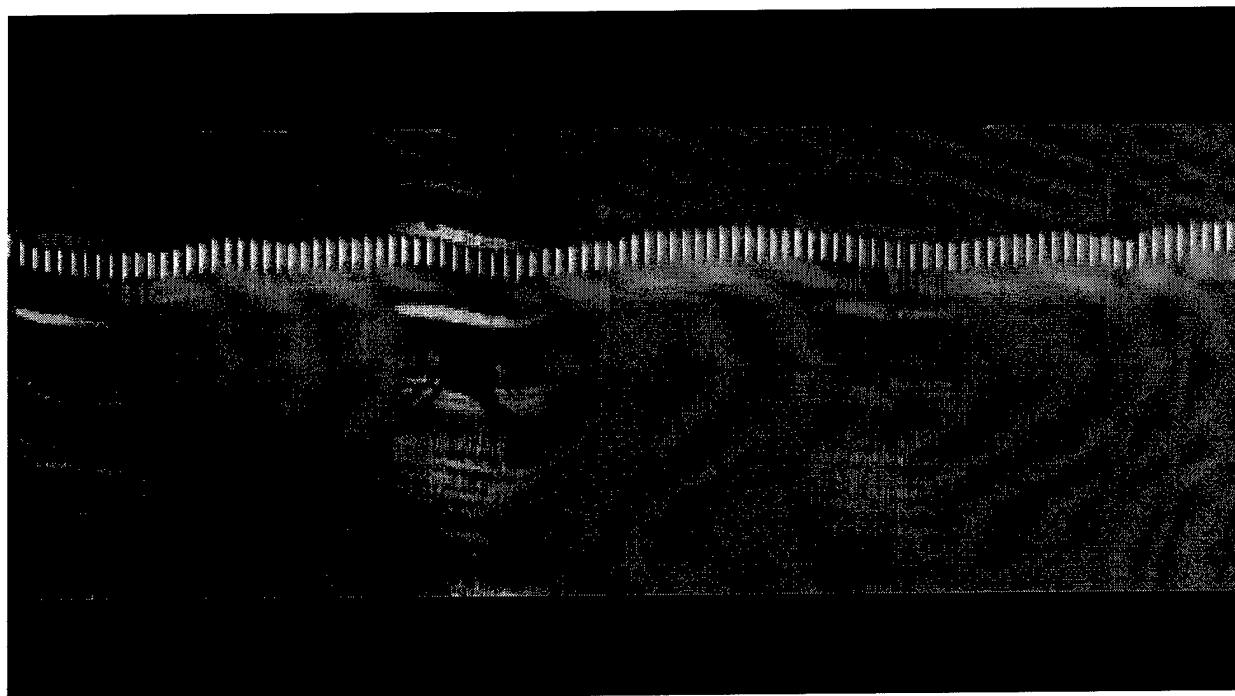


Figure 8. A column slice of the test-target scene vs. time, before registration. The column selected bisects the calibration plates. Vertical motion represents camera drift.

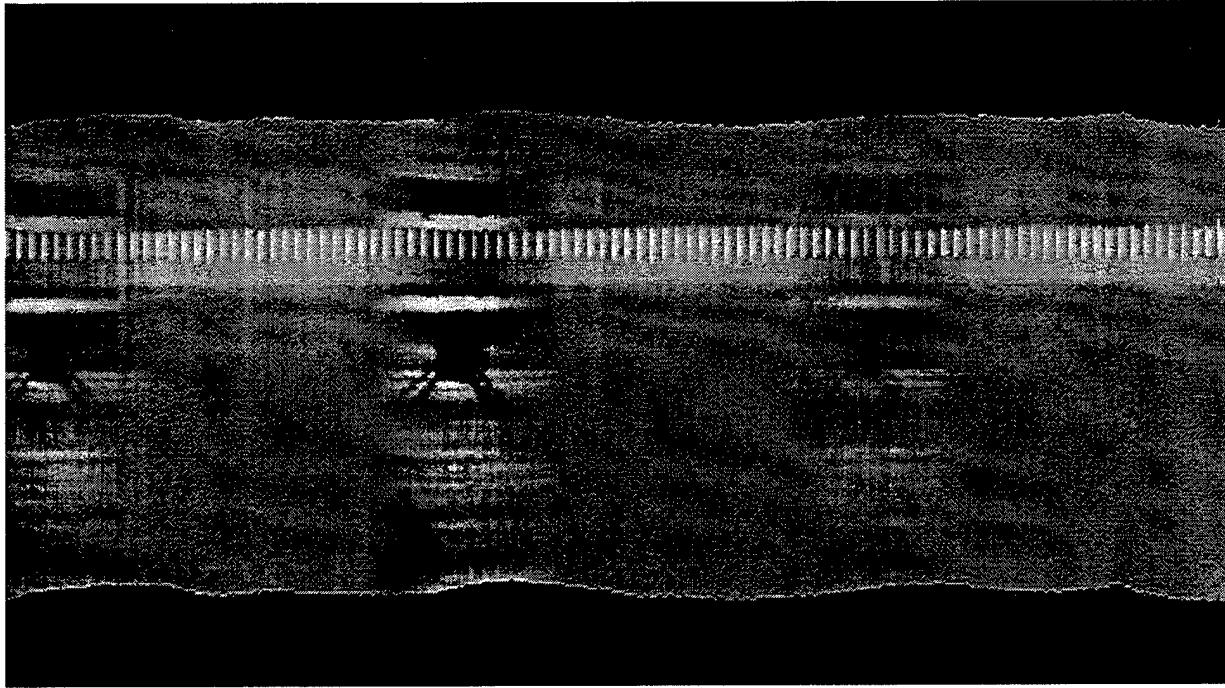


Figure 9. The same column slice vs. time as in Figure 8, after registration.

1.4 THE ITASCA EXPERT SYSTEM

The development of ITASCA, a knowledge-based system, is an outgrowth of a need for tools that provide the best weather forecasts in a situation where there is lack of an experienced forecaster and unavailability data from a central station. The ITASCA expert system was developed for short-range weather forecasts from limited observational data. In this system ITASCA follows some methods to forecast the weather. These rules and methods are generally based on three categories. The first is inheritance in which the object of the same property is inherited from its parent. The second method is through a set of actions in which the object is determined from an external source such as a function, using another knowledge base object, querying of the user, and/or the assignment of a default value. The object can be determined by the third method which is through an "if change" mechanism. The object can also be evaluated from a combination of these three methods [Jaspersen, *et al.*, 1992].

In order to perform a meaningful evaluation of the ITASCA software package, a large amount of meteorological data was required. Air Force Combat Climatology Center (AFCCC) archive data was identified as an appropriate source. The evaluation was designed to run using the AFCCC observations and compare them with the ITASCA forecast quantities.

The data used in the evaluation are the surface and upper air data provided by AFCCC. The surface data is WBAN Hourly Surface Observation 144 from the Data Processing Division, Air Force Combat Climatology Center. The surface data package contains about a year of meteorological data

for several stations in the United States. The stations have been organized into 6 geographic areas. The station groups are:

- Set 1) Monterey CA, Oakland CA, San Francisco CA, and Livermore CA
- Set 2) Albuquerque NM, Denver CO, and Pueblo CO
- Set 3) Abilene TX, Amarillo TX, Lubbock TX, and Austin TX
- Set 4) Green Bay WI, Madison WI, Eauclair WI, Dubuque IA, and Milwaukee WI
- Set 5) Atlantic City NJ, Dover DE, Harrisburg PA, and Pittsburgh PA
- Set 6) Norfolk VA and Parkersburg WV

The surface data contain most of the meteorological data given in one row up to 80 columns for each hour in alphanumeric format. The upper air data is DATSAV2 Upper-Air Database from AFCCC. The Data cover a one year period beginning in January 1989.

1.4.1 Evaluation Process

A number of routines were developed to read the ITASCA forecast output data and generate ASCII data suitable for a plotting package software. This included choosing the desired date and time of the day, and generation of difference and average difference data from the ITASCA forecast and AFCCC observed data.

After initial testing of data with ITASCA, we ran into some problems with simulation of data with the ITASCA. We determined the problems mostly resulted from incomplete, and in some cases, incorrect data from AFCCC. Therefore, modifications were made to the AFCCC to ITASCA translator routines to write reasonable data for the missing and incorrect records. This approach was unsuccessful and problems making runs with ITASCA continued. It was then decided to modify the translator to throw out all the incomplete data, but continue to make minor corrections to data such as total sky and total opaque coverage, and dew point temperature. These modifications led to running the ITASCA prediction package for all sets of 6 stations for at least 12 hours of observation data.

1.4.2 The Evaluation Results and Analysis

The ITASCA analysis is based on comparing the AFCCC observed data with the ITASCA forecast data for 3 to 12 hours of history. The quantities that will be analyzed here are pressure, temperature, visibility, and wind speed. The other quantities such as, wind direction, cloud information, total sky and opaque sky covers, rain and snow falls, and others are not discussed here mostly because of either incomplete data, and/or lack of data given in AFCCC surface data.

Running ITASCA produces 12 hours of weather forecast for each hour, and therefore it produces 144 hours of forecast data for a run of 12 hours. For each case presented here, ITASCA has been run for

up to 12 hours of history. The quantities such as pressure, temperature, wind speed, and visibility have been plotted for 3, 6, 9, and 12 hours of forecast history. These plots represent several stations including Atlantic City, New Jersey, Harrisburg, Pennsylvania, Parkersburg, West Virginia, Des Moines, Iowa, and Amarillo, Texas. All the quantities are plotted for several days in January 1990. The average quantities represent from 8 to 15 days of data in the month of January. The Des Moines, Iowa data are not provided by AFCCC and it came with ITASCA for testing purposes. The Des Moines data are for less than three days of data and the average plots presented here are only for two days.

Figure 10 shows observation and forecast temperature results for Parkersburg WV during January 1990. The ITASCA forecast does a good job of predicting the temperature using 9 hours of weather history.

Figure 11 shows average wind speed difference for Des Moines, IA during January, 1990. Runs using from 3 to 12 hours of weather history to make the forecast are shown. In this case ITASCA is able to use the 12 hour weather history to improve its forecast.

1.4.3 Summary and Conclusion

There are some problems with ITASCA. It does not adequately reject unreasonable data supplied to it. The forecast temperature shows normal expected temperature variation for individual days in which it increases as the day progresses and reaches its peak in early afternoon. However, it fails to forecast any abnormal and sudden change in temperature.

The plots of pressure, wind speed, and visibility show a good forecasting prediction in most of the cases. The ITASCA software is able to make forecasts of reasonable accuracy for up to 12 hours into the future. This was demonstrated for several geographic locations.

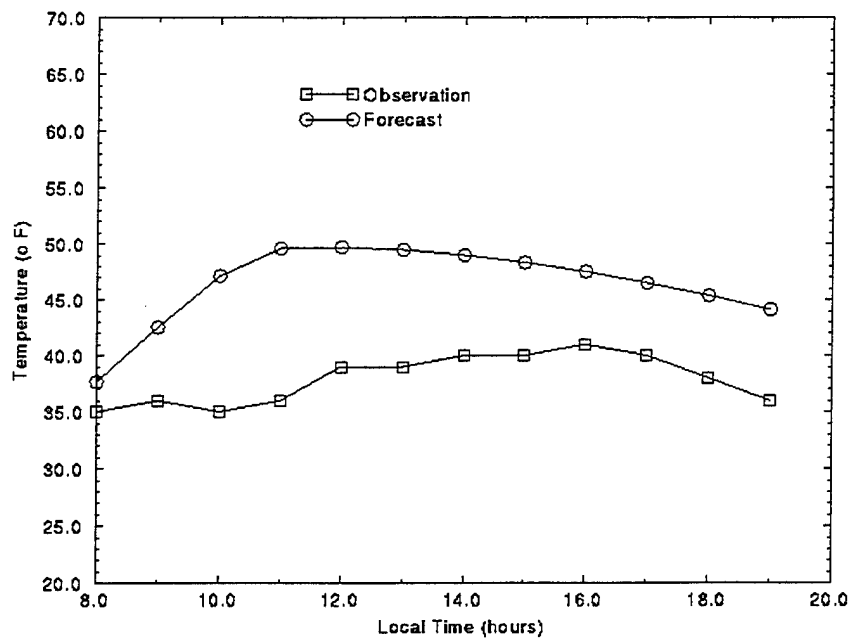


Figure 10. 12 hours observation and forecast temperature profiles, January 3, 1990, Parksburg, WV, at 12:00GMT with 9 hours of weather history.

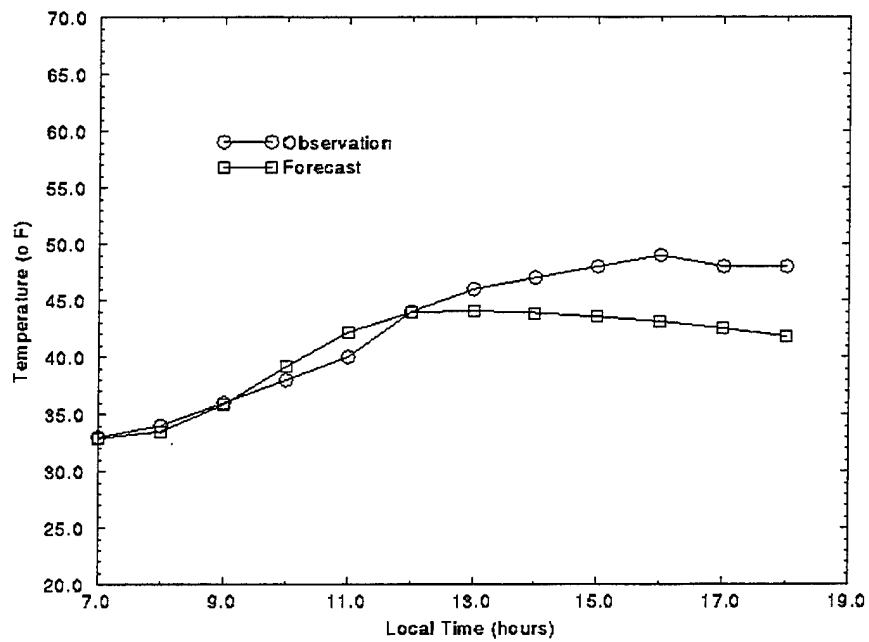


Figure 11. 12 hours observation and forecast average wind speed difference, selected days in January, 1990, Des Moines, IA.

2. SCINTILLATION NETWORK DECISION AID (SCINDA)

After two decades of intensive theoretical and experimental investigations, the space-time variability of nighttime F-region irregularities remains an outstanding problem [Basu and Basu, 1985; Basu, *et al.*, 1996]. These irregularities cause amplitude and phase scintillation of satellite signals which cause serious concern with system engineers. Scintillations affect satellite communication and navigation systems in various ways [Aarons and Basu, 1985; Basu, *et al.*, 1995]. Amplitude scintillations induce signal fading which can produce message errors in satellite communication systems and may cause the loss of position fix or degradation of accuracy in Global Positioning System (GPS) navigation systems.

Forecasts of equatorial scintillation are needed to be certain that the outages are caused by scintillation and not by system failures, and also, to develop alternate methods of communication and navigation. This need has been emphasized in the interagency "National Space Weather Program (NSWP) Strategic Plan".

The climatology of equatorial scintillation is quite well established and its features can be reproduced by use of the upgraded scintillation model, WBMOD [Secan, *et al.*, 1995]. However, scintillation weather information can not be provided due to the extreme temporal and spatial variability of scintillation.

There are, at least, two types of nighttime F-region irregularities arising in the equatorial region, namely, those related to plasma bubbles [Harendel, 1973; McClure, *et al.*, 1977; Scannapieco and Ossakow, 1976; Ossakov, 1981; Kelley, 1989], and the other type called the bottomside sinusoidal (bss) irregularity [Valladares, *et al.*, 1983].

2.1 PL-SCINDA

The Phillips Laboratory Scintillation Network Decision Aid was developed as a "proof of concept" system with the purpose of providing near real-time warning of communication outages due to equatorial spread F (ESF) instabilities [Kelly, 1989]. The ESF phenomenon results in plasma density depletions or bubbles in the topside ionosphere. Data is collected at two South American locations which continuously monitor the scintillation index S_4 . The complete process of downloading the data through analysis is described [McNeil, *et al.*, 1997]. The data are analyzed with the Discrete bubble Model (DSBMOD) [McNeil, *et al.*, 1997] which detects, characterizes, and propagates the depletion bubble to provide a picture of current outage conditions and to forecast predicted outages for the next few hours. Output from the model consists of three-dimensional depletion bubbles which are mapped along magnetic field lines; have characteristic top-side heights, time durations, and turbulence strengths; are calculated from the measured S_4 , and are dependent on the geometry of the station and satellite link where the measurement was made. A data-driven model of the anomaly crest is used to predict the scintillation level along the latitudinal extent of the bubble and

a phase screen model [Rino, 1979] is used to compute the equivalent S_4 for arbitrary ground station and satellite pairs.

The model results are displayed and manipulated by a visualization tool incorporating several options of operational significance. The tool has full ephemeris capability for any satellite in the current data base. Bubbles are displayed in three dimensions along with selected ground station to satellite links, and continental outlines or a surface photograph are rendered for orientation. Links are colored to indicate outage conditions. In addition to the real-time capability, the tool has a playback option for anomaly analysis. Two-dimensional maps can also be generated showing ground projections of the bubbles with S_4 index computed for a chosen satellite and frequency. The 2-D maps can be projected ahead in time up to a maximum of three hours to show the predicted outages at future times. Hard copy of these maps, suitable for facsimile transmission, can be generated in support of mission operations. To provide global coverage and to forecast when scintillation has not been observed or data is not available, the tool displays the predictions of the Wideband Model WBMOD [Secan, et al., 1995]. This version of WBMOD is itself driven by real-time scintillation data, where available. The overall concept of SCINDA is diagramed in Figure 12.

The two sensors now in place have been operational for more than two years. Climatological information gathered from the rather unique configuration is currently being analyzed and is expected to contribute to our understanding of equatorial ionospheric irregularities. The system is being expanded to provide coverage in regions of military significance and to investigate the global behavior of scintillation. GPS scintillation units have been installed at the South American sites and the unit at Antofagasta is now fully integrated into SCINDA. In November of 1997 a dual GPS/UHF system will come on-line at Ascension Island, and shortly thereafter a GPS in Northern Australia will become available.

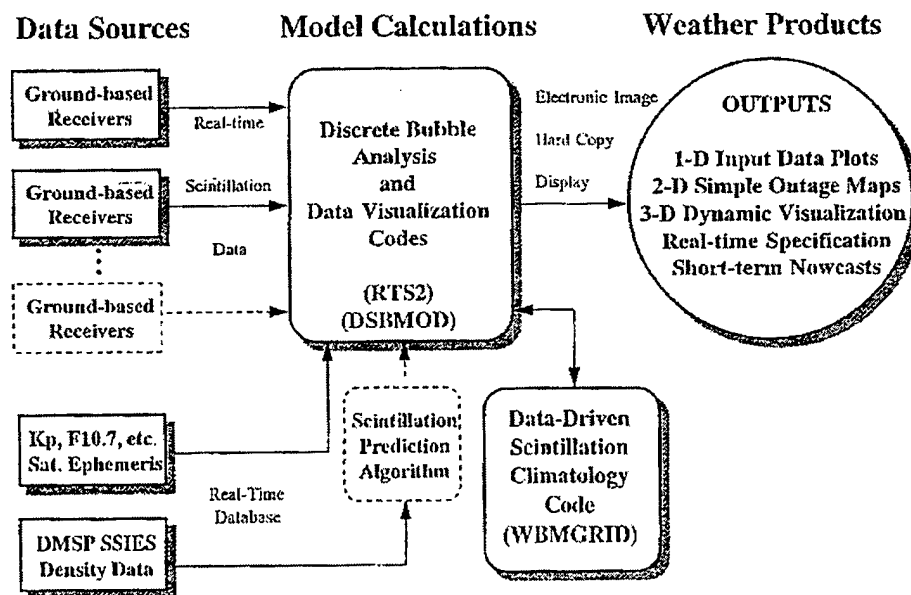


Figure 12. SCINDA system concept.

2.2 GEOMETRY OF OBSERVING STATIONS

The locations of the ground stations used to provide scintillation in this discussion are shown in Figure 13. The Ancón, Peru station is located near the magnetic equator and Antofagasta, Chile is situated close to the crest of the equatorial anomaly at a magnetic latitude of about 11° South. Both receivers are tuned to 250 MHz geosynchronous satellites at 99° west longitude and 23° west longitude measuring UHF scintillation. They are also tuned to the GOES-8 satellite which is approximately overhead, providing scintillation measurements in the L-band. The locations were chosen so that the ionospheric penetration points of the westward link at Antofagasta and the eastward link at Ancón lie approximately along the same field line. The intersection of the propagation paths from the two 250 MHz satellites with the ionospheric height of 300 km, namely the sub-ionospheric points, are indicated dots.

Measurements at Ancón are about 1 degree above the magnetic equator and those from Antofagasta are about 11 degrees below, near but somewhat north of the peak of the anomaly crest. The separation in longitude of the penetration points allow for observation of longitudinal variations in climatology and of the time evolution of plume structures. Taken together, the configuration covers about 12 degrees in longitude from about 66 degrees to 78 degrees West. Measurements are made throughout the night and throughout the year. On-site processors compute an S_4 value for each link about once per minute and one-half. Redundant measurements from antennae displaced about 100 meters to the east are used to calculate the eastward drift of the ionosphere, providing a drift velocity at the same frequency. Typical scintillation data are shown in Figure 14.

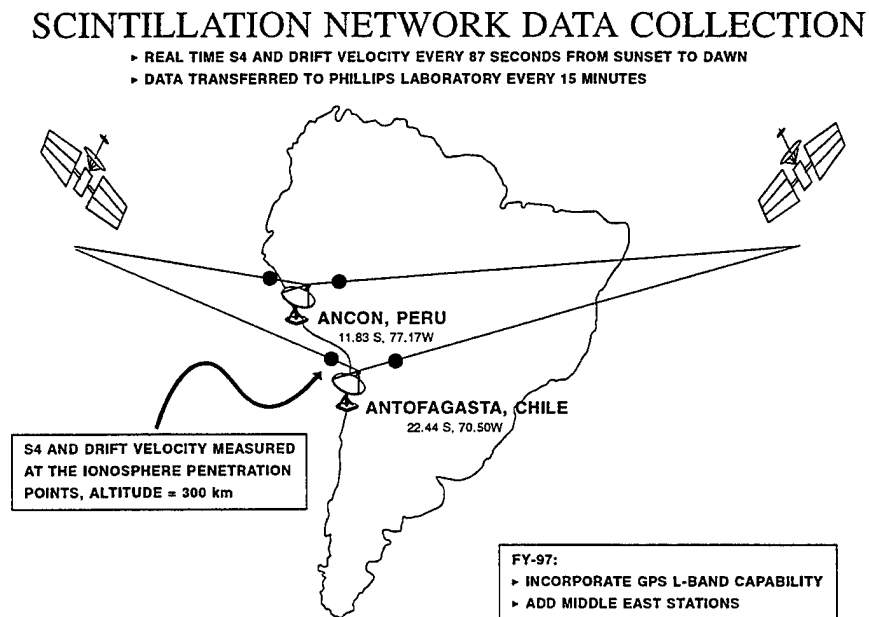


Figure 13. Schematic diagram of receiver locations and ionospheric penetration points for the current configuration.

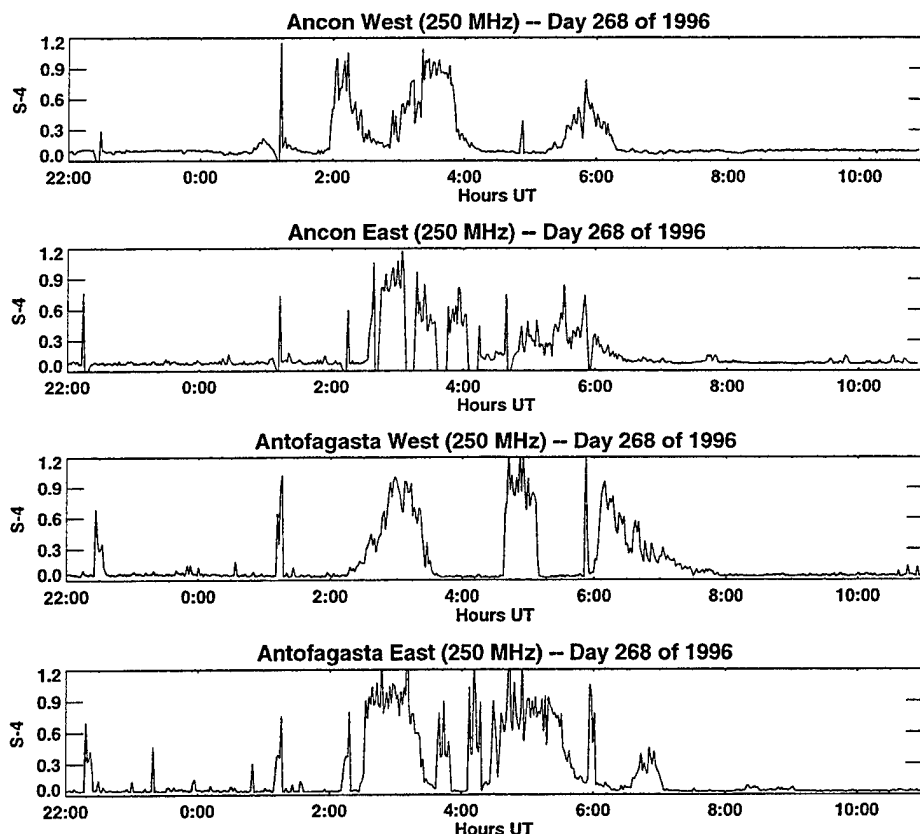


Figure 14. Sample scintillation data from the four links comprising the current scintillation bubble model.

2.3 THE BUBBLE MODEL

The scintillation data are introduced into the Discrete Scintillation Bubble Model (DSBMOD) which attempts to extend the information garnered from the stations over the entire operational theater, extrapolating both spatially in latitude and forward in time for forecasting. The S_4 values are averaged over 5 minute intervals, then normalized by computing an equivalent S_4 for an equatorial station located at Ancón and viewing a synchronous satellite at an elevation of 45 degrees to the east. This normalization compensates for the various elevations and angles relative to the geomagnetic field of the measured links. Added to the measured S_4 observed throughout the night are measured ionospheric drift velocity and several assumptions about scintillation bubble formation, evolution, and destruction. These assumptions include the rate of growth of the bubble topside, the rate of decay of the turbulence strength parameter $C_k L$, and the latitude dependence of the scintillation strength. The last of these is modeled from the observed scintillation along the common field line. The generation and destruction of bubbles detected at the four station-to-satellite links is governed by rules which are different for each link.

2.3.1 Bubble Recognition

Bubbles are generated by examining the S_4 data from each of the four links from sunset up to the present time. A bubble is created whenever two consecutive 5-minute S_4 values are encountered above a set threshold. A bubble is terminated whenever two points below the threshold are obtained. If scintillation persists above the threshold at a particular link for more than 30 minutes, the current bubble is terminated at the half-hour and a new bubble is begun. This technique allows for longitudinal variations in the modeled S_4 since each bubble is assigned an individual turbulence strength. Bubbles lasting less than 15 minutes are discarded. This is an additional technique for differentiating between scintillation structures and noise. Figure 15 shows the discrete bubbles that were generated from the data taken on Day 268 of 1996 along the 5-minute normalized S_4 values.

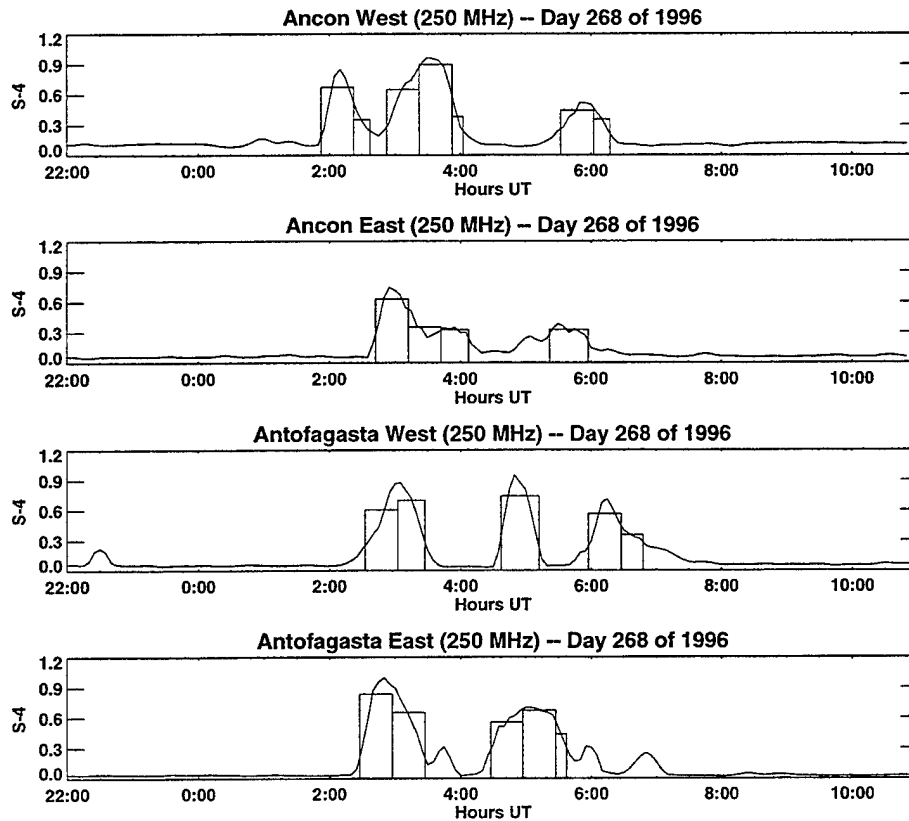


Figure 15. Edited and averaged S_4 data along with the bubbles generated from the night shown in Figure 14.

The figure illustrates how scintillation is allowed to vary over the course of a single event by the half-hour limit for any particular bubble duration. It is clear in the smoothed data that the boundary between scintillation periods is not sharp in most cases. We have chosen to represent the bubbles as periods of constant $C_k L$ for the sake of simplicity in the subsequent computations and display. For UHF communication, warnings are issued when S_4 reaches a value of 0.3. Whether or not events below this level are retained or not in the data is not important.

2.3.2 Bubble Propagation

Once detected, bubbles are propagated forward from the time of detection to the present time or to the time for which an outage projection is desired. Bubbles emanate from the penetration points of the respective links and move eastward with the modeled ionospheric drift velocity. Bubbles are characterized by a topside altitude at the magnetic equator and by a longitudinal extent. The initial and final topside altitude of a bubble depends on the link from which the bubble originates. Bubbles are assigned an initial topside altitude and allowed to grow upward at a rate of 50 m/s based on the age of the bubble. However, bubbles that are simply continuations of previous half-hour segments grow according to the first bubble in the segment. Bubbles from Ancón begin with an equatorial topside of 350 km and bubbles from Antofagasta begin at 450 km in order to put the bottom edge of the bubble at the Antofagasta penetration points. Bubbles shapes are computed along the field line intercepting the magnetic equator at the topside altitude and the geographic longitude of the bubble. The bottom side of the bubble is taken to be 300 km regardless of the bubble age. Bubbles grow to a maximum of 1,000 km for the purpose of field line tracking. However, the maximum height of any point in a bubble is limited to 650 km for display and for computation of the outages. This empirical restriction limits the region of scintillation to between 300 and 650 km, regardless of the height of the depletion. This is due to the fact that the ionosphere above 650km is sufficiently sparse, so that plasma depletions cause no significant fade.

Bubbles from Ancón West are allowed to grow and travel eastward until they come to the penetration point for Ancón East (equals Antofagasta West). There, they are destroyed since this scintillation, if it has not died away, should be picked up in the eastward link. Bubbles from Ancón East are generated at the link and move eastward, but grow only to a maximum topside of 400 km. This puts the bottom edge of the bubble a degree or two north of the Antofagasta West link. These are used to represent bottom side turbulence that does not develop into full-sized plumes. Plumes generated at Antofagasta West will occupy the same geographic area but will appear overtop the bubbles from Ancón East. Antofagasta West bubbles grow and drift eastward to the Antofagasta East link, where they are destroyed. Bubbles generated at Antofagasta East grow and drift and persist until sunrise. After local midnight, bubble topsides are gradually increased so that all bubbles, except those from Ancón East, achieve the maximum topside altitude. This represents the assumption that the late night plumes are more or less fully developed. An example of an early night bubble configuration and propagation is shown in *McNeil, et al. [1997]*.

2.4 ALL-SKY DEPLETION REGIONS AND GPS DATA VALIDATIONS

A data set containing reconstructed Eastward and Westward edges of four ionospheric depletion bands seen in 630 nm airglow images over Agua Verde was received from Ed Weber. The data, from the night of October 1, 1994, spanned nearly two hours beginning at 0000 UT and continuing through 0200 UT. GPS signal-to-noise (SNR) and total electron content (TEC) for the same evening were also provided. In Figure 16, the depletion regions are shown, in 10 minute time steps, as a gray shaded areas. The ionospheric penetration points of the GPS satellites at 300 km are included as

solid circles for satellites above a selected minimum elevation angle. They are shaded either light gray ("not scintillating") or black ("scintillating"). The two independent systems agree quite well when considering the geometrical effects of locating the precise bubble edges.

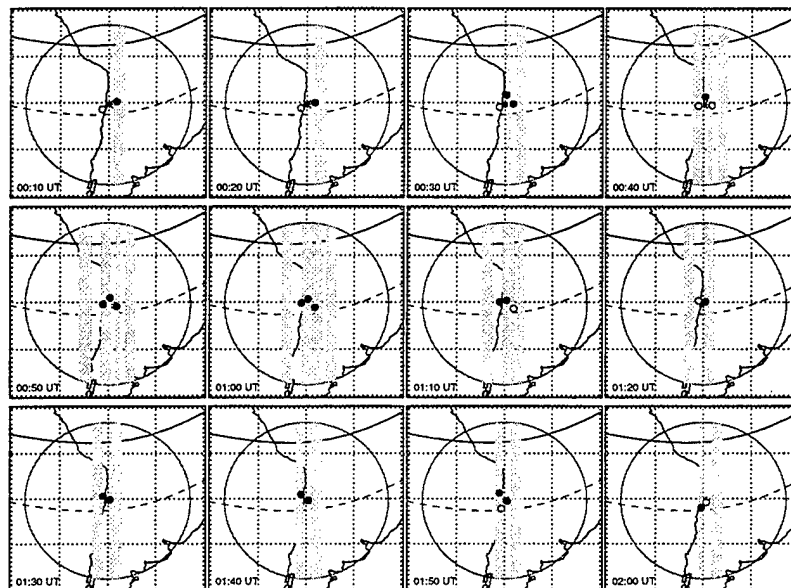


Figure 16. Depletion Regions of October 1, 1994.

Several steps were involved in producing the image in Figure 16. First, the Eastward edge of one of the four reconstructed depletions, which originally contained only a Westward edge between 0130 and 0200 UT, was extended to 0200 UT. This was accomplished by computing the average longitudinal extension of the bubble prior to 0130 UT and calculating the appropriate values to fill in the region. The extended area is shown in light gray in Figure 17, where the longitudinal extent of all four bubbles are shown versus time.

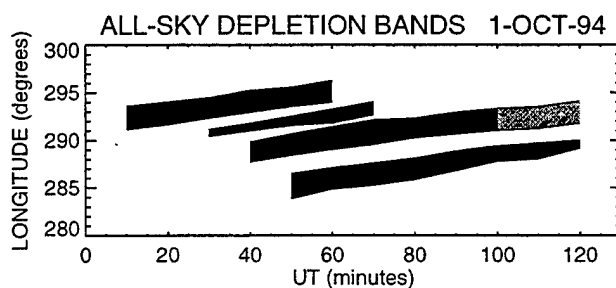


Figure 17. Depletions regions, longitudinal extent versus time.

Next, the ephemeris of each GPS satellite was generated, using the appropriate orbital elements. The ionospheric penetration points, along the line to Agua Verde, were then calculated, assuming an altitude of 300 km. Because we were interested in S_4 levels, we calculated an S_4 value from the SNR. To be consistent with PL-SCINDA calculations, 5-minute averages were used. The S_4 values were found using the following equation from *Aarons and Basu* [1985]:

$$(S_4)^2 = \frac{\langle P^2 \rangle - \langle P \rangle^2}{\langle P \rangle^2} \quad (1)$$

where P is defined as the power in dB. Because the power was not included in the data set, we used the SNR values and the following equations to define P as :

$$SNR = 10 \log_{10}[P] \quad (2)$$

or

$$P = 10^{\frac{SNR}{10}} \quad (3)$$

Because the reconstructed depletion band edges from the all-sky data were available in 10-minute intervals, the 5-minute average S_4 values were converted to 10-minute averages.

Weber, et al. [1996] suggested that a peak-to-peak fluctuation in the SNR of 7 dB, commonly seen in the 1 Oct 1994 data from GPS satellites numbers #21-22-23, corresponds to an S_4 index of approximately 0.35. Our values tend to agree with this, producing values of approximately 0.3 for GPS #21 during the heaviest scintillation. These numbers may be slightly lower than suggested, however, they are consistently calculated, allowing us to distinguish scintillation levels relative to all satellites.

2.5 PL-SCINDA: VISUALIZATION AND ANALYSIS TECHNIQUES

The PL-SCINDA system has been developed with the idea of displaying real time scintillation information from a network of monitoring stations. The main display of the SCINDA system, 3D Main View, is a three dimensional representation of the earth with scintillation structures and satellites shown above the earth, as illustrated in Figure 18. The display has many features which allow the operator to customize how the display will represent the data. Additionally, there are several components to the system including an Outage Map viewer, Comlinks selector, and DataPlot window. The entire system is based around use of the DSBMOD model. The structures are corrected to indicate the scintillation intensity at a forty five degree elevation angle.

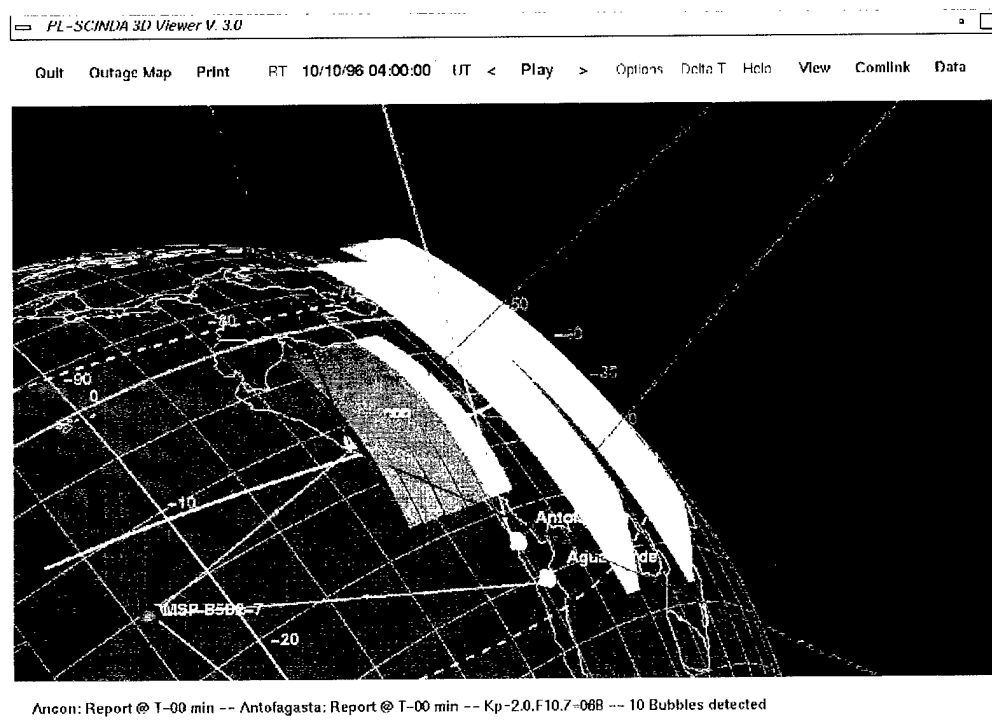


Figure 18. PL-SCINDA 3D Main View.

2.5.1 View Controls

In the main SCINDA display the view point can be controlled by two methods. The main display accepts events from mouse movement; rotation, translation and zoom features are available via the mouse. There is also a View Controls dialog window that has slider bars that can be used to precisely orient the display.

2.5.2 Map Selection Capabilities

The earth can be displayed whole, or with only the section of interest. A map selection dialog box allows sections by either latitude and longitude values, or by dragging over a map of the earth with the mouse and selecting a region.

2.5.3 Threshold Selection Capabilities

A dialog box allows the operator to determine which levels should be displayed in red, yellow, and green. The operator can input the thresholds in either S_4 (scintillation index) or dB fade units. The conversion between these values is calculated using the Nakagami - M distribution function.

2.5.4 Printing Capabilities

The main display has a dialog box that allows the contents of the display to be output into several file formats. Currently the IRIX RGB, GIF, and Postscript file formats are supported. Additionally, this dialog includes the ability to input a print command so that hardcopy will be generated directly from the SCINDA 3D Main View. This feature is also present in the Outage Map program.

2.5.5 Communication Links Program (Comlinks)

This is designed to allow an operator to keep track of any number of satellite to ground station communication links. A list of satellites from the NORAD orbital element database is displayed. Additionally, a satellite may be created using the mean elements of the satellite trajectory. The communications link is then created by matching a satellite with a ground station location, which can be entered by latitude and longitude. The final element to the communication link is the specification of the communications frequency. Many communication links can be grouped together and saved to files for later retrieval, and the telemetry data will be automatically updated with the new orbital element database information.

In the 3D Main View display, shown in Figure 19, these communication links are shown as colored lines to indicate if the communications pathway is passing through a scintillation structure. Green indicates a clear path, and red indicates an intersection with observed scintillation structures.

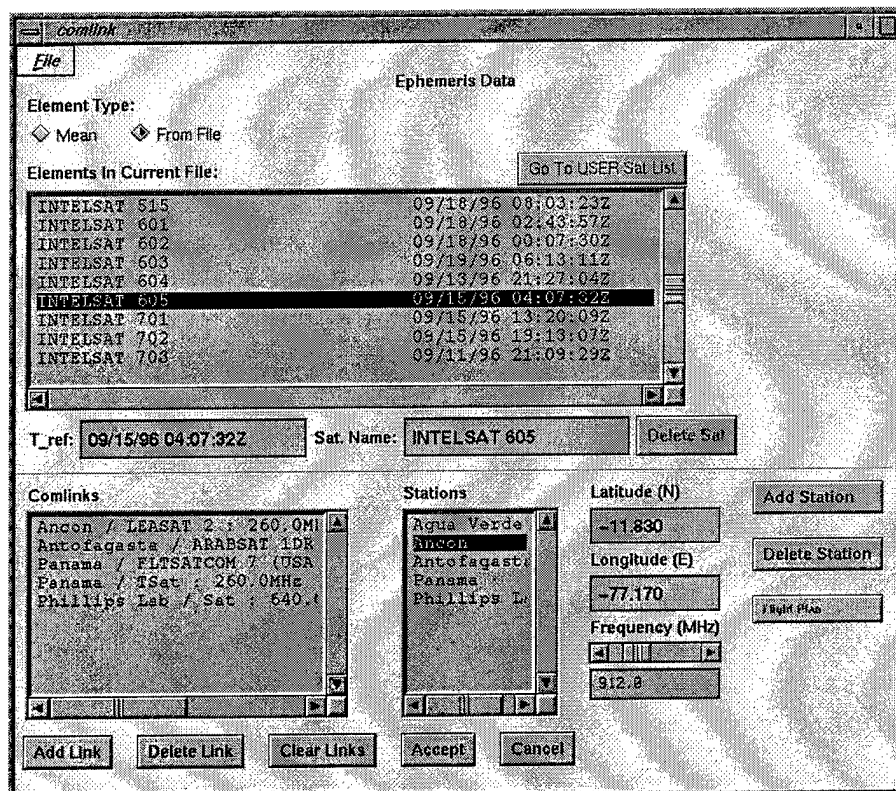


Figure 19. 3D main view display showing communications links.

2.5.6 Data Plotting Program (DataPlot)

A data plotting program has been developed to show an X-Y plot of the data currently coming in from the remote stations. Multiple data windows can be displayed at one time allowing a user to see all of the data simultaneously with the three dimensional visualization of the scintillation structures. The system is configured to update all data plot windows with the time displayed in the 3D Main View.

2.5.7 Outage Map Products

The Outage Map program was designed to give a scintillation weather report in terms that a field communications user can quickly understand. The outage regions are frequency corrected geometric projections from a selected satellite to the ground. The display, seen in Figure 20, shows only yellow and red regions superimposed on a map, based on selected dB fade margins. Solid areas denote warnings, indicating that scintillation structures have been observed that will degrade satellite communications in a region. Watch areas are displayed in an "x & o" pattern, and are based on the WBMOD climatology. The program used is called WBMGRID. The system currently has a three hour prediction capability built in.

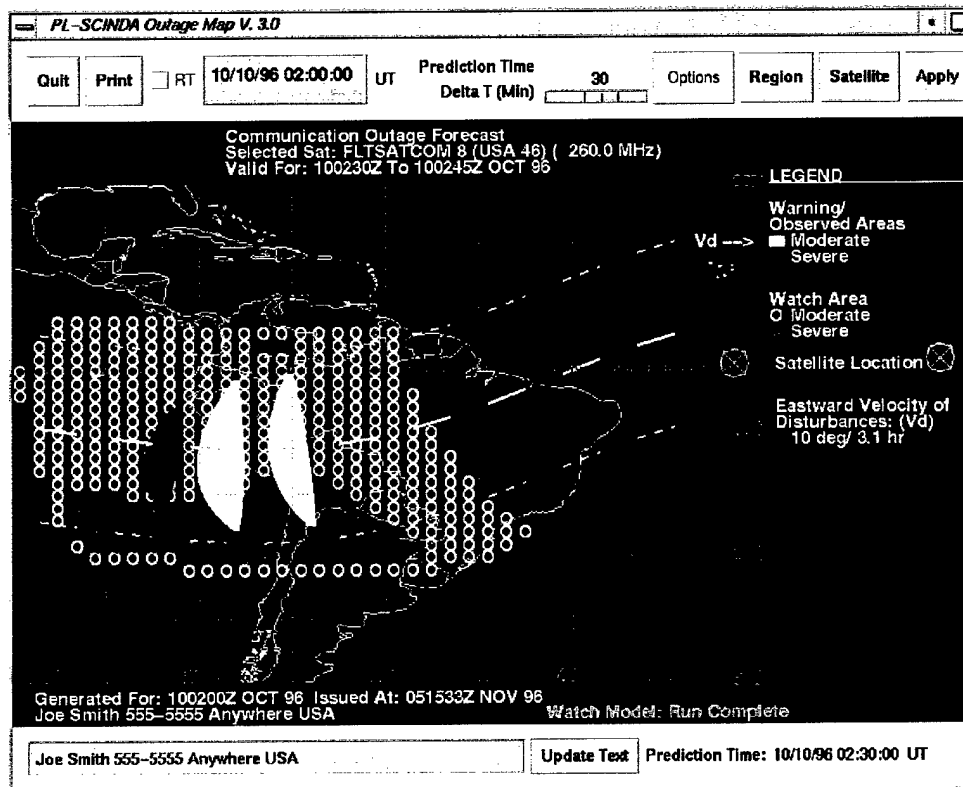


Figure 20. Outage map display.

The operator can selectively disable information displayed on the outage maps, such as coastal outlines and satellite location and frequency, making maps sent to the field practically useless to anyone except the intended user. Information can be given concerning satellite position, name and operational frequency. Map features and coordinates can be removed, and messages can be written into the printable display. Once an operator gets a request for an ionospheric weather report, the built in print feature can be used to produce and send information to a unit in the field.

2.6 SUPPORT OF PL-SCINDA INSTALLATION AT FALCON AFB

In April 1996 the first demonstration version of PL-SCINDA was installed at Falcon AFB in the operations center of 50th AWS. The original system had data to play back for the month of December 1995, and included only the preliminary capabilities of the SCINDA system.

In November of 1996 PL-SCINDA Version 3.0 was installed at 50th AWS and had a real-time capability. Though data transmission issues remained, the software installed had the capability of using real time data if it was transmitted to Falcon. This real-time capability was demonstrated for three nights in the month on November 1996 using a modem connection.

In early 1997, two deliveries of upgrades were made to 50th AWS and copies of the software were made available to the SWC and 76th SOPS at Falcon AFB. This consisted of versions 3.01 and 3.02. Most of the improvements dealt with bug fixes in the models and display features.

3. THE PL-GEOSPACE CODE

The PL-GEOSpace code for three-dimensional (3D) visualization of the dynamic space environment has been developed as one aspect of support for Space Weather for the Air Force. The program imports a variety of models of the near-Earth space environment including the ionosphere, aurora, and magnetosphere for both operational and scientific use. The code facilitates the assessment of space environmental hazards by bringing many environmental models together in a user-friendly graphics intensive program. With its 3D visualization capability and its variety of models the code provides an effective tool for magnetostatic and ionospheric research and education. The PL-GEOSpace program has been implemented on Silicon Graphics (SGI) workstations under UNIX operating systems (IRIX 5.x, 6.x). It uses a X/Motif widget interface and OpenGL is employed for graphics rendering. The executive system is written mainly in C++ using object-oriented concepts while the lower level coding can be in FORTRAN or C. The program is divided into science, application, data, graphics and worksheets modules. The current science objects are the radiation belt models (CRRESELE, CRRESPRO, CRRESRAD) [*Kerns and Gussenhoven, 1992; Meffert and Gussenhoven, 1994; Gussenhoven, et al., 1993; Brautigam, et al., 1992*], the Auroral Precipitation model [*Hardy, et al., 1985; 1989*] with 3D extensions, the parameterized ionospheric model (PIM)

[*Daniell and Anderson*, 1995], and the ionospheric wide-band scintillation code WBMOD [*Secan and Bussey*, 1994]. The application modules include orbit propagation using either LOKANGL [*Bass, et al.*, 1976] or SPACETRACK [*Hoots and Roehrich*, 1980], orbit integration of the CRRES data, magnetic field models (dipole, IGRF, Olson-Pfizer [*Olson and Pfizer*, 1974], Hilmer-Voigt [*Hilmer and Voigt*, 1995], *Tsyganenko* [1989], and specialized PIM graphics and ray tracing codes. The data module reads several Phillips Laboratory (PL) specific data formats, including electron and ion distributions from DMSP measurements [*Mullen*, 1996]. The graphics modules can display 1D line plots, 2D/3D coordinate slices, 2D/3D orbit plane slices, 3D isocontours, 2D/3D field line traces, and 2D/3D orbits along with satellite detector, earth and star background and axes depictions. Graphics options such as clipping, transparency, and various lighting modes can be utilized to enhance the views as well as the standard translate, rotate and zoom manipulations. The worksheets module is provided for support calculations such as calendar dates and various coordinate transformations.

3.1 DEVELOPMENT OF PL-GEOSPACE

The initial phase of effort was done to compare the PL-GEOSpace code, originally developed by R. Biasca at PL, with alternative programs using available graphics packages EXPLORER and IDL. The choice of PL-GEOSpace was made mainly on the basis of design flexibility and superior 3D graphics performance. Much work has been subsequently done to further develop and verify the PL-GEOSpace program.

- * Development of modules for displaying the CRRES data, both for 3D distribution plots and for calculation of orbit integrated fluxes.
- * Implementation of a prototype time dependent module for displaying dynamic models, with the input parameters being accessed from a master time file.
- * Implementation of a module to trace particle orbits through a given magnetic field, using the guiding center approximation.
- * Implementation of a prototype module for the interplanetary shock time of arrival (STOA) code.
- * Upgrading the module for displaying the Hardy average auroral flux model by adding an option for inputting the intermediate magnetic field and solar wind velocity.
- * Development of a module to read and depict DMSP high energy electron monitor (HEEM) data files of flux and count rates and displaying the corresponding satellite orbits.
- * Development of PL-GEOSpace module STARS that provides accurate celestial map including the position, brightness and color of visual stars down to 8th magnitude as well as the positions of the moon, sun and major planets for any given date.

* Development of PL-GEOSpace module DETECTOR that provides a 3D representation of the solid angle acceptance for a detector on a given earth orbiting satellite, as provided by the PL-GEOSpace module ORBITAPP. A two-dimensional "foot-print" of the intersection of the solid angle acceptance with the earth's surface is a user option.

In support of the PL-GEOSpace effort, work has been done on real-time database development and system management.

* Development of SQL database code ORBEL to access satellite orbital elements from the database of the 55th Weather squadron for input to PL-GEOSpace. Shell scripts have been provided to access these data on a daily basis and are currently providing daily updates at the 55th and Phillips.

* Development of SQL database code GLOBALS to access 3-hour K_p , a_p , F10.7, and sunspot number hourly from the database of the 55th Weather Squadron for real-time input into PL-GEOSpace.

* RMU archival scripts to perform daily incremental and monthly full backups of the database of the 55th Weather Squadron.

* System Administration duties on VMS and LINUX Systems.

The next sections will describe some of the PL-GEOSpace modules, the database development and system management in more detail.

3.2 THE CRRESPRO MODULE

The CRRESPRO science and application modules are a UNIX port of the PC program CRRESPRO developed and released by USAF Phillips Laboratory. The following is a brief description of CRRESPRO, based on the PC documentation. The CRRESPRO software uses flux models created from data collected by the proton telescope (PROTEL) on board the Combined Release and Radiation Effects Satellite (CRRES) flown from 25 July 1990 to 12 October 1991 during solar maximum. CRRES was in a geosynchronous transfer orbit with an inclination of 18 degrees, a perigee of 350 km, and an apogee of 33000 km. It traversed the radiation belts twice per orbit with a period of 9 hours 52 minutes. In March 1991, a magnetic storm caused a reconfiguration of the inner magnetosphere, resulting in, among other features, double proton belts forming over a certain energy range. Because of this change, two CRRES models were created. The quiet model uses data from July 1990 to March 1991, and the active model uses data from March 1991 to October 1991. The data is organized in terms of 2D arrays by normalized magnetic field and McIlwain L-shell.

3.2.1 The CRRESPRO Science Module

After the PL-GEOSpace user selects which data set is desired, the CRRESPRO science module calculates the B-L coordinates for each grid point in the user-specified magnetic field model. The resulting flux is then obtained from the B-L coordinates and the chosen data file. That flux is assigned to the grid point. In this manner, a fully 3D map of the proton flux data may be made from the CRRES data.

CRRESPRO Science Module Inputs

The CRRESPRO science module requires the user to specify the following information to determine the data set case.

B Model

The B-Model parameter chooses the magnetic field model to use to convert from the B-L coordinates to 3D space. The default is the B Model used to reduce the CRRES data, i.e., the International Geomagnetic Reference Field (IGRF85) with the Olsen-Pfitzer static model to represent the external field. Additional choices are a dipole field, a tilted dipole, a tilted-offset dipole, and the IGRF85 field with no external contributions. The IGRF85 internal field uses the Year, Day, and UT Global Parameters. Though less consistent with the original data reduction, models are computed significantly faster when the dipole field options are chosen.

Energy Channel

The energy channel parameter selects which of the proton flux data sets corresponding to twenty-two PROTEL energy channels between 1 and 100 MeV is to be considered.

Activity

The activity parameter specifies whether the QUIET (obtained before the 24 March 1991 storm) or ACTIVE (obtained after the 24 March 1991 storm) proton flux data sets are to be used.

CRRESPRO Science Module Outputs

The CRRESPRO science module returns a 3D Gridded Data Set of the proton flux for the selected energy channel and activity level in units of $\#/\text{cm}^2/\text{s}/\text{MeV}$. This data set can subsequently be viewed with the PL-GEOSpace graphics module.

3.2.2 The CRRESPRO Application Module

The CRRESPRO-APP module calculates proton omnidirectional fluence (differential and integral) over the energy range 1-100 MeV for user specified orbits and quiet or active geophysical conditions. Fluences are calculated from the CRRES proton flux maps and the input orbit. The explanation below is based on the CRRESPRO documentation. To calculate differential omnidirectional fluences per year for an orbit input by the user, the time in seconds spent in each $(L, B/B_0)$ bin is calculated and the differential flux for each bin is multiplied by the time in seconds spent in that bin. The individual bins are then summed and the resulting number is then multiplied

by seconds per year divided by the sum of time in seconds for all bins (including the time the orbit spends outside the model region). Integral omnidirectional fluence for a given energy channel is calculated from the differential omnidirectional fluence by summing over all energy channels with energy greater than the given channel (eliminating those with overlapping energy ranges) and multiplying by appropriate bandwidths. The CRRESPRO application module is independent of the CRRESPRO science module.

CRRESPRO Application Inputs

The inputs to the CRRESPRO application module are the orbit elements needed to calculate the satellite trajectories. The widget set presented upon creation of a CRRESPRO application module is the same as that used for the orbit application in PL-GEOSpace. The spacecraft can be selected from an ephemeris list available from and updated daily by the Air Force Institute of Technology (AFIT).

CRRESPRO Application Outputs

The CRRESPRO application module generates a text window which can be saved to a file. Included in the text are the input orbit elements and tables of both the differential and integral omnidirectional fluences (in units of $\#/(cm^2 \text{ MeV yr})$ and $\#/(cm^2 \text{ yr})$, respectively) calculated for twenty-two retained energy channels and for both active and quiet conditions. Also generated is a 1D Gridded Data Set giving the position of the satellite as a function of time.

3.3 THE HIGH ENERGY ELECTRON MONITOR (HEEM) DATA MODULE

The HEEM data module provides the capability to monitor the activity of radiation belt MeV electrons in near real-time using data from the Defense Meteorological Satellite Program (DMSP) satellites. The J4 electron and ion sensors flown on the DMSP spacecraft starting with F6 were designed to measure electrons and ions from a few tens of eV up to 30 keV. The DMSP auroral particle sensors have provided a wealth of data in this energy range for over twenty years which have been used extensively for scientific investigations and near-real time space weather forecasting. Software has been developed to display the data in L-shell versus time with an option for daily averages on every DMSP pass. There is an option for running orbits through the displays to show when and where the spacecraft encounter high energy outer belt electron populations. The DMSP SSJ4 sensor data displayed by the HEEM module is automatically processed and written to directories accessible to PL-GEOSpace every time a DMSP data pass is transmitted to 50WS. By default, PL-GEOSpace stores 60 days worth of data for HEEM up to the current day. Data from the years 1991 and 1994 are also included in the GEOSpace data directories to be used as examples of conditions at and just after solar maximum, respectively. Examination of the 1991 data shows the creation of a new radiation belt following the 24 March 91 great magnetic storm. The 1994 data includes examples of effects due to recurrent high-speed solar wind streams.

3.3.1 HEEM Module Inputs

The HEEM data module requires the user to specify the following information to determine the desired data set to be viewed.

Year:

The year specifying the input data file.

Mode:

Select whether the data is to be viewed as daily averages or fifteen minute time averages obtained from the DMSP orbit passes. The default limits on the length of time to be displayed are daily averages = last 30 days, pass by pass averages = last 2 days.

Orbit:

This selection button is used to load a satellite orbit for display in the 2D HEEM Display Window. The orbit must have been previously created by the PL-GEOSpace orbit application module and must have, at least in part, the time interval selected to view the HEEM data. The last day of the actual orbit involved in the HEEM calculations may be viewed with the orbit graphics module in a regular 2D or 3D PL-GEOSpace graphics window.

Orbit slider:

This slider sets the position of the satellite along the orbit as shown in the 2D HEEM display window. The time corresponding to the slider percentage is displayed below the widget.

Satellites:

The user can select to plot data from up to three different DMSP satellites. The satellite names will be displayed at the top of the 2D HEEM display window. Note that there might not always be three DMSP satellites transmitting useful SSJ4 data. If this is the case, and if three satellites are selected, the program will display whatever is available.

Species:

The species parameter selects between the nominal 30 keV electron and 30 keV ion channel. Comparing the output of the two channels will give the user a better feel for the 2-4 MeV electron population that contaminates both.

Normalization:

The normalization factors are set to even out the measurements between the different satellite instruments. Turning this parameter on should result in a slightly smoother plot.

Background Interpolation:

The user can select here whether to fill in the gaps between the measurements displayed in the pass-by-pass mode. The gaps are replaced with linear interpolates using nearest earlier and later data. The plot will look completed if this option is checked on. The exact times when there are no

measurements will be clear when this option is checked off.

3.3.2 Plot Options

Clicking this button pops up a menu with options for viewing the data in the 2D HEEM Display Window. This menu contains a scale option to choose between linear data and log to the base 10. The day range for the data output can be set (For the day averages mode the range can be up to 400 days. For the time averages mode the range must be ≤ 5 days to keep the plots at manageable size.). The L-shell limits for the data can also be set as well as other formatting options for displaying the plots.

3.3.3 HEEM Module Outputs

The HEEM data module automatically creates a HEEM 2D display window when executed. At the top of the window the species, mode, Year and satellites selected will be displayed. If the Daily Averages mode has been selected the window will contain a 2D color intensity plot of the daily averaged count rate as function of day and L-shell for the time and L-shell intervals selected. If the Pass-by-Pass mode has been selected the window will contain a 2D color intensity plot of the fifteen minute averaged count rate along each DMSP orbit as function of time and L-shell for the time interval and L-shell intervals selected. If the Background Interpolation option has been chosen, data gaps in time will be filled by linear interpolation between earlier and later measurements. Note that HEEM only uses DMSP data taken in a longitude quadrant centered on the South Atlantic Anomaly. If a satellite orbit has been selected, the L position of the satellite as a function of time will be superimposed on the 2D color intensity plots. The location of the satellite along its orbit is shown and can be changed by moving an orbit slider.

3.4 GRAPHICAL OBJECT MODULE STARS

A realistic visualization of the near earth magnetospheric background requires a 3-dimensional rendering of the visual stellar and planetary background. In addition, as some models of the solar wind and interplanetary propagation of the charged particle flux into the earth's magnetosphere require knowledge of the position of the sun, the inner planets and the earth's moon, we have created a graphical objects module to calculate and plot the positions of the visible stars and major planets as seen from the earth.

The Stars graphical object renders the celestial background as seen from the earth for a given date and time. Stars as dim as visual magnitude eight, the planets and the moon can be represented with this module. This module uses the Yale Bright Star catalogue [Hoffleit and Warren, 1991], compiled by D. Hoffleit, as a stellar data base. Apparent equatorial coordinates are computed for the equinox of date from J2000 catalogued positions; these are corrected for stellar proper motion as well as the precession and nutation of the earth. Lunar and planetary positions are computed from the FORTRAN codes ELP82B [Chapront-Touze and Chapront, 1983] and PLANETAP [Simon, et al.,

1994], as obtained from the Astronomical Data Center of Goddard Space Flight Center. These codes provide precise lunar and planetary positions without numerical integration of the gravitational equations of motion -- a procedure that would take far too much computational time for its use in a real-time simulation of the near earth magnetospheric space environment. Apparent planetary positions in the earth's frame of reference are also corrected for precession and nutation [Montenbruck and Pfleger, 1991].

The Stars graphical object can be plotted in either a 2D or 3D window. In a 2D window the Stars graphical object plots a flat projection of the celestial sphere as seen from the earth, with Right Ascension increasing in the horizontal direction from left to right, and Declination increasing (decreasing) from 0 to +/- 90 degrees as one moves vertically up (down).

In a 3D window, the Stars graphical object plots the celestial sphere as a 3-Dimensional background to the near earth space environment. An option exists to plot this background as a 3-dimensional sphere of varying radius.

The Stars graphical object support the Window, Clipping, Lighting, and Material options.

3.4.1 Stars Inputs:

Detail

The user can select buttons in this section to determine which objects are drawn in the celestial sphere. The choices are:

Planets

Locate and draw the eight major planets. Planets are color coded, and are approximately the colors seen by the human eye through a small telescope -- Mercury and Venus are white, Mars is red, Jupiter is a sandy brown, Saturn is yellowish, Uranus is aquamarine while Neptune is a dark turquoise.

Moon

Locate and draw the earth's moon. Plotted as a white sphere and is drawn to the same scale as the earth 3D object.

Color

Plot stars in color. Rendered colors are based on stellar spectral classification type (OBAFGKM) and are approximately those seen by the human eye at the earth's surface.

Grid Options

Several types of grids may be placed upon the surface of the celestial sphere. An option to output positions the moon and planets is included in this section. The options are:

Lat/Lon Grid

Render a grid showing geographic latitude and longitude upon the celestial sphere. The local sky for an observer at a given latitude and longitude can thus be determined. The resolution is ten degrees.

RA/Dec Grid

Render a grid showing Right Ascension and Declination of the background celestial sphere. Resolution is ten degrees.

Ephemeris Output

When enabled in conjunction with either the Planets or Moon toggle button, this button will output planetary and lunar positions to standard output for the input date and time. Estimated precision is better than 10 seconds of arc for the period 1980 - 2000.

Max. Magnitude

The user can use this slider to select the maximum visual stellar magnitude down to a minimum brightness of magnitude eight that will be plotted from the data base. A total of 9110 stars are catalogued in this data base. Relative brightness is modeled within the code by adjusting the pixel size and rgb color intensity of a plotted star, and corresponds approximately to the visual magnitude as catalogued in the Yale data base.

Maximum Size

This slider controls the number of pixels used to plot the brightest stars. The slider values are scaled to the maximum pixel size of the brightest star, i.e., Sirius. Down to an area of one pixel, the brightness of the star is represented by the size of the star in pixels. Below one pixel size, we reduce the intensity of the individual pixel. Thus, the larger the value of the maximum pixel size, the dimmer the star that will be visible in the window.

Finite Radius

Plot stars on the surface of a sphere with a radius determined by the Celestial Radius slider.

Celestial Radius

The radius of the celestial sphere, in earth radii, can be adjusted with this slider.

R=Infinity

Plot stars in a perspective view. The viewing angle can be changed using the zoom function available in the Show View options window accessible through the Admin column in the menu bar of the Plot3D windows.

3.5 DETECTOR OBJECT GRAPHICS MODULE

A new graphics module has been implemented within PL-GEOSpace to calculate and display the solid angle acceptance cone of a detector located on an earth-orbiting satellite. Both the 3D solid

angle cone of acceptance and its 2D intersection with the earth's surface, the satellite "footprint", were desired. In this section we discuss the numerical algorithm for the calculation of the solid angle acceptance and the graphical implementation of this feature into the DETECTOR module of PL-GEOSpace.

3.5.1 Coordinate Transformation to the Earth Centered System

The detector solid angle may be represented as the distribution of points constituting the boundary of a cone with origin at the center of an orbiting satellite. The detector may be oriented in any direction in the general case. To express this distribution in terms of the Earth Centered frame, used within GEOSpace, we perform a series of rotations and translations on the detector coordinate system,

$$X_e = R_{sat_e} * T_{sat_e} * R_{det_{sat}} * X_{bar} \quad (4)$$

where X_e and X_{bar} are 3-dimensional vectors representing points in the Earth Centered and detector frames respectively. The Earth Centered frame may be chosen as either a geocentric frame or the Earth Centered Inertial (ECI) frame. While R_{sat_e} represents a simple coordinate translation (vector addition) along the earth-satellite radial vector, the operators R_{sat_e} and $R_{det_{sat}}$ can be represented as 3-dimensional rotation matrices acting on the vector in the bar-frame. Expressions for rotation matrices in a right-handed coordinate system may be obtained from standard textbooks in mathematical physics [Arfken, 1985]. There are a total of four independent angles that must be considered in the two rotations in a spherical representation between the two systems. For the Earth Centered system, a convenient choice for these angles is the latitude λ , and longitude ϕ , corresponding to the instantaneous position of the satellite as viewed from the center of the earth. These are also the natural coordinates chosen within GEOSpace. For the angles within the rotated detector coordinate frame, we choose the pitch (polar) and azimuth angles as measured instantaneously with respect to vertical at the satellite position.

Using the appropriate rotation matrices, we may calculate the coordinates of points in the earth-centered system for any given point in the rotated detector frame. Our approach to rendering a 3D representation of the rotated detector solid angle is to calculate the points on the boundary of a rotated cone in the detector system, then transform these points to the Earth Centered system so that OpenGL functions can be called within GEOSpace to render the image.

We choose as a simple representation for the solid angle of a detector on an orbiting satellite a circular cone with its vertex at the center of the detector. The intersection of this cone with the earth's surface, the so-called satellite "footprint", would thus be the solution to the intersection of a sphere of radius 1 earth radii, with the equation of a circular cone, transformed from the rotated detector system to the Earth Centered system.

Our first attempt at a solution to this problem started with the equation of a circular cone in the rotated detector system, rotating this equation to the Earth Centered system, and then solving this equation numerically on the grid of points consisting of the sphere represented at the surface of the

earth. This method will work for any grid of points representing the earth's surface (not just a sphere) and for any orientation of the detector. However, for the desired accuracy the computation of the locus of points representing the intersection of these two surfaces was found to be too long to presently be of use for a real-time computer simulation of the footprint for an orbiting satellite.

We thus considered a second method which is applicable to a spherical representation of the earth's surface. In the rotated detector frame, the locus of points representing the boundary for the base of a cone of half-opening angle α and length r_{cone} is simply $\{r_{\text{cone}}/\cos\alpha, \alpha, \phi\}$ $\{0 < \phi < 2\pi\}$, where α is the polar angle and ϕ is the azimuth angle in spherical polar coordinates. If one considers the simple case where the detector is pointed towards the center of the earth, the intersection will be a circle on the earth's surface centered at the latitude and longitude of the satellite. There is a maximum value of the polar angle, α , for which the radius of the circle will be so large that there will be no intersection with the earth's surface. In such cases, a value of α is selected which will be tangent to the Earth's surface. We use a similar method for the case of a rotated detector.

To calculate the boundary of the solid angle cone, we choose points varying in ϕ between $[0, 2\pi]$ to map out the circular boundary of the base of the cone in the detector frame of reference. These selected points are then transformed to the Earth Centered system and a conical surface is approximated by a series of triangular fans emanating from the detector origin using OpenGL functions.

3.5.2 User Interface to PL-GEOSpace

The DETECTOR graphical object can be plotted in either a 2D or 3D window. In a 2D window the DETECTOR graphical object plots the satellite footprint of the detector on the earth's surface. In a 3D window, the DETECTOR graphical object plots the solid angle acceptance cone of a satellite detector orbiting the earth. Options exist to vary the solid angle acceptance of the detector, its pitch and azimuth with respect to vertical. The DETECTOR graphical object supports the Window and Transparency options.

DETECTOR Inputs

Cone Color: Option for selection of the color for each solid angle acceptance cone drawn.

Orbit Color: Option for selection of the color of the calculated orbit of the satellite.

FOV: Slider for selection of opening angle (deg) of solid angle acceptance cone.

PITCH: Slider for selection of the pitch angle (deg) of the detector. This angle corresponds to the angle θ_{3p_d} for the polar angle of the detector in the satellite frame as given in the transformation equations above.

AZIMUTH: Slider for selection of the azimuth angle (deg) of the detector. This angle corresponds to the angle ϕ_{3p_d} for the azimuth angle of the detector in the satellite frame as given in the

transformation equations above.

Orbit: This option menu is used to select the ORBIT. This option must be set before rendering is allowed. The option menu contains a list of valid, previously produced orbits.

Data: This option menu is used to select a main data set for display along the ORBIT trajectory. The option menu contains a list of valid, previously run science, data, and application data sets. When a data set is selected, the orbit should appear colored, representing interpolated data values along the track. If the Data option is off, the orbit trajectory appears as a single color.

Position: The position along the selected orbit. The value is percentage of UT with respect to the minimum and maximum UT of the orbit. A small red sphere depicts the current position of the satellite

Step: The arrows increment the orbit forward or backward by one UT step

Marker: The marker draws a label at the current position of the satellite. The available labels are:

- the satellite name tag, set when it was created
- the satellite position in spherical coordinates.
- the satellite position in Cartesian coordinates.
- the interpolated data value at the satellite position
- the current time, from the position slider.

Choose Color: This widget enables one to color the field lines in an arbitrary way.

Reference Frame: The reference frame option determines how the ORBIT should be rendered. The two options are geocentric (GEOC) and inertial (ECI).

Geocentric: Render the ORBIT in geocentric coordinates. Since these coordinates are rigidly attached to the spinning earth and represent a non-inertial frame, the trajectory will not be approximately elliptical in shape.

Inertial: Render the ORBIT in earth centered inertial coordinates. Here the trajectory will have an approximately elliptical shape. Note that the position of the orbit is rotated so that the satellite has the same location as in the geocentric coordinates.

In Figure 21 we show present 2D and 3D GEOSpace windows showing an earth orbiting satellite, the solid angle acceptance cone of a detector on the satellite aimed towards the earth, and the satellite footprint produced by the graphics module DETECTOR, as well as the celestial background of stars produced by the module STARS.

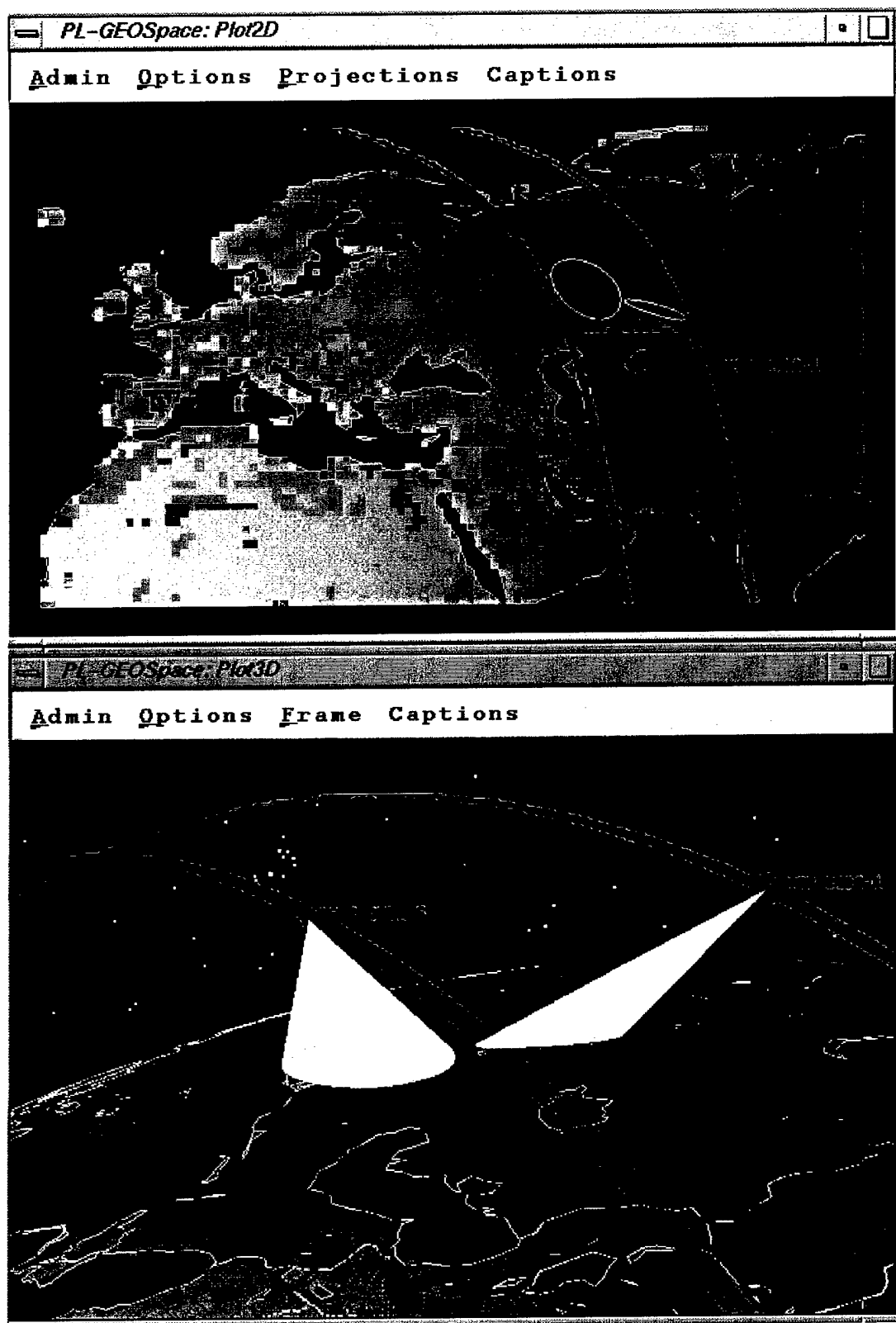


Figure 21 GEOSpace 2-D and 3-D windows.

3.6 VISUALIZATION/REAL TIME MAGNETOSPHERE

A series of SQL data base codes have been produced to access real-time information from the database of the 55th Weather Squadron at Falcon AFB, Falcon CO. Codes ORBEL and GLOBALS use FORTRAN drivers to call SQL module language commands that access current satellite orbital elements, solar and geophysical parameters on a hourly basis from the RDB/VMS database of the 55th. These data are stored on the disk shared between the VMS machines and SGI workstation at Falcon in a format that can be accessed by the code PL-GEOSpace for operations at the 55th. These data are also downloaded daily to Phillips laboratory over the SLIP connection installed between Phillips and the 55th to provide researchers with the most current input model parameters for model development and prediction.

The code ORBEL selects current orbital elements from the database file SAT_DB.orbel in the RDB/VMS database at the 55th. These elements are converted into the 2-line NORAD format and output to disk. The date and time of the access is noted, and a log file produced. A VMS-DCL command file runs daily to give a complete listing of satellite orbital elements for a period of 7 days prior to the access. Typically about 800 entries are listed, including repeated entries for the same satellite over the several day period. This file is copied to a directory area accessible by GEOSpace running on the SGI at Falcon, as well as to the SLIP connection from Phillips.

The code GLOBALS selects solar and geophysical data from the Falcon database for use as starting global parameters for the models within GEOSpace. The driver for GLOBALS is coded in FORTRAN; it calls SQL module language commands, compiled in a separate module, that access sunspot number, 3-hour k_p and a_p , and F10.7. These are output to a file in the format used by the National Geophysical Data Center (NGDC) for their archived solar and geomagnetic indices.

The output solar sunspot number is the total number of sunspots observed from different observing stations for a single day, suitably averaged over different observations for varying seeing conditions, as extracted from the table comm_db.spots_sunspot. 3-hour k_p and a_p are the current values, taken once every hour, for the previous 3 hour time period. The final values for each three hour time period for a single day are binned in the output file in 8 three-hour time bins. Along with F10.7, these values are obtained from the table ap_db.geomag_index in the Falcon database. As with the orbital elements, the final output file is copied to a directory accessible both to the Falcon SGI and the Phillips daily retrieval codes via SLIP.

3.6.1 VMS and LINUX System Administration

Proposals have been made to archive the entire data base of the 55th Weather Squadron here at Phillips. We have installed a sample of the full database at Phillips, and have written test archival command files using the RMU facility of the RDB/VMS system installed at Phillips on our Digital Alpha running under VMS. This sample database system was installed by us in collaboration with personnel from the 55th. In addition, we have provided system administration support for the VMS-alpha, creating user accounts and privileges, enhancing system performance, making system

backups, debugging peripheral hardware problems, and installing software applications necessary for the efficient performance of the system. Several of these applications have been ported to our networked UNIX workstations and PC operating under DOS/WINDOWS for the use of staff at Phillips.

We are also currently exploring the possibility of installing a LINUX version of OpenGL and porting PL-GEOSpace to both portable and desktop PC's. If successful, this will greatly expand the availability of the PL-GEOSpace distribution to our customer base. The Slackware 3.2 distribution of the LINUX operating system has been installed on a Pentium based portable PC. Non-destructive disk partitioning allowed the retention of both DOS/Windows-95 and LINUX partitions, with the ability to choose either of the two systems at boot time. X-windows (XFree86-3.3.1) and a proprietary version of Motif for LINUX have been installed and have been shown to perform well on the 800 x 600 pixel SVGA LCD screen with graphics applications that are currently running on our Silicon Graphics UNIX workstations. Versions of OpenGL for LINUX are currently being evaluated for use on PC's for use with PL-GEOSpace.

3.7 CONCLUSION

The PL-GEOSpace program provides a convenient package for running near space environment models from PL/GP and collaborators on a common UNIX platform with a user-friendly graphics interface emphasizing 3D visualization and animation. It gives easy access to the models and provides common application and 3D visualization tools. Because of the intrinsic 3D nature and time variation of the space environment, effective use of the models requires the capability to display multiple data sets, change the view quickly, and update the models in time. These capabilities are provided by PL-GEOSpace which fills the gap between space environment models scattered throughout the space community and working space system operators who desire a quick and complete description in the shortest possible time. We will continue to expand and enhance the PL-GEOSpace program and to develop its capabilities to meet evolving user needs.

4. ATMOSPHERIC METAL DEPOSITION

The influx of cosmic dust to the Earth averages about 40,000 tons per year. The masses of dust particles which contribute most to the Earth's atmospheric metal layers range from 10^{-8} to 10^{-4} grams [Hughes, 1975]. Larger particles which produce visible meteors, are too infrequent to significantly contribute to the layers. Cosmic dust enters the upper atmosphere with velocities between approximately 11 km/s and 70 km/s [Hughes, 1992] with the most probable velocity near 15 km/s.

As cosmic dust travels through the atmosphere, heating and ablation of the material causes deposition of the metals at altitudes between 80 and 110 km. The exponential increase in atmospheric density along the cosmic dust particle's path leads to increasing ablation with decreasing altitude. However, frictional deceleration of the particle causes it to reach a terminal velocity which corresponds to a temperature below that at which ablation takes place. Therefore, ablation from a single particle is deposited in a narrow layer, the altitude of which depends on particle mass and particle velocity. At high enough velocities, above about 30 km/s, cosmic particles ablate completely. At low velocities, a major fraction of the material falls to earth unablated. The metallic species include Fe, Mg, Ca, Na, K, and Al. These metal atoms ablate, from the cosmic dust, diffuse, and undergo chemical reactions. Mg and Fe are the most abundant metal species in cosmic dust, amounting to about 12% by weight each [Plane, 1991]. Ninety percent of meteorites are chondrites. The meteoric abundance of Na and Ca are approximately equal and only about 5% of Mg [Plane and Helmer, 1994]. However, the amount of neutral Na in the atmosphere is about 100 times that of Ca [Granier, et al., 1989]. The atmospheric abundance of neutral Mg is not yet known due to strong absorption of its 285.2 nm radiation by ozone. Thermospheric radiance measurements [Viereck, et al., 1996] have shown an abundance of neutral Na above 100 km and preliminary comparative modeling indicates that the depletion of Mg may be comparable to Ca.

The depletion of Ca relative to Na cannot be readily explained by chemical mechanisms since the chemistry of Ca and Na are too similar. It has been found that the Ca and Na layers can be reasonably well modeled if the ratio of ablating Ca to Na is taken to be about 1:30 [Plane, 1991]. Although the deposition process and the subsequent kinetics of the metals is intimately related, it is often necessary to separate the modeling effort into phases, the first of which produces a source function for the appearance of metal atoms. With this, one can next address the diffusion problem by considering the transport of all species containing a particular metal. This is valid if the important chemistry takes place below the turbopause, where atmospheric turbulence leads to a mass independent scale height for minor species. Under these assumptions, the diffusion equation can be solved for the steady state concentration of the total number of atoms containing the metal. Then, a kinetic model can be developed and solved in the steady state to give the relative amount of each particular molecular metal species. Implicit in this solution is the assumption that the removal of all metal molecules is uniform, which is not completely true for the complexes that are the eventual result of the chemistry. The assumption is quite good in the metal layer itself, however, since diffusion is rapid there, compared to the non-diffusive removal mechanisms.

4.1 COSMIC DUST DEPOSITION

The evolution of a particle after it enters the Earth's atmosphere can be modeled as follows; in a time dt , the particle encounters a mass of atmosphere equal to

$$M = A \left(\frac{m}{\rho_m} \right)^{2/3} \rho_a V dt \quad (5)$$

where ρ_a is the atmospheric density, V is the geocentric velocity, i is the mass of the particle and A

is a dimensionless shape factor, equal to about 1.2, which allows the expression to be written in terms of mass and density rather than radius. The impact of the particle with the air serves to heat the air and the particle, leading to the ablation of metal atoms, and to slow down the meteor. The change in velocity with time contains both the acceleration of the particle due to gravity and the atmospheric drag.

$$\frac{dV}{dt} = -\frac{\Gamma A \rho_a V^2}{m^{\frac{1}{3}} \rho_m^{\frac{2}{3}}} + \frac{\mu}{(h + h_0)^2} \quad (6)$$

where the first term is the drag expression [Hughes, 1992], and the second is the acceleration due to gravity. In Eq. 5, m and ρ_m are the cosmic dust particle mass and density, respectively, ρ_a is the atmospheric density, A is a shape factor, Γ is the drag coefficient, h is the altitude, h_0 is the radius of the earth, and μ is the gravitational constant. The maximum possible energy released in the air/particle collision is equal to the energy that would be imparted to the air molecules if they were raised to an air velocity equal to the particle velocity, or,

$$E_{\max} = \frac{1}{2} A \left(\frac{m}{\rho_m} \right)^{2/3} V^3 \quad (7)$$

which follows from Eq. 5. It is assumed that some fraction of this energy, Λ , goes toward heating the material in the particle instead of toward heating the air. With this, one can write the mass loss due to ablation as

$$\frac{dm}{dt} = \frac{\Lambda A m^{2/3} \rho_a V^3}{2 \xi \rho_m^{2/3}} \quad (8)$$

where ξ is the heat of sublimation, equal to about 5×10^{10} erg/g. Hughes [1992] gives a range for Λ from 0.1 to 0.6. Eqs. (6) and (8) can be solved [McNeil, et al., 1995] by using standard Runge-Kutta methods for given initial mass and velocity to yield the velocity, size, and sublimation rate at any future time. Using the cosmic dust mass distribution [Hughes, 1975], we track a representative series of meteoric particles through the atmosphere. The composite solution gives a deposition profile when normalized by the assumed total mass influx. In this calculation, we take $\rho_m = 3.2$ g/cm³, $\Gamma = 0.75$, $\xi = 7 \times 10^{10}$ ergs/g, and the initial particle velocity, $V = 14$ km/s. The curve has been normalized to a total cosmic dust influx rate of 500 g/s. However, it should be noted that the actual flux could be several times greater or less.

4.2 DIFFERENTIAL ABLATION

The calculation of deceleration and ablation used in this model follows closely the treatment given by [Love and Brownlee, 1991] and the formulation of the problem is presented in that work. Cosmic dust particles are tracked through the atmosphere accounting for the deceleration due to friction and the acceleration due to gravity. The steady state temperature is computed by balancing the energy

input from friction with the sum of the energy loss from radiative cooling and from vaporization of the liquid. The different aspects of the ablation process are introduced through temperature dependent vapor pressure laws.

In computing the vapor pressures for various mixtures, a model resembling that of *Fegley and Cameron* [1987] is used. Their model assumes a thermodynamic equilibrium of gaseous metal atoms and oxides above a solution of metal oxides. We presume a certain mixture of metal oxides in the cosmic dust melt, use the Fegley and Cameron formulation to calculate vapor pressure at various temperatures, then use these vapor pressure laws in the Love and Brownlee formulation to compute the deceleration and mass loss at all points along the particles trajectory. Our vapor pressure model for Na ablation consists of a 5% Na_2O solution in equal amounts of SiO_2 and MgO . For this system, the vapor consists almost entirely of oxygen and atomic Na. Due to this and for simplicity, the Na ablation has been modeled as if the incoming particles were made entirely of Na_2O but having the vapor pressure of the 5% Na_2O solution. The ablation of Mg is modeled with a vapor pressure law calculated for a 50:50 mixture of SiO_2 and MgO , these being the major constituents of cosmic dust. For Ca, the same vapor pressure law is used except that the deposition is reduced by a factor of 20 to represent the meteoric metal ratio of Mg and Ca. Ca is assumed to ablate along with the major constituents of the cosmic dust. The deposition profiles shown in Figure 22 were computed from an ensemble of cosmic dust particles following a mass distribution proposed by *Hughes* [1975]. The Na profile is then scaled so that the neutral column density is $4 \times 10^9 \text{ cm}^{-2}$. The Ca profile is scaled by the same amount to represent the approximately equal Na to Ca abundance in meteorites. The Mg profile is scaled by a factor of 20 larger than the Na profile, again to represent the meteoric abundance. The important feature in Figure 22 is the altitude at which the Na ablates relative to the Ca and Mg. The ablation peak is broader and about 8 km higher for Na.

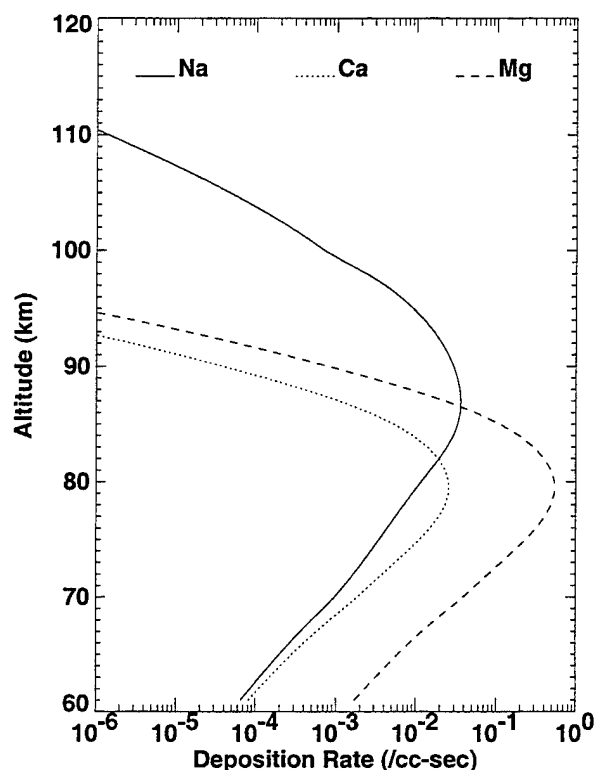
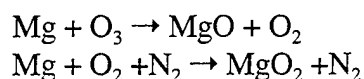


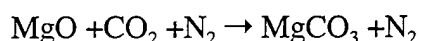
Figure 22. The deposition rates for the three metals assuming an entry velocity of 15 km/s.

4.3 CHEMISTRY AND DIFFUSION

The chemical reactions of Na, Ca, and Mg follow closely those used in [McNeil, *et al.*, 1997]. The neutral chemistry for the three metals is essentially the same. Using Mg as the metal atom neutral, it reacts as shown:



The MgO_2 is assumed to be converted immediately to MgO . Then the MgO reacts as follows



and is removed from the system forever, or the MgO reacts with O to form Mg and O_2 and is recycled back to the neutral metal. For this work, the same neutral chemistry has been maintained to emphasize the effect of differential ablation on relative atmospheric abundance of the various metals. Na and Ca react similarly. The densities are computed in a time-dependent fashion [McNeil, *et al.*, 1996]. Molecular and eddy diffusion are incorporated as in ion drift due to the equatorial electric field.

4.4 RESULTS

The ablation profiles are calculated assuming a single incoming velocity of the cosmic dust. Although the velocity is actually some distribution, the results are illustrative of the impact of differential ablation on the relative abundances of the metals. Table 1 gives the resulting neutral column density ratios for three different velocities, along with the meteoric abundance ratios and the measurements of *Granier, et al.* [1989].

TABLE 1. Relative Neutral Abundances			
Model or Observation	Na:Ca	Mg:Ca	Mg:Na
Meteoric Abundance	1	20	20
Measured Column	128	?	?
11 km/sec Model	3,500	37	0.01
15 km/sec Model	43	27	1
30 km/sec Model	3	22	10

The minimum entry velocity of about 11 km/s represents cosmic dust particles which are initially at rest in inertial space. These particles give rise to a tremendous overabundance of Na relative to Ca. The “average” velocity of 15 km/s, as quoted by Hughes [1992], gives a Ca depletion of approximately a factor of 50, close to the observations. Incoming dust at 30 km/s results in a much lower reduction factor. The 30 km/s particles are almost completely ablated and increasing the velocity above 30 km/s would not change the result appreciably. Figure 23 shows the mesospheric peaks of the three metals for the 15 km/s entry velocity model.

A peak Ca layer density of 20-30 cm⁻³ is approximately what is observed. The overall shapes of the Na and Ca layers are quite similar, and consistent with observation. The model predicts a Mg layer that is of approximately the same peak density as the Na layer and perhaps 3-4 km lower in altitude. Validation must await measurement of the neutral Mg layer.

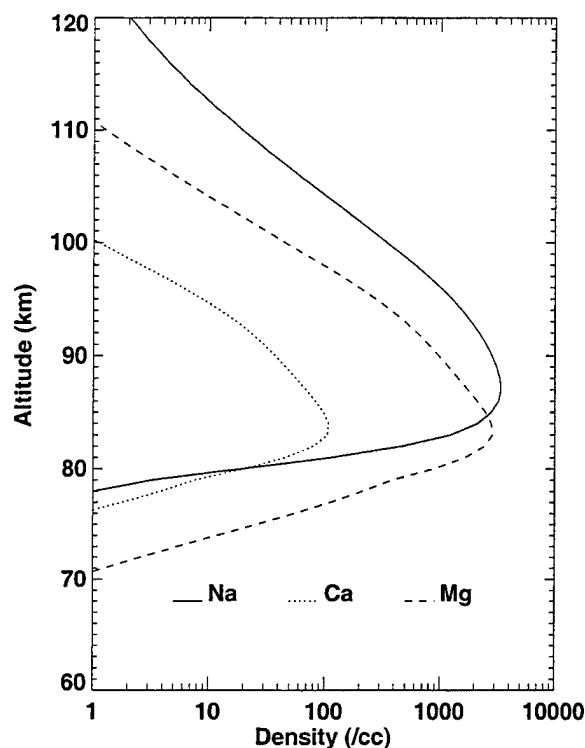


Figure 23. Mesospheric neutral metal layers as calculated in the 15 km/s model.

4.5 CONCLUSION

This model suggests that the sequential ablation of Na followed by Ca may give rise to a large depletion of Ca in the atmosphere. The model predicts that the depletion of Mg, not yet directly observed, would be similar. Although the model results in some degree of enrichment of the meteoroid in Ca and Mg, by a factor of approximately five for 15 km/s cosmic dust, an essential element is a delay in the ablation of these metals relative to Na. This results in deposition of Ca about 8 km lower than Na. Deposition of the metal a few kilometers lower in the atmosphere results in a neutral sink that is perhaps two orders of magnitude stronger for Ca and Mg than it is for Na. It has been suggested in the past that the precise form of the deposition profile is not critical to the modeling of atmospheric metals. If enrichment of the meteoroid takes place, it is necessarily accompanied by deposition of the various species at different altitudes. The results presented here indicate that the height of deposition is a determining factor in the relative abundances of the various metal species.

5. SOLAR WIND ACTIVITY

5.1 THE 22-YEAR CYCLE OF GEOMAGNETIC AND SOLAR WIND ACTIVITY

The 22-year cycle or double-solar-cycle (DSC) in geomagnetic activity is characterized by high activity during the second half of even-numbered solar cycles and the first half of odd-numbered cycles. *Cliver, et al.* [1996] presented new evidence for the DSC by using the aa magnetic index for the years 1844-1994. The DSC was observed through differences between the decay phases of even- and odd-numbered cycles in (1) average values of a 27-day recurrence index; (2) the results of a χ^2 "event" analysis of 27-day recurrences of both disturbed days; and (3) an apparent annual modulation of the 27-day peak in the power spectrum of the aa index. The 22-year variation is currently attributed to the *Russell-McPherron* [1973] solar wind-magnetosphere coupling mechanism working in conjunction with the *Rosenberg-Coleman* polarity effect [*Rosenberg and Coleman*, 1969]. The work by *Cliver, et al.* [1996] showed that an intrinsic 22-year solar variation, other than polarity reversal, is the dominant cause of the 22-year cycle in geomagnetic activity. This is revealed in the systematic low-high alternation of even-odd sunspot maxima within the last six complete Hale cycles.

Cliver, et al. [1996] repeated the various analyses (averages [*Chernosky*, 1966], time series [*Sargell*, 1986], event days [*Hapgood*, 1993]) that have been used to document the 22-year variation in geomagnetic activity and also examined a new parameter -- the composition of the 27-day spectral line from FFT analysis of geomagnetic indices during the decay phases of alternate solar cycles -- for evidence of a DSC variation. The investigation of the 22-year cycle is based on *Mayaud's* [1972] aa index, which is available from 1868 to the present, and a recent extension of this index back to 1844, that is based on a single station observation at Helsinki [*Nevanlinna and Kataja*, 1993]. The emphasis was on the declining phase of the 11-year cycle during which geomagnetic activity is dominated by 27-day recurrent storms.

The 11-year sunspot numbers have exhibited a systematic variation since 1860; the maxima of odd-numbered cycles in even-odd pairs are always larger. This sunspot variation can be expected to reveal itself in cycle-to-cycle variations of the solar wind and, therefore, geomagnetic activity.

5.1.1 Analysis

Annual averages of sunspot number (SSN) and the geomagnetic index aa for the 150-year period from 1844 to 1994 are given in Figures 24a and 24b, respectively. A long-term upward trend is apparent in the aa record. The dashed vertical lines are drawn through magnetic activity minima which, as can be seen in Figure 24b, generally occur within a year of SSN minima.

Because the DSC in geomagnetic activity is apparent as differences between the rise and fall portions of consecutive cycles, it was necessary in several of the analyses below to define two “halves” of an 11-year cycle. The 11-year geomagnetic cycle (defined as the interval between the midpoints of years of minimum annually averaged aa values) varied from 9 to 12 years over the 150 years considered. To normalize the cycle length, the length of the rise (decay) phase is defined to be 0.5 of the total magnetic cycle length (L). These intervals are referred to as “1st half” and “2nd half”; the “1st half” (rise phase) began at the midpoint of the year of minimum aa value and the “2nd half” (decay phase) ended at the midpoint of the year of subsequent 11-year aa minimum [Cliver, *et al.*, 1996].

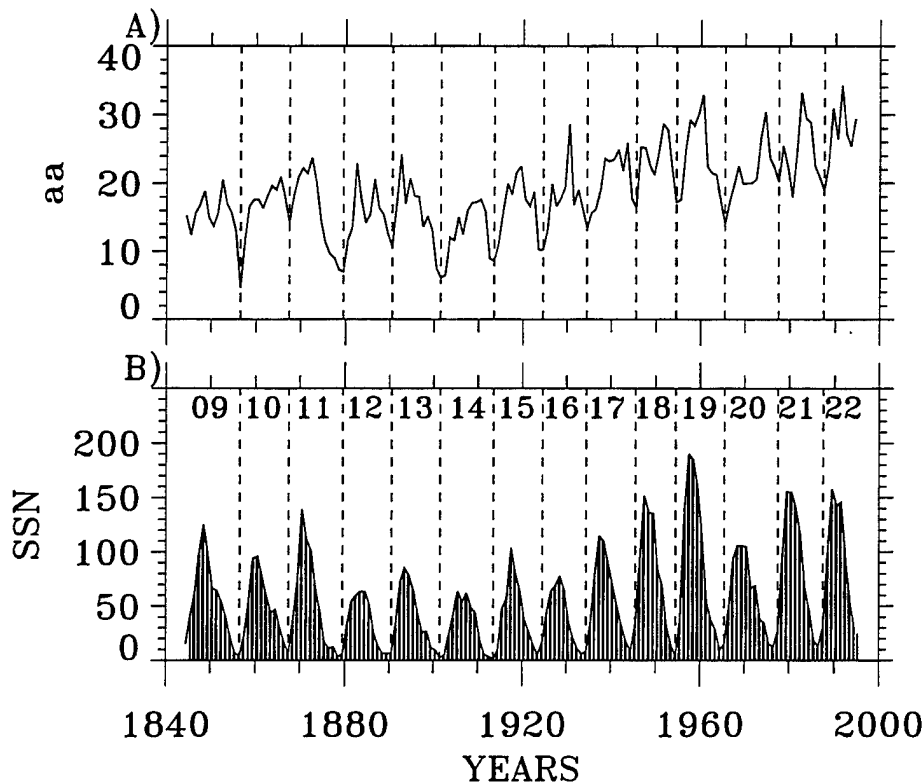


Figure 24. (a) Yearly averages of the geomagnetic aa index, 1844-1994. Vertical dashed lines indicate the 11-year geomagnetic minima. (b) Yearly averages of the sunspot number (SSN), 1844-1994. The sunspot cycles are numbered at the top of the panel.

Annual Averages of aa for Even and Odd Solar Cycles

Figure 25a shows a composite of annual averages of aa for the six even-numbered (numbers 10, 12, 14, 16, 18, 20) and six odd-numbered cycles (numbers 11, 13, 15, 17, 19, and 21) that make up the six complete Hale cycles occurring between 1844-1994. The weights of the

yearly averaged values that make up the composite average are inversely proportional to their standard deviations (σ). The error bars in Figure 25a are $\pm 2\sigma$. The corresponding SSN data are presented in Figure 25b. The starting point for each “11-year” geomagnetic and sunspot cycle corresponds to the minimum listed in the SSN compilation by McKinnon [1987].

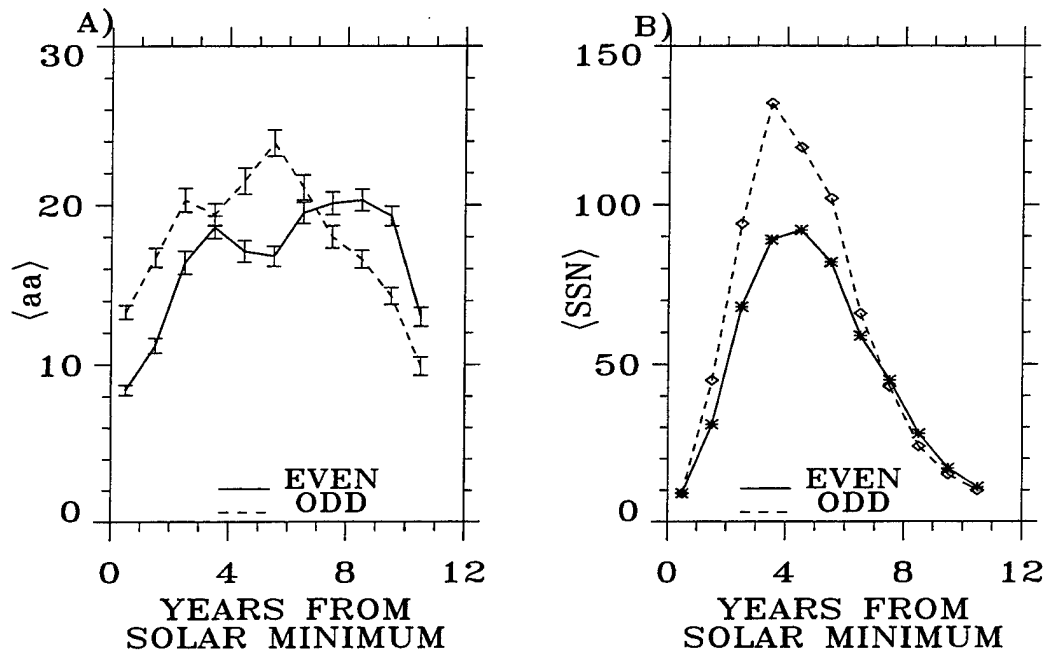


Figure 25. (a) Composite weighted annual averages of aa for the six even-numbered and six odd-numbered solar cycles that made up complete Hale (22-year)cycles since 1844. Error bars are $\pm 2\sigma$. (b) Corresponding composite averages of SSN for even- and odd-numbered solar cycles that formed complete Hale cycles, 1844-1994.

The composite even-numbered geomagnetic cycle has two distinct maxima, the first at year 4, corresponding to the year of SSN maximum, and the second, a broad peak, spanning years 7-10. The composite odd geomagnetic cycle has a subpeak at year 3 and a well-defined maximum centered on year 6. The first peak in the even cycle aa curve is attributed primarily to transient solar activity and the second peak primarily to coronal hole activity [Cliver, *et al.*, 1996].

Such a separation is less obvious for the odd-numbered cycles, although recurrent activity will play an increasingly important role after sunspot maximum. Note that the even- and odd-numbered sunspot cycles also exhibit differences, with the odd cycles having

characteristically larger peak SSNs - 35% higher on average over years 3-6 of the cycle (Figure 25b). As noted above, this SSN variation is systematic over cycles 10-21; the even cycles of Hale even-odd pairings are always smaller (Figure 24b).

Time Series Analysis

Time series analyses have been used by *Sargent* [1986] to show that recurrent storms are more prominent during the decay phase of even cycles than during the corresponding phase of odd cycles. Sargent's recurrence index (RI) for a given Bartels' rotation (j) is defined as follows:

$$RI_j = \frac{100}{13} \sum_{k=-6}^6 r(j+k, j+k+1) \quad (9)$$

where r is the correlation coefficient for the linear regression relationship between the 12-hr aa indices of two consecutive Bartels' rotations.

Correlation coefficients are averaged over 13 rotations to approximate the 13-month running average used for smoothed sunspot numbers and multiplied by 100 to convert RI_j to a whole number index. Sargent's RI for the 150-year series of aa data is presented in Figure 26a. As *Sargent* [1986] pointed out, intervals of recurrent activity, falling on the decay of the sunspot cycle, tend to last longer following the maxima of even-numbered cycles (3-5 years) than is the case for odd-numbered cycles (1.5-3 years).

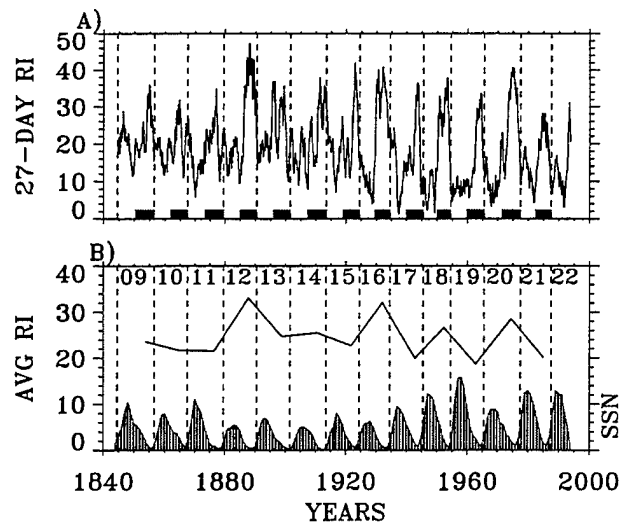


Figure 26. (a) *Sargent's* [1986] recurrence index (RI) for 150 years of aa data. The dashed vertical lines indicate 11-year minima in the aa indices and the shaded rectangles at the bottom of the panel indicate the "2nd half" periods used to obtain the average RIs plotted in (b). The average RI value is plotted at the midpoint of each interval. Yearly averages of SSN are also shown in the lower panel.

Figure 26b contains a plot of RI averaged over the “2nd half” of each geomagnetic cycle vs. time since 1844. This focus on the 2nd half of the cycle provides evidence for the DSC in geomagnetic activity back to 1880 but not for earlier cycles [Cliver, *et al.*, 1996].

Event Analysis

To avoid the high recurrence tendency for low geomagnetic activity when carrying out the time series analysis to identify 27-day recurrences of significant activity, Hapgood [1993] devised methods that only considered recurrent activity above a given level. Each day is classified either as a storm day with a given geomagnetic index meeting or exceeding some threshold or a quiet day if the index falls below that level. The 27-day recurrence rate of storm days is then examined.

Because the event or storm days analysis involves a threshold, it was necessary to detrend the 150 years of data under consideration before applying Hapgood's [1993] technique. The detrending of the aa data was done by subtracting the aa value corresponding to the annual average aa of either the first or last year of a given 11-year geomagnetic cycle, depending on which was lower, from the daily aa value for all days during that cycle.

The principal output of the analysis is the χ^2 statistic for a recurrence period of 27 days, given by

$$\chi^2 = \frac{(O - E)^2 n}{E(n - E)} \quad (10)$$

where n is the total number of days in the interval considered, O is the observed number of recurrent storm days, and E is the expected number of recurrent storm days (given by $m - (m-1)/(n-1)$ where m is the total number of storm days in the interval). The χ^2 value is a measure of the probability that 27-day recurrences of storm days with aa \geq a given threshold during a given interval did not arise by random chance. Table 2 gives the results of this analysis for an aa threshold of 20 nT for both the “1st half” and “2nd half” intervals of all complete geomagnetic cycles between 1884-1994.

A 22-year periodic behavior is most evident for aa = 20 nT, although, even for this selected threshold, the χ^2 maxima for cycles 10 and 14 are relatively weak [Cliver, *et al.*, 1996].

TABLE 2. Calculation of χ^2 Statistic for a 27-Day Recurrence Period for Storm Days (aa \geq 20 nT). Period lengths: 50% and 50% of Full Cycle						
Cycle	Period	n	m	O	E	χ^2
9	1845.5 - 1851.0	2009	338	99	56.7	32.4
	1851.0 - 1856.5	2010	377	135	70.6	61.0
10	1856.5 - 1862.0	2010	339	93	57.0	23.3
	1862.0 - 1867.5	2009	484	198	116.4	60.7
11	1867.5 - 1873.5	2192	517	171	121.8	21.1
	1873.5 - 1879.5	2191	137	22	8.5	21.5
12	1879.5 - 1885.0	2010	264	75	34.6	48.1
	1885.0 - 1890.5	2009	299	128	44.4	161.2
13	1890.5 - 1896.0	2009	407	148	82.3	54.7
	1896.0 - 1901.5	2009	223	77	24.7	112.5
14	1901.5 - 1907.5	2191	177	32	14.2	22.4
	1907.5 - 1913.5	2192	312	112	44.3	105.7
15	1913.5 - 1919.0	2009	317	98	49.9	47.6
	1919.0 - 1924.5	2010	298	104	44.1	83.4
16	1924.5 - 1929.5	1827	213	44	24.7	15.2
	1929.5 - 1934.5	1826	378	182	78.1	144.5
17	1934.5 - 1940.0	2009	286	62	40.6	11.5
	1940.0 - 1945.5	2010	388	149	74.7	76.6
18	1945.5 - 1950.0	1644	246	50	36.7	4.9
	1950.0 - 1954.5	1644	358	178	77.8	135.5
19	1954.5 - 1960.0	2009	430	128	91.9	14.9
	1960.0 - 1965.5	2010	352	116	61.5	49.8
20	1965.5 - 1971.5	2191	261	43	31.0	4.7
	1971.5 - 1977.5	2192	468	222	99.8	157.0
21	1977.5 - 1982.5	1826	257	61	36.1	17.6
	1982.5 - 1987.5	1826	316	113	54.5	64.6

Annual Modulation of the 27-Day Recurrence Period of the Power Spectra

The power spectra of the aa index are characteristically different during the decay phases of even- and odd-numbered solar cycles. Specifically, during even-numbered cycles, spectra near the 27-day recurrence period (central spectral peak is actually 27.3 ± 0.2) are more likely to show adjacent lines near 25 and 29 days. This can be seen in Figure 27 which shows FFT spectra for the decay portions (2nd half) for composite or averaged spectra of the even (Figure 27a) and odd (Figure 27b) 11-year geomagnetic cycles. In Figure 27, the spectra are normalized to the largest peak. For even cycles, spectral peaks near 27-day appear at $29.3 (\pm 0.2)$ and $24.9 (\pm 0.2)$, and are likely due to a yearly modulation. For odd cycles, the sidelobe peaks are less pronounced and are located at $33.6 (\pm 0.2)$ and $24.1 (\pm 0.1)$, suggesting a semi-annual modulation. The harmonics are also seen at periods of 13.4 and 9.0 days, approximately.

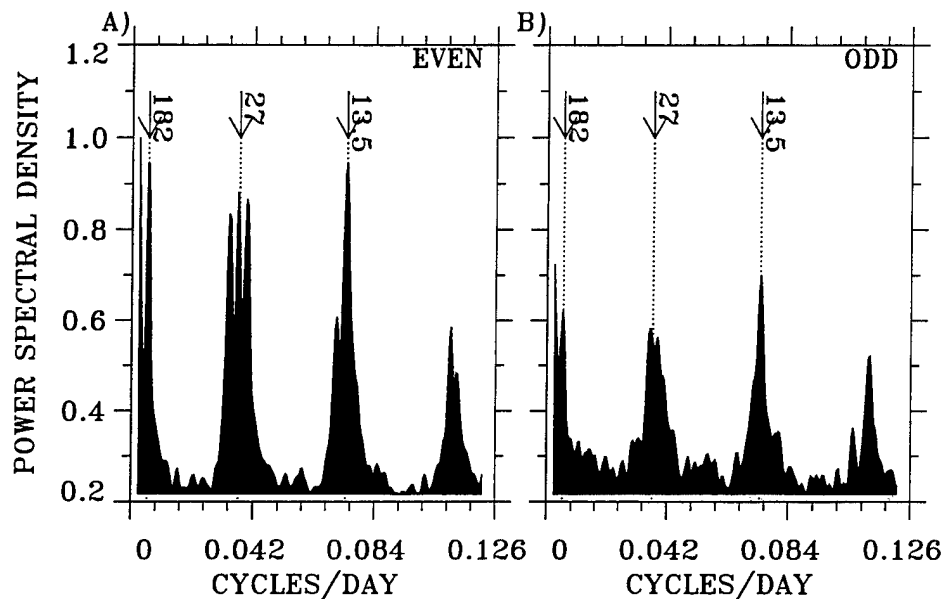


Figure 27. (a) Composite FFT spectra of aa for the declining phase (2nd half) of even-numbered solar cycles since 1855. (b) Averaged FFT spectra of aa for the “2nd half” of odd-numbered solar cycles since 1855. To facilitate comparison, the amplitudes of spectral lines in both Figures 31a and 32b are normalized to the largest peak occurring in either plot. Arrows indicate the semiannual peak and the 27-day peak with first harmonic.

One of the requirements in using the FFT algorithm is that the total number of input data be in powers of 2. We compute the Fourier transform of the correlation coefficients and not that of the aa series. The unbiased correlation estimates total as many lags as needed to meet the above requirement: The total number of lags is set to be a power of 2 number that is higher or equal to that of aa series. We make up for the difference between the number of lags and

the actual number of data points by padding zeroes to the end of the aa series. For a period of five years, the total number of daily aa is 1826 or 1827 (depending of whether one or two leap years falls in this period). We then used an FFT of 2048. A 7-point smoothing using the Hanning window was used to smooth the periodogram spectral estimates. The spectral resolution is then approximately 0.24 cycle/1000 days.

The apparent 22-year control of this annual modulation indicates that solar variability is somehow important for the yearly variation. The *Cliver, et al.* [1996] finding that the 27-day triplet in Figure 27 comes and goes with a 22-year period indicates that the Sun itself has a more active role in the annual modulation of geomagnetic activity than previously thought. Specifically, *Cliver, et al.* [1996] suggested that the longest-lived recurrent streams during even cycles characteristically last for more than a year's worth of 27-day rotations (and thus reveal the annual modulation) while those following the maxima of odd cycles do not. *Cliver, et al.* [1996] suggested that the 22-year variation in geomagnetic activity (high activity on the decay of even cycles and the rise of odd cycles) is a reflection of a 22-year solar variation.

Simulation of the aa Power Spectra

Boriakoff, et al. [1997] were able to simulate the spectra of the even- and odd-numbered cycles as seen in Figures 28 and 29 by assuming longer sequences of recurrent storms (greater than a year and showing annual modulation) during even cycles and shorter, more random, sequences during odd cycles.

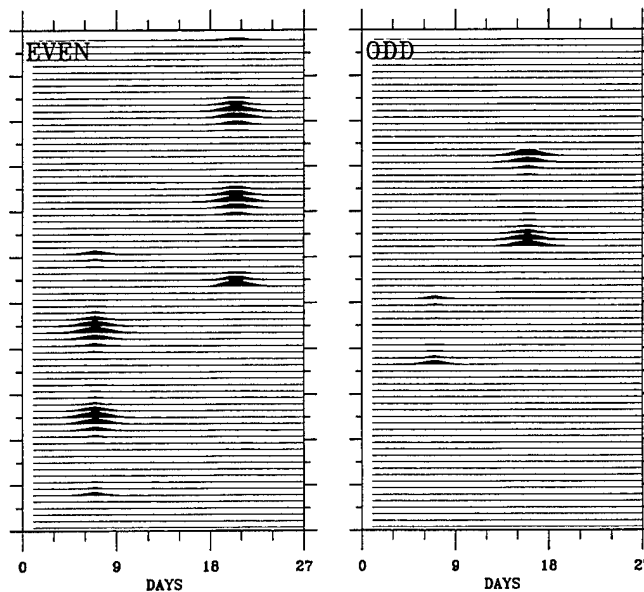


Figure 28. The simulated aa time series.

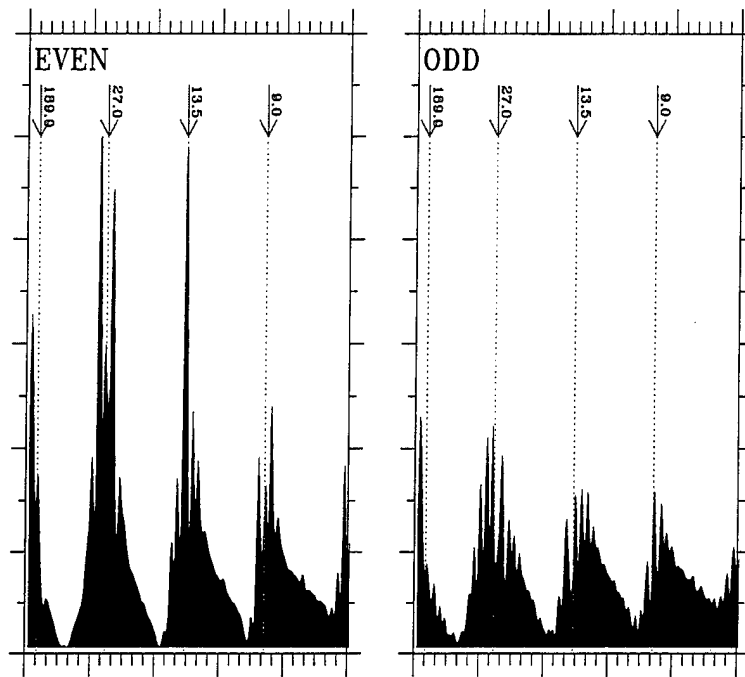


Figure 29. The FFT spectra of simulated aa for the declining phase of even- and odd- numbered solar cycles.

Power spectra of the geomagnetic aa index for the decay phase of even-numbered solar cycles characteristically exhibit an apparent annual modulation of the 27-day recurrence tendency that is not present in the corresponding spectra of odd-numbered cycles. We simulate this difference by assuming the existence of longer sequences of recurrent activity during even-numbered cycles than in odd cycles (up to ~2 years vs. ~1 year). The difference between the aa spectra of even- and odd-cycles cannot be simulated simply by assuming a reduced coupling efficiency of the solar wind to the magnetosphere following the maxima of odd cycles. Rather, the even-odd differences appear to be a manifestation of an intrinsic 22-year variation of solar activity [Boriakoff, *et al.*, 1997].

5.1.2. Conclusion

Various lines of evidence indicate that the 22-year cycle of geomagnetic activity has persisted over the 150 years for which processed geomagnetic data are available. The DSC variation in geomagnetic activity manifests itself as enhanced transient activity during the rise and maxima of odd-numbered solar cycles and enhanced 27-day recurrent activity during the decay of even-numbered solar cycles. An intrinsic 22-year variation of solar activity and the resultant solar wind is the principal cause of the DSC in geomagnetic

activity. The low-high even-odd pattern of sunspot maxima within the last six complete Hale cycles indicates a relative excess of coronal mass ejections during the rise phase and maximum of odd-numbered solar cycles [Cliver, *et al.*, 1996]. In addition, analyses of geomagnetic data reveal more persistent patterns of 27-day recurrent activity during the decline of the solar cycle. It is evident that the DSC in geomagnetic activity is primarily due to an intrinsic 22-year variation in solar output when considering the close correspondence between the amplitudes of the 22-year geomagnetic variation and sunspot activity over the last 150 years [Cliver, *et al.*, 1996].

5.2 THE SOLAR WIND FROM L1 THROUGH THE MAGNETOPAUSE

An effort is underway at Phillips Laboratory to model the flow of the solar wind from a solar-wind sensor in the vicinity of the L_1 Lagrange point to Earth [Heinemann, *et al.*, 1996]. Radex has been involved in the development of operational space weather forecasting software for delivery to AF 50th Weather Squadron.

The development of an operational space weather forecasting system can be divided up into two related but distinct parts: the propagation of solar disturbances to L_1 and then Earth, and the impacts of the disturbances after they have reached a point (e.g. L_1) where a reliable measurement is possible [Heinemann, *et al.*, 1996]. The L_1 point is one percent of the distance between Earth and the Sun, about 240 Earth radii toward the Sun from Earth. By observing the solar photosphere or corona, one can predict with reasonable fidelity the propagation of disturbances to 1 AU, hence build a complete solar-terrestrial forecasting system. The goal here is to be able to make two-day-or-so predictions, corresponding to the transit time of solar plasma from the Sun to Earth [Heinemann, *et al.*, 1996].

The solar wind constitutes a principal driver in the modeling of the energy flow that constitutes space weather. With reliable, high-quality solar-wind data (like those of the WIND or eventually ACE spacecraft), a numerical space weather forecasting system can be developed.

Our approach to developing a front end to the space weather forecasting system has been to focus on shock waves. One reason for this is that the interplanetary (IP) shocks can affect the Earth's magnetic field and often result in geomagnetic storms. Detecting these shocks can be very beneficial for spacecraft operations. Using the ISEE-3 solar wind data near the L_1 libration point during the solar maximum of cycle 21 and more recently the WIND data, one may detect shocks in real-time in order to forecast geomagnetic storms. Rubin, *et al.* [1996] devised a shock detection algorithm, based on an earlier version by Vandev, *et al.* [1986]. It detects a discontinuity by simply correlating the solar wind data and the IMF with a finite width step function. The values of the step function $f(t)$ are ± 1 at the data sampling rate. The number of samples is arbitrary. For the ISEE-3 data we have taken an 8-sample window with 2 samples at or immediately after the test point. For a sampling rate of 5 minutes, this

minutes, this means that we must wait at most 10 minutes before we detect a discontinuity. An ideal discontinuity (i.e. infinite derivative) will result in a correlation coefficient of unity, while a zero derivative will lead to a correlation coefficient of zero. Figure 30 shows an ideal shock with a 10% noise level of the solar wind parameters.

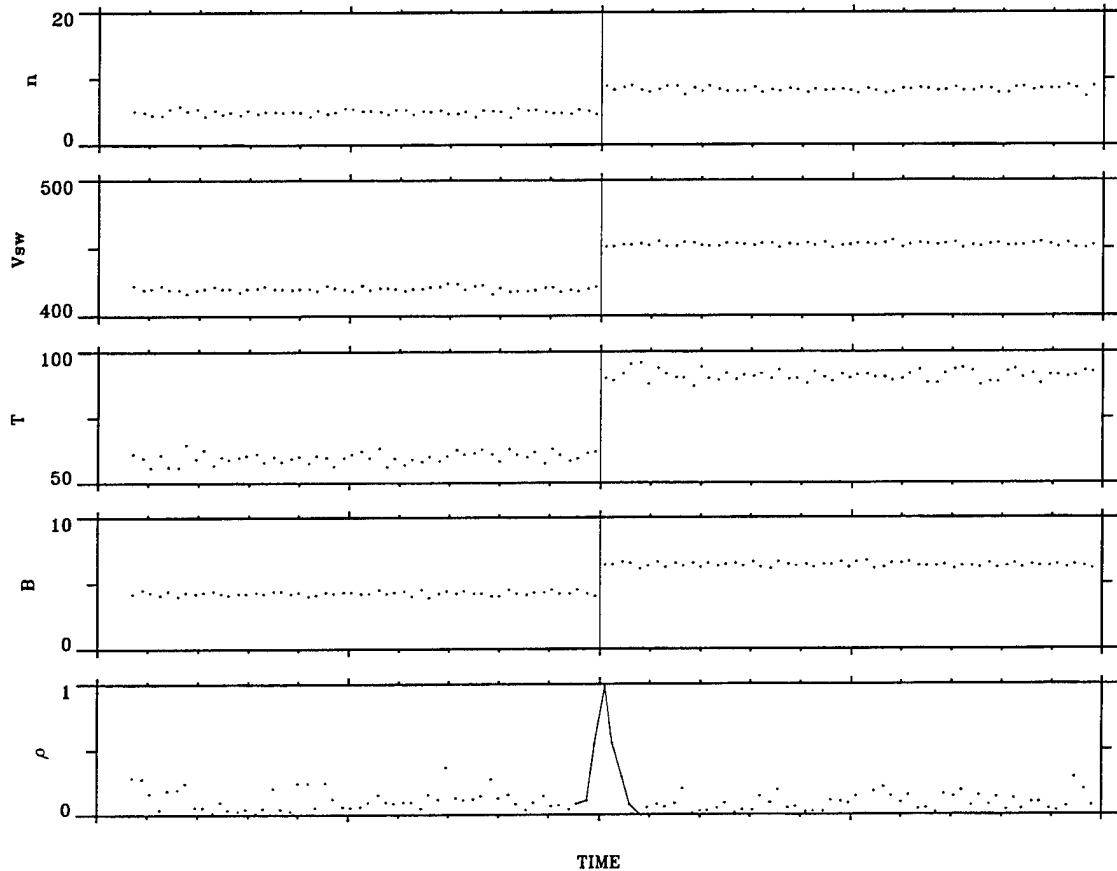


Figure 30. An ideal case with a correlation coefficient of 0.98 at the discontinuity.

5.2.1 Interplanetary Shock Detection Algorithm

The algorithm is applied to a vector X which is composed of n , V , T , and B . All four inputs were normalized by their peak-to-peak range within the window. The normalized values will then vary from 0.0 to 1.0. Data are checked for gaps at the point being tested for discontinuity. If there are more than 2 consecutive samples missing, then a gap is noted. Averages of normalized n , V , T , and B are obtained before and after the discontinuity point. The changes from before to after the jump of these averages must all be positive. The ratio of averaged n after to before the jump must be at least 1.2.

Let $X(k,j) = [n(j), V(j), T(j), B(j)]$, $j=1,2, \dots, L(=8)$, then the variance for each k ($=1,\dots,4$) is

$$var(k) = \frac{1}{L-1} \sum_{j=1}^L [x(k,j) - 0.5]^2 \quad (11)$$

and the corresponding covariance

$$cov(k) = \frac{1}{L-1} \sum_{j=1}^L [x(k,j) - 0.5] \cdot f(j) \quad (12)$$

and the correlation coefficient is then

$$\rho = \frac{1}{\sigma_f^2} \sum_{k=1}^4 \frac{[cov(k)]^2}{var(k)} \quad (13)$$

where σ_f is the standard deviation of $f(t)$ and is equal to L .

The correlation coefficient ranges from 0.0 to 1.0. A correlation threshold of 0.8 or 0.9 was employed. An increase in the threshold value decreases the false alarm rate and increases the miss rate.

5.2.2 Performance of the Algorithm Using the ISEE-3 Database

The ISEE-3 spacecraft was in orbit about the L1 point 240 Earth radii upstream of the Earth from August 18, 1978 to November 30, 1979. In order to test effectiveness of this algorithm we used 42 forward shocks, which were reported by *Zwickl [1994]*. The experiment was conducted during the sunspot maximum of solar cycle 20. Ten large Dst events occurred in this period, with $Dst < -100$ nT, [*Gonzalez and Tsurutani, 1989*]. The ISEE-3 plasma and field data, available at a sampling rate of 5 minutes over this interval, are employed in the testing of the shock detection algorithm.

The behavior of the shock detector is shown in Figure 31 for the interplanetary shock of 09 March 1979; the data shown are ISEE 3 five-minute averages. The shock, occurring at 0720 UT, shows strong jumps in the density (top panel), speed (second panel), temperature (third panel), and total magnetic field strength (fourth panel). The bottom panel shows the correlation coefficient, calculated for an equally weighted combination of the four individual correlations. It is fairly noisy, oscillating between 0.1 and 0.7 away from the shock. At the shock it rises from about 0.1 to a peak exceeding 0.9 and then drops back to about 0.1. The peak indicates the time of the shock with an error of about 2.5 minutes. This algorithm has been implemented in detecting IP shocks based the NASA/WIND measurements. These data have a time resolution of 92 seconds, hence the shock time measurement would have an improved accuracy of about a minute.

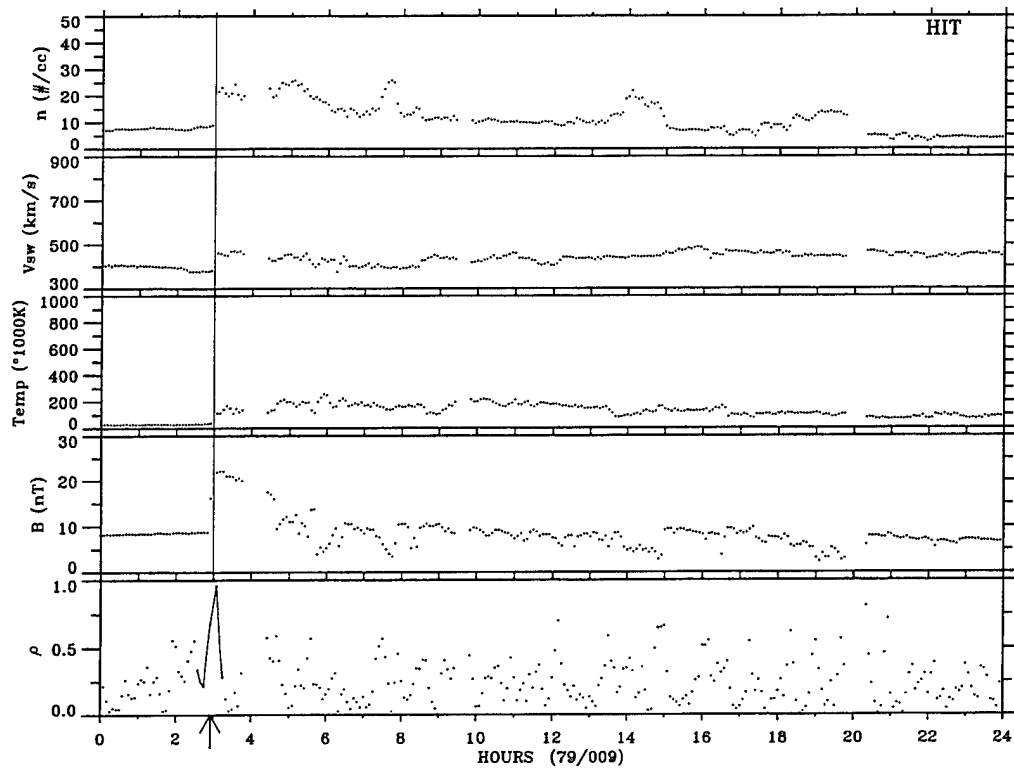


Figure 31. Example of a shock detection. This particular shock on 09 March 1979 resulted in a SSC 40 minutes later [Gonzalez and Tsuratani, 1989].

For a correlation threshold of 0.8 (Table 3),

$$\frac{\text{FALSE ALARMS}}{\text{TOTAL NUMBER OF EVENTS}} = \frac{15}{42} = 35.7\%$$

and for a correlation threshold of 0.9 (Table 4) it drops to 21.4%.

TABLE 3. Summary of the Results for Correlation Threshold of 0.8			
SHOCK TYPE	REPORTED	DETECTION	MISS
CLEAR	25	23 (92.0%)	2 (8.0%)
SMALL	17	12 (70.6%)	5 (29.4%)
TOTAL	42	35 (83.3%)	7 (16.7%)

TABLE 4. Summary of the Results for Correlation Threshold of 0.9			
SHOCK TYPE	REPORTED	DETECTION	MISS
CLEAR	25	17 (68.0%)	8 (32.0%)
SMALL	17	8 (47.1%)	9 (52.9%)
TOTAL	42	25 (59.5%)	17 (40.5%)

5.2.3 Conclusion

The algorithm when employed with a threshold condition on the correlation and the density ratio and for all positive jumps of shock parameters works well in detecting strong shocks in the 1978-79 ISEE-3 database. The correlation coefficient is noisy but can be improved. This algorithm must be tested and certain parameters adjusted based on the time resolution of the WIND and eventually ACE data.

5.3 A PREDICTION OF THE PEAK SUNSPOT NUMBER FOR SOLAR CYCLE 23

An accurate prediction of the peak amplitude of solar cycle 23 is useful input for planners of upcoming low-Earth orbit space missions. The consensus view of the space physics community is that the maximum of cycle 23 will be relatively high, comparable to the maxima of cycles 21 (13-month smoothed sunspot number (SSN) = 164.5) and 22 (158.5). The panel convened by the NOAA Space Environment Center and the NASA Office of Space Science [Joselyn, *et al.*, 1997] surveyed the results of 28 predictions made by six separate techniques and found reasonable agreement for a peak SSN of 160.

Bounar, *et al.* [1997] used a precursor technique based on the geometric aa index during the decline (last 30%) of solar cycle 22 to predict a peak sunspot number of 161 ± 18 for cycle 23, under the assumption that solar minimum occurred in May 1996. This method appears to be as reliable as those that require a year of data surrounding the geomagnetic minimum, which typically follows the smoothed sunspot minimum by about six months. It is generally accepted that the precursor approach or method is the most reliable way to predict the peak SSN.

5.3.1 Analysis

The 13-month smoothed aa minimum typically follows the SSN minimum (12 of 13 cases since 1850) with a median delay of about six months (range from 1-14 months) [Cliver, *et al.*, 1996]. In an attempt to determine an optimum time span, we performed a regression analysis of peak SSN (SSN_{max}) vs. average aa ($\langle aa \rangle$) over cycles 10-22 for a range of

intervals for the input aa average. These intervals began at specified points during the decline of a solar cycle (corresponding to 50%, 40%, 30%, 20%, and 10% of the cycle length, measured backwards from sunspot minimum) and ended either at the smoothed sunspot minimum or 10% of the way through the following cycle. The results for the correlation coefficient (C.C.) and the standard error of estimate (S.E.) of SSN_{max} are shown in Figures 32a and 32b, respectively, where the solid and dot-dash lines represent intervals ending at sunspot minimum and 10% of the way through the next cycle, respectively. From Figure 32, the highest correlations (and lowest standard errors) are obtained for the intervals containing the last 30% of the input cycle. There is no significant difference between the correlation coefficient for the “30%” interval ending at sunspot minimum in Figure 32a (solid line; $r = 0.904$) and that ending 10% of the way through the following cycle (dot-dash line; $r = 0.906$), so waiting for the magnetic minimum does not seem to provide an advantage [Bounar, *et al.*, 1997].

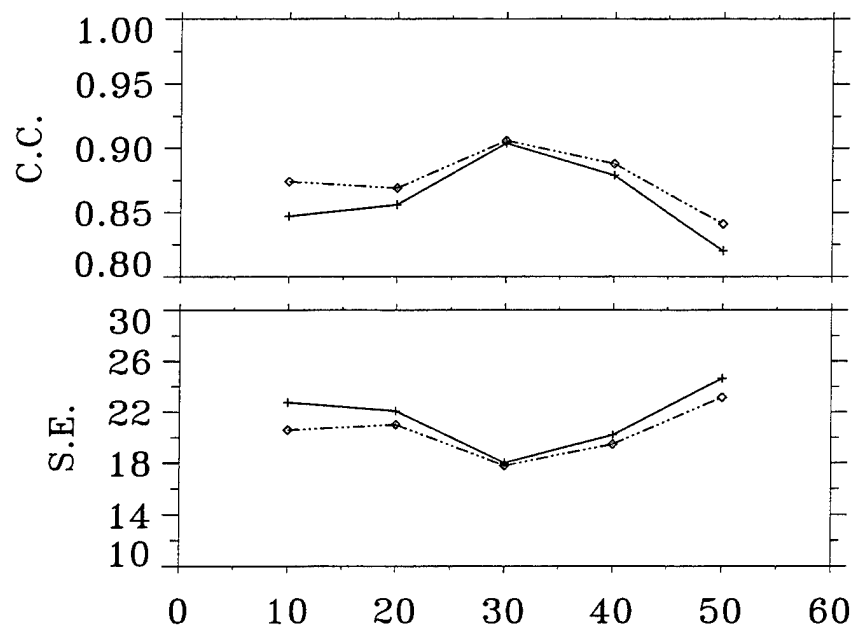


Figure 32. (a) Correlation coefficients (C.C.) for the aa-SSN relationship as a function of various averaging times for aa. The solid line is for time periods that end at the smoothed minimum at the end of a sunspot cycle and begin at a point corresponding to the indicated percentage of a cycle, measured backward from the minimum. For the dot-dash line, the end point of the time range corresponds to 10% of the way through the following cycle, measured forward from the same sunspot minimum. Same as (a) for the standard error of estimate (S.E.) of SSN_{max} .

The equation of the “30% to SSN minimum” line is

$$SSN_{\max} = 6.99\langle aa \rangle - 9.05 \quad (r = 0.904) \quad (14)$$

and the standard error of estimate is 18.0. This equation was derived in a somewhat different manner from the standard practice. Usually, $\langle aa \rangle$ is taken to be the independent variable and all error or uncertainty is assigned to the dependent variable, SSN_{\max} . In our analysis, we first obtained two regression lines, by using both $\langle aa \rangle$ and SSN_{\max} as independent variables in turn. Equation (14) was then determined by the geometric mean of the slopes of the two lines and their point of intersection. The $\langle aa \rangle$ and SSN_{\max} data on which Eq. (14) is based are plotted in Figure 33.

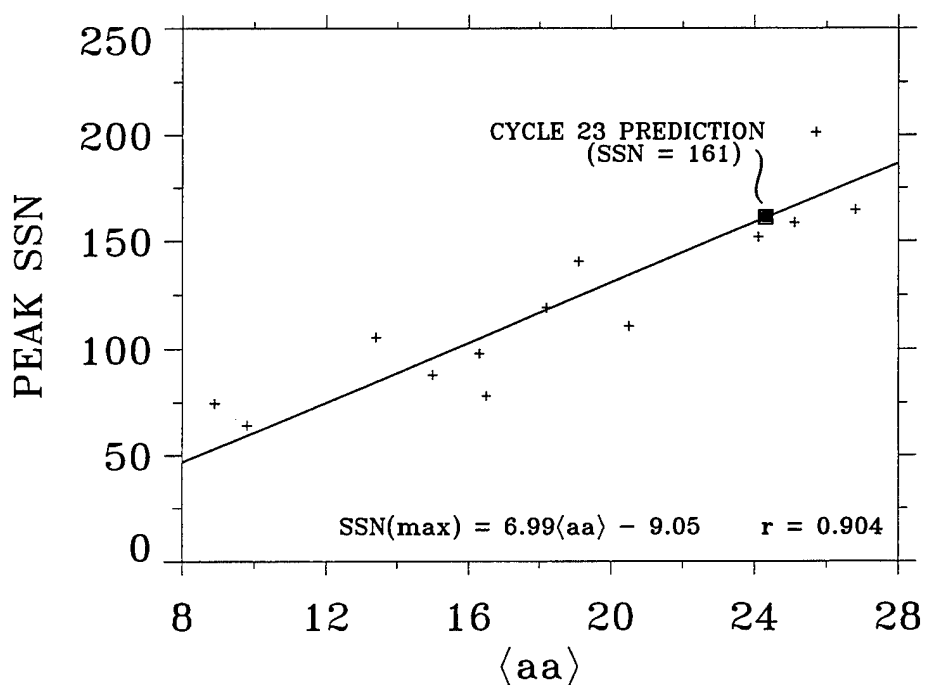


Figure 33. Regression line for peak SSN of a cycle vs. aa averaged over the last 30% (measured backward from the smoothed sunspot minimum) of the previous cycle. The filled square indicates the prediction (161) for cycle 23.

It now appears likely that May 1996 was the month of minimum between cycles 22 and 23. According to the Boulder *Preliminary Report and Forecast of Solar Geophysical Data*, the 13-month smoothed SSNs for April, May, June, and July 1996 were 8.6, 8.1, 8.6, and 8.5, respectively. If the May 1996 minimum holds up, the average aa over the last 30% of cycle 22 was 24.3 nT and we predict a peak SSN of 161 for cycle 23. Wilson, et al. [1996] estimate that the maximum of the smoothed cycle will occur in January 2000.

5.4 THE SOLAR WIND DURING THE MAUNDER MINIMUM

An empirical technique based on SSN measurements was used to show that the average level of geomagnetic activity as measured by the aa index during the Maunder Minimum was only about a third of that observed during recent 11-yr cycles ($\sim 4\text{--}7$ nT vs. ~ 24 nT) [Cliver, *et al.*, 1997]. This implies either that the average solar wind speed during the Maunder Minimum was lower by as much as a factor of two (~ 230 km s⁻¹ vs. ~ 440 km s⁻¹) or that the southward component of the interplanetary field was lower by up to a factor of four (0.3 nT vs. 1.2 nT), or that both parameters had values significantly less than at present. These differences in solar plasma emission between the Maunder Minimum and the present epoch stand in contrast to the estimated 0.24% change in total radiative output of the Sun between these intervals [Cliver, *et al.*, 1997].

A linear regression line based on “11-year” averages of sunspot number ($\langle \text{SSN} \rangle_{11}$) and the geomagnetic index aa ($\langle \text{aa} \rangle_{11}$) was obtained over a ~ 150 -year period,

$$\langle \text{aa} \rangle_{11} = 0.22 \langle \text{SSN} \rangle_{11} + 6.3 (\text{nT}) \quad [r = 0.96] . \quad (15)$$

where the interval used for the averaging process was based on minima of the 11-year sunspot cycle [McKinnon, 1987] and included the preceding and following half cycles. The regression lines are determined by using both parameters in turn as independent variables in order to minimize the effect of errors or uncertainty in either variable and basing the final relation on the geometric mean of the slopes of the two regression lines and their point of intersection. The resultant regression line, shown in Figure 34, is used to obtain the average aa index during the Maunder Minimum on the basis of the tabulated SSNs given by Eddy [1976]. The maximum average sunspot number for any consecutive 11-year interval is 3.5 for 1676-1686 during the depth of the Maunder Minimum (1650-1700). A $\langle \text{SSN} \rangle_{11}$ of 3.5 yields a maximum $\langle \text{aa} \rangle_{11}$ of 7.1 nT for this 50-year period, versus 6.3 nT for $\langle \text{SSN} \rangle_{11} = 0$ [Cliver, *et al.*, 1997].

There is a tendency for the $\text{aa}_{\text{min}}/\langle \text{aa} \rangle_{11}$ ratio to decrease with the general level of geomagnetic (and solar) activity. If we extrapolate this trend (Figure 35) to Maunder Minimum conditions, we obtain aa_{min} values ~ 1.9 (for $\langle \text{SSN} \rangle_{11} = 3.5$ and $\langle \text{aa} \rangle_{11} = 7.1$ nT) during that period, higher than the values obtained from the precursor technique for Eddy's peak SSNs which range from 3-11 between 1650-1700.

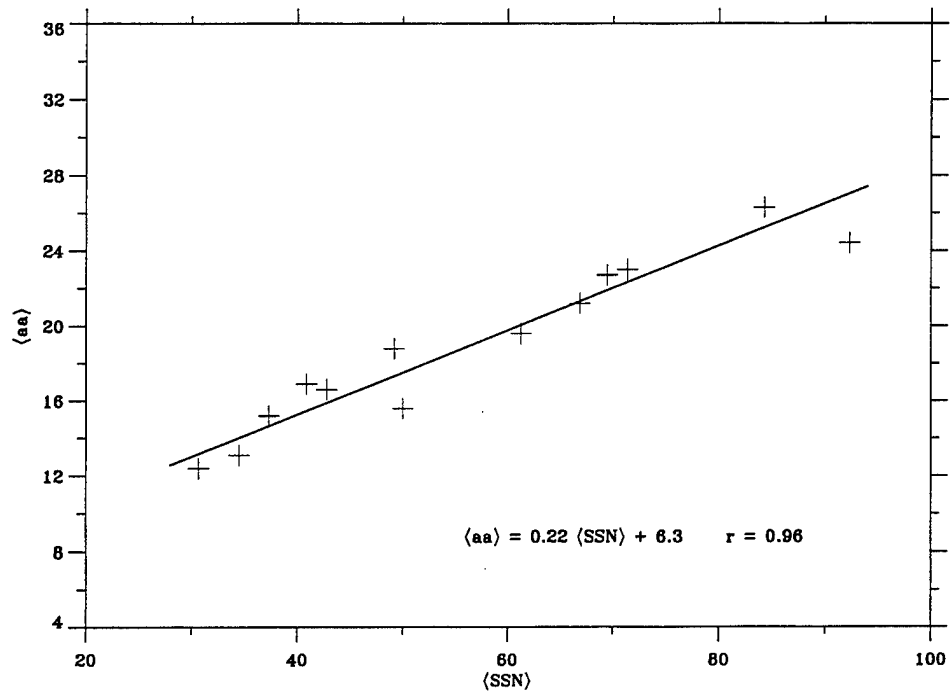


Figure 34. Correlation between 11-yr averages of aa and SSN.

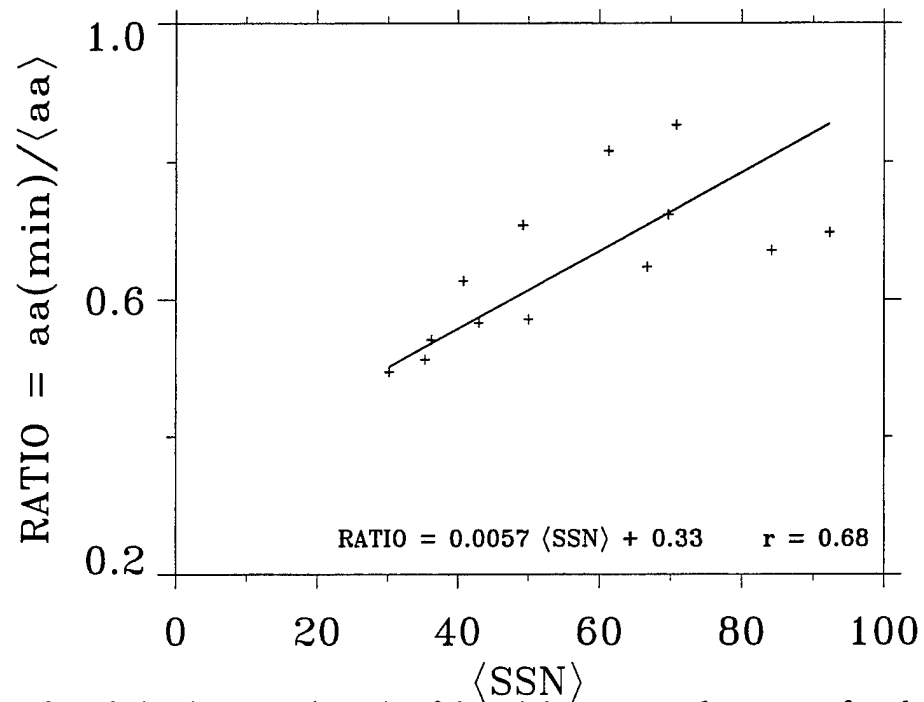


Figure 35. Correlation between the ratio of the minimum annual average of aa during an 11-year cycle (aa_{min}) to the average aa value during that cycle ($\langle aa \rangle_{11}$) and the average sunspot number ($\langle SSN_{11} \rangle$) over the cycle. The length of the cycle corresponds roughly to the interval between consecutive sunspot maxima.

The approach of *Feynman and Crooker* [1978] is used to relate the average aa values to solar wind parameters to derive a relationship between aa and the product of the square of the solar wind velocity, v^2 , and the absolute value of the z component of the interplanetary magnetic field, $|B_z|$ for a single solar cycle. The OMNI data tape available from the National Space Science Data Center A was used to update this relationship and obtain the following equation,

$$\langle aa \rangle = 8.9 \cdot 10^{-5} \langle v^2 B_s \rangle + 1.7(nT) \quad [r = 0.89] \quad (16)$$

based on the data for the years 1964-1994 (solar wind data coverage was at least -30% for each six month averaging interval during this period). Only those three-hourly aa values were used for which solar wind v and B_s data existed. The principal difference between equation (8) and that of Feynman and Crooker is our division of the absolute value of B_z by a factor of two to convert it to B_s , the southward component of the interplanetary magnetic field (in Geocentric Solar Magnetospheric (GSM) coordinates).

aa values of 7.1 nT correspond to typical conditions during the Maunder minimum based on a $\langle SSN \rangle_{11}$ of 3.5. The average solar wind v (444 km s^{-1}) and B_s (1.18 nT) were observed from 1964-1994. If the average solar wind speed of the current epoch is applied during the Maunder Minimum, then the average B_s value would have been lower by as much as a factor of four ($\sim 0.3 \text{ nT}$ vs. $\sim 1.2 \text{ nT}$). Similarly, an average B_s value unchanged from the present epoch implies a solar wind speed a factor of up to two lower during the Maunder Minimum ($\sim 230 \text{ km s}^{-1}$ vs. $\sim 440 \text{ km s}^{-1}$). The average conditions during the Maunder Minimum almost certainly lie between these approximate extrema, suggesting values of both v and B_s to be significantly below their present day averages, but above the given lower limits.

Precursor relations and our $aa_{\min}/\langle aa \rangle_{11}$ analysis raise the interesting possibility that the solar wind might have been intermittent during the Maunder Minimum because a value of $aa \approx 1.9 \text{ nT}$ in Eq. (16) implies a weak ("solar breeze?") or absent wind during the minimum years of the 11-year cycle. Such a pronounced 11-year wind variation stands in contrast to present conditions where the average wind speeds during the minimum years of 1964, 1976, and 1986 were $\sim 419 \text{ km s}^{-1}$, 445 km s^{-1} , and 453 km s^{-1} , respectively, versus an average speed of $\sim 440 \text{ km s}^{-1}$ over the entire 1964-1994 interval.

Cliver, et al. [1997] found that the solar wind was significantly slower and less disturbed during the Maunder Minimum than at present and may have even have been qualitatively different in character, i.e., being absent or "breezelike" near minima of individual 11-year cycles.

6. CRRES SATELLITE RESULTS

6.1 PROTEL

The Earth's radiation belt is a region in space in which charged particles (electrons, protons and ions) are trapped by the Earth's magnetic field. The motion of a trapped particle is generally a spiral up and down the magnetic field lines. At a given instant of time, the velocity vector of the charged particle makes an angle α with respect to the magnetic field vector; the angle α is called the pitch angle. During the motion of a charged particle, the pitch angle of the particle as it crosses the magnetic equator determines the latitude at which the particle "mirrors", at which the particle reverses direction along the direction of the magnetic field. As a result, it is customary to characterize the motion of trapped charged particles by their equatorial pitch angle and its L-shell value, the length of the radius vector to the magnetic equator field line crossing (in Earth radii). Charged particles are "lost" when they encounter (collide with, or are scattered by) neutral or other charged particles in regions of higher density. Thus, for lower L - shell values, charged particles will be absent from the ends (for equatorial pitch angles α near 0° and 180°) of the distribution. For stable populations of charged particles, the distribution in equatorial pitch angle will be (nearly) symmetric around 90° . The range of values of equatorial pitch angle for which particles will be absent is referred to as the loss cone, and will be characterized by the loss cone angle α_c . The pitch angle range for stable particles is: $\alpha_c < \alpha < 180^\circ - \alpha_c$.

Neglecting the loss cone, because of the symmetry around 90° it is customary to mathematically fit equatorial pitch angle distributions to functions of the form $\sin^N \alpha$. To represent the effect of the loss cone, it is preferable to use (what we shall call here) a "modified" $\sin^N \alpha$, that is, a distribution of the form:

$$j(\alpha, E, L) = A(E, L) \left(\frac{\sin^2 \alpha - \sin^2 \alpha_c}{1 - \sin^2 \alpha_c} \right)^{\frac{N(E, L)}{2}} \quad (17)$$

With the normalization chosen above, $A(E, L)$ is the flux at $\alpha = 90^\circ$. Note that α_c depends upon L. The above distribution reduces to the $\sin^N \alpha$ distribution when $\alpha_c = 0$.

In this report, we shall model the effects of the 8.5° aperture of the Proton Telescope (PROTEL) High Energy Head (HEH), and the flux averaging resulting from rotation upon the HEH flux measurements. We will assume that the actual equatorial pitch angle distribution is a modified $\sin^N \alpha$ distribution (Eq. (17)). During the 1 second integration period, the spacecraft rotates through an angle of 12° . When the axis of the satellite is parallel to Earth's magnetic field, the detector will sweep through the loss cone. The effect of the aperture size and rotation will be an apparent shrinking of the loss cone and the detection of protons entering the detector from outside the loss cone.

In the analysis used to produce the PROTEL quiet and active flux models, the flux in the first bin

below the loss cone was attributed to contamination (particle entry into the detector of higher energy protons through the passive shielding triggering responses which appear valid to the coincidence/anticoincidence detector logic). The loss cone flux was subtracted from the observed fluxes, and the resulting data was fit to a single modified $\sin^N \alpha$ distribution, and to the sum of two such distributions (as described below).

Much of the PROTEL Quiet and Active Model equatorial pitch angle distribution data fits well to a single distribution of the form of Eq. (17). In many cases, a fit to the sum of two such distributions (performed as described below) provides a substantial improvement.

Section 6.1.1 describes the assumptions and methodology used to simulate the effects of the PROTEL HEH aperture and rotation upon the flux measurements for a modified $\sin^N \alpha$ pitch angle distribution. Section 6.1.2 provides the results of the simulations. Section 6.1.3 provides a summary of the conclusions. Tables and graphs will be provided.

6.1.1 Methodology

For each channel, the PROTEL detector measures the number of protons hitting the detector with energy in the channel range during a single integration period (~1 second). The observed proton count is used to compute the corresponding flux for the local pitch angle bin (determined from the spacecraft orientation, magnetometer data, and computed magnetic field vector (the latter obtained from magnetic field model)), and L-shell bin. The corresponding data is mapped to an equivalent equatorial pitch angle bin and averaged over a data collection time interval. For the Quiet and Active models the time intervals were the duration of the data collection periods for the models.

The approach used here is to simulate the effect of detector aperture and rotation upon observations of a “pure” modified $\sin^N \alpha$ pitch angle distribution by computing the average instantaneous flux over the aperture and then averaging the result over the 12° rotation.

In order to compute the flux integral, the following coordinate system (fixed relative to the PROTEL HEH axis) was used. The unit normal \mathbf{n} (also the PROTEL HEH symmetry axis) to the first detector surface is the z-axis $\mathbf{n} = (0,0,1)$. The orientation in the spin plane is described by an angle of rotation, γ , with the reference direction $\gamma = 0$ chosen such that the projection of the Magnetic field vector \mathbf{B} upon the PROTEL HEH spin plane is taken to be the y direction. The unit vector \mathbf{b} in the direction of \mathbf{B} is given by:

$$\mathbf{b} = (\sin i, \cos i \sin \gamma, \cos i \cos \gamma) \quad (18)$$

where i is the angle between the mirror plane and spin axis, and γ is the angle in the spin plane describing the current orientation of the PROTEL HEH relative to the projection of \mathbf{B} onto the spin plane. The unit vector \mathbf{u} pointing to the direction of an arbitrary incoming particle is given by

$$\mathbf{u} = (\cos \phi \sin \theta, \sin \phi \sin \theta, \cos \theta). \quad (19)$$

The particle count corresponding to a given differential flux is given by the following integral:

$$N(E,L) = \int_{\Delta t} dt \int_{\Delta E} dE \int_{\Omega} \eta(\Omega, \dots) j(E,L,\Omega) \mathbf{u} \cdot \mathbf{n} d\Omega \quad (20)$$

where t is the time, E the energy, j the differential flux, Ω solid angle, and η describes the detection efficiency. Here we choose $\eta = 1$ for directions within the PROTEL HEH acceptance cone, and 0 otherwise.

We are therefore interested in evaluating the following integral for each value of N and γ of interest:

$$\int_{\theta=0}^{8.5^\circ} \int_{\phi=0}^{360^\circ} \left(\frac{\sin^2 \alpha - \sin^2 \alpha_c}{1 - \sin^2 \alpha_c} \right)^{\frac{N}{2}} \cos \theta \sin \theta d\theta d\phi \quad (21)$$

where $\cos \alpha = \mathbf{b} \cdot \mathbf{u}$. An analytic expression of this integral is not available. Monte Carlo methods were used to compute this integral for each appropriate angle bin for selected values of N ranging from 2 to 100 at intervals of γ of 0.5° .

For the Monte Carlo integration, for each value of N and γ , 10,000 trials were used. For each trial, the integrand was computed, where θ and ϕ were randomly chosen from a uniform distribution in the range between 0° and 8.5° and $0^\circ - 360^\circ$ respectively. The sum of the integrand (over the number of trials) was then computed. The normalization is obtained by performing the parallel sum of $\sin \theta \cos \theta$. The ratio represents the average value of the differential flux (for the value of N and γ) over the aperture.

The effect of rotation is then taken into account by computing the average of the computed flux over a 12° interval (in γ) centered at each of the PROTEL pitch angle bin angles. For fixed N and i , a simulated "observed" pitch angle distribution is obtained by computing the pitch angle α corresponding to γ using the equation $\cos \alpha = \cos i \cos \gamma$.

In order to emulate the data reduction procedure used for the PROTEL pitch angle observation data, the value of the (simulated) flux for the first PROTEL pitch angle bin below $\alpha = \alpha_c$ was subtracted from each of the flux bins. The resulting data was then fit to both a single and the sum of two functions of the form (1) using the same value for the loss cone boundary α_c .

The final simulated pitch angle distributions obtained in this manner reflect the combined results of the simplified modeling of the PROTEL HEH detector, the flux averaging due to the rotation of the spacecraft, and of the data reduction methods used to generate the CRRES Active and Quiet Model

database, as applied to the case of a single pitch angle distribution of the form (1).

Fits of the Active and Quiet model equatorial pitch angle distributions to functions (a single, and the sum of two distributions) of form (1). For the case of a fit to a single modified $\sin^N \alpha$, linear least squares fits were made to $\log_{10} j(E, L, \alpha)$, for which the basis functions are given by:

$$1, \quad \frac{1}{2} \log_{10} \left(\frac{\sin^2 \alpha - \sin^2 \alpha_c}{1 - \sin^2 \alpha_c} \right) \quad (22)$$

The fits to the sum of two distributions of the form (1) were performed as follows:

A fit to a single distribution was made using a set of points (usually from 5° to 35° above α_c). The fluxes corresponding to the fits were computed, and subtracted from the observed fluxes. The differences were then used for a fit to a second distribution, using a set of points (spanning $\sim 30^\circ$) near $\alpha = 90^\circ$. To compare the results of a single and a “double” fit, correlation coefficients were computed between the $\log_{10}(\text{flux})$ from the original data, and the result $\log_{10}(\text{fit values})$ of the fit.

6.1.2 Results

Monte Carlo computations for the flux were performed for $N = 4, 5, 6$ and 8 , for L -values of $1.25 - 3.70$ at 0.05 intervals. The L - dependence arises from the dependence of α_c on L ; the same values of α_c were used for the fitting of the PROTEL Quiet and Active model data. Figure 6.1 below shows the computed equatorial flux (incorporating the effects of the HEH aperture and rotation) at $\alpha = 90^\circ$, as a function of L for the four N values. Note that α_c ranges from 47.5° on the left, to 0.25° on the right. The low values on the left hand side of the graph result from the subtraction of the “loss cone” flux. Figure 36 provides an estimate of the error in the flux for equatorial pitch angles of $\alpha = 90^\circ$. Caution should be used in using the data in Figure 36 for estimates at other pitch angles.

The resulting pitch angle distributions have been fit to both a single, and the sum of two modified $\sin^N \alpha$ equatorial pitch angle distributions. The quality of these fits are generally not as good as those obtained from the actual active and quiet model data in much of the radiation belt regime. For single fits to the actual data, it was found that if data points near the loss cone were included in the fitting process (usually a single point!), that the values of N obtained (as a function of L) were very “noisy”. The same behavior was found in attempting to fit the “simulated” pitch angle distributions. A test was performed, in which different “seeds” for the random number generator were used for the same case, in which fit parameters varied only slightly ($\sim 2\%$). For the simulation, it was found necessary to exclude data points from within at least 2.5° of the loss cone from the fit.

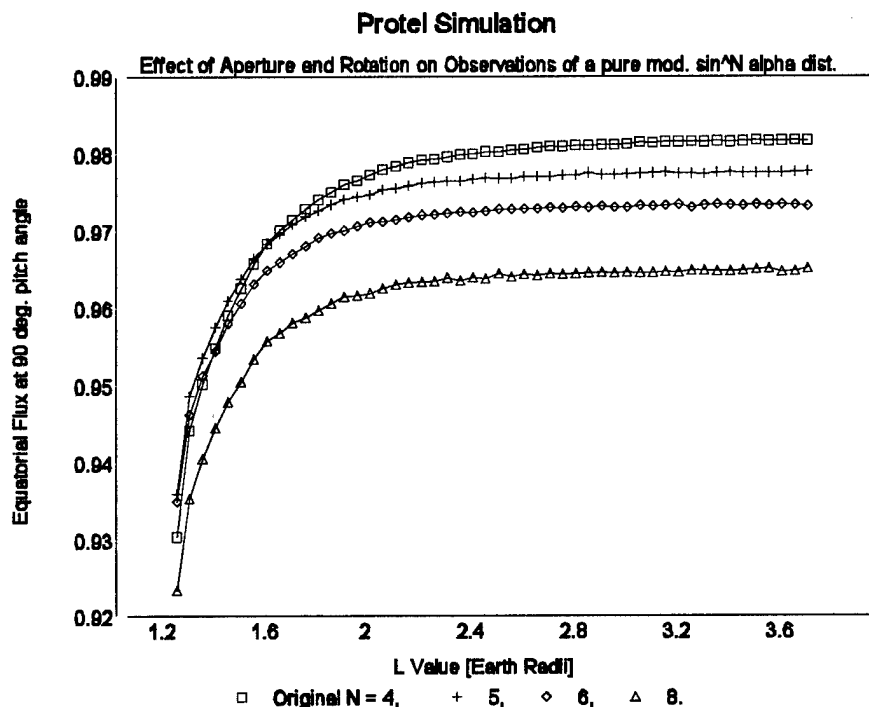


Figure 36. Computed equatorial flux at $\alpha = 90^\circ$ (incorporating the effects of the PROTEL HEH aperture and rotation), as a function of L for modified $\sin^N \alpha$ distributions for N=4, 5, 6, and 8. Note that α_c ranges from 47.5° on the left to 0.25° on the right. For the original distributions, $A(E,L)$ was taken to be 1.

Figure 37 is a graph of $A(E,L)$ obtained from the fit to a single modified $\sin^N \alpha$ distribution; if the quality of the fits were better, the data represented here should be approximately the same as that found in Figure 36.

In the single fits, the value obtained for $A(E,L)$ was generally below the computed flux at $\alpha = 90^\circ$. Data from the single fits was used to compute the equatorial omnidirectional flux. The results of the computations are provided in Figure 38, in which the vertical axis represents the ratio of the omnidirectional flux (computed from the fit of the simulation data/nominal).

The fits of the simulation pitch angle distributions to the sum of two modified distributions were only slightly better, but $A_1(E,L) + A_2(E,L)$ from the dual fits is in good agreement with the computed equatorial omnidirectional flux. Figure 39 provides the dual-fit version of the data presented in Figure 38.

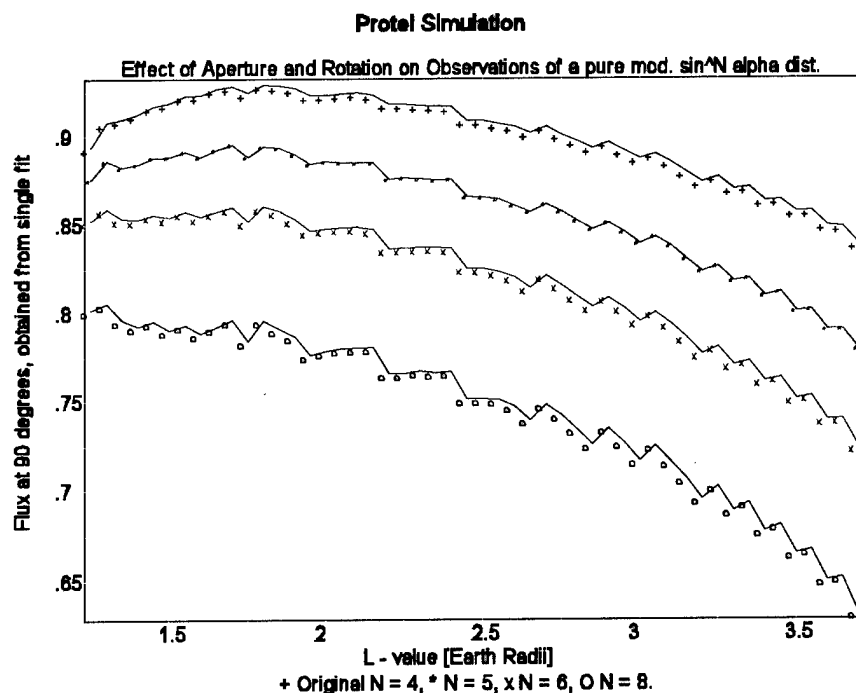


Figure 37. The computed distributions (incorporating the effects of aperture and rotation) have been fitted to a single modified $\sin^N \alpha$ distribution. $A(E, L)$ from the single fits is plotted vs L for $N = 4, 5, 6$, and 8 .

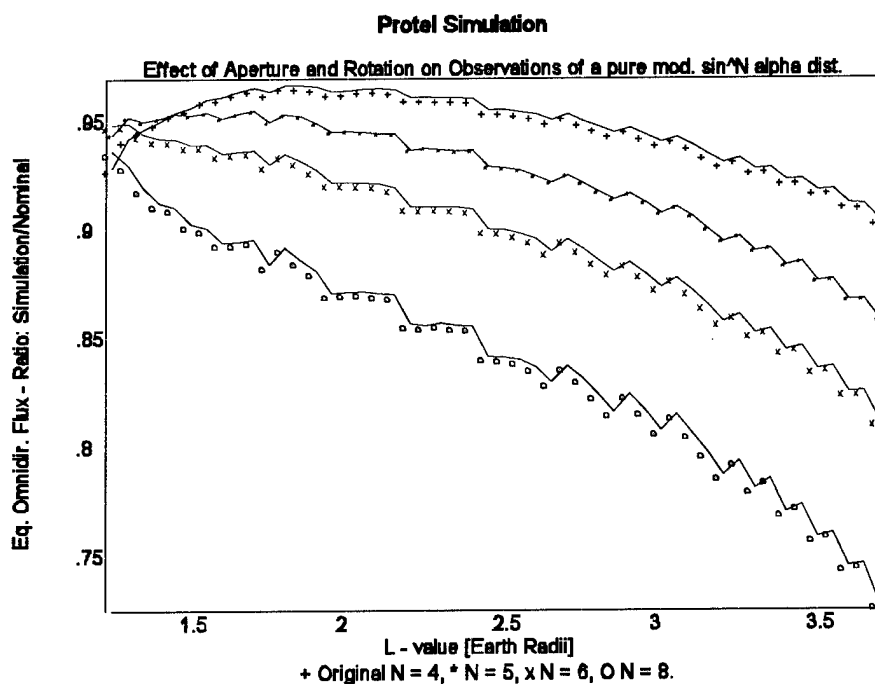


Figure 38. Ratio of equatorial omnidirectional flux (from fits of the computed pitch angle distribution to a single modified $\sin^N \alpha$ distribution) to that of the original modified $\sin^N \alpha$ distribution is plotted as a function of L for $N = 4, 5, 6$, and 8 .

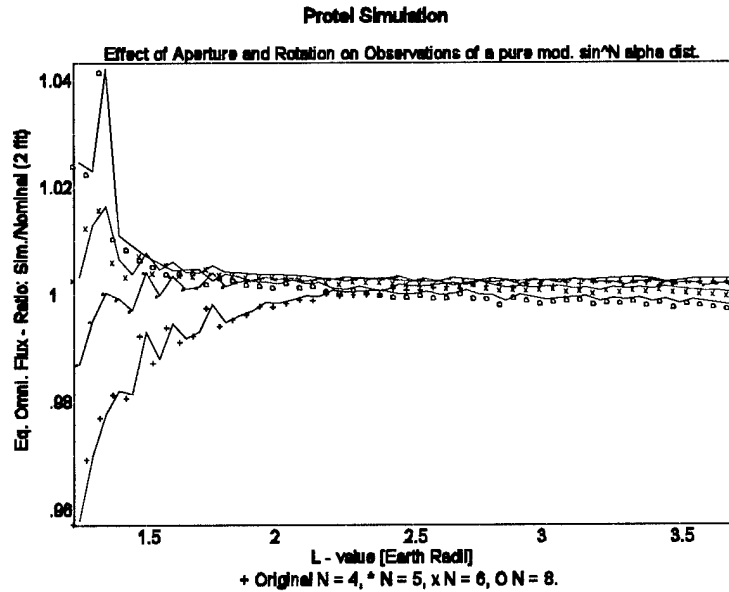


Figure 39. Ratio of equatorial omnidirectional flux (from fits of the computed pitch angle distribution to the sum of two modified $\sin^N \alpha$ distributions) to that of the original modified $\sin^N \alpha$ distribution is plotted as a function of L for original $N = 4, 5, 6$ and 8 .

A direct comparison of the original and simulated pitch angle distributions is provided in Figure 40, for the case of $N = 4$, $L = 1.25$. Other cases illustrate similar behavior, the only difference is the scale of the differences which appears to be proportional to the differences at $\alpha = 90^\circ$ (see Figure 36).

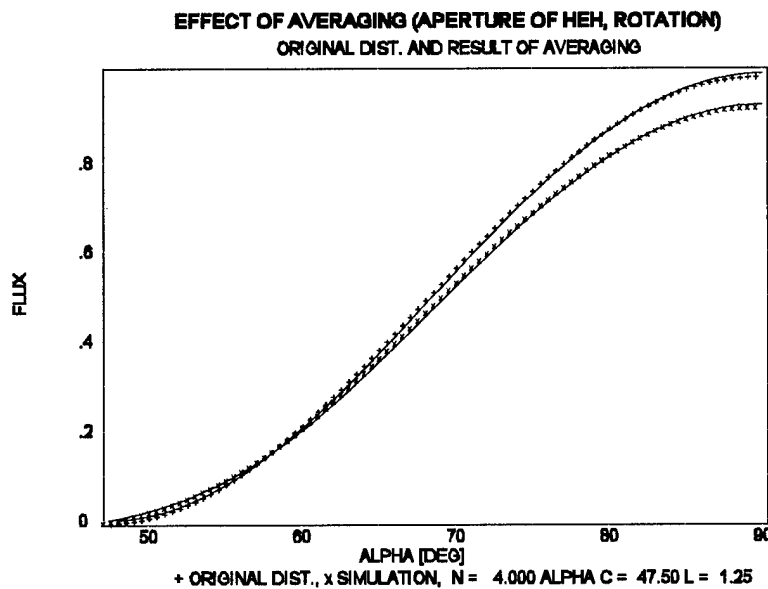


Figure 40. Sample comparison ($N = 4$, $\alpha_c = 47.5$, $L = 1.25$) of the computed pitch angle distribution with the original modified $\sin^N \alpha$ pitch angle distribution.

6.2 DOSAGE PREDICTION AND OBSERVATION COMPARISON

The CRRES Quiet and Active proton models were derived from observations from the Protel (Proton Telescope) instrument package corresponding to the "Quiet" and "Active" (before/after the March 1991 storm) data collection periods. The Protel instrument collected proton flux data in 22 energy channels within the 1-100 MeV range. The model data has been made available to the research community in both the CRRESPRO and PROSPECT software packages. The CRRESPRO package provides access to the measured omnidirectional flux as a function of L and magnetic latitude or B/B_0 , while PROSPECT provided proton pitch angle distributions.

The CRRES dosimeter consists of four detectors, each of which lies at the center of a hemispherical dome of aluminum. The domes have different thicknesses, which were selected to exclude charged particles having energies which lie below certain thresholds. The CRRES dosimeter measured the dose, primarily due to protons and electrons. For each detector, there are two channels, LOLET and HILET, which measure the accumulated energy deposited by individual events in the energy loss range 0-1 MeV and 1-10 MeV respectively. Based upon dosimeter observations, PL has also developed dosage models for the Quiet and Active periods, and a software package CRRESRAD to make the dose models available to the research community.

This report describes the results of a series of computations based upon the CRRES Protel proton models, which estimate the dose, due to protons, which would be detected by the CRRES dosimeter. It also provides a comparison of these computations with the actual dosimeter observations. The calculations described below have only been performed for the equatorial (magnetic) case, but the software developed for the purpose can also handle the full range of B_0/B for which CRRES Protel Active and Quiet model data is available.

The transport codes (flux to dose computations) used are based upon the Yates-Rothwell algorithm, and upon the CRRES dosimeter Path Length distribution codes for isotropic, mirror plane, and modified $\sin^N \alpha$ pitch angle distributions. For the HILET Channel 1 computations, particularly for the Quiet Model, there is reasonably good agreement between the various transport codes used and the actual observations. For the Quiet model, the Rothwell-Yates algorithm and the isotropic path length distribution method computations consistently overestimate the HILET dose for channels 2-4. For the Active model, the results are more complex, and will be described below.

In examining the proton pitch angle observation data from Protel Quiet and Active data collection periods, we have found that best analytic representation of the proton equatorial pitch angle distribution data for much of the radiation belt is either as a single modified $\sin^N \alpha$ pitch angle distribution, or as the sum of two such distributions. We have adapted the Monte Carlo based path length distribution software to compute path length distributions and response functions for spin averaged modified $\sin^N \alpha$ distributions for arbitrary α_c and arbitrary inclinations with respect to the magnetic field vector. We have limited our computations here to the case in which the inclination is 0 - that is - the magnetic field vector direction lies within the spin plane.

Using this approach, we have obtained much better agreement with the HILET channels 2-4 for the Quiet model data. For the Active model, parallel computations were performed, with the result that, as a function of L, there are significant underestimates of the computed dose in the second ("new") radiation belt. Since high energy electrons also contribute to the HILET channel, there is a strong possibility that the differences may be due to the presence of high energy electrons in the new radiation belt. The contributions due to electrons has not been examined, but may be the subject of a future study.

This section describes the computations outlined above, providing graphs and a brief discussion of the results. Section 6.2.1 describes a mathematical description of the modified $\sin^N \alpha$ distribution. Section 6.2.2 describes the fit procedure used for the Protel pitch angle data (Quiet and Active models). Section 6.2.3 describes the Rothwell-Yates codes, and the corresponding isotropic path length distribution codes. Section 6.2.4 describes the spin-averaged modified $\sin^N \alpha$ computation, and Section 6.2.5 provides graphs and descriptions of the results.

6.2.1 Modified $\sin^N \alpha$ Pitch Angle Distributions and their Properties

The stability of the radiation belts results from a balance between the loss of charged particles by scattering and other means and the production of newly charged particles by various processes, primarily from particle injections induced by solar-magnetic storms and CRAND (Cosmic Ray Albedo Neutron Decay) and others. The primary loss mechanism results from particles being scattered by neutral atoms near their mirror points at low altitudes, and their resulting recombination with free ions. Thus, for a range of L-shell values there will be a "forbidden" portion of the proton equatorial pitch angle distribution - the so called loss cone. The modified $\sin^N \alpha$ distributions take the loss cone into account. Since the charged particles are "trapped" to move along the magnetic field lines, the equatorial loss cone cut-off α_{co} is dependent on L-shell value, and may be computed by magnetic field line tracing to an altitude at which there is a sufficiently high atmospheric density.

Using Liouville's Theorem, it is possible to "map" the modified $\sin^N \alpha$ pitch angle distributions down a magnetic field line, as a function of B_0/B . Mapped in this way, for example, the omnidirectional flux is given by:

$$\left(E, L, \frac{B_0}{B}\right) = \frac{2 \pi^{\frac{3}{2}} A(E, L) \Gamma\left(\frac{N}{2} + 1\right)}{\cos^N \alpha_c \left(\frac{B_0}{B}\right)^{\frac{1}{2}} \Gamma\left(\frac{N+3}{2}\right)} \left(\frac{B_0}{B} + \cos^2 \alpha_c - 1\right)^{\frac{N+1}{2}} \quad (23)$$

For the magnetic equator ($B_0/B = 1$) the above equation reduces to:

$$J(E, L, \frac{B_o}{B}=1) = 2 \pi^{\frac{3}{2}} \cos \alpha_c A(E, L) \frac{\Gamma\left(\frac{N}{2} + 1\right)}{\Gamma\left(\frac{N + 3}{2}\right)} \quad (24)$$

6.2.2 Modified $\sin^N \alpha$ Fits of the Protel Active and Quiet Model Data

To avoid numerical problems, the values of α_c actually used were taken to be the lower bin boundary of the bin containing the loss cone boundary. This procedure was implemented in both MODVIEW, a program which displays the derived omnidirectional flux as a function of L, E, and magnetic latitude for the Protel Quiet and Active Models (and corresponding fits to a single distribution of the above form) and AFITSSSA, which displays the corresponding pitch angle distribution data and the corresponding fits to a single, and to the sum of two modified $\sin^N \alpha$ pitch angle distributions.

The following procedure was used to obtain a fit to the sum of two distributions of the above form for each L value, and for each energy channel:

- (1) A fit was performed (\log_{10} flux vs $\sin \alpha$) to a single distribution, using values of α from $\alpha = 90$ to $\alpha_c + 10$ degrees. This fit was used to provide a comparison with other fits, to be described below.
- (2) The fit to the sum of two modified $\sin^N \alpha$ pitch angle distributions was performed as follows: First a fit was performed to a single distribution using values of α from $\alpha_c + 10$ degrees to $\alpha_c + 40$ degrees. The flux from the resulting fit was subtracted from the actual data, and the difference was used to perform a second fit, for n values, from $\alpha = 90, 85, ..$ where the value of n was chosen to be in the range of 5 to 12. The sum of the fluxes corresponding to the two fits was computed, and χ^2/n' , where n' is the total number of points used in the fit, was computed to provide an estimate of the error.

For a given energy channel, and value of L, the program implementing the above computation displays a graph displaying the model data, the first and second fits, and the flux obtained from the sum of the second and third fits.

- (3) Correlation coefficients were then calculated for the single and double fit cases, and the double fit solution was used only if it had a higher correlation coefficient than the single fit.

6.2.3 Rothwell-Yates Proton Dose Computation

The original Rothwell-Yates codes were written to compute the dose which would be observed at a given location in space from either electrons or protons after passage either through a aluminum spherical shell, or behind an infinite slab (aluminum) having a given thickness. A common

application was to use a satellite ephemeris code to compute an orbit over an extended period of time, and use the orbital data to compute the average dose/day which would be detected. The code permitted the use of various NASA radiation belt models (electron or proton models). For the proton contribution, a simple undocumented Monte Carlo algorithm was used. The relevant portions of the Yates-Rothwell code containing the algorithm for computing dose for protons have been incorporated into a new code which computes the sum of the HILET and LOLET doses (the Rothwell-Yates code does not have the capability to differentiate between HILET and LOLET doses for the CRRES dosimeter). Since the Rothwell Yates code computes the dose at the center of a sphere from particles arriving from a solid angle of 4π , the result is multiplied by 0.5 for comparison with the dosimeter observation data, for which particles enter only from a hemisphere.

A code was then written to read the CRRESPRO proton Active and Quiet model omnidirectional flux data files, and use the equatorial flux data to compute the dose (at the center of an aluminum sphere) using the Yates - Rothwell proton algorithm. The thicknesses of the various dosimeter domes were used for the computations. The resulting data was compared to the corresponding HILET channel data; comparison graphs of the results are provided below for the quiet and active models. Similar graphs are provided for the spin average modified $\sin^N \alpha$ computations.

The Rothwell-Yates algorithm produced significant over-estimates of the dose over most of the range.

The isotropic path length distribution code, one of the codes developed to model the CRRES dosimeter, was then adapted to compute the dose using the same proton data files. Both the HILET and LOLET calculations were performed. It was found that the LOLET contributions were small in comparison to the actual LOLET data, verifying the fact that the LOLET dose is primarily due to electrons. The isotropic path length distribution HILET dose computations agreed closely with the Rothwell-Yates results.

6.2.4 Spin Averaged Modified $\sin^N \alpha$ Pitch Angle Path Length Distribution Calculations

The path length distribution method was used to develop software to model the performance of the CRRES dosimeters, in order to better understand the effects of protons on dose measurements. Earlier modeling of the DMSP dosimeters were made based upon the infinite slab approximation, which is valid in cases when the solid state detectors are thin (in particular, for a disk-shaped detector, the thickness/radius ratio is small). For the first CRRES dosimeter detector, that ratio is $\sim .79$. The path length distribution modeling effort for the CRRES and DMSP dosimeters is described in *Hein and Bass* [1993]. In that reference, the effects of the following proton pitch angle distributions on the dosimeter measurements are described: isotropic, mirror plane and $\sin^N \alpha$ distributions. The software developed was modified to compute the dose for the Protel Active and Quiet models for the isotropic case. Additional adaptations of the software were made to model the effects of modified $\sin^N \alpha$ distributions.

The Monte Carlo approach is sufficiently flexible to take into account the case of modified $\sin^N \alpha$ distributions. The software developed also permitted the selection of the angle I between the magnetic field direction and the spin plane ($I = 0$ if the magnetic field vector lies in the spin plane). The actual computations were performed by assuming that $I = 0$. The spin averaging was performed by randomly selecting the orientation in the spin plane (relative to the projection of the magnetic field vector onto the spin plane). These calculations require an increase of the number of "trials" compared to the isotropic case, and therefore, an increase in the computation time.

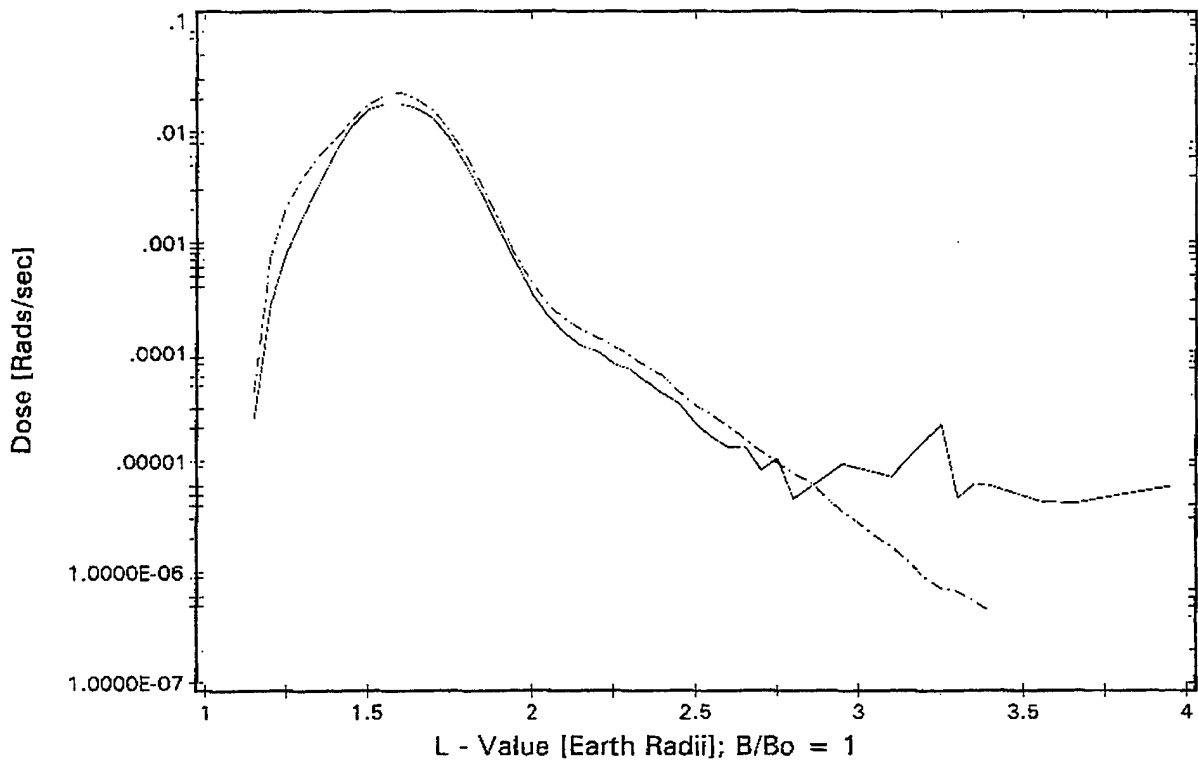
Since α_c is L -dependent, it was necessary to compute the path length distributions and then the response functions for each of the CRRES dosimeter HILET and LOLET channels for each of the 56 L - values, for several values of N . The values $N = 0, 5, 10, 20$ and 40 were chosen because it was found that the response functions changed sufficiently slowly with N that a linear interpolation scheme in N was adequate to compute the response function for arbitrary N . Since, as a function of N , the response function changes very slowly for large N , if a fit was obtained in which $N > 40$, the value for $N = 40$ response function was used.

For each value of E , the value $A(E, L)$ was interpolated from the best fit table for the appropriate (Active or Quiet) model, using log/log interpolation if bracketing values were available, or linearly (to 0) otherwise. The results of these computations are described below.

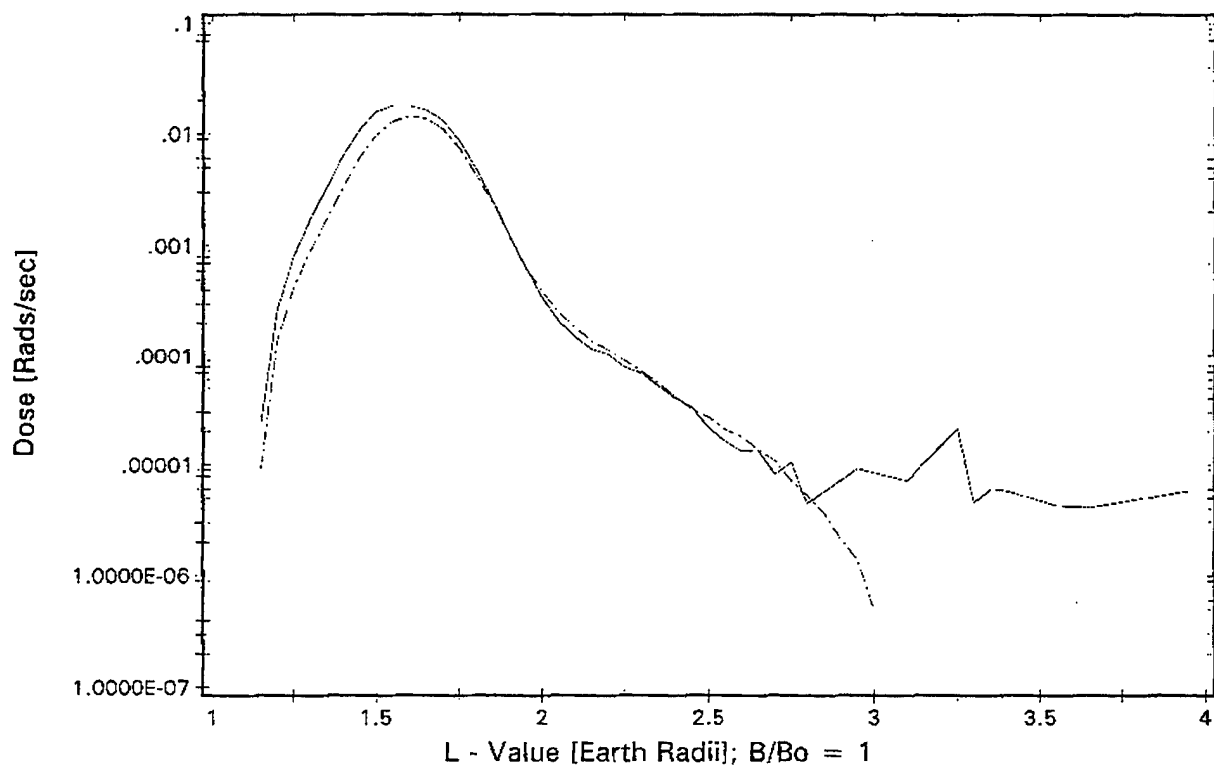
6.2.5 Results

The results of these computations are provided in a series of 16 graphs, which exhibit the comparison of the Rothwell Yates algorithm dose computations with those obtained from the spin-averaged modified $\sin^N \alpha$, both compared with the actual Dosimeter data. Computations based upon the isotropic path length distribution method were also performed; the results of the latter computations exhibit only minor differences when compared with the Rothwell-Yates algorithm computations. In the graphs, the actual data is represented by a solid line, while the computations are represented by a dashed line. For $L > \sim 2.8$, there is an apparent discrepancy between the predictions and the actual data which is due to the fact that the Active and Quiet PROTEL models excluded the solar proton contribution which is present in the dosimeter. In Figures 41 to 48, the top chart is the data obtained from the Rothwell-Yates code, and the bottom chart is that obtained using the spin-averaged modified $\sin^N \alpha$ calculations.

For the both the quiet model the Rothwell-Yates computations consistently overestimate the dose, particularly for dosimeter channels 2, 3 and 4. For the active model, the dose is consistently overestimated for the inner belt, and underestimated for the outer (new) belt. The corresponding graphs for the spin-averaged modified $\sin^N \alpha$ computation provide improved agreement in the L -value range of 1.7 - 2.75 earth radii for the quiet model, and in the inner belt for the Active model. For the most part, the active model spin-averaged modified $\sin^N \alpha$ computations underestimate the dose, except for a small range of L values for Channels 1 and 4.



solid: Measured, dashed: modified Rothwell-Yates code computations using PROTEL data



solid: Measured, dashed: CARES dosimeter computations based upon mod sin²N alpha pld, and PROTEL data

Figure 41. Computed and measured dose of the Quiet Model, dosimeter HILET data, channel #1.

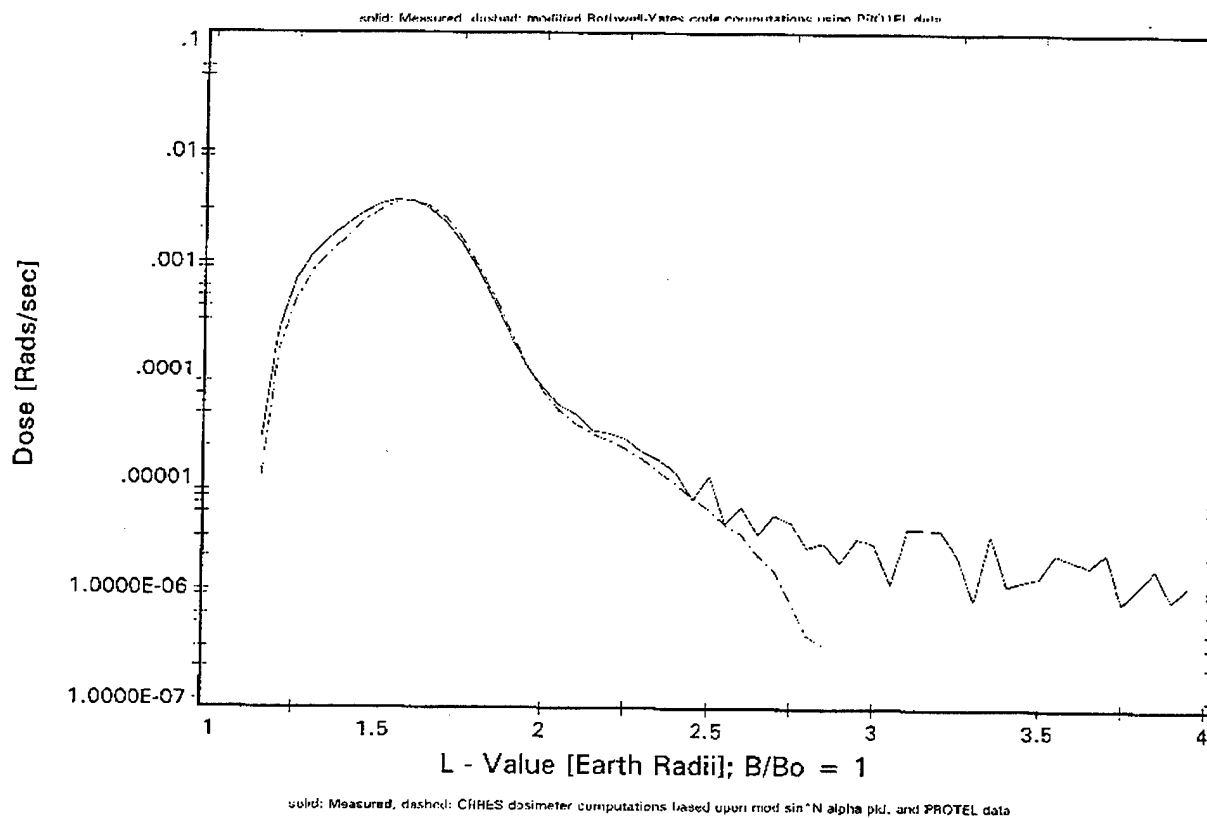
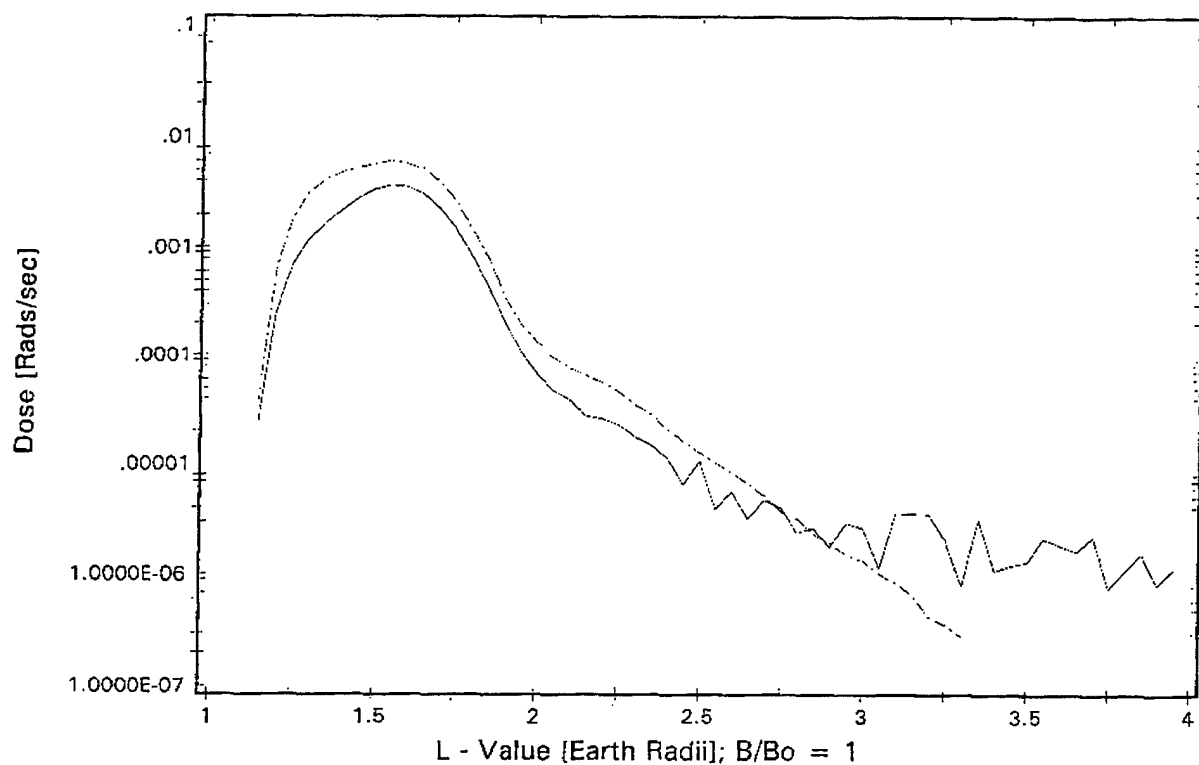
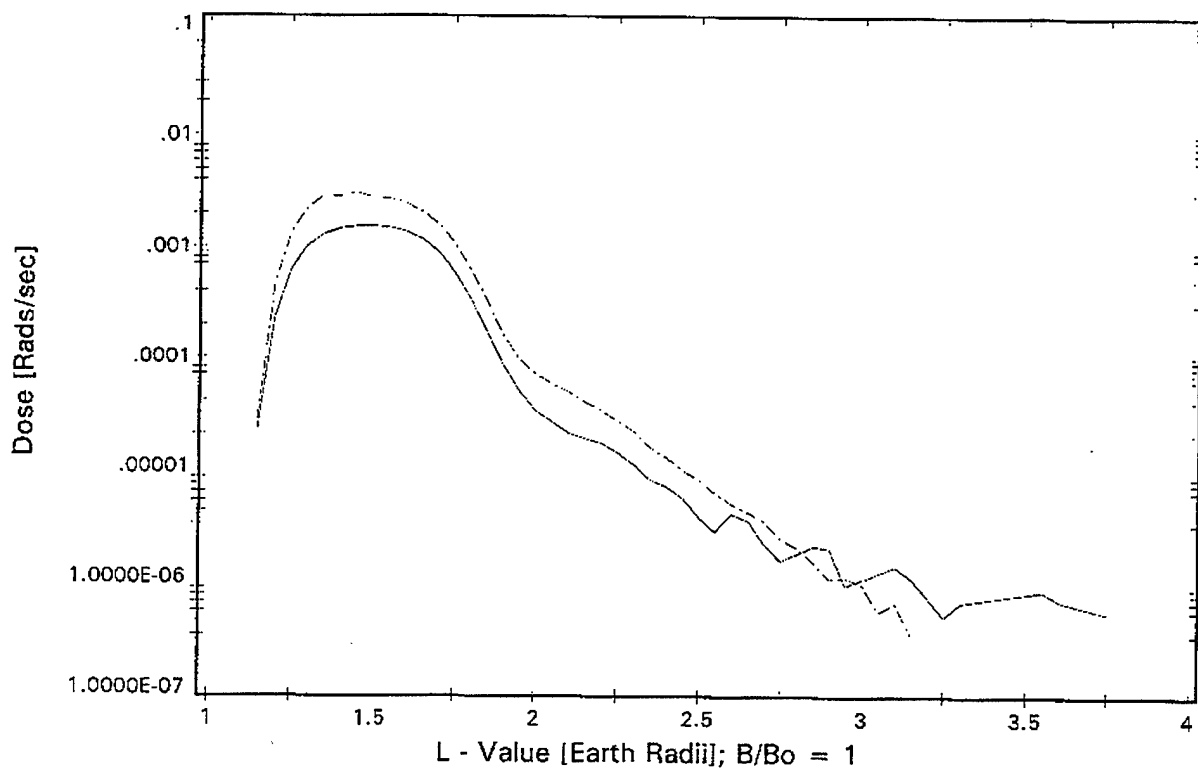
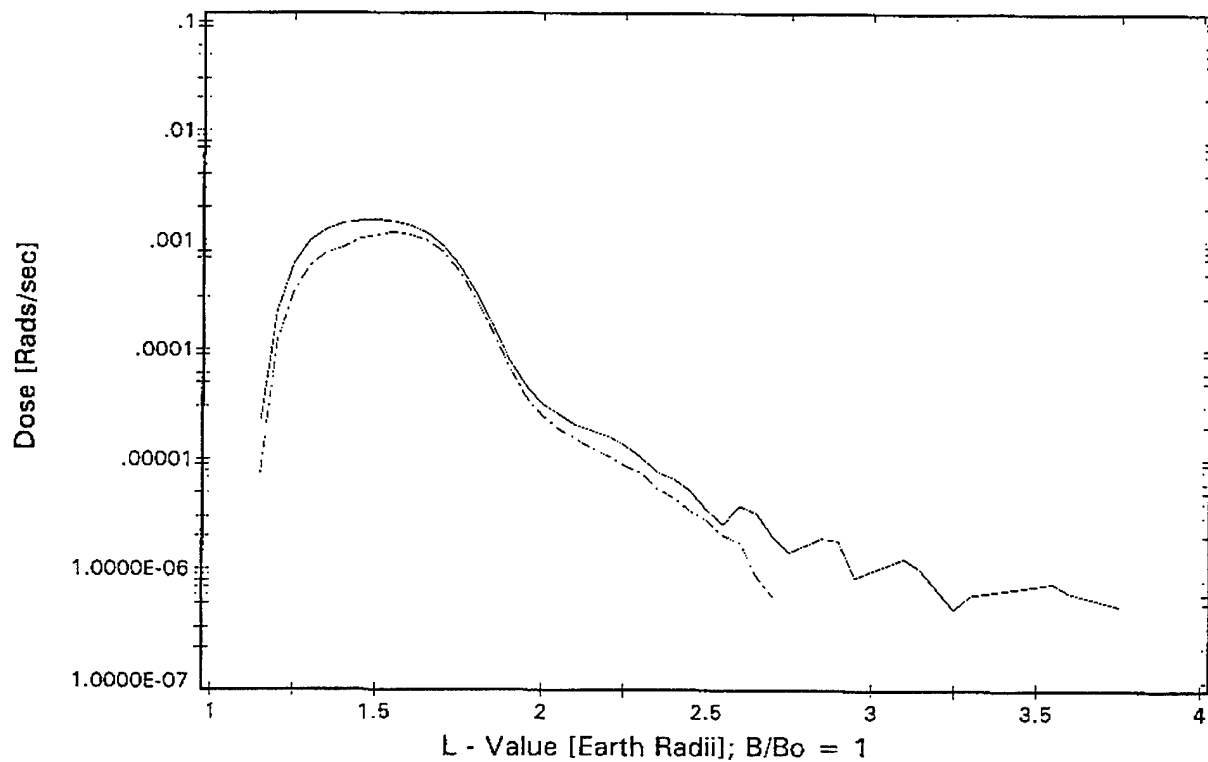


Figure 42. Computed and measured dose of the Quiet Model, dosimeter HILET data, channel #2.



solid: Measured, dashed: modified Rotllwell-Yates code computations using PROTEL data



solid: Measured, dashed: CRRES dosimeter computations based upon mod sin²N alpha pld. and PROTEL data

Figure 43. Computed and measured dose of the Quiet Model, dosimeter HILET data, channel #3.

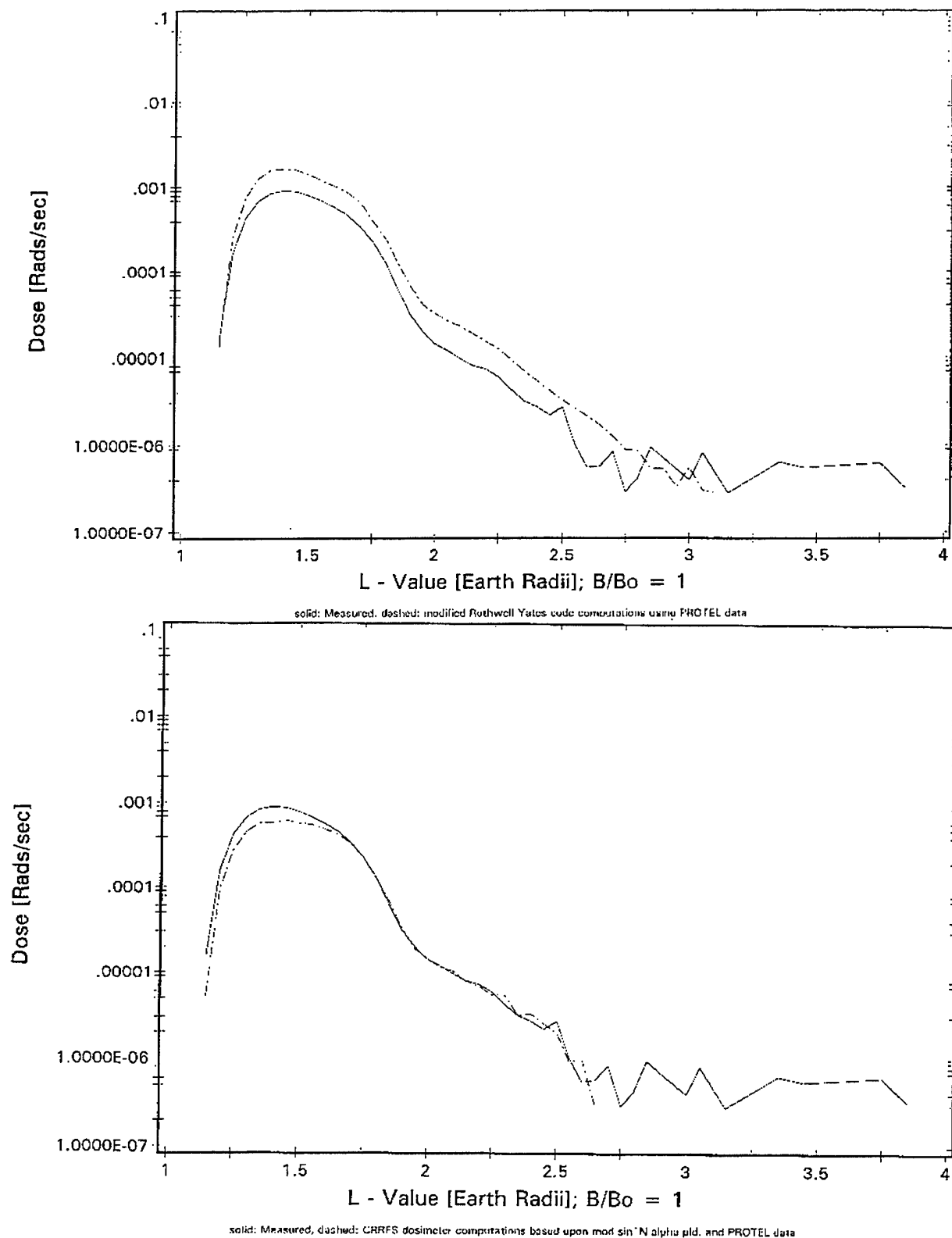
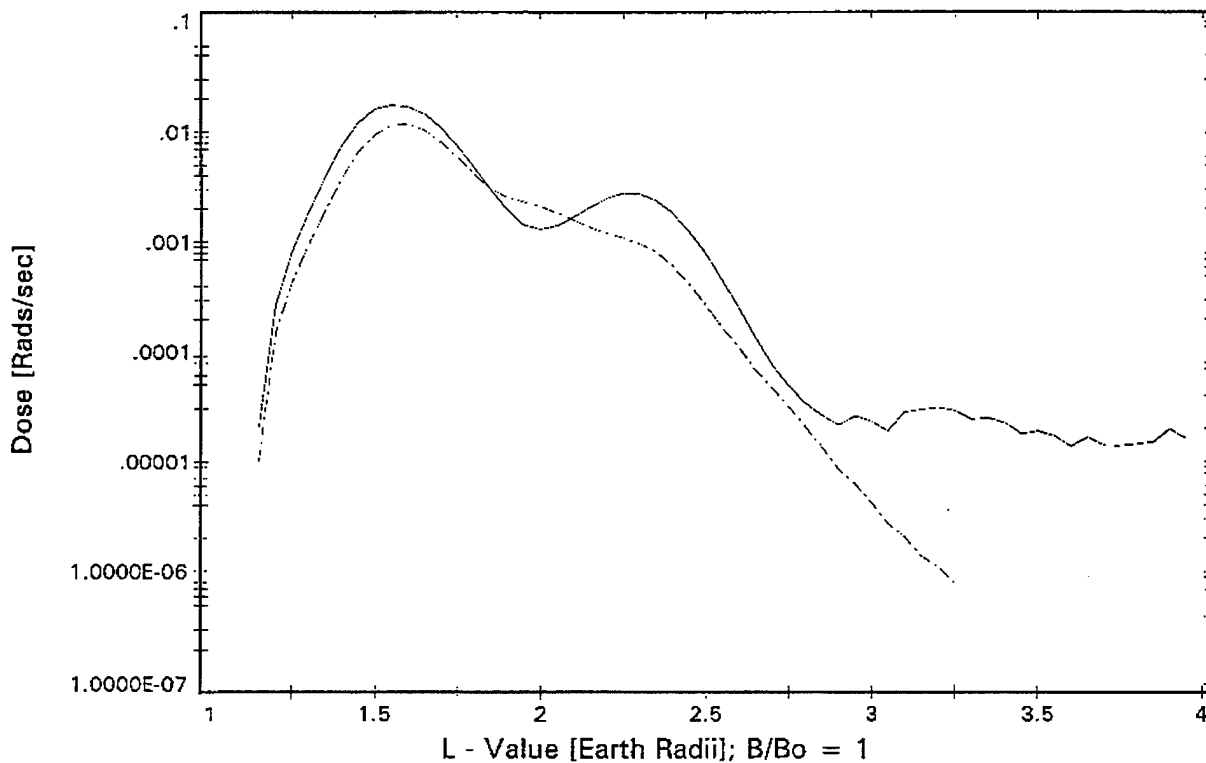
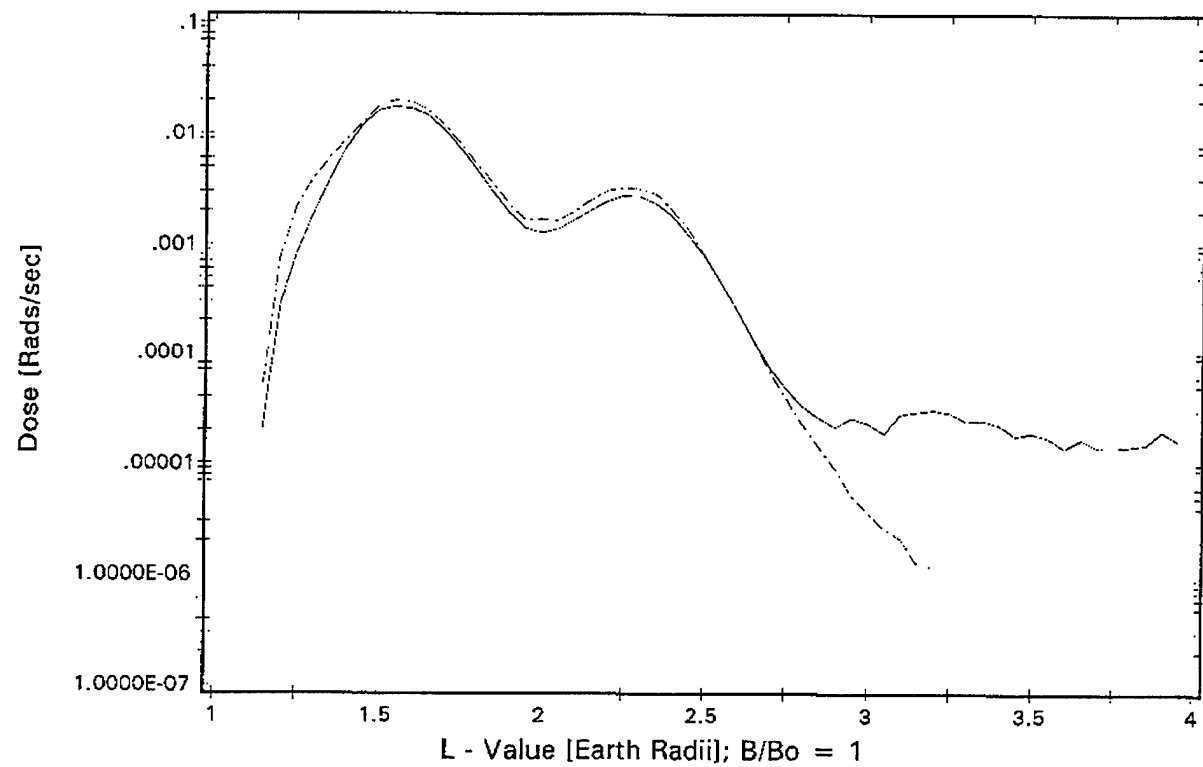


Figure 44. Computed and measured dose of the Quiet Model, dosimeter HILET data, channel #4.



solid: Measured, dashed: CRRES dosimeter computations based upon $\sin^2 N$ alpha pld. and PROTEL data

Figure 45. Computed and measured dose of the Active Model, dosimeter HILET data, channel #1.

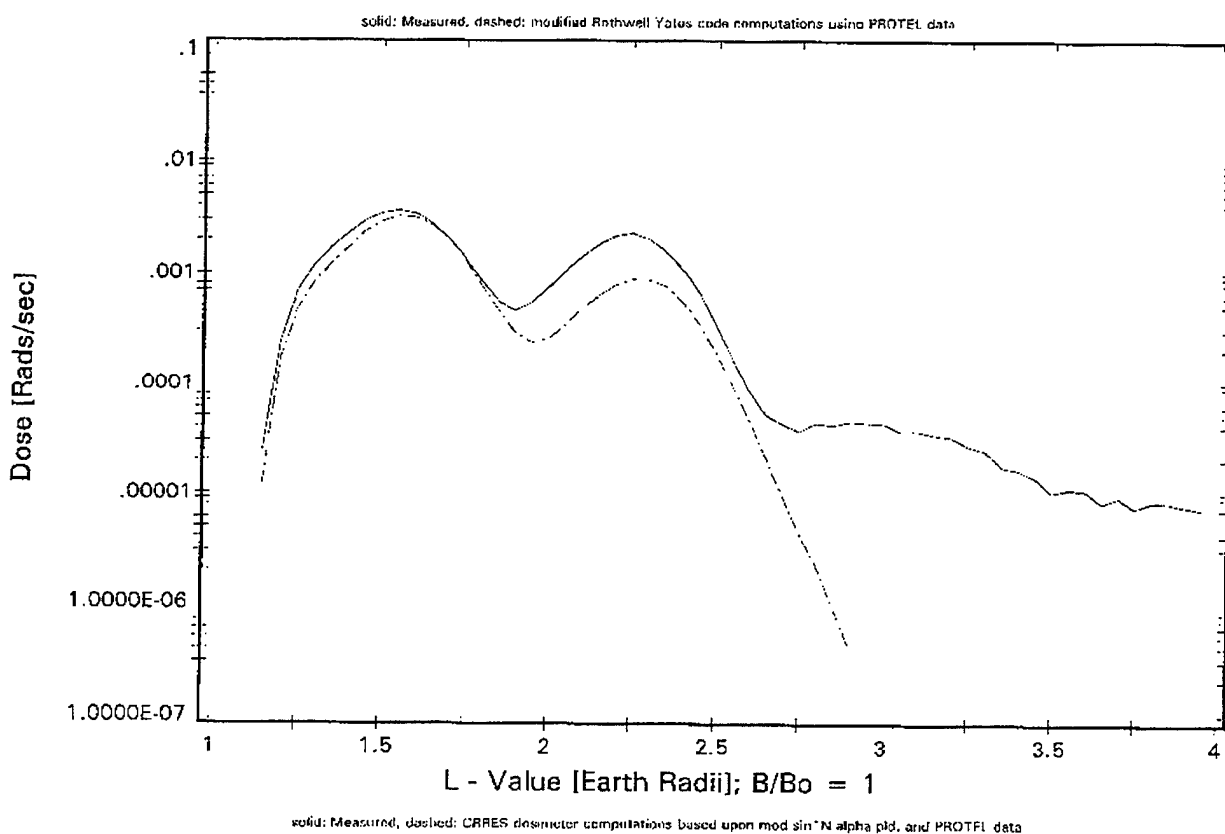
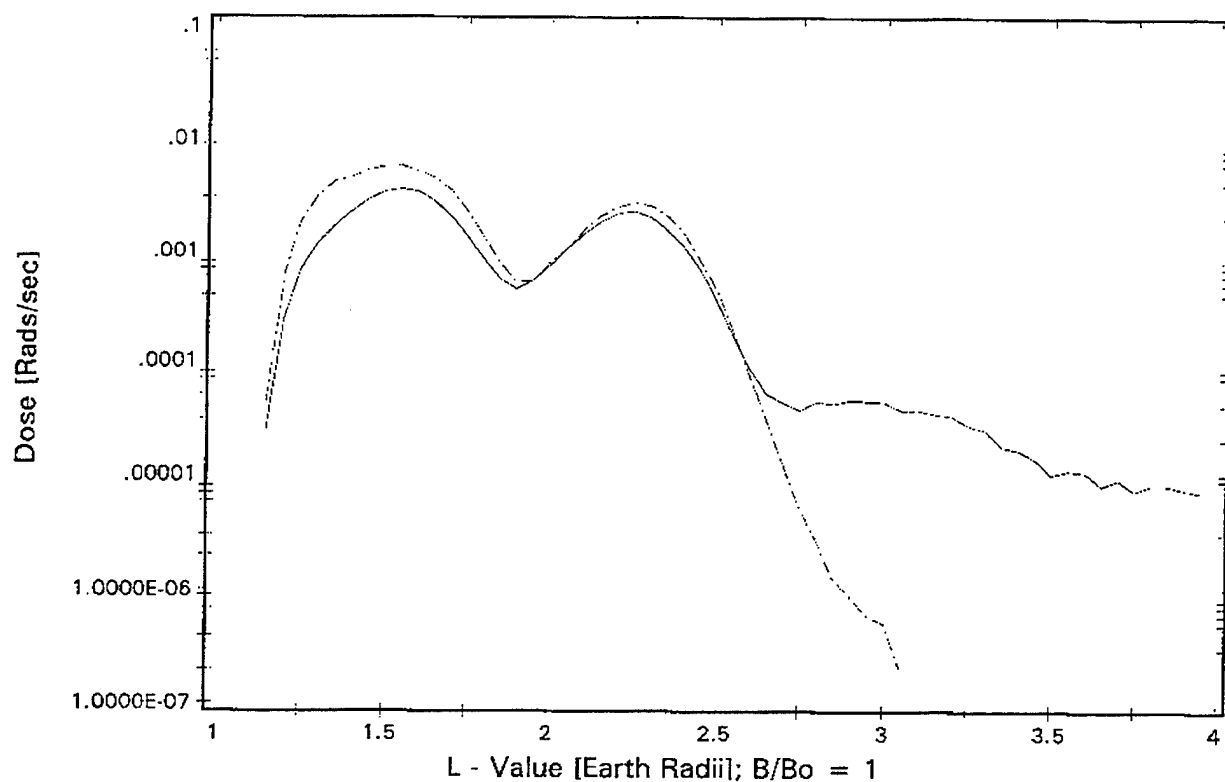
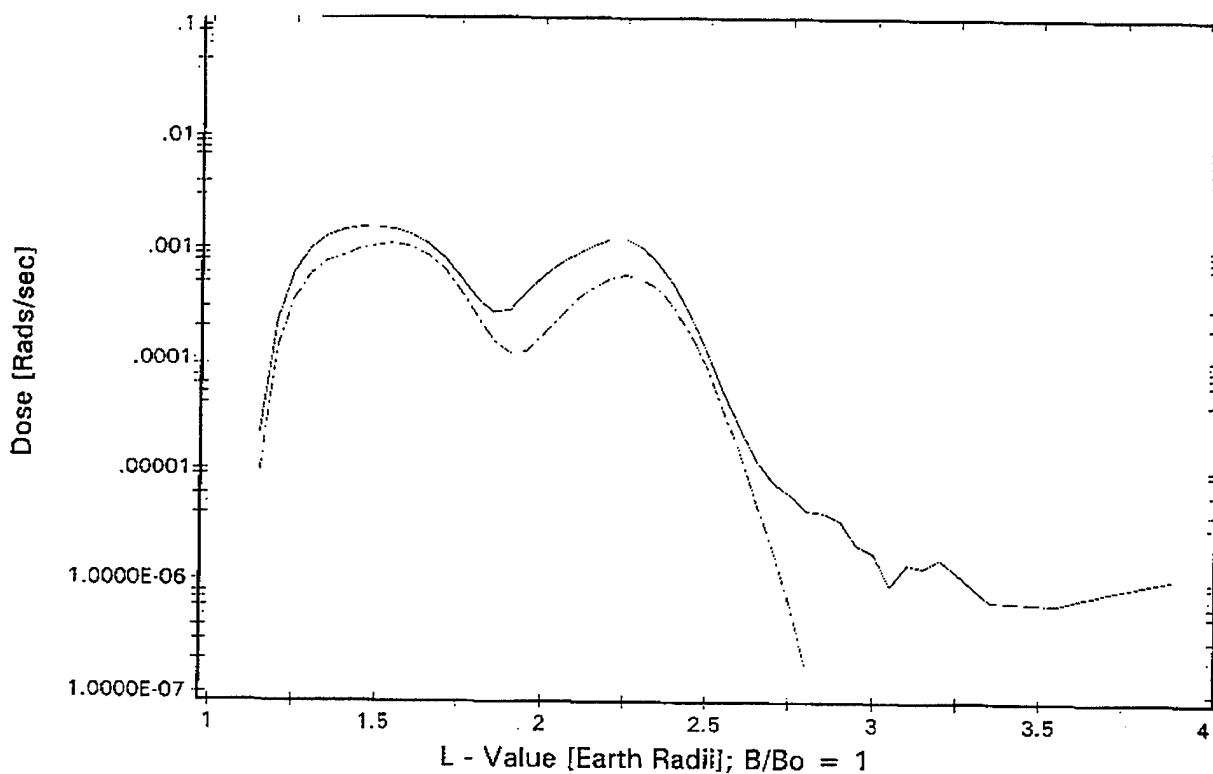
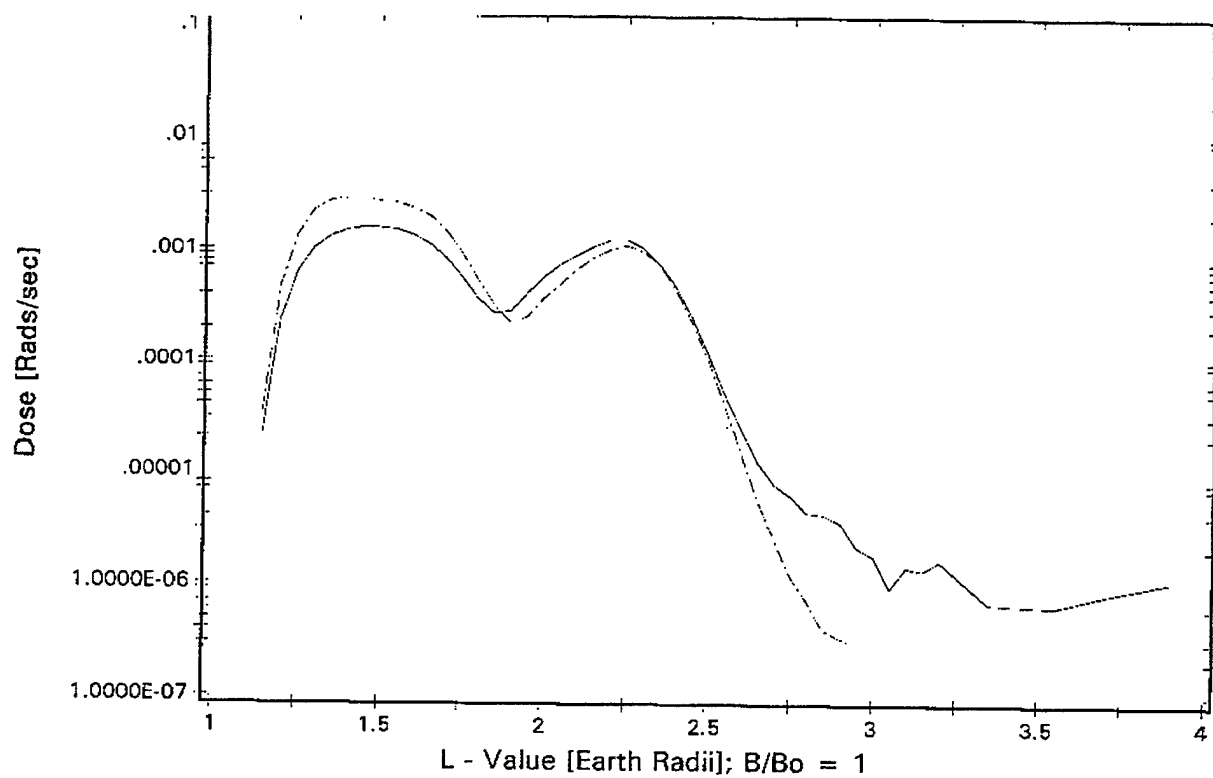


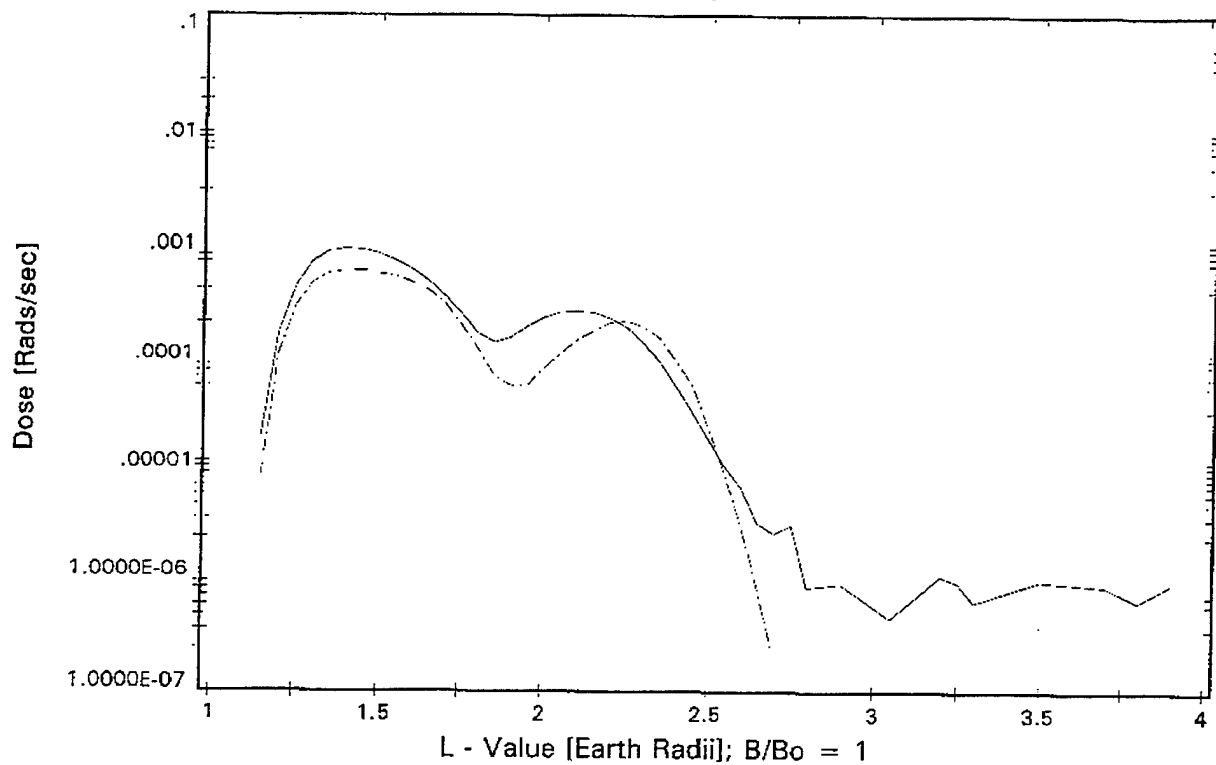
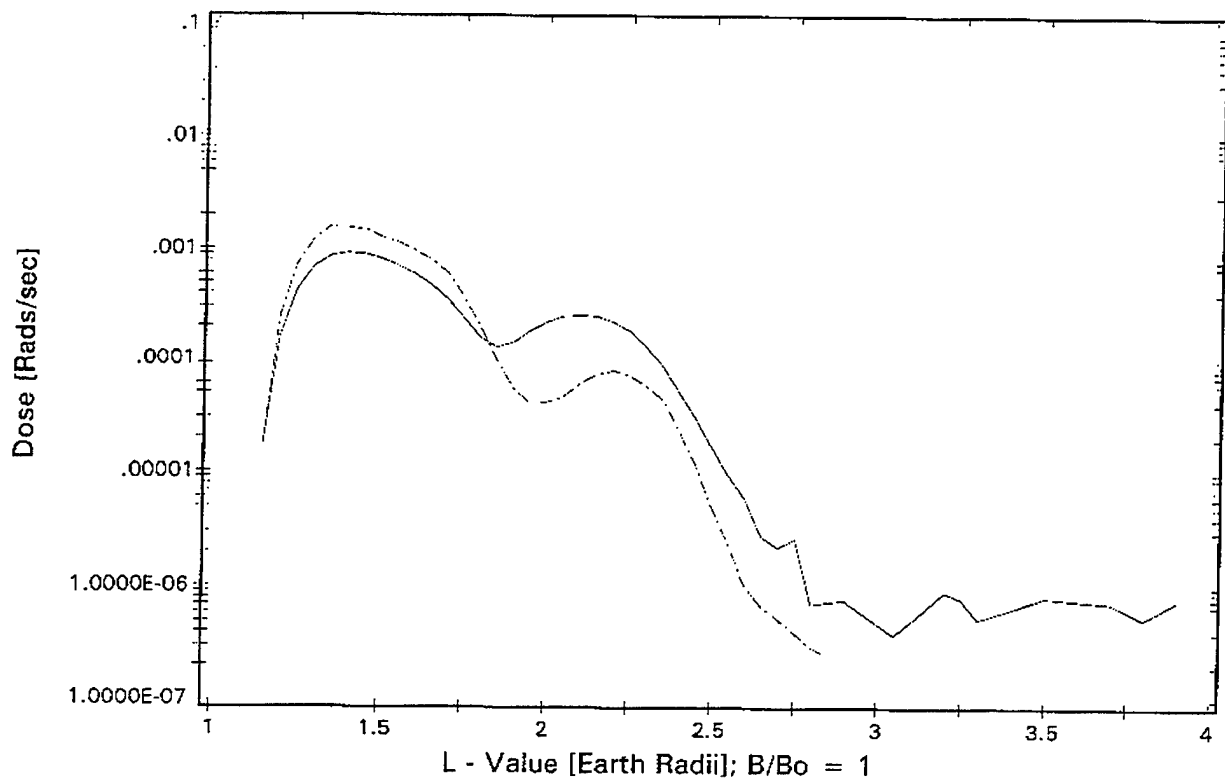
Figure 46. Computed and measured dose of the Active Model, dosimeter HILET data, channel #2.



solid: Measured, dashed: CRRES dosimeter computations based upon model sin²N alpha pld. and PPO IEL data

DATE RUN: 11/2/98

Figure 47. Computed and measured dose of the Active Model, dosimeter HILET data, channel #3.



solid: Measured, dashed: CRRFS dosimeter computations based upon mod sin²N alpha pld, and PROTEL data

Figure 48. Computed and measured dose of the Active Model, dosimeter HILET data, channel #4.

6.3 NUMERICAL COMPUTATION OF OMNIDIRECTIONAL FLUX

CRRES energetic particle detectors measured differential directional fluxes of energetic electrons and ions. As described by *Gussenhoven, et al.* [1993], the data were analyzed to produce models of equatorial differential unidirectional fluxes as functions of energy in 5° equatorial pitch angle bins and $0.05 R_E L$ bins, where L is the magnetic field line shell parameter, an approximate measure of the equatorial distance of the field line from the center of the earth. The procedures included mapping the measured fluxes from the position of the satellite up the magnetic field line to its equatorial crossing; sorting the data by equatorial pitch angle and L bins, in which average fluxes were obtained for each selected orbit, merging of the selected orbits, and when appropriate, correction for contamination.

To complete the models it was necessary to map back down the field lines to derive the model omnidirectional fluxes at non-equatorial locations. The omnidirectional flux at a certain location is computed by

$$J(B/B_0) = 4\pi \int_0^{\mu_c} j(\mu, B/B_0) d\mu \quad (25)$$

where $j(\mu, B/B_0)$ is the local unidirectional flux, B is the local magnetic field magnitude, B_0 is the equatorial magnetic field magnitude, μ is the cosine of the local pitch angle, and μ_c is the cosine of the local pitch angle at the lip of the loss cone. From Liouville's theorem the local flux $j(\mu, B/B_0)$ is mapped from the equatorial flux $j(\mu_0)$ by

$$j(\mu, B/B_0) = j(\mu_0) \quad (26)$$

where μ_0 is the cosine of the equatorial pitch angle:

$$\begin{aligned} \mu_0^2 &= \mu^2 B_0/B + x^2 \\ \text{where} \\ x &= (1 - B_0/B)^{1/2} \end{aligned} \quad (27)$$

as follows from the adiabatic relation $B_0/B = \sin^2 \alpha_0 / \sin^2 \alpha$.

When the relationship (Eq. 27) between μ and μ_0 is used to transform the integral in Eq. (25) with respect to the local pitch angle to an integral with respect to the equatorial pitch angle, we obtain:

$$J(B/B_0) = 4\pi B/B_0 \int_x^{\mu_{c0}} \frac{\mu_0 j(\mu_0)}{(\mu_0^2 - x^2)^{1/2}} d\mu_0 \quad (28)$$

where μ_{c0} is the cosine of the equatorial pitch angle at the lip of the loss cone. This equation, except for notational differences is the same as Eq. (20) in *Roberts* [1965], and Eq. (4) in *Vette* [1966].

Following the latter, we express the integral as a sum over pitch angle bins, assuming a constant flux value may be used for each:

$$J(B/B_0) = 4\pi B/B_0 \sum j_i \int_{\mu_{li}}^{\mu_{ui}} \frac{\mu_0}{(\mu_0^2 - x^2)^{1/2}} d\mu_0 \quad (29)$$

The summation is only over those bins in equatorial pitch angle such that the particles mirror at higher B/B_0 than the point of interest. This means that the cosine of the lower pitch angle limit of the bin must exceed $x = [1 - B_0/B]^{1/2}$. For each such bin, the lower limit μ_{li} is the maximum of x and the cosine of the upper pitch angle boundary of the bin. The upper limit of the integral is the cosine of the lower pitch angle boundary of the bin. Thus the integral is only over that portion of the bin for which $\mu_0^2 - x^2$ is not less than zero. We will assume that a bin is either entirely inside or entirely outside the loss cone. Then bins in the loss cone may be included in the summation, by assuming their j_i is identically zero. The integral itself is done analytically:

$$\int_{\mu_{li}}^{\mu_{ui}} \frac{\mu_0}{[\mu_0^2 - x^2]^{1/2}} d\mu_0 = [\mu_{ui}^2 - x^2]^{1/2} - [\mu_{li}^2 - x^2]^{1/2} \quad (30)$$

The bins appearing in the summation are the CRRES pitch angle bins, 19 in all. Bins 2-18 are 5 deg in width, centered at 5 deg multiples. Bins 1 and 19 are each 2.5 deg wide.

SUBROUTINE NUMOMNI(PAD,NBB0,BB0,OMNI) performs the computations. The first three arguments are inputs, as follows:

PAD - the bin-averaged directional fluxes in the 19 pitch angle defined above;
 NBB0 - number of B/B_0 values for which to compute the omnidirectional fluxes
 BB0 - the B/B_0 values

The output is the array OMNI, containing the omnidirectional fluxes for the specified nbb0 B/B_0 values.

The procedure was tested by direct comparisons with the analytically known omnidirectional fluxes for the generalized $\sin^n \alpha$ distribution:

$$j(\alpha_0) = (\sin^2 \alpha_0 - \sin^2 \alpha_{c0})^{n/2} \quad (31)$$

where α_0 is the equatorial pitch angle and α_{c0} is the pitch angle (equatorial) at the lip of the loss cone. The omnidirectional flux due to this distribution is

$$J = 2\pi^{3/2} (B_0/B)^{n/2} x_c^{n+1} \frac{\Gamma(n/2+1)}{\Gamma(n/2+3/2)} \quad (32)$$

where

$$x_c = \cos(\alpha_c) = \sqrt{1 - (B/B_0) \sin^2(\alpha_{c0})} \quad (33)$$

The “constant” fluxes for the 19 CRRES pitch angle bins, for use in the numerical formula, were generated by evaluation of Eq. (31) at the pitch angle midpoints of the bins. However, when j varies rapidly with pitch angle, *Vette* [1966] indicates careful selection of the pitch angle at which to evaluate j for the “constant” flux in a bin is prudent. The highest pitch angle bin which contributes is the most critical, since the denominator of the integrand goes to zero at the lower limit. In other words, this bin contributes to the omnidirectional flux the quantity:

$$I = \int_x^{x+\beta} \frac{j(\mu_0) \mu_0 d\mu_0}{(\mu_0^2 - x^2)^{1/2}} \quad (34)$$

where j is the directional flux, μ_0 is the cosine of the equatorial pitch angle, and

$$x = (1 - B_0/B)^{1/2} \quad (35)$$

If j is constant in the interval, I can be integrated analytically, as we have seen. If one expands j in a Taylor series about x , substitutes into the integral, through linear terms, one can obtain the “constant value” of j such that the analytic expression is equal to the integral. Then one can furthermore obtain the pitch angle at which j has this value, again retaining the expansion for j only through linear terms:

$$\overline{\mu_0} = 1/2 \left\{ \beta + x + \frac{x^2}{(2x\beta + \beta^2)^{1/2}} \log \left[1 + \frac{\beta + (2x\beta + \beta^2)^{1/2}}{x} \right] \right\} \quad (36)$$

Vette then extends this to the contributions of the other pitch angle bins by substituting the lower and upper μ_0 limits of the bin for x and $x+\beta$, respectively

Therefore results were obtained using j evaluated at Vette’s optimum pitch angle for each interval as well as the j at the midpoint pitch angle of each interval. In addition the effects of the coarseness of the CRRES bins were conducted by computing the omnidirectional flux for a pitch angle distribution specified over 190 bins obtained from the 19 CRRES bins by splitting them 10-fold. Table 5 shows a sample. Here the column “Analytic” is the result given by Eq. (32), the column “Numerical” is the result of the numerical calculation using the CRRES bins with j evaluated at their mid-points, “Numerical 10” is the result using the finer bins, again with j evaluated at the midpoints, and “Vette” is the numerical result using the CRRES bins with j evaluated at the Vette’s optimal pitch angles. We see that the various numerical results agree well with the analytic result until one approaches the loss cone. Then only the numerical results with the fine bins continues to agree. This indicates that the main source of error in the numerical computation, is the coarseness of the bins, rather than in the determination of the optimum “constant” flux in each bin.

TABLE 5. Omnidirectional Flux
for n = 10.0 loss cone edge = 30.0 Deg

B/B0	Analytic	Numerical	Numerical 10	Vette
1.002	9.443E-01	9.428E-01	9.443E-01	9.791E-01
1.012	8.792E-01	8.832E-01	8.793E-01	9.220E-01
1.033	7.632E-01	7.718E-01	7.634E-01	8.133E-01
1.066	6.153E-01	6.195E-01	6.156E-01	6.609E-01
1.112	4.537E-01	4.464E-01	4.530E-01	4.854E-01
1.170	3.157E-01	3.079E-01	3.161E-01	3.399E-01
1.250	1.937E-01	2.070E-01	1.933E-01	2.317E-01
1.350	1.075E-01	1.180E-01	1.074E-01	1.351E-01
1.460	5.757E-02	5.822E-02	5.754E-02	6.870E-02
1.605	2.595E-02	2.160E-02	2.608E-02	2.670E-02
1.785	9.925E-03	1.278E-02	9.839E-03	1.612E-02
1.990	3.378E-03	4.027E-03	3.410E-03	5.533E-03
2.250	8.535E-04	5.997E-04	8.565E-04	9.500E-04
2.565	1.488E-04	3.343E-04	1.523E-04	5.352E-04
2.930	1.523E-05	1.517E-05	1.568E-05	3.589E-05
3.400	3.005E-07	5.249E-06	3.012E-07	1.242E-05
4.010	0.000E+00	0.000E+00	0.000E+00	2.330E-09
4.685	0.000E+00	0.000E+00	0.000E+00	2.032E-10
5.560	0.000E+00	0.000E+00	0.000E+00	0.000E+00
6.755	0.000E+00	0.000E+00	0.000E+00	0.000E+00
8.249	0.000E+00	0.000E+00	0.000E+00	0.000E+00
10.189	0.000E+00	0.000E+00	0.000E+00	0.000E+00
12.755	0.000E+00	0.000E+00	0.000E+00	0.000E+00
16.190	0.000E+00	0.000E+00	0.000E+00	0.000E+00
20.860	0.000E+00	0.000E+00	0.000E+00	0.000E+00
27.315	0.000E+00	0.000E+00	0.000E+00	0.000E+00
36.405	0.000E+00	0.000E+00	0.000E+00	0.000E+00
49.485	0.000E+00	0.000E+00	0.000E+00	0.000E+00
68.735	0.000E+00	0.000E+00	0.000E+00	0.000E+00
97.820	0.000E+00	0.000E+00	0.000E+00	0.000E+00
143.050	0.000E+00	0.000E+00	0.000E+00	0.000E+00
215.700	0.000E+00	0.000E+00	0.000E+00	0.000E+00
337.050	0.000E+00	0.000E+00	0.000E+00	0.000E+00
549.000	0.000E+00	0.000E+00	0.000E+00	0.000E+00
938.800	0.000E+00	0.000E+00	0.000E+00	0.000E+00
1703.000	0.000E+00	0.000E+00	0.000E+00	0.000E+00
3321.000	0.000E+00	0.000E+00	0.000E+00	0.000E+00
7092.000	0.000E+00	0.000E+00	0.000E+00	0.000E+00
17057.500	0.000E+00	0.000E+00	0.000E+00	0.000E+00
48240.000	0.000E+00	0.000E+00	0.000E+00	0.000E+00
172660.000	0.000E+00	0.000E+00	0.000E+00	0.000E+00
900100.000	0.000E+00	0.000E+00	0.000E+00	0.000E+00

6.4 PROTON SPECTRAL AND PITCH ANGLE DISTRIBUTION UTILITY

Program TRANS computes model 1-100 MeV proton energy and local pitch angle distributions in the radiation belts. The models are based on measurements by the PROTEL instrument aboard The Combined Release and Radiation Effects Satellite (CRRES) from July, 1990, to October, 1991 [Gussenhoven, *et al.*, 1993]. CRRES operated in a geosynchronous transfer orbit (perigee 350 km; apogee 3500 km; orbital period 10 hr; and inclination 18.2°). Midway in the lifetime of CRRES, 24 March, 1991, a significant solar event occurred, which dramatically changed the state of the magnetosphere. Thus, two models have been developed from the data, a quiet model, for the period from launch to this solar event, and an active model, for the period from the solar event to the end of the data collection.

TRANS computes the pitch angle distributions and omnidirectional fluxes for the 22 PROTEL energy channels at a series of times and locations specified by the user. These results are output on a binary file. TRANS is part of the PROSPEC software [Meffert, *et al.*, 1996], which includes a front-end user interface to prepare the inputs to TRANS, and a graphical post-processor to display and list the results on the TRANS output file.

The input to TRANS may be either an ASCII or binary file. In the ASCII file, the user may provide his input in any of several available coordinate systems. The binary file is actually an output file of program LOKANGL [Hein, *et al.*, 1991], in which the points are specified in earth-fixed geocentric coordinates (latitude, longitude, and radius). PROSPEC uses the ASCII file to pass interactive input of a single point to TRANS, while the binary file is used for the PROSPEC option for using an orbit. Although the number of cases considered in a single run of PROSPEC will be limited to one in the ASCII file option, and 9 in the binary option, TRANS is able to handle any number of cases, within resource limits, on either file.

The next section contains a user's guide for operating TRANS. This is followed by a detailed description of the mathematical procedures.

6.4.1 User's Guide

TRANS is activated at the command line with the file name as an optional parameter. If the file name is not given as a parameter, the user is prompted for it at the beginning of execution. In either case the file name must be of the form xxx.POS or xxx.SPH where xxx is any 1-8 character string, and the .POS or .SPH is mandatory, to indicate whether the file is ASCII or binary, respectively. The ASCII format allows the user to select a coordinate system in which to specify the location at which to perform the computations, while the binary file inputs a series of locations from a satellite orbit, in earth-fixed spherical coordinates. In addition to the .POS or .SPH input file, the following files must reside in the current directory:

- quiet and active proton flux model files QFLUXZ.BIN and AFLUXZ.BIN
- internal magnetic field model files IGRF85.DAT and IGRF85S.DAT

ASCII INPUT FILE

The ASCII input file contains 7 lines per case. Each line is free formatted, that is if there is more than one item, the items are separated by spaces. The format is as follows:

Line 1
Year, month, day (integers)

Line 2
UT in seconds (real)

Line 3
Coordinate system type (integer)
1. ECI
2. PQW
3. Earth-fixed
4. Magnetic
5. Shell

Line 4
Coordinate form (integer)
1. Rectangular
2. Spherical
3. Geodetic (earth fixed system only)
For shell coordinates, line 4 is blank

Line 5
Units of length (integer)
1. km
2. R_E ($1 R_E = 6371.2$ km)
For shell coordinates, line 5 is blank

Line 6
For ECI
Epoch (integer)
1. 1950
2. 2000
3. Date
For PQW
Orbital angle parameters in degrees (real)
Argument of perigee (0-360)
Right ascension of ascending node (0-360)
Inclination (0-180)
For Magnetic
Specific system and origin (integer)
1. GSM, origin at eccentric dipole
2. SM, origin at eccentric dipole
3. GSM, origin at earth center

4. SM, origin at earth center
 For Earth fixed and shell coordinates, line 6 is blank
 Line 7
 Position Coordinates (real)
 Rectangular: x,y,z
 Spherical
 ECI
 Declination (-90 to +90 deg)
 Right ascension (0-360 deg)
 Radius
 Earth fixed and PQW
 Latitude (-90 to +90 deg)
 Longitude (-180 to +180 deg)
 Radius
 Magnetic
 Latitude (-90 to +90 deg)
 Local time (0-24 hr)
 Radius
 Geodetic
 Latitude (-90 to +90 deg)
 Longitude (-180 to +180 deg)
 Altitude
 Shell
 L (1.0 to 5.5 R_E)
 B/B₀ (>1.0)
 Radius, x, y, z, altitude in km or R_E , as specified in line 5

In line 1, if the year is not the full 4-digit specification, it is assumed to be relative to 1900. Thus 85 translates to 1985. Although the coordinate systems are described in more detail elsewhere[Bhavnani and Vancour, 1991], a brief description is give here.

ECI (Earth-Centered Inertial) refers to the “inertial” system in which in which the x axis points to the ascending crossing of the ecliptic and equator(sometimes called vernal equinox or first point of Aries), the z axis coincides with the earth's axis of rotation, positive towards the north, and the y axis completes a right-handed coordinate system. Due to precession and nutation of the earth's rotation axis, it is necessary to specify a specific epoch when using ECI. The commonly used are the true of date, which corresponds to the instantaneous orientation at the time of interest, 1950, which corresponds to the mean orientation (neglecting nutation) on 1 Jan., 1950, and 2000, which corresponds to the mean orientation 1 Jan, 2000. Thus the user has the option of specifying any one of these three epochs (line 6). Because the effects of nutation are less than 0.01° , it is neglected in TRANS.

The PQW system is oriented according to a satellite orbit. The x axis ("P") points toward perigee, the y axis ("Q") is perpendicular to the x axis, and lies in the plane of the orbit such that the satellite moves from +x to +y, and the z ("W") axis is normal to the orbital plane, completing a right-handed coordinate system. For this system the user must specify in line 6 the orientation angles of the orbit: argument of perigee, right ascension of ascending node, and inclination. The ascending node is the position in the orbit at which the satellite crosses the ECI equator of date from south to north. Its right ascension is the angle measured along the ECI equator eastward from the ECI x axis. The argument of perigee is the angle measured in the orbital plane from ascending node to perigee. The inclination is the angle between the earth's rotational axis and the PQW z axis.

The earth-fixed system has its z axis parallel to the earth's axis of rotation, and its x axis in the equatorial plane, pointing toward the Greenwich meridian. For this case line 6 on the input file must be blank.

The magnetic systems all have the z-x plane coincide with the plane containing the earth's dipole axis and the earth-sun line. In the GSM system, the earth-sun line is the +x axis, while in the SM system the dipole axis is the +z axis. The origin may be either at the center of the earth or at the eccentric dipole. All these particulars are specified in line 6.

The shell coordinates are L and B/B₀. In this case the information in lines 1, 2, and 4-6 are immaterial. Lines 1 and 2 may contain any date and UT the user desires. Lines 4-6 should be blank.

In any of the first four coordinate systems, the coordinates may be input as rectangular or spherical. Additionally, in the earth-fixed system, geodetic coordinates may be input. The specific quantities input for spherical coordinates depend on the coordinate system type, as listed above under line 7.

BINARY INPUT FILE

The binary input file contains earth-fixed spherical coordinates. Each record contains [*Kerns and Gussenhoven, 1993*]:

Year-1900	: 2 byte integer
Day number in year	: 2 byte integer
UT (seconds)	: 4 byte real
Latitude (deg)	: 4 byte real
Longitude (deg)	: 4 byte real
Radius (km)	: 4 byte real

PROTON FLUX MODEL INPUT FILES

The model input files for the active and quiet model are binary files containing mean equatorial directional differential fluxes in L and equatorial pitch angle bins for the 22 PROTEL channels. Each file contains a 76 character header record which is read, but not used, by TRANS. This is followed by a data record of 4-byte real numbers, in a three-dimensional array of 22 energies by 90 L bins by 19 pitch angle bins. The data for a single energy resides in consecutive locations in the record. Within the data for a single energy, consecutive pitch angle bins occupy consecutive

locations. Thus the record begins with the lowest energy channel. For that channel, all the data for the lowest L value is grouped consecutively, from lowest to highest pitch angle. Then comes all the data for the next L shell, etc., until all the data for the first energy is completed. Then follows all the data for the next energy, etc, and the remaining energies, in similar fashion.

The lowest pitch angle bin is $0-2.5^\circ$. The remaining 18 pitch angle bins are 5° wide, centered at multiples of 5° . The L bins are $1/20 R_E$ wide, beginning with the bin $1.0-1.05 R_E$, and ending with the bin $5.45-5.5 R_E$. The 22 PROTEL energies are shown in Table 6.

TABLE 6. PROTEL Energies	
Channel Number	Energy (MeV)
1	1.5
2	2.1
3	2.5
4	2.9
5	3.6
6	4.3
7	5.7
8	6.8
9	8.5
10	9.7
11	10.7
12	13.2
13	16.9
14	19.4
15	26.3
16	30.9
17	36.3
18	42.3
19	47.5
20	57.0
21	67.5
22	82.9

INTERNAL MAGNETIC FIELD MODEL INPUT FILES

The ASCII file IGRF85.DAT contains the coefficients (refer to Eq. (44), below) in nT for the IGRF85 model at epoch 1 Jan, 1985. IGRF85S.DAT contains the secular rates of the coefficients, in nT/yr, allowing the model to be updated to a future date. The two files are similarly formatted. The first line is a character string descriptor ('IGRF85' or 'IGRF85s'). The remaining lines are free formatted, as in the xxx.POS file. The second line contains the maximum degree (the maximum value of the index n in Eq. (44)) and the mean earth radius, in km, which is the value to use for a in Eq. (44). The remaining lines are as follows:

IGRF85.DAT : n, m, g_n^m, h_n^m
 IGRF85S.DAT : $n, m, g_n^m \text{ rate}, h_n^m \text{ rate}$

The coefficients in IGRF85.DAT are in nT, and the rates in IGRF85S.DAT are in nT/year. Each such line thus contains coefficients or rates for the designated indices n and m . Only the non-zero coefficients or rates need be given.

OUTPUT FILE

The output file is a binary file xxx.FLX where xxx is the name of the .POS or .SPH input file without the extension. It contains for each case, the following:

Header :

- Year (2-byte integer)
- Month (2-byte integer)
- Day (2-byte integer)
- UT (sec) (4-byte real)
- Earth-fixed spherical coordinates (0 for shell coordinates):
 - Latitude (deg) (4-byte real);
 - Longitude (deg) (4-byte real)
 - Radius (R_E) (4-byte real)
- Local L value (R_E)
- Local B/B_0 value

Two data records, the first for quiet model, the second for active model:

(all 4-byte reals)

For each of the 22 energies:

- The omnidirectional flux J ($\# / (\text{cm}^2 \text{ s MeV})$)
- The differential flux j ($(\# / (\text{cm}^2 \text{ s ster MeV}))$)
 - given for local pitch angles $90^\circ - 5^\circ$ in 5° steps
- The distribution function f ($\text{km}^{-6} \text{ s}^3$)
 - at the same pitch angles

The results for each energy will be given together, the lowest energy first. For each energy the omnidirectional flux will be given first, followed by the differential flux for the 18 pitch angles, 90° first, followed by the 18 distribution function values, in the same order.

6.4.2 Program Flow and Mathematical Description

TRANS begins with initialization which consists of obtaining the input file name, determining from the extension whether the file is ASCII or binary, and initializing a table to be used for the proton radiation belt model interpolation. Then for each case on the input file, TRANS reads the data and performs the computations required to obtain the model fluxes. These include:

Transformation of the coordinates to earth-fixed spherical, if not already in that form;
 Computation of L-shell parameters and equatorial pitch angles;
 Computation of model differential directional fluxes;
 Computation of distribution functions and omnidirectional fluxes.

COORDINATE TRANSFORMATION

If the coordinate system is not earth-fixed then a transformation to rectangular earth fixed performed, preceded by a transformation from spherical to rectangular in the input coordinate system, if the input coordinates are spherical, followed by a transformation from earth-fixed rectangular to earth-fixed spherical. If the input system is earth-fixed rectangular or earth-fixed geodetic, the appropriate transformation to earth-fixed spherical is performed.

Spherical to Rectangular Transformation

The spherical to rectangular transformation is given by:

$$\begin{aligned}x &= r \cos \theta \cos \phi \\y &= r \cos \theta \sin \phi \\z &= r \sin \theta\end{aligned}\tag{37}$$

where r is the radius, θ is the declination (ECI systems) or latitude (PQW and magnetic systems), and ϕ is the right ascension (ECI), longitude (PQW), or $15^\circ t + 180^\circ$ (magnetic systems), where t is the magnetic local time in hours.

Rectangular Transformation to Earth-Fixed System

The rectangular transformations are of the form $\mathbf{v}' = \mathbf{R}\mathbf{v}$ where \mathbf{v}' is the transformed column vector of the transformed coordinates x', y', z' , \mathbf{R} is the appropriate 3 by 3 transformation matrix, and \mathbf{v} is the original vector of untransformed coordinates x, y, z .

ECI

The ECI reference epoch 1950 and reference epoch 2000 coordinates require two transformations; first transform to ECI reference epoch of date; second transform to earth-fixed. The ECI epoch of date coordinates require only the second transformation.

The three ECI reference systems arise from the secular precession of the earth's mean rotation axis about the ecliptic polar axis, with a period of approximately 26000 years, and short-period motions, called nutation, of the instantaneous rotation axis about the mean, the main term having an amplitude of 17". TRANS neglects the nutation, resulting in errors of less than 0.01° . For the elements of the transformation matrix from epoch 1950 to date due to precession, TRANS uses expressions given by Minka [1965], pp. 12-13:

$$\begin{aligned}
R_{xx} &= 1 - 0.2226036 \times 10^{-12} d^2 - 0.267 \times 10^{-20} d^3 \\
R_{xy} &= -R_{yx} = -0.6119036 \times 10^{-6} d - 0.5067 \times 10^{-14} d^2 + 0.453 \times 10^{-19} d^3 \\
R_{xz} &= -R_{zx} = -0.26603997 \times 10^{-6} d + 0.1552 \times 10^{-14} d^2 + 0.197 \times 10^{-19} d^3 \\
R_{yy} &= 1 - 0.1872158 \times 10^{-12} d^2 - 0.308 \times 10^{-20} d^3 \\
R_{yz} &= R_{zy} = -0.813972 \times 10^{-13} d^2 - 0.61 \times 10^{-21} d^3 \\
R_{zz} &= 1 - 0.353878 \times 10^{-13} d^2 + 0.41 \times 10^{-21} d^3
\end{aligned} \tag{38}$$

where d is the time elapsed in days from 1 January 1950, 0 h.r UT.

For the transformation from epoch 2000, TRANS uses expressions given in *Explanatory Supplement to the Astronomical Almanac*, 1992, pp. 103-4:

$$\begin{aligned}
R_{xx} &= \cos \iota_A \cos \theta_A \cos \zeta_A - \sin \iota_A \sin \zeta_A \\
R_{xy} &= -\cos \iota_A \cos \theta_A \sin \zeta_A - \sin \iota_A \cos \zeta_A \\
R_{xz} &= -\cos \iota_A \sin \theta_A \\
R_{yx} &= \sin \iota_A \cos \theta_A \cos \zeta_A + \cos \iota_A \sin \zeta_A \\
R_{yy} &= -\sin \iota_A \cos \theta_A \sin \zeta_A + \cos \iota_A \cos \zeta_A \\
R_{yz} &= -\sin \iota_A \sin \theta_A \\
R_{zx} &= \sin \theta_A \cos \zeta_A \\
R_{zy} &= -\sin \theta_A \sin \zeta_A \\
R_{zz} &= \cos \theta_A
\end{aligned} \tag{39}$$

where

$$\begin{aligned}
\zeta_A &= 2306.2181t + 0.30188t^2 + 0.017998t^3 \\
\iota_A &= 2306.2181t + 1.09468t^2 + 0.018203t^3 \\
\theta_A &= 2004.3109t - 0.42665t^2 - 0.041833t^3
\end{aligned} \tag{40}$$

Here the angles are expressed in seconds of arc, and t is the time in Julian centuries (1 Julian century = 36525 days) from 1 January, 2000, 12 hr. UT.

The transformation from the ECI epoch of date to the rectangular earth-fixed coordinates is a simple rotation about the z axis by the Greenwich mean sidereal time angle, given in *Explanatory Supplement*, 1992, p. 50:

$$GMST = 24110.54841 + 864018.812866t + 0.093104t^2 - 6.2 \times 10^{-6}t^3 \tag{41}$$

where the angle is in seconds of sidereal time (1 second sidereal time = 15 seconds of arc).

PQW

The transformation matrix for PQW has the form

$$R = \begin{pmatrix} P_x & Q_x & W_x \\ P_y & Q_y & W_y \\ P_z & Q_z & W_z \end{pmatrix} \quad (42)$$

where the columns 1, 2, and 3 contain the rectangular components of the vectors P, Q, and W, respectively, in the ECI epoch of date coordinate system. These are given by *Escobal* [1965], pp. 77-78:

$$\begin{aligned} P_x &= \cos\omega\cos\Omega - \sin\omega\sin\Omega\cos i \\ P_y &= \cos\omega\sin\Omega + \sin\omega\cos\Omega\cos i \\ P_z &= \sin\omega\sin i \\ Q_x &= -\sin\omega\cos\Omega - \cos\omega\sin\Omega\cos i \\ Q_y &= -\sin\omega\sin\Omega + \cos\omega\cos\Omega\cos i \\ Q_z &= \cos\omega\sin i \\ W_x &= \sin\Omega\sin i \\ W_y &= -\cos\Omega\sin i \\ W_z &= \cos i \end{aligned} \quad (43)$$

where ω , Ω , and i are the argument of perigee, the right ascension of the ascending node, and the inclination.

Magnetic

The rectangular systems described thus far all have their origins at the center of the earth. The magnetic systems may optionally have their origins either at the center of the earth or at the eccentric dipole (sometimes called offset dipole). The location of the eccentric dipole, in the earth-fixed system, as well as the dipole vector itself, are defined from the spherical harmonic expansion of the internal magnetic field potential [*Chapman and Bartels*, 1940, p. 651]:

$$V = a \sum_{n=1}^N \left(\frac{a}{r} \right)^{n+1} \sum_{m=0}^n (g_n^m \cos m\phi + h_n^m \sin m\phi) P_n^m(\cos\lambda) \quad (44)$$

where a is the mean earth radius, r is the radius to the point, λ is the colatitude of the point, i. e., $\pi/2$ -latitude, and ϕ is the longitude (r , θ , ϕ are earth-fixed spherical coordinates). The P_n^m are the associated Legendre functions normalized in the Schmidt convention. The vector magnetic field is computed as $-\nabla V$. TRANS uses the updated IGRF85 in Eq. (44). The earth-fixed x , y , and z

components of the dipole vector are g_1^1 , h_1^1 , and g_1^0 . The coefficients for $n>1$ are depend on choice of origin. The location of the eccentric dipole is that choice of origin which minimizes the sum of the squares of the $n=2$ coefficients. This is given, in earth-fixed rectangular coordinates, as:

$$\begin{aligned}x_0 &= a(L_1 - g_1^1 E)/3H_0^2 \\y_0 &= a(L_2 - h_1^1 E)/3H_0^2 \\z_0 &= a(L_0 - g_1^0 E)/3H_0^2\end{aligned}\tag{45}$$

where

$$\begin{aligned}L_0 &= 2g_1^0 g_2^0 + (g_1^1 g_2^1 + h_1^1 h_2^1)\sqrt{3} \\L_1 &= -g_1^1 g_2^0 + (g_1^0 g_2^1 + g_1^1 g_2^2 + h_1^1 h_2^2)\sqrt{3} \\L_2 &= -h_1^1 g_2^0 + (g_1^0 h_2^1 - h_1^1 g_2^2 + g_1^1 h_2^2)\sqrt{3} \\E &= (L_0 g_1^0 + L_1 g_1^1 + L_2 h_1^1)/4H_0^2 \\H_0 &= \sqrt{g_1^0 g_1^0 + g_1^1 g_1^1 + h_1^1 h_1^1}\end{aligned}\tag{46}$$

In the GSM system the x axis is along the earth-sun line, positive toward the sun. The positive y axis is parallel to the cross product $\mathbf{d} \times \mathbf{x}$, of the dipole vector and the +x direction. The positive z direction completes a right-handed system, $\mathbf{z} = \mathbf{x} \times \mathbf{y}$. In the SM system, the positive y axis is the same as in the GSM system. The positive z axis is parallel to the dipole vector, and the positive x direction completes a right-handed coordinate system.

The earth-sun direction cosines in the epoch of date ECI system are computed, to 0.01° accuracy in direction, using equations on p. C24 of *The Astronomical Almanac*, 1984. These are transformed to the earth-fixed system in the manner described previously.

As with the PQW system, the transformation matrix for GSM or SM can be written as 3 column vectors; the first column contains the earth-fixed components of the magnetic x unit vector, the second contains the components of the magnetic y unit vector, and the third column contains the components of the magnetic z unit vector.

Rectangular to Spherical Transformation

The spherical coordinates are $r = [x^2 + y^2 + z^2]^{1/2}$; $\theta = \sin^{-1}(z/r)$; $\phi = \text{atan2}(y, x)$, where atan2 is a function that evaluates $\tan^{-1}(y/x)$, then assigns the proper quadrant according the signs of x and y.

Geodetic to Earth-Fixed Spherical (Geocentric)

The radius r, latitude θ , and longitude ϕ , are given by:

$$\begin{aligned}
r &= \sqrt{x_p^2 + z_p^2} \\
\theta &= \tan^{-1}(z_p/x_p) \\
\phi &= \phi_{gd}
\end{aligned} \tag{47}$$

where ϕ_{gd} is the geodetic longitude, and

$$\begin{aligned}
x_p &= r_g \cos \theta_g + h \cos \theta_{gd} \\
z_p &= r_g \sin \theta_g + h \sin \theta_{gd} \\
r_g &= a / \sqrt{1 + \epsilon \sin^2 \theta_g} \\
\theta_g &= \tan^{-1}[(1 - e^2) \tan \theta_{gd}]
\end{aligned} \tag{48}$$

Here a is the earth's equatorial radius, h is the geodetic altitude, θ_{gd} is the geodetic latitude, and

$$\begin{aligned}
\epsilon &= e^2 / (1 - e^2) \\
e^2 &= 2f - f^2
\end{aligned} \tag{49}$$

where f is the earth's flattening ratio, $(a-b)/a$, where b is the earth's polar radius.

For the earth figure model, TRANS uses the reference model adopted by IAU in 1984: $a=6378.140$ km, $f=1/298.257$.

COMPUTATION OF L-SHELL AND EQUATORIAL PITCH ANGLES

The L-shell and equatorial pitch angle are computed for each of the local pitch angles $5^\circ, 10^\circ, \dots, 85^\circ, 90^\circ$. The equatorial pitch angle α_e is given by

$$\sin^2 \alpha_e = \frac{B_0}{B} \sin^2 \alpha \tag{50}$$

where B_0 is the minimum magnetic field magnitude along the field line through the point of interest, B is the local magnetic field magnitude at the point of interest, and α is the local pitch angle. For each pitch angle, the L-shell value [McIlwain, 1961] used is the one that is defined at the mirror point, which is the point on the field line for which the magnetic field magnitude is $B_m = B/\sin^2 \alpha$. These computations, requiring field line tracing, are performed by code provided by Pfitzer [1991], which also outputs B_0 and B to be used in Eq. (50). This code uses a magnetic field model composed of the sum of the IGRF model internal field and the Olson-Pfitzer static tilt-dependent model external field [Olson and Pfitzer, 1977].

If shell parameters are input directly, the input L is used for all pitch angles, i. e., dependence of L on pitch angle is neglected. The equatorial pitch angles are computed from Eq. (50), as for the other coordinate systems.

Determination of Differential Directional Fluxes

For each of the 22 energy channels, the fluxes are computed by interpolation of a table of average values for 2-dimensional equatorial pitch angle- L bins. There are 19 pitch angle bins, the first of which covers $0-2.5^\circ$. The remaining 18 bins are 5° wide centered at multiples of 5° . The L -bins are $1/20 R_E$ wide, with the lowest bin having its inner boundary at $1.0 R_E$. There are 90 contiguous bins, the last running from 5.45 to $5.5 R_E$. For the purpose of interpolation, the bin average values are assumed to apply to the midpoints of the bins. Thus, the pitch angles are taken to be $1.25^\circ, 5^\circ, 10^\circ, \dots, 85^\circ$, and 90° . The L value assumed for the i th L -bin is $0.975 + 0.05i R_E$.

The vanishing of the fluxes at L -dependent loss cone boundaries results in substantial variation of the flux as a function of L for fixed pitch angle. Therefore it is convenient to replace the pitch angle with a quantity that is constant at the loss cone edge and at 90° . TRANS uses the quantity

$$q = \frac{\sin^2 \alpha_e - \sin^2 \alpha_c}{1 - \sin^2 \alpha_c} \quad (51)$$

where α_c is the L -dependent cutoff equatorial pitch angle, tabulated for each L bin in the appendix. To find α_c at arbitrary L , this table is interpolated linearly.

The fluxes are interpolated by two-point straight line fits through the tabular values. This is done first for the target q value at the two L -bin centers bracketing the target L . The final result, at the target L , is obtained by straight line fit through these results. Where possible, the interpolation is done on the log of the flux as a function of L and $\log q$. One exception occurs if the pitch angle is in the loss cone ($q \leq 0$) for the given L value, in which case the flux is set to zero without interpolation. A second exception is when the pitch angle is just outside the loss cone, such that the next lower tabular point is inside the loss cone. In this case the flux is determined by a power law fit through the closest two tabular points outside the loss cone. The other exception is when the flux is zero at one or both of the tabular points through which the interpolation is done, in which case the interpolation is on the flux directly, rather than on the log of the flux.

COMPUTATION OF DISTRIBUTION FUNCTIONS AND OMNIDIRECTIONAL FLUXES

The distribution function is given by

$$f = \frac{m^2}{2E} j \quad (52)$$

where m is the ion mass, and j is the directional differential flux. If j is in $\#/(cm^2 \cdot s \cdot ster \cdot MeV)$, E is in MeV, and f is in $km^{-6} \cdot s^3$, then this can be expressed as $f = (x/E)j$, where x is 5.45×10^{-7} .

The omnidirectional flux is given by

$$J = 4\pi \int_0^1 j(\mu) d\mu \quad (53)$$

where $j(\mu)$ is the differential directional flux, and μ is the cosine of the local pitch angle. Following Vette [1966], we express the integral as a sum over pitch angle bins, assuming a constant flux value may be used for each:

$$J = 4\pi \sum j_i (\mu_{2i} - \mu_{1i}) \quad (54)$$

where j_i is the directional flux at local pitch angle $5i$ deg, while μ_{2i} and μ_{1i} are the cosines of the pitch angles at the boundaries of the bins:

1. 2.5-7.5 deg
2. 7.5-12.5 deg
-
17. 82.5-87.5 deg
18. 87.5-90 deg

The contribution from pitch angles less than 2.5° has been neglected.

Note that there is considerable simplification relative to Vette's formulation. This is due to the fact that here the omnidirectional flux is derived directly from the local pitch angle distribution, whereas Vette dealt with the problem of determining the local omnidirectional flux from the equatorial pitch angle distribution.

6.5 DERIVATION OF NEAR-EARTH MAGNETOSPHERIC PLASMA MOMENTS FROM LEPA MEASUREMENTS

The near-earth plasma sheet plays a large role in the dynamics of the inner magnetosphere. Charged particles from this region contribute to the ring currents that encircle the earth and to field-aligned currents that couple the magnetosphere to the ionosphere. The ring currents modify the near-earth magnetospheric magnetic field which traps the energetic particles in the radiation belts. Particles flowing down magnetic field lines from the plasma sheet to low altitudes are responsible for high latitude auroras. The low energy plasma analyzer (LEPA) was included in the instrument package of the Combined Release and Radiation Effects Satellite (CRRES) to measure particles in the 10 eV-30 keV energy range, which account for a significant fraction of the energy density in the plasma sheet [Hardy, *et al.*, 1993a,b]. CRRES was launched on 25 July 1990 and provided measurements of the radiation belts, their surrounding magnetospheric environment, and their effects on operational spacecraft systems, until 12 October 1991. CRRES operated in a Geosynchronous Transfer Orbit (GTO) with perigee altitude 350 km, apogee altitude 33000 km, inclination 18° , and orbital period 9.85 hr.

LEPA is capable of sampling up to 120 energy steps per sweep, 64 sweeps per spin, resolving the entry angle with respect to the spin plane to within 1° . Since such a wealth of data would overload the telemetry system, LEPA instead operates at any given time in one of a set of modes that can be selected by ground control. These modes implement tradeoffs between energy, direction, and time resolution. In the two modes on which this report is based, the energy sweeps contain 30 steps. In mode 10, the counts of each 4 consecutive sweeps are combined in each of 8 entry angle zones before transmission to the ground. This provides a spin phase resolution of 22.5° and an entry angle resolution of 16° . In mode 0, the ions are treated the same as for mode 0. The electrons are sampled in only 4 sweeps per spin, two when the magnetic field vector is near the entry fan of the detector, and two when the magnetic field is approximately perpendicular to the entry fan. For each of these LEPA supplies counts in 16 entry angle zones, 8° wide. For the two sweeps near the magnetic field vector there is a further subdivision of the zone nearest the magnetic field into 1° fine zones. Other modes exist which, for example sample the energy in 120 steps, but with only two steps per spin.

Kerns [1993] describes how to extract differential directional fluxes, time tags, look direction in the spacecraft coordinate system, and pitch angle. However complete specification of the three dimensional distribution function requires a second directional parameter, azimuth about the magnetic field direction. *Griffin and Bass* [1995] define this in terms of a magnetic field meridian (MFM) coordinate system. This coordinate system specifies the local measured magnetic field direction as its z axis. The x axis is parallel to the vector cross product of the local magnetic east direction and the magnetic field vector. Magnetic east is the y or "D" direction in the VDH coordinate system (see Fig. 3-20 of *Bhavnani and Vancour* [1991]). The MFM y axis then completes the right-handed coordinate system with z and x. The azimuth is then the angle of rotation from the x axis, positive in the usual sense that the y axis is $+90$ degrees. Using the CRRES attitude [McNeil, 1991] and magnetometer [Singer, et al., 1992; McNeil, 1993] data bases, *Griffin and Bass* [1995] developed software to sort the measurements of each channel into pitch angle-azimuth bins. Typically 12 bins are assigned for each angle. Uniform azimuth bins then are 30° wide. Pitch angle bins at the loss cones (0 and 180°) are half the width of the others. This results in loss cone bin widths of $\sim 8^\circ$, while the other bins are $\sim 16^\circ$ wide. Data files are created containing the averages and standard deviations of the fluxes per channel per pitch angle-azimuth bin. The averages are performed for a user-defined number of 15-second half spins (typically 32). Known spacecraft charging events exceeding 100 V are excluded.

This report describes the use of these bin-averaged fluxes to obtain moments of the three-dimensional distribution function. Following an overview of definitions in the next section, the details of the method are given in Section 6.5.2, followed by a discussion of error analysis in Section 6.5.3.

6.5.1 Overview of Moments Computation

The distribution function is computed from the differential directional flux as:

$$f = \frac{m^2}{2E} j \quad (55)$$

where m is the mass, E the energy, and j the differential flux in $\#/(cm^2 \text{ sec sr keV})$. From the distribution function we may define the moments

$$M^{(n \ p \ q \ r)} = \int v_x^p v_y^q v_z^r f(v) v^{2+n} dv d\Omega \quad (56)$$

where v_x, v_y , and v_z are the x , y , and z components of the velocity vector.

Table 7 indicates the particular moments that are computed. Also shown are physical parameters that are obtained by these moments and the factors one must multiply the moments by to obtain the parameters.

TABLE 7. Moments and Associated Parameters					
p	q	r	n	Parameter	Factor
0	0	0	0	Number Density	1
0	0	0	1	Omnidirectional Number Flux	1
0	0	0	2	Total Energy Density	$m/2$
1	0	0	0	Number Flux (x Component)	1
0	1	0	0	Number Flux (y Component)	1
0	0	1	0	Number Flux (z Component)	1
2	0	0	0	Energy Density (x Component)	$m/2$
0	2	0	0	Energy Density (y Component)	$m/2$
0	0	2	0	Energy density (z Component)	$m/2$
0	0	0	3	Omnidirectional Energy Flux	$m/2$
1	0	0	2	Energy Flux (x Component)	$m/2$
0	1	0	2	Energy Flux (y Component)	$m/2$
0	0	1	2	Energy Flux (z Component)	$m/2$

We briefly clarify the terminology used in column 5. The omnidirectional number flux is the sum (or integral) of the directional flux over solid angle. The directional flux is the number of particles, per unit time and solid angle, crossing a disk of unit area normal to a given direction from a narrow cone centered about that direction. These fluxes are integrated over the energy range of the instrument, in contrast to the differential directional fluxes, which pertain to particular energies. The

component of the number flux along a Cartesian axis is the difference in the rates of particles crossing a flat disk of unit area normal to the axis from the positive and negative sides of the disk. The Cartesian coordinate system considered here is the one defined previously in which the z axis is parallel to the magnetic field direction. Therefore the x and y axes relate to drift perpendicular to the magnetic field, while the z axis relates to field-aligned flows.

The energy density components are the densities of the quantities $(1/2)mv_x^2$, etc., whereas the total energy density is the density of $(1/2)mv^2$. Thus the total energy density is the sum of the densities of its components. For a fully isotropic plasma, all three components of the energy density are equal. For a gyrotropic plasma in a magnetic field, the two components normal to the magnetic field are equal to each other, but are not necessarily equal to the parallel energy density. Thus, in a coordinate system with the magnetic field as the z axis, we can define a pressure tensor with only diagonal components. The first two are each equal to twice the perpendicular (x or y) energy density, while the third component is twice the parallel (z) energy density. Thus the perpendicular and parallel pressure define the pressure tensor, which in an arbitrary cartesian coordinate system is [Rossi and Olbert, 1970].

$$P_{ij} = P_{\perp} \delta_{ij} + (P_{\parallel} - P_{\perp}) \frac{B_i B_j}{B^2} \quad (57)$$

The definitions for energy flux are similar to those for number flux, except that number of particles is replaced by the total energy $(1/2)mv^2$.

Some other quantities can be derived immediately from these moments. For example dividing certain of them by the number density gives an appropriate average quantity. Division of number flux by number density gives average velocity, and similarly we can obtain average energy. Furthermore, multiplication of number flux by mass gives momentum density.

6.5.2. Methodology

Due to structural considerations, LEPAS's angular coverage is limited to 90% of the full 4π solid angle. The obstructed regions are principally along the spin axis. To perform the integrations defined in Eq. (56) with these holes in the data, programs MOMCALC and MOMCALC1 implement two methods, the summation and fitting method, respectively. In the summation method, the integrals are performed by summing over the occupied directional bins, at the same time accumulating the total solid angle of the occupied bins. The final result is then the product of the summation with the ratio of 4π to the occupied solid angle. In the fitting method, the azimuthal variation for each pitch angle and energy is fit to a sinusoidal function. Then the azimuthal dependence is integrated analytically for each moment to be computed, and the results summed over energy and pitch angle.

Summation Method

The integration is approximated by a sum over the covered directional bins, normalized by a factor which is equal to the ratio of 4π to the total solid angle of the covered directions:

$$M^{(npqr)} = \frac{4\pi}{\sum_l \Delta\Omega_l} \sum_{k\ell} \Delta\Omega_l v_{xk\ell}^p v_{ykl}^q v_{zkl}^r f_{k\ell} v_k^{2+n} \Delta v_k \quad (58)$$

where $\Delta\Omega_l$ is the solid angle subtended by the ℓ th directional bin, $f_{k\ell}$ is the mean distribution function of the k th channel in the ℓ th bin, replacing negative values with zero, v_k is the velocity magnitude corresponding to the k th channel, Δv_k is the weight assigned to channel k , and $v_{ik\ell}$ is the i th component of the velocity in bin ℓ , channel k .

The solid angle subtended by a directional (pitch angle-azimuth) bin is

$$\Delta\Omega_l = \frac{2\pi}{n_\phi} (\cos\theta_{l-} - \cos\theta_{l+}) \quad (59)$$

where n_ϕ is the number of azimuth bins and θ_{l-} and θ_{l+} are the lower and upper bounds of the pitch angle bin.

Each $f_{k\ell}$ is computed from the mean differential flux in the corresponding channel and bin. These mean values are averages of individual samples corrected for background by subtracting an estimated background count from the raw count. This background subtraction could lead to negative fluxes for some samples. In the averaging these negative results were retained, rather than setting them to zero, because doing the latter introduces a positive bias. However, in performing the summations required for the moments computation, it is necessary to set the negative averages to zero. This is because, unlike the averaging, the summations in the moments computation contain unequally weighted terms, $\sim v^n$, for example. Thus if a high energy (high v) flux were negative, it would compete advantageously against a lesser weighted positive contribution from a low energy channel.

In the $v_{ik\ell}$, the index i refers to x, y, z , where in our coordinate system, $+z$ is in the positive magnetic field direction, $+x$ is perpendicular to the plane containing the magnetic field vector and magnetic east, and points radially outward, while $+y$ completes a right-handed orthogonal system. The velocity components are thus given by:

$$\begin{aligned} v_{xk\ell} &= v_k \sin\theta_l \cos\phi_l \\ v_{yk\ell} &= v_k \sin\theta_l \sin\phi_l \\ v_{zk\ell} &= v_k \cos\theta_l \end{aligned} \quad (60)$$

where θ_l is the central pitch angle of bin ℓ , and ϕ_l is the central azimuth of bin ℓ .

The weighting factors Δv_k are:

$$\begin{aligned}\Delta v_k &= \frac{1}{2} |v_{k+1} - v_{k-1}| \quad \text{if } k_{\min} < k < k_{\max} \\ &= \frac{1}{2} |v_{k+1} - v_k| \quad \text{if } k = k_{\min} \\ &= \frac{1}{2} |v_k - v_{k-1}| \quad \text{if } k = k_{\max}\end{aligned}\tag{61}$$

In using the summation method it was noted that misleading results would be obtained for vector components, such as those of number flux, if all 7 available combined zones of LEPA were used. This is because an uneven sampling about the spacecraft equatorial plane would result, favoring look directions "north" of the equator relative to those "south" of the equator. Thus for the summation method it is recommended that zone 0 data be excluded.

Fitting Method

The data for each energy and pitch angle are fit to a function of the azimuth. This function is integrated analytically over azimuth, and the corresponding results summed over all energy channels and pitch angle bins.

The functional form we use is:

$$f(v, \theta, \phi) = f_0(v, \theta) + f_c(v, \theta) \cos \phi + f_s(v, \theta) \sin \phi\tag{62}$$

where v is the particle speed (i. e., $\text{energy} = 1/2 mv^2$), θ is the pitch angle, and ϕ is the azimuth. The integral in Eq (56) can be written as

$$\int F^{(p,q,r)}(v, \theta) v^{2+n} dv \sin \theta d\theta\tag{63}$$

where

$$F^{(p,q,r)}(v, \theta) = \int v_x^p v_y^q v_z^r f(v, \theta, \phi) d\phi\tag{64}$$

Using $v_x = v \sin \theta \cos \phi$, $v_y = v \sin \theta \sin \phi$, $v_z = v \cos \theta$, where θ is the pitch angle and ϕ is the azimuth, we obtain

$$\begin{aligned}
F^{(000)} &= 2\pi f_0 \\
F^{(100)} &= \pi v \sin \theta f_c \\
F^{(010)} &= \pi v \sin \theta f_s \\
F^{(001)} &= 2\pi v \cos \theta f_0 \\
F^{(200)} &= \pi v^2 \sin^2 \theta f_0 \\
F^{(020)} &= \pi v^2 \sin^2 \theta f_0 \\
F^{(002)} &= 2\pi v^2 \cos^2 \theta f_0
\end{aligned} \tag{65}$$

These are computed for each channel-pitch angle bin pair. Then the moments can be computed by summing:

$$M^{(n \ p \ q \ r)} = \sum_{kl} F_{kl}^{(p \ q \ r)} \Delta \cos \theta_l v_k^{2+n} \Delta v_k \tag{66}$$

where $\Delta \cos \theta_l = \cos \theta_{l-} - \cos \theta_{l+}$, where θ_{l-} and θ_{l+} are the lower and upper bounds of the l^{th} pitch angle bin, and v_k is the velocity magnitude corresponding to channel k . The Δv_k factors are the same as for the summation method.

Determining Azimuthal Dependence (i. e., Determining f_0 , f_c , and f_s)

For the ions, if all available data values for a particular pitch angle-energy combination are positive, and there are 3 or more values available, they are fit by a straightforward linear least squares method, with equal weighting to all values. If any of the values are not positive, or there are less than three available, or the resulting fit function is not positive over the entire 2π azimuthal range, then the azimuthal dependence is dropped: f_c and f_s are set to zero, and f_0 is obtained by averaging the available data values. In this case any individual negative values are retained in the averaging, but a negative result (f_0) is set to zero. The condition for positive f over all azimuth is that $f_0 - \sqrt{f_c^2 + f_s^2} > 0$, since the expression on the left hand side is the minimum value of the function.

For the electrons no azimuthal dependence is determined. The coefficient f_0 is determined by averaging, as for the ions when azimuthal dependence is not determined.

If there are no available values for a particular pitch angle-energy combination, f_0 is determined by linear interpolation or extrapolation, as a function of $\cos(\theta)$, using the nearest-neighbor values, and there is no azimuthal dependence. If more than NUMPA/4 consecutive pitch angle bins lack data, where NUMPA is the total number of pitch angle bins, the entire moments computation is dropped for the species (ions or electrons) and data segment.

Rational for Fitting Method

To understand our selection of section of the sinusoidal fitting functional form, we note that typical plasma drift velocities in the magnetosphere are small compared to the total velocity. Thus we assume that the azimuthal portion of the distribution function can be expanded in powers of V_d/V_\perp , where V_d is the drift velocity magnitude, and V_\perp is the total velocity magnitude perpendicular to the magnetic field. We examine these points in detail.

1) $\mathbf{E} \times \mathbf{B}$

In the case of pure $\mathbf{E} \times \mathbf{B}$ drift, the motion relative to the guiding center is a circle perpendicular to the field, with constant velocity. Thus the distribution function, in the plane normal to the magnetic field, should depend only on the magnitude of the velocity V_{GCS} relative to the guiding center. For convenience in the following, we express this function as $f(V_{GCS}^2)$. Then, if V_\perp is the perpendicular velocity in the observer's reference frame, we have

$$f(V_{GCS}^2) = f((V_\perp - V_d)^2) \approx f(V_\perp^2) \left(1 - V_\perp^2 \frac{d \ln f}{d V_\perp^2} \frac{2V_d}{V_\perp} \right) \quad (67)$$

where V_d is the drift velocity (in this case the $\mathbf{E} \times \mathbf{B}$ drift velocity), and ϕ is the angle between V_d and V_\perp . The final expression is obtained by expanding the middle expression to first order in V_d/V_\perp . For a Maxwellian distribution the derivative in the last term is $-m/(2kT)$, where m is the particle mass, k is Boltzman's constant and T is the temperature. Integrating Eq (13) over energy gives us the expected average velocity V_d . However the average velocity at fixed energy in the observer's frame of reference in general depends on energy.

As pointed out by Roederer, the energy in the observer's frame of reference is not constant during the orbital motion, due to the alternately positive and negative work done by the electric field. This net work vanishes, leading to a constant average energy equal to the sum of the orbital and drift energies. As we sample different directions at fixed energy in the observer's frame of reference, we in fact sample different orbital energies. Thus the angular distribution at fixed total energy depends in the shape of the distribution f with respect to orbital energy, as expressed by the derivative in the last term.

2. Gradient-Curvature Drift

The case of constant total energy in the observer's frame of reference occurs in the case of pure gradient B drift. Here no work is done, since the magnetic force is perpendicular to the velocity. In this case, unlike $\mathbf{E} \times \mathbf{B}$ drift, there is instead an energy variation in the GCS, which Roederer attributes to the work done by the induced electric field that appears in that frame of reference. At fixed energy, the relative population at any angle is inversely proportional to the angular velocity, $qB/(4\pi m)$. The variation of the angular velocity, due to the spatial variation of B in the orbit of radius $\rho = mv/qB$, is

$$\frac{\omega}{\omega_0} = 1 - \frac{\nabla_{\perp} B}{qB_0^2} \frac{mV_{\perp}^2}{V_{\perp}} \cos\phi = 1 - 2 \frac{V_d}{V_{\perp}} \cos\phi \quad (68)$$

where ω_0 and B_0 are the angular velocity and magnetic field magnitude at the guiding center, V_{\perp} is the velocity perpendicular to the magnetic field, and V_d is the drift velocity associated with the gradient of the magnetic field:

$$V_d = \frac{\hat{b} \times \nabla B}{qB^2} (1/2mv_{\perp}^2) \quad (69)$$

Thus we will find that the azimuth distribution varies approximately as $(1 + 2V_d/V_{\perp} \cos\phi)$, which gives the expected mean velocity V_d .

The case of field line curvature drift is like the electric field case, in that there is a centrifugal force that alternately increases and decreases the perpendicular energy. However, since there can be no total energy variation without a true electric field, it is evident that there must be canceling decreases and increases in the parallel energy, without which there would be no curvature drift.

6.5.3 Error Analysis

Several potential error sources have been identified: statistical error in the raw data; finiteness of the resolution of the data within LEPA's measurement parameter space (angles, energy); attitude determination errors; charging events; and errors introduced by the approximations in the moments computation methods. The resolution errors encompass both those inherent in the finite resolution of the instrument in energy and angle and the width of the bins imposed in the analysis. We expect these errors to be negligible if the distribution function is linear within a bin or resolution width of the instrument. Attitude errors are known to be $\sim 2^\circ$ [McNeil 1993], and should thus introduce directional errors of similar magnitude in the computed vector moments, such as velocity. Since charging events > 0.1 keV were identified and excluded from the data processing, only smaller charging events are of concern. These should shift ion and electron spectra by amounts equal (electrons) or opposite (ions) to the charging potential (< 0.1 keV). This should effect correspondingly the average energy and velocity magnitude of the particles. In addition the lowest energy portion of the decelerated specie would be suppressed, reducing the number density. The moment computation methods introduce errors related to the inherent assumptions assumption in their methods. In the summation method) it is assumed that the contribution of incoming flux in the obstructed directions is on average proportional to that measured in the allowed directions. The fitting method assumes high order terms in v_d/v_{perp} are negligible. The similarity of the results obtained by the two methods indicates that these errors are small compared to the point-to-point scatter in the derived moments. Therefore detailed analysis was performed only on the the statistical

error associated with the raw measurements. The errors in the results of the summation and the fit methods were estimated as follows:

Summation Method

We estimate the error in the resulting summation, due to random errors in the bin-averaged distribution function values, as the rms of the sum of the errors of the individual terms in the summation:

$$\sigma_M^{npqr} = \frac{4\pi}{SA} [\sum_{kl} (\Delta\tau_{kl})^2 g_{kl}^2(n,p,q,r) (\sigma_f^{(kl)})^2]^{1/2} \quad (70)$$

where SA is the sum of the solid angles of the occupied bins, and $\Delta\tau_{kl}$ is the volume element in momentum space, $v_k^2 \Delta v_k \Delta\Omega_l$. The factors g_{kl} are $v_k^n v_{xkl}^p v_{ykl}^q v_{zkl}^r$. The σ 's are obtained from the bin standard deviations, which are retained in the bin-average flux data bases that had been created according to *Griffin and Bass* [1995]. These are taken as estimates of the individual measurement errors. The error in the mean is the bin standard deviation divided by the square root of the number of samples in the bin. These are flux standard deviations which are then converted to distribution function standard deviations by the factor $m^2/2E$.

Such quantities as mean velocities are ratios of the appropriate moments to the number density. With B a positive quantity, we take the σ for a ratio A/B to be $\sigma_A/B + (|A|/B^2) \sigma_B$.

Fit Method

Analogous to the summation method, we estimate the error as the square root of the sum of the squared errors of the individual terms in Eq. 12:

$$\sigma_M^{(npqr)} = [\sum_{kl} (v_k^2 \Delta v_k \Delta\cos\theta_l v_k^n \sigma_F^{(kl;pqr)})^2]^{1/2} \quad (71)$$

where the σ 's are the errors of the $F_{kl}^{(pqr)}$:

$$\begin{aligned}
\sigma_F^{(kl;000)} &= 2\pi\sigma_f^{(0kl)} \\
\sigma_F^{(kl;100)} &= \pi v_k \sin\theta_l \sigma_f^{(ckl)} \\
\sigma_F^{(kl;010)} &= \pi v_k \sin\theta_l \sigma_f^{(skl)} \\
\sigma_F^{(kl;001)} &= 2\pi v_k \cos\theta_l \sigma_f^{(0kl)} \\
\sigma_F^{(kl;200)} &= \pi v_k^2 \sin^2\theta_l \sigma_f^{(0kl)} \\
\sigma_F^{(kl;020)} &= \sigma_F^{(kl;200)} \\
\sigma_F^{(kl;002)} &= 2\pi v_k^2 \cos^2\theta_l \sigma_f^{(0kl)}
\end{aligned} \tag{72}$$

where the $\sigma_f^{(ikl)}$ are the errors in the fit coefficients f_{ikl} , where $i=0, c, \text{ or } s$.

To simplify the following discussion of the errors in the fit coefficients, we again drop the energy and pitch angle indices k and l . In the least squares determination, we obtain a set of 3 simultaneous linear equations for f_0 , f_c , and f_s , expressed in matrix form as

$$Qf = M \tag{73}$$

where elements of the matrix Q are

$$Q_{ij} = \sum_m \frac{\partial d_m}{\partial f_i} \frac{\partial d_m}{\partial f_j} \tag{74}$$

where the d_m are the data (bin-averaged distribution function values in the filled azimuth bins), and the partials are given by:

$$\begin{aligned}
\frac{\partial d_m}{\partial f_0} &= 1 \\
\frac{\partial d_m}{\partial f_c} &= \cos\phi_m \\
\frac{\partial d_m}{\partial f_s} &= \sin\phi_m
\end{aligned} \tag{75}$$

with ϕ_m the central azimuth of bin m . The elements of M are

$$M_i = \sum_m d_m \frac{\partial d_m}{\partial f_i} \tag{76}$$

The solution vector is then $Q^{-1}M$. Defining the matrix $R=Q^{-1}$, each element f_i is then given by

$$f_i = \sum_j R_{ij} M_j \quad (77)$$

Errors in the data (the d_m) influence the f_i through the elements of the vector M . The squared error in f_i due to these is

$$(\Delta f_i)^2 = \sum_{jk} R_{ij} R_{ik} \Delta M_j \Delta M_k = \sum_{jk} R_{ij} R_{ik} \sum_{mn} \frac{\partial d_m}{\partial f_j} \quad (78)$$

To get the mean squared error of f_i , we assume that the d_m are uncorrelated, meaning that the mean of $\Delta d_m \Delta d_n$ vanishes for $m \neq n$. Then we obtain for the mean squared error in f_i :

$$(\sigma_f^{(i)})^2 = \sum_{jk} R_{ij} R_{ik} \sum_m \frac{\partial d_m}{\partial f_j} \frac{\partial d_m}{\partial f_k} \sigma_m^2 \quad (79)$$

where σ_m is the mean squared error in the bin m averaged distribution function value.

Originally, in the summation method, our estimate of σ_m was $\sigma_s/n^{1/2}$, where σ_s is the sample standard deviation of the data in the bin, and n is the number of measurements in the bin. However it occurred to us that this estimate could be unstable when there are few points in the bin. In particular if there is only one point, we have no estimate at all. In the summation method we used 0 for this situation. Therefore, for a more stable estimate we used for the fit method, the sample standard deviation over all the data covering all azimuthal bins for the given pitch angle-energy bin. This may account for some slightly errors in the fit method. We should redo the summation method with this revision.

In case we are not doing the full azimuthal fitting ($f_c = f_s = 0$) then we take the error in f_0 , the pitch angle binned average to be as above, the $\sigma_s/n^{1/2}$.

Results

The results obtained for the two methods are similar: For number and energy densities the errors are less than 1 % for electrons in both methods, while for ions the number density error is generally 1-2% while the energy density is ~0.5%. For velocities the errors in each component for electrons are < 30 km/sec for the summation method, < 50 km/sec for the fit method. For ions the errors are < 3 km/sec in both methods.

7. VERTICAL CLOUD STRUCTURE

The ability to ascertain the vertical structure of clouds from analysis of passive remote sensor data obtained from orbiting satellites is of great interest for obvious reasons. Having information of this sort would be of great benefit to aviation, meteorology, and atmospheric research. Unfortunately, the current status of satellite retrieval technology precludes the determination of cloud vertical structure below the uppermost cloud surface. In order to remedy this situation, an extensive research initiative was proposed. Work in the area of the first phase of the proposal, modeling of the atmosphere using radiative transfer models, is the subject of this report. Data collection from satellites, ground based sensors, and aircraft will be the next step. The third and final phase will be to perform retrieval experiments, which, when combined with the data collection and modeling results, will lead to the identification of the type of remote sensors required, as well as recognizing specific mathematical methods to use with data that the sensors provide.

7.1 RADIATIVE TRANSFER MODELING

An important tool in the science of remote sensing is radiative transfer modeling. In this section, we describe the application of the radiative transfer codes, RADTRAN and FASE, to explore the sensitivity of cloud vertical structure to brightness temperatures in the microwave region under various atmospheric conditions. Inherent in these modeling codes are "sub-models", part of the radiative transfer equation. For example, there are various models one can use for describing the attenuation of microwave radiation by water droplets in clouds.

We evaluated several attenuation models to determine which one best suited our needs. Various models for the surface emissivity were also investigated. A discussion of the attenuation and emissivity models we considered and subsequently selected for use in the radiative transfer codes is contained in the first two sub-sections. Then follows a presentation of the radiative transfer modeling work done for the atmospheric conditions of interest.

7.1.1 Attenuation

The first step in selecting an appropriate attenuation model is to define the physical situation to be described. For our initial purpose, a simple non-precipitating cloud in a typical atmosphere would suffice. Under these circumstances, the Rayleigh absorption approximation can be used instead of the MIE theory [Bohren and Huffman, 1983], since the scattering wavelength in the microwave region is much larger than the size of the water droplets in the cloud. In this regime, attenuation depends not on the droplet size distribution, but rather on the concentration of liquid water in the cloud. A key variable in computing the attenuation is the complex permittivity of liquid water which depends on frequency and temperature. Different models used to describe the attenuation process are based upon different descriptions of this particular variable.

A common attenuation model that has been used for many years is that of Ray [1972]. We investigated the use of this model to describe attenuation of microwaves for our cloud case along with a more recent model by Liebe, *et al.* [1991; 1989], hereafter referred to as the LHM model. Two variations of the LHM model were studied. In the first consideration, the temperature dependence of the primary relaxation frequency was modeled with a quadratic form. The second variation used an exponential function to describe the dependence. Figure 49 shows the results of our study. It is observed that the agreement among the three cases under consideration is considerably better at higher temperatures than at lower temperatures. The reason for the substantial disagreement at low temperatures is due to the fact that data used to construct these models does not exist at colder temperatures. In effect, we are attempting to use these models outside the region of temperatures for which they are considered valid. Nevertheless, it is necessary to have a model that functions down to -40°C because supercooled liquid water droplets can occur in clouds at sub-zero temperatures. It was hoped that it would be possible to extend the attenuation models to operate over the desired temperature range and then choose the best model to suit our purposes. However, since neither the Ray nor LHM models were developed with the use of cold temperature data, neither model can be considered the definitive one at temperatures below -10°C . Therefore, whenever the attenuation was considered to be an interesting factor in our radiative transfer modeling results, computations were carried out in duplicate, employing both the Ray and LHM attenuation models. Otherwise, the LHM model, with the exponential form of the primary relaxation frequency, was used for its simplicity.

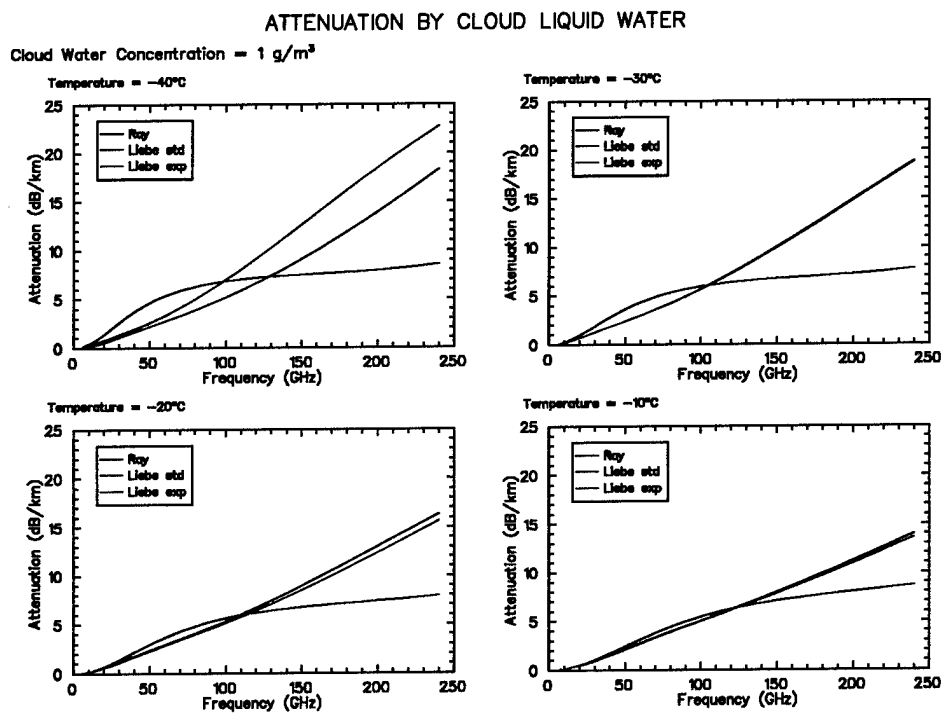


Figure 49. Attenuation rate by cloud liquid water as a function of microwave frequency at the indicated temperatures and a cloud water concentration of 1 g/m^3 . Curves based on the Ray [1972] and LHM [Liebe, *et al.*, 1991] models are shown with the standard (STD) and exponential (EXP) forms of the primary relaxation frequency used for the LHM model.

7.1.2 Emissivity

Another variable in the radiative transfer equation that requires some care in selection is the surface emissivity. This variable controls the amount of radiation emitted by the surface of the earth, as well as the percentage of radiation reflected by the surface and transmitted back into the atmosphere. In order to have anything more than a crude radiative transfer model, it is important to have an accurate model for the surface emissivity.

Since we are interested in two types of surfaces, namely ocean and land, two different models for the surface emissivity are required. For the ocean surface, we chose a refined empirical model which depends upon the salinity and the wind speed at the surface [Kohn, 1995]. This model is well known and is sufficient for our purposes. However, for the land surface, specifically a vegetated one, the choice of models is not so clear. One model we considered that has a variety of parameters that one can look at is the Bauer and Grody (BG) Model [Bauer and Grody, 1995]. The bulk of our efforts in selecting an appropriate land surface emittance model involved the exploration of the effects of changing key parameters in the BG model. Specifically, SOIL_WC, SOIL_ROUGH, VEG_WC, and VEG_COVER were studied. Table 8 lists the values that were tested for these parameters. It was decided that the last set of values listed in the table provided a suitable representation of vegetated land surface.

TABLE 8. Sets of Parameter Values Used to Test the *Bauer and Grody* [1995] Land Surface Emittance Model

SOIL_WC is the volume fraction of the water in the soil; SOIL_ROUGH is the standard deviation of the soil surface height; VEG_WC is the vertically integrated water path due to leaves; VEG_COVER is the fractional area coverage of vegetation

CASE #	SOIL_WC	SOIL_ROUGH	VEG_WC	VEG_COVER
1	0.3	0.01	2.0	0.5
2	0.05	0.01	2.0	0.0
3	0.5	0.01	2.0	0.0
4	0.05	4.0	2.0	0.0
5	0.5	4.0	2.0	0.0
6	0.2	1.0	1.0	1.0
7	0.2	1.0	4.0	1.0
8	0.2	4.0	1.0	1.0
9	0.2	4.0	4.0	1.0
10	0.05	0.1	2.0	0.0
11	0.5	0.1	2.0	0.0
12	0.2	0.1	1.0	1.0
13	0.2	0.1	0.5	1.0
14	0.2	1.0	0.5	1.0
15	0.2	0.01	3.0	0.9
16	0.2	0.05	3.0	0.9
17	0.3	0.01	3.0	0.9
18	0.3	0.05	3.0	0.9
19	0.1	0.01	3.0	0.0
20	0.2	0.01	3.0	0.0
21	0.1	0.01	3.0	0.8
22	0.2	0.01	3.0	0.8
23	0.3	0.01	3.0	0.8
24	0.3	0.02	3.0	0.9
25	0.3	0.03	3.0	0.9
26	0.3	0.04	3.0	0.9

7.1.3 RADTRAN

Once appropriate models for describing the attenuation and emissivity had been chosen, the next step was to use them with a radiative transfer modeling code to calculate radiance, or equivalently, brightness temperature. A code well suited to our purposes is RADTRAN [Falcone, *et al.*, 1979]. We incorporated the above mentioned attenuation and emissivity models into the RADTRAN code, fixing a few bugs in the process, and added additional computations as desired. The result became known as RADTRAN Version 3.0, and it is this version of the code that was used in our study.

A wide range of atmospheric and surface conditions were input into RADTRAN in order to observe the relationship between cloud vertical structure and brightness temperature. The complete set of RADTRAN run results can be divided into groups of runs having common atmosphere profiles and background conditions. Each of these groups of runs is the result of varying cloud parameters, such as cloud thickness, cloud water content, relative humidity below the cloud, and number of clouds. The first atmosphere profile that we investigated is the Atlantic Stratocumulus (ASc) case. It was modeled with an ocean surface having a wind speed of 0m/s and salinity of 35ppt. Figure 50 shows the temperature/dew point temperature profiles for a set of ASc runs, each profile having a different cloud thickness. The atmospheres labeled PROSC1A through PROSCF7 are in order of decreasing cloud thickness, but identical in all other attributes.

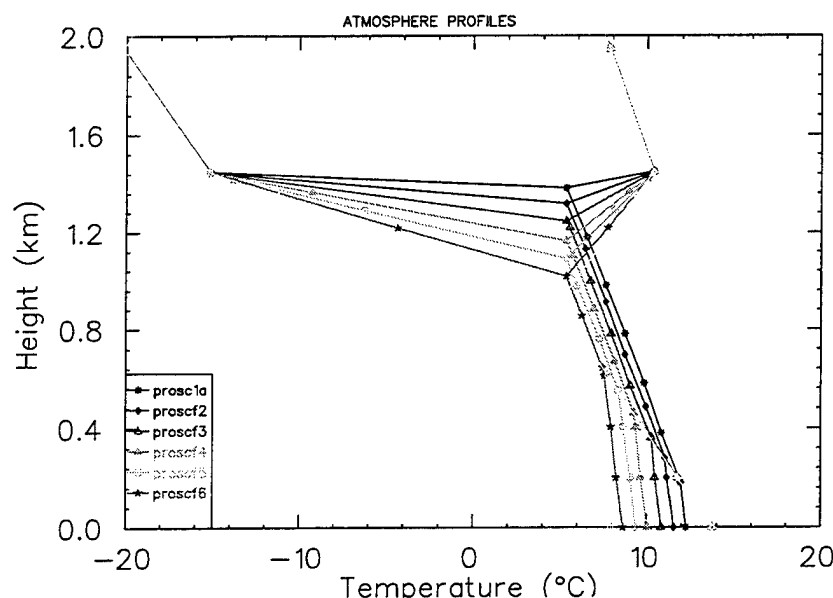


Figure 50. Temperature and dew point temperature profiles for seven Atlantic stratocumulus profiles, each having a different cloud thickness.

By varying specific parameters pertaining to cloud characteristics, one can perform sensitivity experiments to observe how sensitive the brightness temperature is to the parameter in question. For the ASc atmosphere, both the sensitivity to cloud thickness and to total cloud water content were investigated. The results are shown in Figures 51 and 52. From the figures, it is clear that some frequencies provide more sensitivity than others, and would be better suited to yield the desired information from experimental measurements.

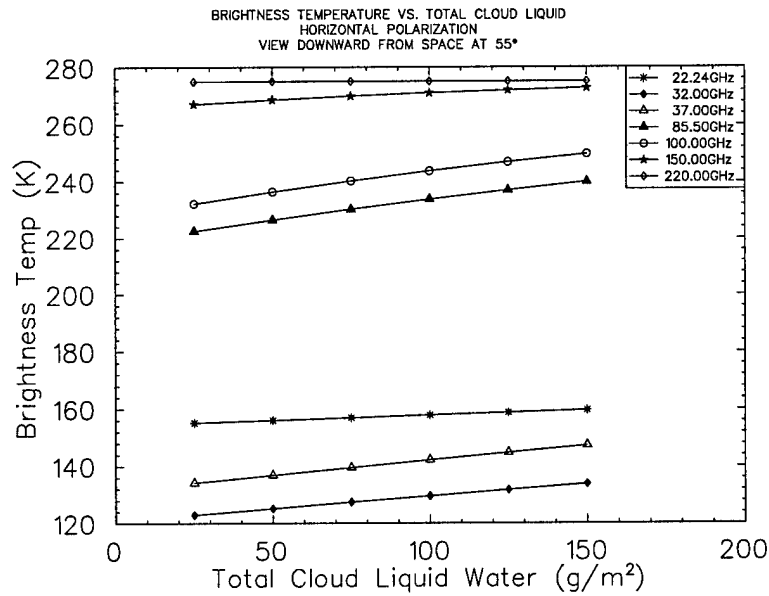


Figure 51. Brightness temperature in horizontal polarization as a function of the amount of total cloud liquid water for an Atlantic stratocumulus atmosphere as calculated by RADTRAN.

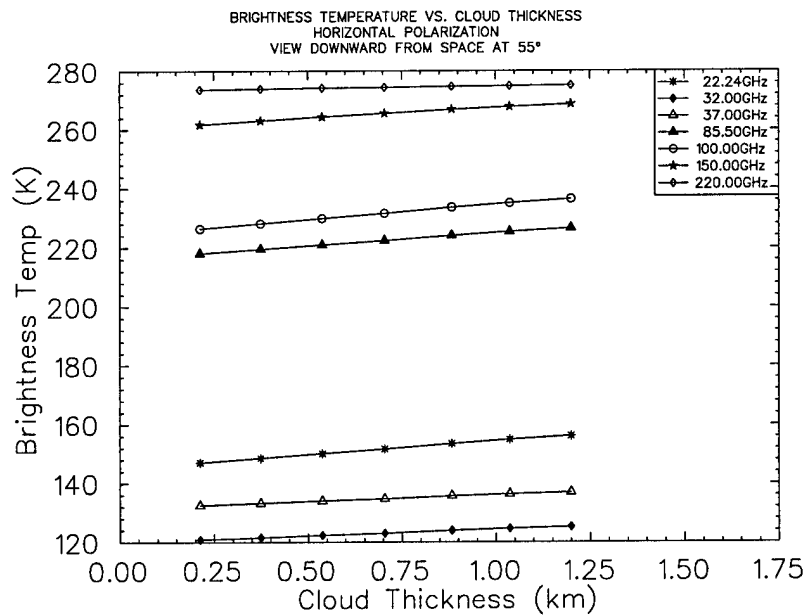


Figure 52. Same as Figure 51, but with cloud thickness as the abscissa.

Having run RADTRAN with variations in cloud water content for every variation in cloud thickness, it is possible to construct a matrix of brightness temperatures for a given zenith angle and frequency. The matrix can then be plotted as a contour plot to better understand the behavior of brightness temperature as a function of cloud thickness and water content. Figure 53 shows such a plot at 55° and 100GHz.

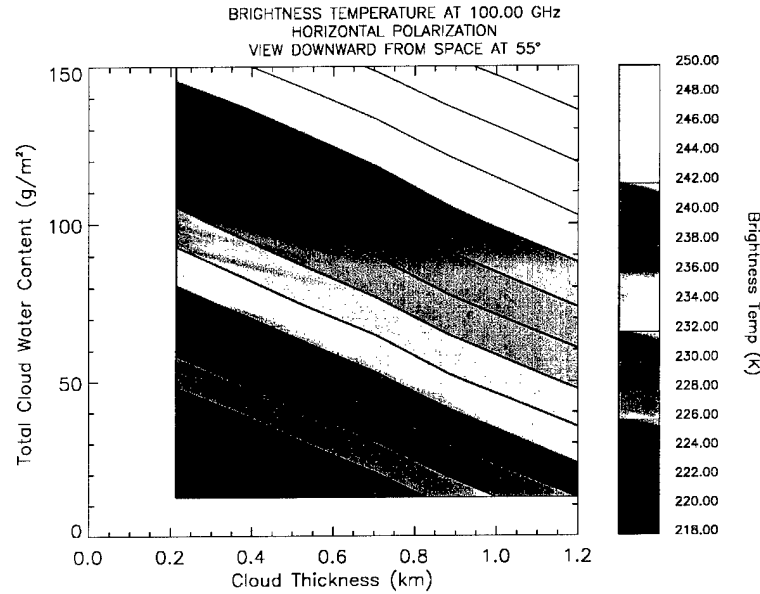


Figure 53. Brightness temperature in horizontal polarization for an Atlantic stratocumulus atmosphere as calculated by RADTRAN showing the contours of cloud thickness and cloud water content. The view is downward from space at 55°. The 100 GHz channel is shown.

From the data used to create one of these contour plots, a quantitative analysis can be done to gain further insight. Specifically, we let T_1 represent the brightness temperature in the lower left corner of the plot, and T_2 , T_3 , and T_4 represent the brightness temperature values at the remaining corners of the plot going in a clockwise direction. Let δ_i and ω_i represent the corresponding cloud thickness and water content at corner i in the plot. Then a gradient G can be defined as

$$\begin{aligned}\vec{G} &= \frac{T_4 - T_2 + T_3 - T_1}{2D_x} \hat{i} + \frac{T_4 - T_3 + T_2 - T_1}{2D_y} \hat{j} \\ &= G_x \hat{i} + G_y \hat{j} \quad (80)\end{aligned}$$

$$D_x = \frac{d(3) - d(1)}{d(3) - d(1)}, \quad D_y = \frac{w(2) - w(1)}{w(2) - w(1)}$$

Here Δx and Δy are the normalized cloud thickness and cloud water content, calculated from the appropriate values at the corners of the plot. If we compute the gradient for two different frequencies, ν_1 and ν_2 , we can compute the quantity R , defined as

$$R = \left| \bar{G}_{\nu_1} \times \bar{G}_{\nu_2} \right| \quad (81)$$

This quantity can be taken as a figure of merit of how well a measurement of the brightness temperature at two different frequencies can specify cloud thickness and water content together. Furthermore, an additional quantity, $\Delta\delta$, can be calculated to describe how well a brightness temperature measurement could determine cloud thickness alone. For given uncertainties in brightness temperature measurements at frequencies ν_1 and ν_2 , ΔT_{ν_1} and ΔT_{ν_2} , it can be shown that

$$\Delta\delta = C\Delta(3)$$

where

$$c = \frac{a \cos \beta + b \cos \gamma}{\sin(\gamma - \beta)}, \quad (82)$$

$$a = \frac{\Delta T_1}{(Gx_{\nu_1}^2 + Gy_{\nu_1}^2)^{1/2}}, \quad b = \frac{\Delta T_2}{(Gx_{\nu_2}^2 + Gy_{\nu_2}^2)^{1/2}},$$

$$\gamma = \tan^{-1} \frac{Gx_{\nu_1}}{Gy_{\nu_1}}, \quad \beta = \tan^{-1} \frac{Gx_{\nu_2}}{Gy_{\nu_2}}$$

Table 9 lists the values of R and $\Delta\delta$ calculated from the contour plots at the specified frequency and zenith angle from the ASc RADTRAN results. The values tabulated are with respect to 22 GHz (i.e., = 22 GHz) and both ΔT_{ν_1} and ΔT_{ν_2} were set to 1K.

In order to gain confidence in the interpretation of the RADTRAN results for ASc profiles, it is instructive to look at the behavior of individual terms in the radiative transfer equation. Consider two atmospheres with different cloud characteristics. For the first atmosphere profile, the radiative transfer equation can be written

$$T_{B_1} = \tau_{s_1} \epsilon_s T_{s_1} + \int_{UP} T_1 d\tau_1 + \tau_{s_1} (1 - \epsilon_s) \int_{DOWN} T_1 d\tau_1 + \tau_{s_1}^2 (1 - \epsilon_s) T_c \quad (83)$$

where T_B is the brightness temperature, τ_s is the surface to space transmittance, ϵ_s is the surface emissivity, T_s is the surface temperature, T is the air temperature, and T_c is the cosmic background temperature. The first term on the right side of Eq. (83) is the surface term, the radiation emitted by the surface and transmitted upward through the atmosphere. The second term is the radiation emitted by the atmosphere in the upward direction and referred to as the direct term. The third term represents the radiation emitted downward by the atmosphere, undergoing reflection at the surface, then propagated upward. This term will be referred to as the reflected term. The last term is attributed to the cosmic background. To simplify our task, we set T_c to zero, although it is normally 2.7K.

TABLE 9. The Results of Applying the Gradient Calculations as Explained in the Text To Atlantic Stratocumulus Contour Plots as Exemplified in Figure 53
(The values of R and $\Delta\delta$ are with respect to 22GHz at the listed angle)

θ (deg)	ν (GHz)	G_x (K)	G_y (K)	R (K ²)	$\Delta\delta$ (km)
0.00	22.24	6.0182	3.0000	0.0000	0.0000
0.00	32.00	2.4924	6.6000	32.2432	0.3573
0.00	37.00	2.5532	8.0727	40.9240	0.3247
0.00	85.50	5.9574	14.5091	69.4467	0.3025
0.00	100.00	7.1125	15.3273	70.9058	0.3102
0.00	150.00	7.2341	9.4364	35.0881	0.4253
0.00	220.00	3.3435	2.4545	4.7417	1.3804
40.00	22.24	8.2067	4.2000	0.0000	0.0000
40.00	32.00	3.5866	9.5455	63.2726	0.2607
40.00	37.00	3.5866	11.6182	80.2829	0.2364
40.00	85.50	7.9635	19.2546	124.5692	0.2259
40.00	100.00	9.5441	20.3455	126.8836	0.2321
40.00	150.00	8.2675	10.6909	53.0134	0.3371
40.00	220.00	2.7963	1.8546	3.4752	2.0907
55.00	22.24	10.8815	5.5091	0.0000	0.0000
55.00	32.00	4.9848	13.5273	119.7350	0.1908
55.00	37.00	5.1064	16.2545	148.7417	0.1756
55.00	85.50	9.6656	23.0727	197.8163	0.1734
55.00	100.00	11.3070	24.0000	198.8640	0.1781
55.00	150.00	7.6596	9.6000	62.2647	0.2912
55.00	220.00	1.5806	0.7636	0.3979	-18.9153
65.00	22.24	13.6170	6.8727	0.0000	0.0000
65.00	32.00	6.9909	18.4909	203.7445	0.1494
65.00	37.00	6.8693	21.8727	250.6303	0.1376
65.00	85.50	10.1520	23.9455	256.2939	0.1443
65.00	100.00	11.6109	23.9455	246.2667	0.1502
65.00	150.00	5.4711	6.3273	48.5570	0.3262
65.00	220.00	0.5471	-0.0545	4.5027	1.8462
70.00	22.24	15.0152	7.5818	0.0000	0.0000
70.00	32.00	8.4498	22.3091	270.9101	0.1324
70.00	37.00	8.1459	25.8545	326.4500	0.1229
70.00	85.50	9.6049	22.0364	258.0580	0.1377
70.00	100.00	10.6383	21.3273	239.5755	0.1448
70.00	150.00	3.7082	3.7636	28.3967	0.4794
70.00	220.00	0.1824	-0.2727	5.4777	1.7207

For an isothermal atmosphere with temperature T_{B_1} and having the same transmittance as atmosphere profile 1, we have

$$T_{B_1} = \tau_{s_1} \epsilon_s T_{B_1} + \int_{UP} T_{B_1} d\tau_1 + \tau_{s_1} (1 - \epsilon_s) \int_{DOWN} T_{B_1} d\tau_1 + \tau_{s_1}^2 (1 - \epsilon_s) T_{B_1} \quad (84)$$

It can be shown that $T_{B_1} = T_{B_1}$, and therefore

$$\begin{aligned} T_{B_1} - T_{B_1} = 0 &= [\tau_{s_1} \epsilon_s T_{s_1} - \tau_{s_1} \epsilon_s T_{B_1}] + [\int_{UP} \tau_1 d\tau_1 - T_{B_1} (1 - \tau_{s_1})] \\ &+ [\tau_{s_1} (1 - \epsilon_s) \int_{DOWN} T_1 d\tau_1 - \tau_{s_1} (1 - \epsilon_s) T_{B_1} (1 - \tau_{s_1})] \\ &+ [\tau_{s_1}^2 (1 - \epsilon_s) T_c - \tau_{s_1}^2 (1 - \epsilon_s) T_{B_1}] \end{aligned} \quad (85)$$

Each of the bracketed terms in Eq. (85) respectively represent the surface, direct, reflected, and space terms. They can be calculated from the output that RADTRAN provides and plotted as a bar graph. Figure 54 illustrates such a graph for two ASc profiles at the extremes of cloud thickness considered. Specifically, we plot terms for ASc profile PROSC1A which has a cloud thickness of 1.2km and PROSCF7 having a cloud with thickness 0.21km. The figure also shows the change in the contribution of each term in going from one atmosphere to the other.

The information displayed in the bar graphs of the terms of the radiative transfer equation can be examined in more detail with the use of channel bar charts. These charts emphasize the weighting of each term in the equation. The weightings for each term is as follows:

surface:	$\tau_s \epsilon_s$
direct:	$(1 - \tau_s)$
reflected:	$\tau_s (1 - \epsilon_s) (1 - \tau_s)$
cosmic:	$\tau_s^2 (1 - \epsilon_s)$

The temperature of each term of Eq. (83) is normalized to these weightings and then plotted as a bar with the width of each bar corresponding to the weighting for that term. A typical bar chart for the ASc atmospheres PROSC1A and PROSCF7 is shown in Figure 55. The brightness temperatures are indicated with solid and dashed lines in the figures. For each term, the area above the brightness temperature line is equal to the magnitude of the corresponding bar in the bar graph of Figure 54. The area between the lines marking T_B (PROSC1A) and T_B (PROSCF7) is equal to the sum of the magnitudes of the bars in the plots showing the contribution change in Figure 54.

Zenith Angle = 55.00°

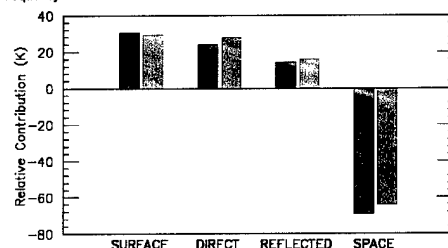
--- $T_B(\text{PROSC1A}) - T_B(\text{PROSCF7})$

■ PROSCF7

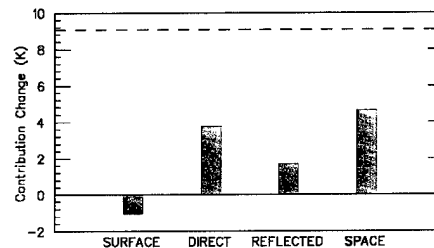
■ PROSC1A

■ PROSC1A-PROSCF7

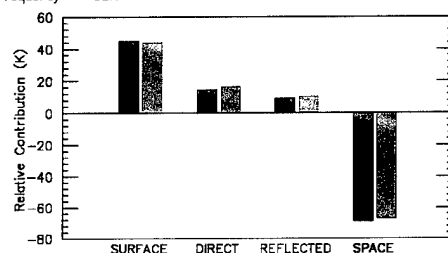
Frequency = 22.24 GHz



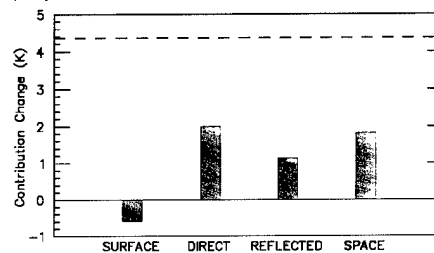
Frequency = 22.24 GHz



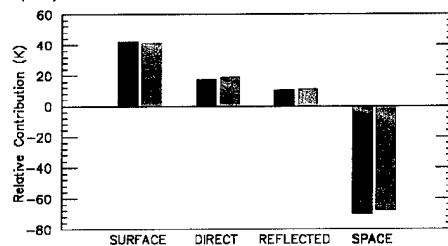
Frequency = 32.00 GHz



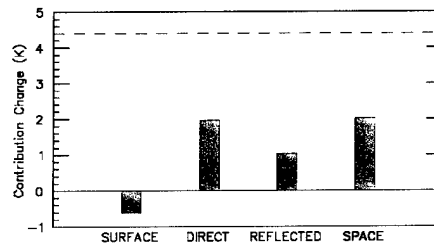
Frequency = 32.00 GHz



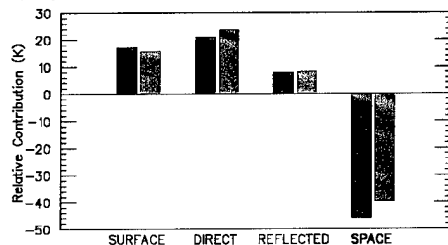
Frequency = 37.00 GHz



Frequency = 37.00 GHz



Frequency = 85.50 GHz



Frequency = 85.50 GHz

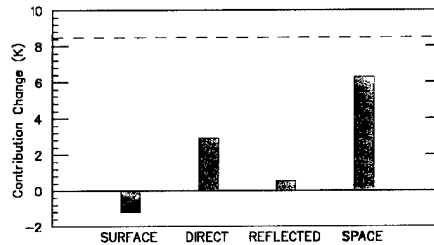


Figure 54. The relative combination of the surface, direct, reflected, and space terms of the radiative transfer equation to the brightness temperature as calculated with RADTRAN. Two extreme cases in cloud thickness of the Atlantic stratocumulus atmosphere profile are shown along with the change in contribution between the two cases.

File1: rad_proscf7_cl.out
 File2: rad_prosc1a_cl.out
 Zenith Angle = 55.00°

Brightness Temp Terms Horizontal

03-Oct-1996
 16:06:16

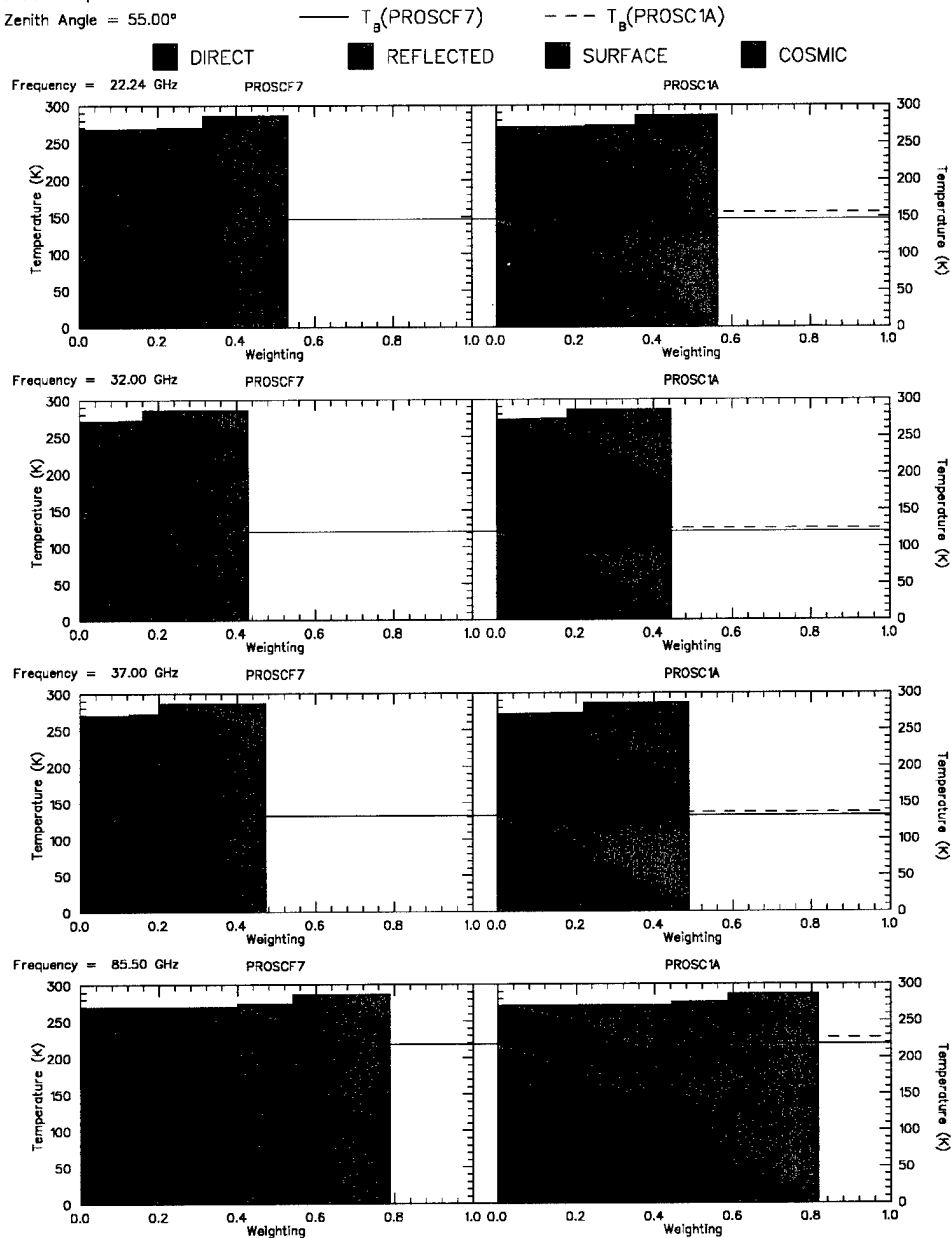


Figure 55. Channel bar chart for the terms of the radiative transfer equation as explained in the text.

Another group of atmosphere profiles that was used with RADTRAN is the mid-latitude summer (MLS) case. The basic MLS profile we constructed is based upon data taken at the Albany County Airport on July 23, 1996. The surface was taken to be a land surface. Our initial study used a fixed surface emissivity of 0.97. At a later point, emissivities based on the Bauer and Grody Land Surface Emittance Model were used. An ocean surface similar to that used for the ASc runs was utilized on a separate endeavor.

As was done for the ASc profile set, profiles with variations in cloud thickness and water content were created for the MLS atmosphere. Figure 56 shows the characteristics of a typical MLS atmosphere profile used as input into RADTRAN. Note the presence of two clouds in this particular example. The introduction of a second cloud in this group of profiles allowed the sensitivity of brightness temperature to cloud separation to be investigated, in addition to the sensitivities to cloud thickness and water content as was done for the ASc group.

An extensive survey was conducted with sets of MLS profiles, each set containing 8 profiles with different cloud altitudes and one set differing from another in some way, such as the surface temperature or relative humidity. A considerable effort was put forth in an attempt to understand the relationship between brightness temperature and a variety of parameters for the MLS profile group. Three of the more interesting variables researched include the altitude of the cloud base, the difference between the surface brightness temperature and the cloud base temperature, and the difference between the brightness temperature at the cloud base altitude for a cloud-free profile and the cloud base temperature. These quantities are plotted in Figures 57, 58, and 59 for several zenith angles. Although the behavior of the brightness temperature as a function of the plotted variable is intriguing, the sensitivity to the variable in question at a given frequency is only a few Kelvin.

A matrix of RADTRAN runs was made for the MLS profile group having two cloud layers. The two clouds in each profile were 1.5km thick with the lowest cloud top at an altitude of 1.5km, and that of the higher cloud at 4.5km. The matrix points were constructed from varying the total integrated cloud water content (CLWC) from 0 to 1000g/m² in steps of 200g/m², and the ratio of the upper cloud water content to the total cloud water content, $cu/(cu+cl)$, from 0.0 to 1.0 in increments of 0.1. For three sets of runs, the Bauer and Grody Land Surface Emittance Model was used with SOIL_WC=0.30, SOIL_ROUGH=0.04, VEG_WC=3.00, and VEG_COVER=0.90. The brightness temperatures associated with the matrix were then plotted as a contour plot for each frequency and angle of interest. Figure 60 shows a typical contour plot. Note that in the region where the total cloud water is zero, specifically along the abscissa, the ratio $cu/(cu+cl)$ is undefined. However, we can argue that it is defined for CLWC arbitrarily close to zero, and should be independent of $cu/(cu+cl)$. In other words, the brightness temperatures should approach their cloud free values in the region near CLWC=0.

The third class of atmosphere profiles that was subjected to testing with RADTRAN is based upon the U. S. Standard Atmosphere of 1962. A set of profiles was constructed from this standard atmosphere, with each profile containing a cloud of differing thickness and/or water content. An ocean surface was taken for the background.

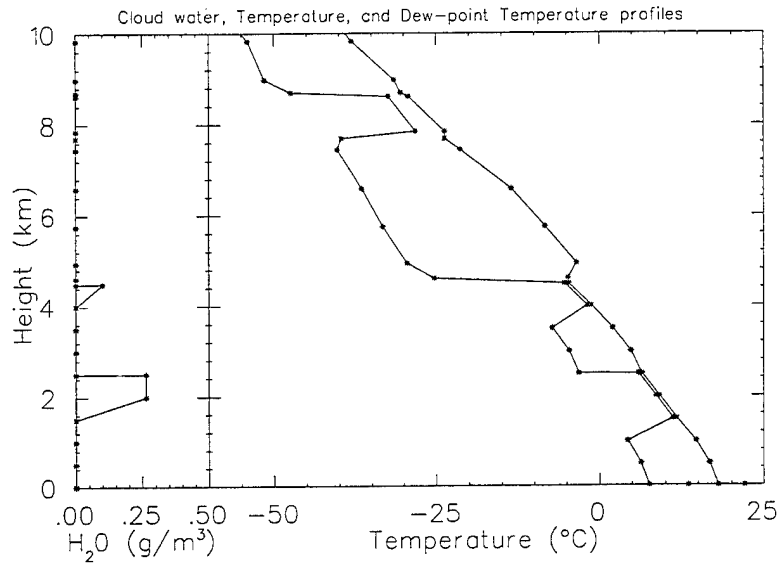


Figure 56. Cloud water, temperature, and dew-point temperature profiles for a typical mid-latitude summer atmosphere used as input into RADTRAN.

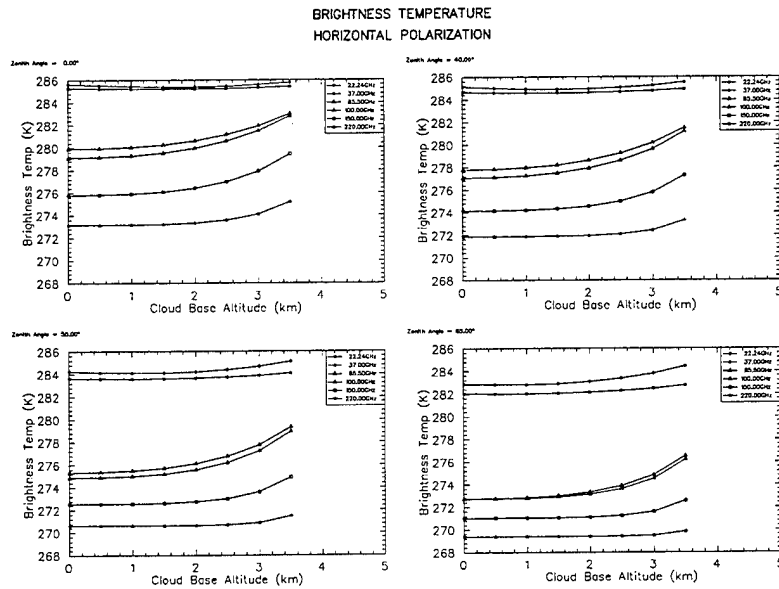


Figure 57. Brightness temperature in the horizontal polarization as calculated with RADTRAN for a set of mid-latitude summer atmosphere profiles as a function of cloud base altitude.

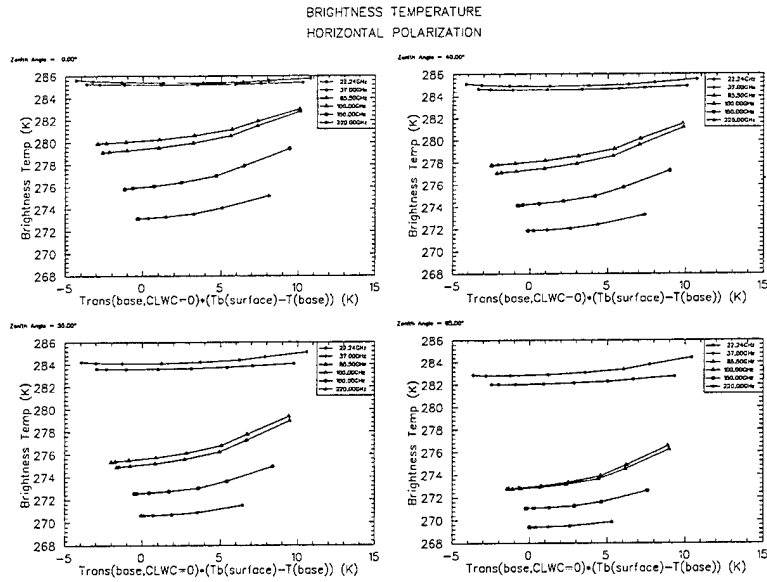


Figure 58. Same as Figure 57, but with the difference between the surface brightness temperature and the cloud base temperature plotted.

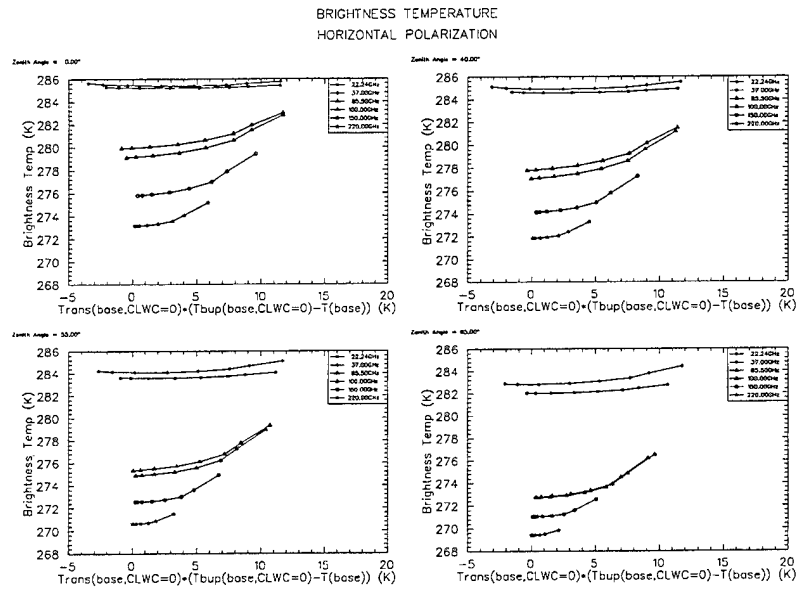


Figure 59. Same as for Figure 57, but with the abscissa as the difference between the brightness temperature at the cloud base altitude for a cloud-free profile and the cloud base temperature.

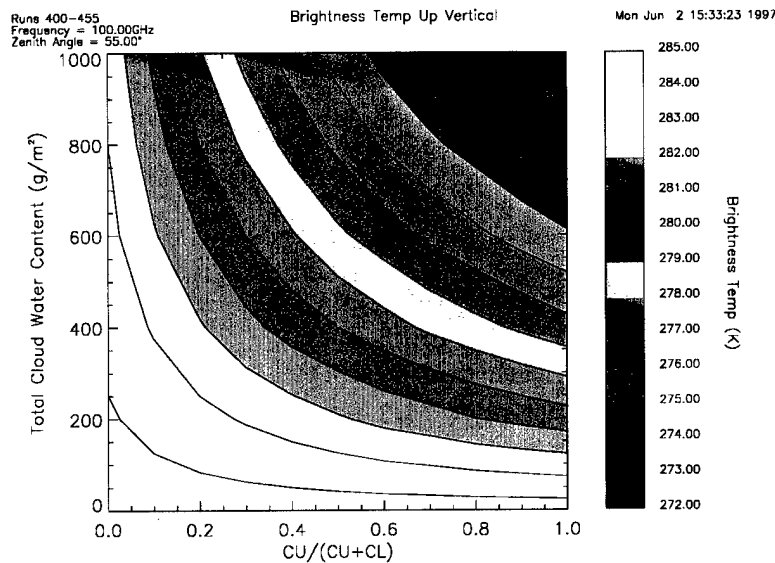


Figure 60. Brightness temperature in vertical polarization for mid-latitude summer atmosphere containing two clouds as calculated by RADTRAN. Contours of cloud water content and the fraction of the water content of the upper cloud to the total are shown for a zenith angle of 55° at 100 GHz.

For the modeling work done with the group of standard atmosphere profiles, sensitivity of brightness temperature to cloud characteristics was not investigated, at least not at the level of effort extended to the ASc and MLS profile groups. Instead, the effects of the Ray and LHM attenuation models were subjected to further scrutiny in the context of their use in RADTRAN. Figure 61 shows the total atmospheric attenuation at nadir for a standard atmosphere containing a cloud with the top of the cloud at the -30°C level. The oxygen, water vapor, and cloud water components are shown individually, with the cloud contribution displayed for both attenuation models under consideration. Noteworthy are the water vapor lines at 22 and 183 GHz, as well as the oxygen peaks near 60 and 118 GHz, and their role in the overall picture. In spite of the fact that there is greater disagreement in the attenuation offered by the Ray and LHM models at the higher frequencies, the role of cloud water attenuation is of greater significance percentage wise at the lower frequencies outside the peak areas of the oxygen and water vapor contributions. However, the effects of attenuation in the calculation of brightness temperature are more complex. Figure 62 shows the differences in brightness temperature, computed with the two attenuation models. The influence of the surface emittance and atmospheric transmittance cause the cloud to appear bright against a dark background at the lower frequencies, but at higher frequencies the background appears brighter than the cloud.

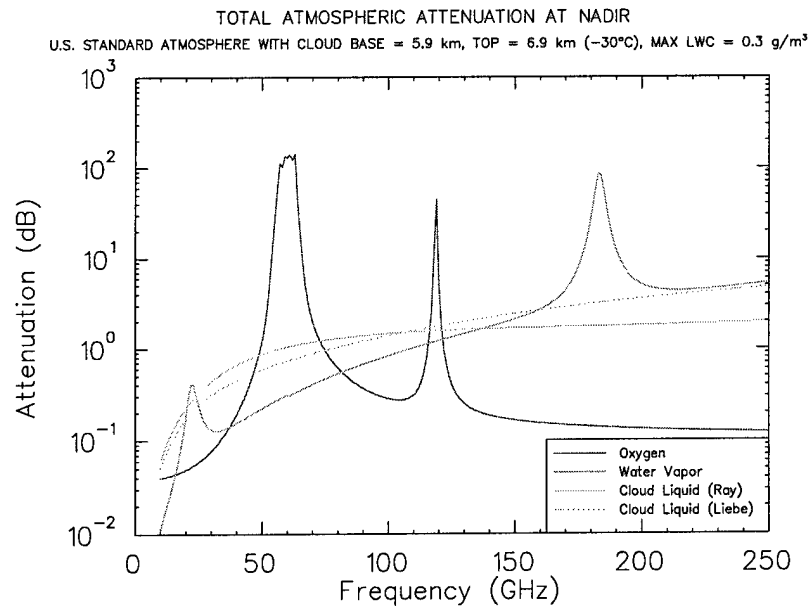


Figure 61. The total atmospheric attenuation as a function of microwave frequency for a nadir view through a U. S. Standard Atmosphere having a cloud with its top at 6.9km or -30°C . The different contributing components are shown, with the part due to cloud water displayed for two attenuation models as discussed in the text.

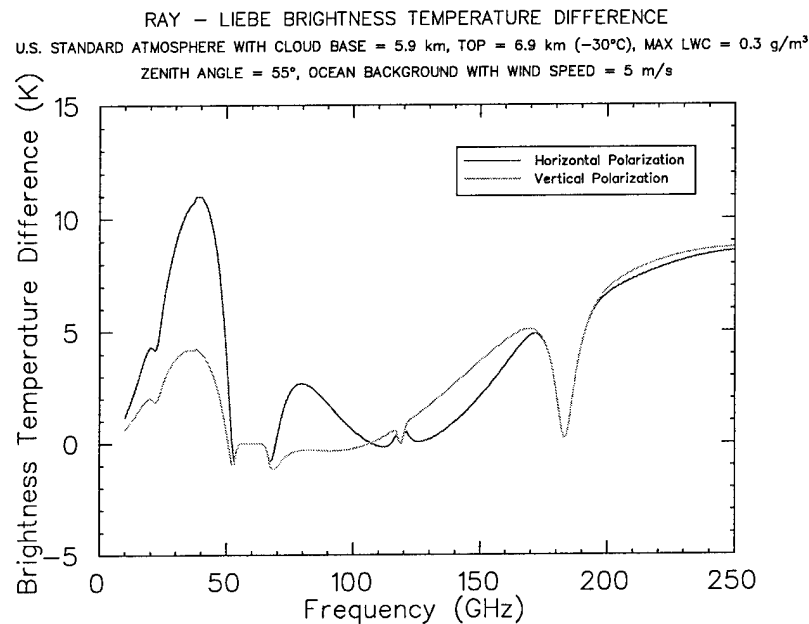


Figure 62. The difference in brightness temperatures calculated by RADTRAN using the Ray or LHM attenuation models.

The standard atmosphere was also used to simulate the retrieval of cloud data that could be obtained from ground and space based sensors. In particular, RADTRAN was run with a standard atmosphere as input. The resulting modeled brightness temperatures were hypothesized to be data that an actual experimental instrument would observe. This artificial data was then manipulated according to methods pertinent to the instrument in question, in an attempt to obtain the amount of cloud liquid water that was used for the RADTRAN run. Both attenuation models were involved in this exercise.

Two simulated retrievals were performed. The first simulation was for a Special Sensor Microwave/Imager (SSM/I), a device used on Defense Meteorological Satellite Program (DMSP) satellites [Hollinger, *et al.*, 1990]. The procedure for retrieving the water content of clouds from brightness temperatures measured with the SSM/I is to use a regression algorithm [Alishouse, *et al.*, 1990]. For our case, we used a popular form that employs four frequency channels of the instrument. Specifically, the total cloud liquid water retrieved can be written as

$$CLWC = a_0 + a_1 Tb_H(19) + a_2 Tb_V(22) + a_3 Tb_V(37) + a_4 Tb_H(85) \quad (86)$$

where the a 's are constants, and $Tb_H(f)$ and $Tb_V(f)$ are the horizontal and vertical brightness temperatures at frequency f , respectively. Simulations and retrievals were made for three separate cloud cases, namely with the cloud top temperature at -10, -20, and -30°C. The zenith angle of the instrument was taken to be 53.1°.

The second simulation and subsequent retrieval was done for an upward-looking microwave radiometer situated at the Earth's surface [Hogg, *et al.*, 1983]. The same atmospheric conditions and vertical view that were used in the SSM/I case were used in these simulations. A regression retrieval algorithm employing two channels, 20.6 and 31.6 GHz, was used to retrieve the total cloud water content. Coefficients for the regression formula were taken from statistical inversion results applied to radiosonde observations at Oklahoma City during April-May, 1975-1977.

The results of our simulations and retrievals are shown in Figures 63 and 64. The results for the two instruments are similar in two regards: the retrieved values increase with decreasing cloud top altitude/temperature, and there is greater variation in the results that used the Ray attenuation model than there is for the LHM model based results.

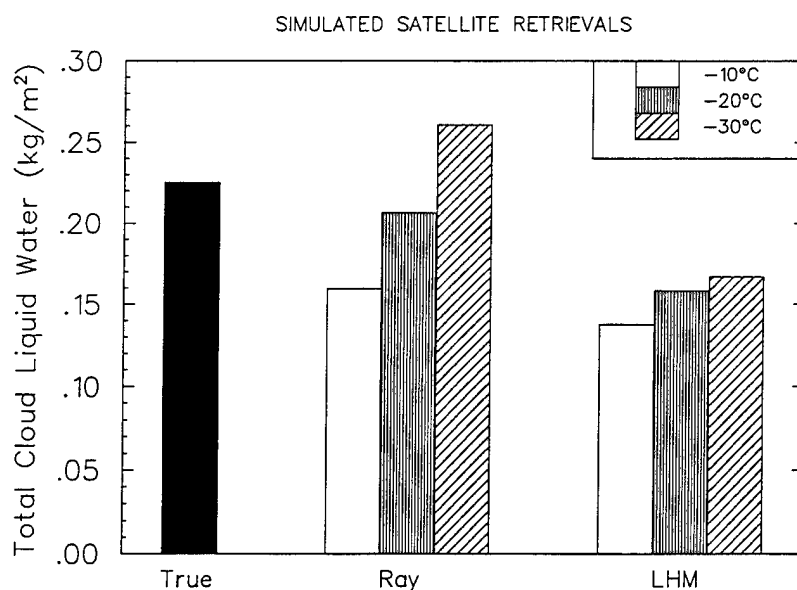


Figure 63. Results of simulating the retrieval of the total amount of cloud liquid water from the SSM/I. The simulated value is shown by the bar labeled true. The retrieved results are shown with bars labeled by the attenuation model used for the cloud water attenuation., Different cloud top temperatures are indicated by the legend.

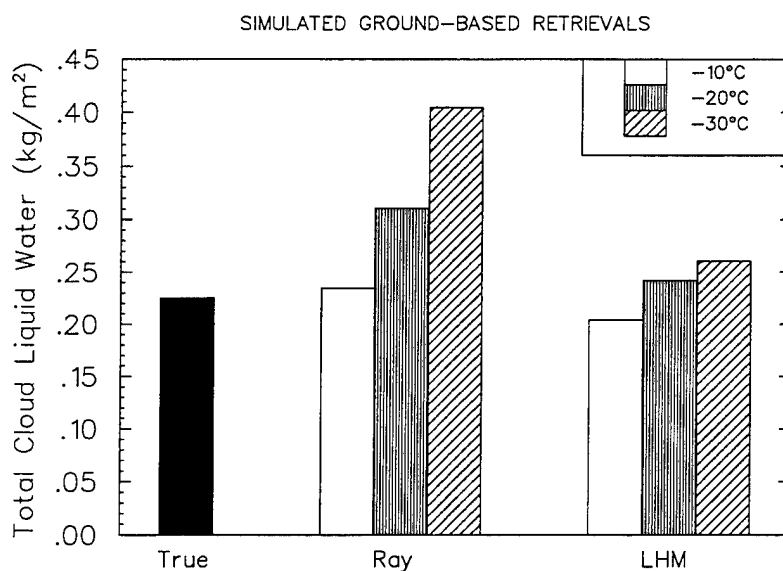


Figure 64. Same as Figure 62, but the retrieved results are for an upward-looking ground-based radiometer.

7.1.4 FASE

In order to identify areas of improvement in the RADTRAN model and gain further insight into model dependencies, an independent effort was undertaken to use the modeling code FASE [Snell, *et al.*, 1996]. By comparing the results of running FASE and RADTRAN with the same atmospheres as input, meaningful conclusions can be drawn about the underlying methodologies that each code emphasizes. Because FASE is a much more complicated program than RADTRAN, and less user friendly, a considerable amount of work was necessary to set up FASE so that it would provide the same information that RADTRAN generates. For example, RADTRAN computes both the upward and downward transmittance, but FASE only one or the other. Thus, FASE had to be run twice for every run of RADTRAN. A separate program had to be written to combine the results of upward and downward FASE results, and calculate the brightness temperatures that RADTRAN gives. Furthermore, the output produced by FASE can take up such a huge amount of disk space when run with the exact same conditions for the RADTRAN runs, that it was deemed impractical to run FASE in this manner. Thus, the atmosphere profiles used with FASE were made to contain less information than had been given to RADTRAN. This was done by reducing the number of layers specified in the profile. A test was made to see how FASE results changed as the top of the atmosphere was chopped off. It was concluded that one could safely remove all atmosphere layers above 30km without adversely affecting the results of FASE.

The first effort made to compare FASE results with RADTRAN results was for a cloudless ASC profile. Figure 65 shows the comparison of the results for the two modeling codes. Although there are some notable differences in the results, the discrepancies can be attributed to the different way the two codes handle the continuum.

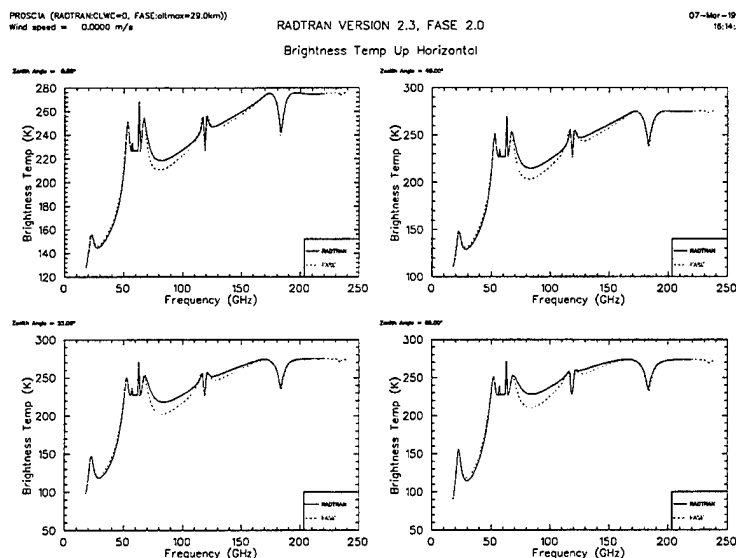


Figure 65. Brightness temperature for a cloudless Atlantic stratocumulus atmosphere as calculated using the modeling codes RADTRAN and FASE.

The next step in making RADTRAN/FASE comparisons is to use an atmosphere containing a cloud. Unfortunately, FASE does not accept user defined cloud information, at least not in the microwave region. Fixing this problem could be a daunting task and funding restrictions have so far prevented much of an effort in this area. However, a new program that combines parts of RADTRAN and FASE is currently under construction in hopes of circumventing the problem of not being able to run FASE with atmosphere profiles containing clouds.

7.2 SUMMARY

Utilizing the radiative transfer code, RADTRAN, we have modeled three types of atmosphere profiles. The sensitivity of the brightness temperature to several cloud characteristics was investigated. This was done with both ocean and land background conditions. Attenuation and surface emissivity models were tested. Simulated data was generated and then manipulated as if it had been measured from a spacecraft or ground station to test retrieval methods of obtaining cloud vertical structure information. A great deal was learned from the modeling runs and areas in which to make further progress have been identified. On the topic of attenuation, there is a need for research to determine the radiative properties of liquid water at temperatures down to -40°C . This would remove the ambiguities in the attenuation models at cold temperatures. In the area of modeling the atmosphere, it would be advantageous to obtain results similar to that provided by RADTRAN from an independent code. This should be the direction of effort in the immediate future, and would give greater confidence in selecting the kind of remote sensors to be used in the data collection phase.

8. ATMOSPHERIC DENSITY MODELS FOR ORBIT DETERMINATION

8.1 EVALUATION OF FIRST PRINCIPLES DENSITY MODELS

The inability to reduce error in thermospheric density estimation by empirical models has led researchers to develop first-principles models. Empirical models are derived from large measurement data bases, by optimal adjustments of parameters to minimize residuals with respect to the data. Although they attempt to approximate the physics of the thermosphere, their main goal is to perform efficiently in operational circumstances, with the mathematics as simple as possible. Therefore they are able to capture the gross features of the thermosphere, but not the fine details of dynamical variations in space and time. A further inadequacy is that the empirical models must use routinely available indices as measures of the energy input into the thermosphere. The solar EUV, which is the main source of thermospheric heating, cannot be routinely measured, since it is absorbed before reaching the surface of the earth. Thus the common measure of the solar radiative input has been the 10.7 cm radio flux, which has almost no interaction with the thermosphere, but is found to correlate well with EUV [Hedin, 1984], whenever both are simultaneously measured. Geomagnetic activity is represented in the empirical models by the K_p activity index, which may not always

correlate well with the main geomagnetic processes of particle precipitation, Joule heating, and ion drag.

The first-principles models are developed by solution of the coupled equations of momentum, energy, and continuity. Although this approach can bring in the dynamical structural details lacking in the empirical models, the first principles models nevertheless require accurate detailed specification of the inputs to be most effective. A distinct disadvantage with first principles models is that they are extremely computer intensive, compared to the empirical models, and therefore not suited for routine operational use. *Killeen and Roble* [1994] have developed a solution for the thermosphere general circulation model (TGCM) [*Dickinson, et al.* 1981; *Roble, et al.*, 1982,1987; *Dickinson, et al.*,1984] and the Thermosphere-Ionosphere General Circulation Model (TIGCM) [*Roble, et al.*,1988]. The results of first principle model runs are used as “data” to derive an “empirical” model. The form of the “empirical” model is a summation of vector spherical harmonics; hence the name VSH. *Killeen and Roble* [1994] furthermore enhanced the storm model, in an attempt to model realistically the time-dependent behavior of the thermosphere during magnetic storms. This was done by introducing a 24-hour time history of the geomagnetic activity index K_p , rather than using just the current 3-hour value. The results of time-dependent runs were represented in geomagnetic, rather than geographic coordinates, and are introduced into VSH as an “add-on” to the baseline quiet model.

The Thermosphere Forecast Model (TFM) [*Fuller-Rowell, et al.*, 1994] incorporates self-consistent thermosphere-ionospheric coupling, like TIGCM, but only poleward of 23° latitude in each hemisphere. Although there is some computation time-saving, relative to complete runs of TIGCM, the requirement is significantly larger than VSH. As far as we know, there does not exist a convenient mathematical formulation of TFM similar to the VSH representation of TIGCM.

8.1.1 Comparison of Models with Data

The VSH model, based on TIGCM was inserted into the density data bases in the “new” model tapes described below in Section 8.2. For convenient access VSH was stored, with and without the storm-time enhancements, with empirical models Jacchia 1970 [*Jacchia* 1970] and MSIS-90E [*Hedin* 1991]. The Jacchia 1970 model is based almost entirely on orbital decay data. It is the simplest and therefore fastest in computation time. The MSIS-90E model is actually an extension to the ground of the MSIS-86 [*Hedin* 1987] model, with only slight adjustment to that model’s thermospheric representation. Neither empirical model depicts winds. However *Hedin* [1991] has provided for MSIS-90E a companion wind model, HMW90. The first principles models incorporate winds directly within their formulations. Although the density data bases therefore include these wind models, no comparisons with data have been made at this time. Since we do not have the computer code for TFM, the results presented here are based on first principles runs by PL personnel [*Marcos*, 1995] for a limited portion of the data described in the previous subsection: the 23-day SETA-1 database.

The basic method of statistical comparison was the evaluation of the mean and standard deviation of the natural log of the measured density to model density ratios. Although one could also use the ratios themselves, the natural log has the advantage of symmetry about the value representing agreement between model and measured density (1.0 for the ratio, 0.0 for the log of the ratio). This is because the linear ratio is limited to zero at the low end, while the log can range infinitely in both directions from perfect agreement. The standard deviation of the natural log was converted to “% standard deviation” by multiplication by 100. For values near zero the standard deviation of the log is approximately equal to the fractional variation between the two quantities compared.

Figure 66 shows a comparison of the two empirical models with the VSH quiet and storm models for June, 1982, SETA-2 data. The standard deviations of the log ratios are shown for low, medium and high geomagnetic activity. The standard deviations provided a measure of how well the model represents variability in the density. Lower standard deviation indicates better representation. The VSH storm model shows dramatic improvement over the quiet VSH model. Although this trend was present at other times, the VSH models (both storm and quiet) did not always exhibit lower standard deviations than the empirical models.

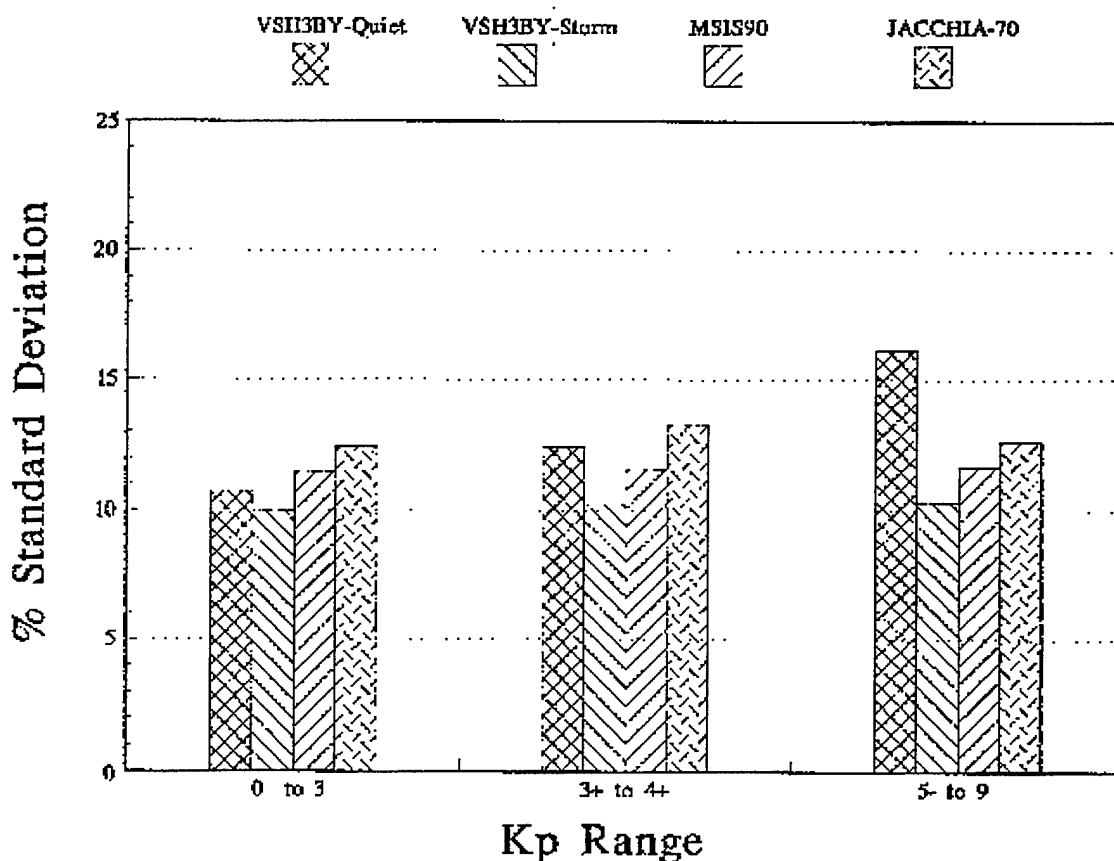


Figure 66. Standard Deviation of the natural log of measured to model density ratio, for the VSH quiet and storm models, the MSIS90E model, and the Jacchia-70 model, for SETA-2 data, June, 1982, for three geomagnetic activity (K_p) levels.

Figure 67 shows a latitude-dependent comparison between the VSH storm model and the empirical models, for the three K_p ranges, for the same period as in Fig. 66. Negative numbers here indicate that the VSH performs less well than the empirical model. It is interesting that, for most specific latitudes and local times, MSIS-90 performs better than VSH storm, despite the latter's better performance when data is integrated over all latitude and local time, as in Figure 66. This possibly indicates that VSH, at least for this period, better represents the latitude-local time dependence of the response of the thermosphere to geomagnetic activity, while time dependence at specific locations in the orbit may be better represented by MSIS-90. Notice that MSIS-90, like VSH storm, uses a K_p history, rather than the value of the index at the time of interest. Jacchia, which uses a single value, does not perform as well as VSH.

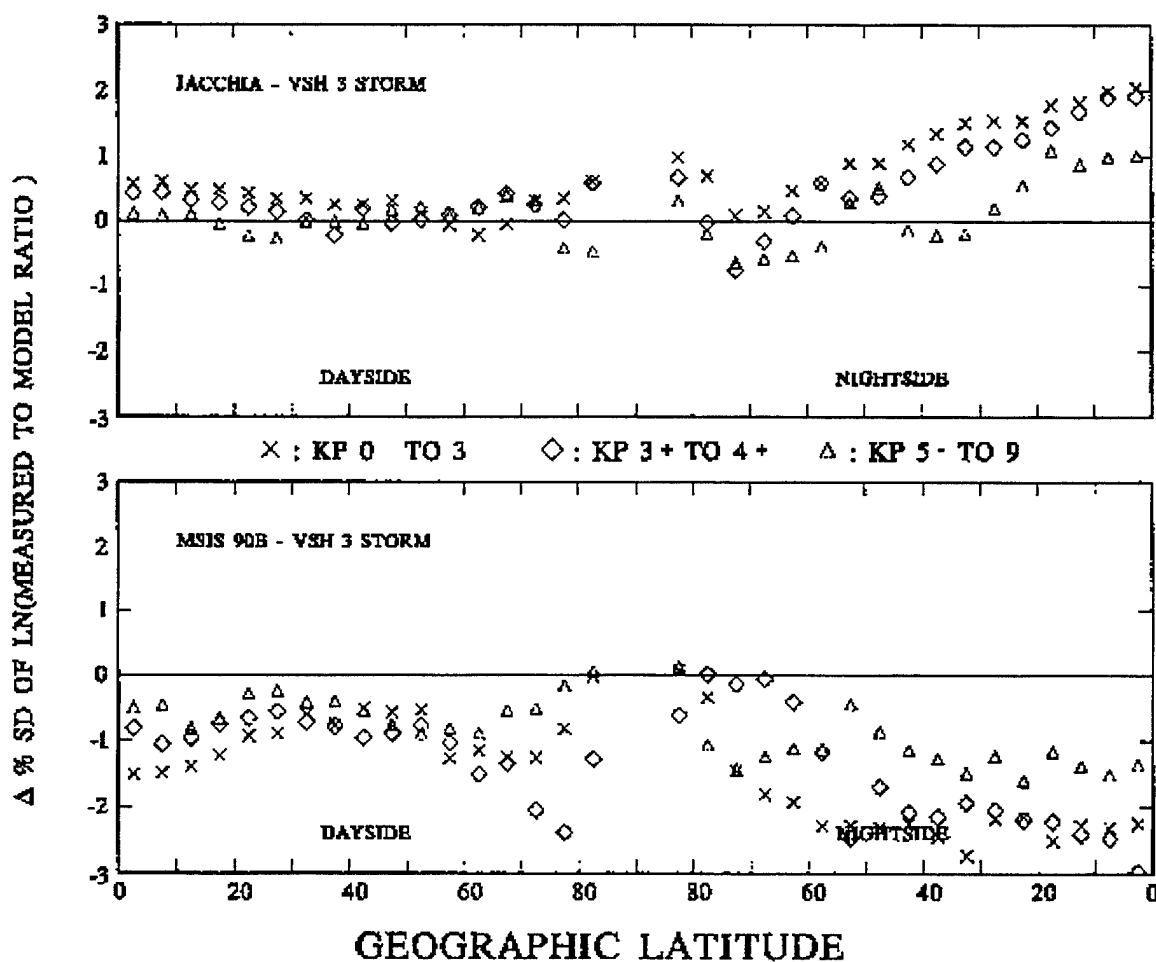


Figure 67. Comparison of standard deviations of log of the ratios of data to model for the VSH storm, Jacchia-70, and MSIS-90E models as functions of latitude-local time, for the same period as in Figure 66. The differences between the empirical model standard deviation and the VSH standard deviation are shown. A negative number indicates that the standard deviation of the log of the ratio of measured to empirical model is lower than the corresponding value for the VSH model

Table 10 shows performance statistics for the SE-S3/1 database period for the J70, MSIS-90 and VSH storm models, for entire data set, and for the 3 K_p ranges. The mean log ratio changes more, from low to high K_p , for VSH than for the other two. The standard deviations are generally highest for VSH as well. Thus, VSH is not predicting the variability as well as the others either for specific K_p ranges, or over all the data. Note that this data set is at low solar activity (Table 10) compared to the SETA vehicles.

TABLE 10. Statistical Summary of Neutral Atmosphere Models
Altitude Range 160 - 250 km

			J70		MSIS90		VSH	
			MEAN	STD	MEAN	STD	MEAN	STD
ATMOSPHERE EXPLORER-C								
	ALL		0.0299	16.78	0.0801	14.90	0.1182	18.37
	LOW	KP	0.0162	16.37	0.0648	14.39	0.0604	16.51
	MOD	KP	0.0351	16.71	0.0816	14.84	0.1532	16.76
	HI	KP	0.0665	17.65	0.1278	15.61	0.2491	18.60
ATMOSPHERE EXPLORER-D								
	ALL		-0.0272	16.45	-0.0670	15.67	0.0726	18.22
	LOW	KP	-0.0258	16.28	-0.0820	15.18	0.0366	16.56
	MOD	KP	-0.0386	16.75	-0.0297	15.92	0.1633	17.17
	HI	KP	-0.0101	17.53	0.0139	16.70	0.2652	20.23
ATMOSPHERE EXPLORER-E								
	ALL		-0.0037	16.08	0.0001	13.17	0.0493	15.62
	LOW	KP	-0.0034	15.88	-0.0167	12.48	0.0239	15.05
	MOD	KP	-0.0134	16.34	0.0392	13.50	0.1090	13.86
	HI	KP	0.0368	17.63	0.1036	14.38	0.2008	16.72
AIR FORCE S3-1								
	ALL		0.0270	15.01	0.0054	14.99	0.1041	18.67
	LOW	KP	0.0297	14.90	-0.0138	15.26	0.0404	17.25
	MOD	KP	0.0182	14.58	0.0155	13.75	0.1471	15.53
	HI	KP	0.0326	16.03	0.0514	14.90	0.2407	18.50

Figures 68-71 show density variations through individual SETA-1 orbits. The measured density is compared with two model densities in the upper panel of each figure, while in the bottom are shown ratios of measured to model densities. The models shown are MSIS-90 and TFM in Figures 68 and 70, MSIS-90 and VSH storm in Figures 69 and 71. Figures 68 and 69 are for orbit 98, which is at high activity, while Figures 70 and 71 are for orbit 114, which is at low activity. The significant structural features in the data are not present in any of the models. This behavior is quite common among all the orbits of SETA-1. It indicates that the attempt of the first principle models to reproduce structural details is not succeeding.

ORBIT NO. 98

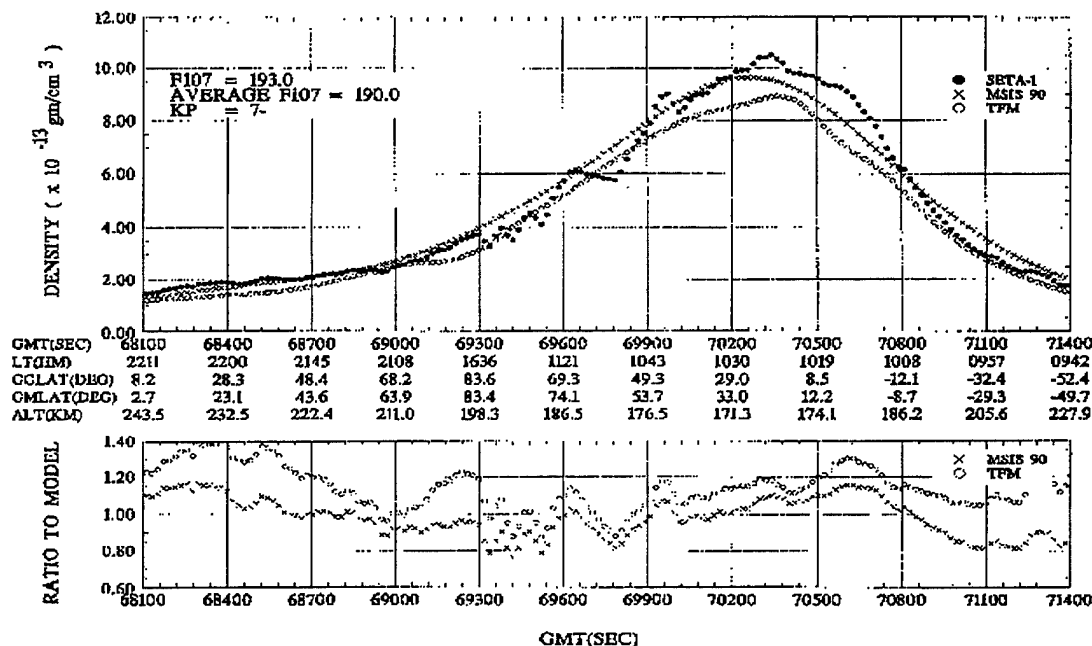


Figure 68. Top panel: Overlay showing measured density, MSIS-90E model density, and TFM model density, for orbit 98, day 81 (1979), SETA-1 data. Bottom panel: measured to model ratio for the two models for the same period.

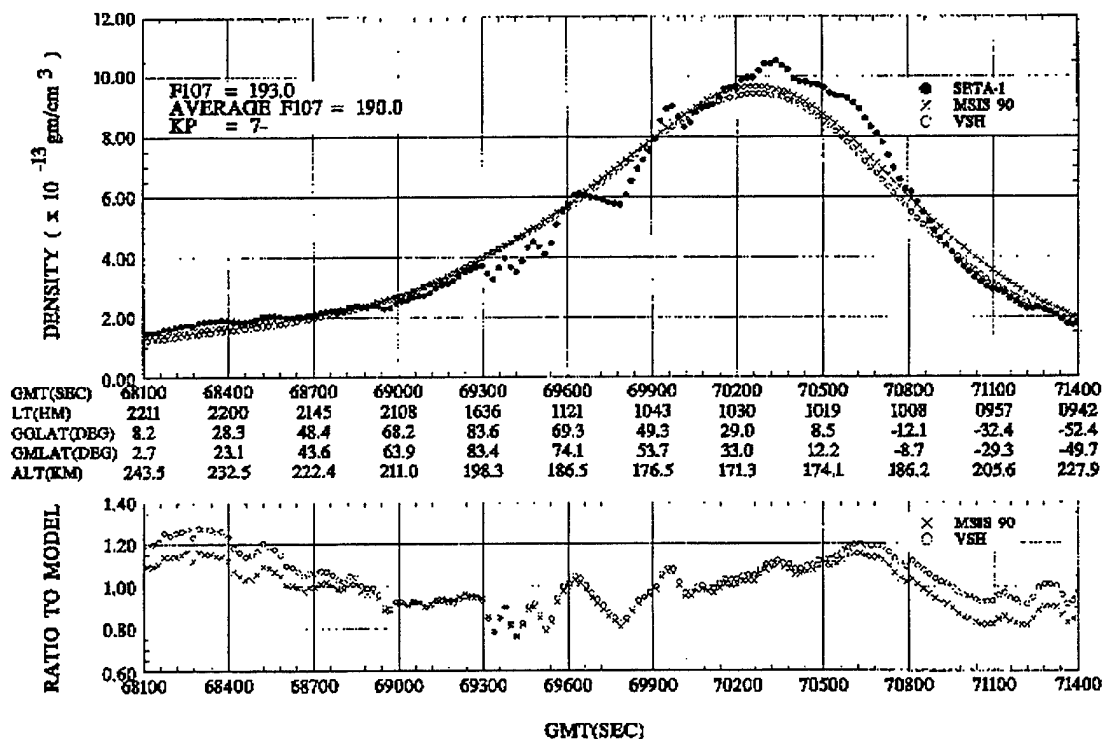


Figure 69. Same as for Figure 68, except that the VSH storm model is shown instead of the TFM model.

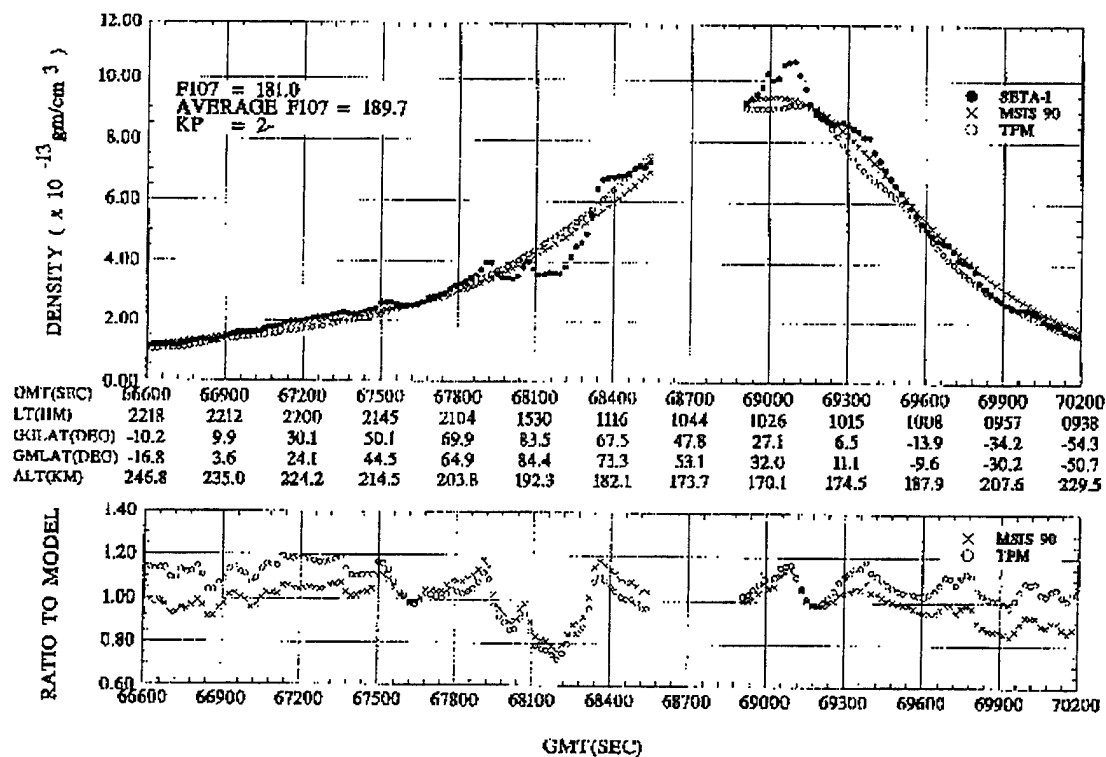


Figure 70. Same as for Figure 68, except that it is for orbit 114.

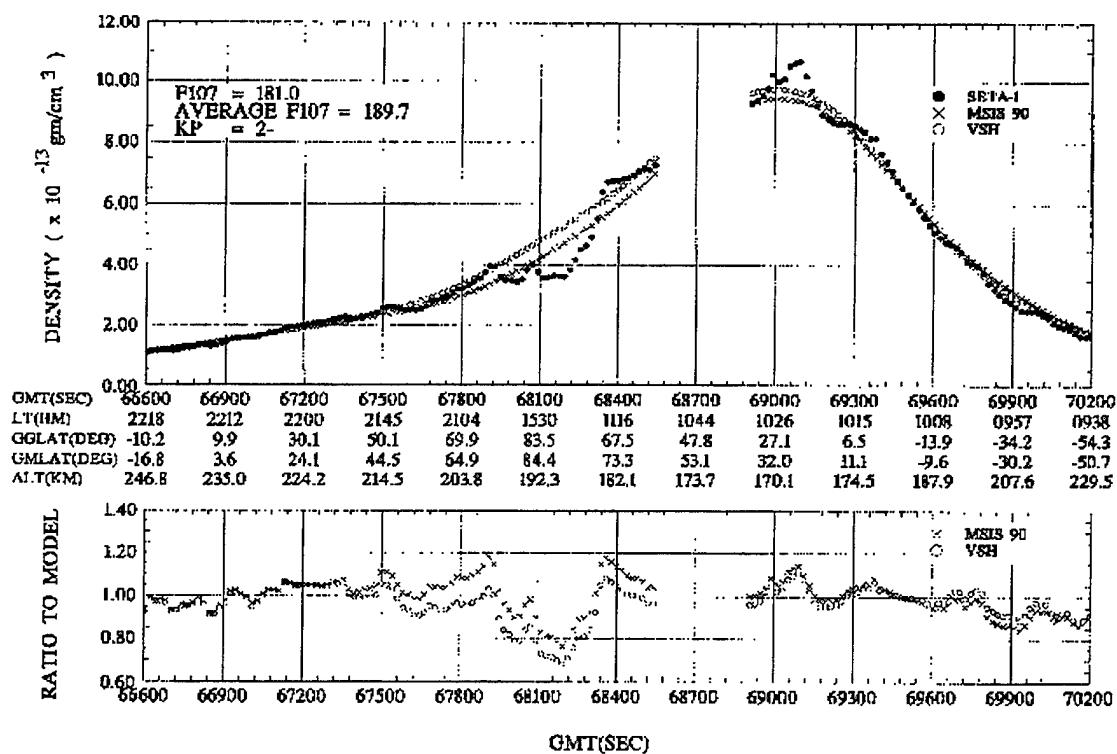


Figure 71. Same as for Figure 69, except that it is for orbit 114.

The results presented here are of insufficient scope to form firm conclusions concerning the comparative performance of the first-principles and empirical models. The best conclusions that one can arrive at is that the time-dependent storm modeling in VSH is an improvement over the quiet model, and that the detailed spatial structures seen in the measurements are not captured well by any of the models, regardless of the geomagnetic activity level.

It is recommended that the effects of the winds be considered. Where the time continuity of the data is sufficient, that is, there is sufficiently regular sampling of the data for numerical differentiation of position with respect to time, the data base includes the velocity of the satellite relative to the rotating earth. Combining this with the appropriate wind model, which exists for MSIS and VSH, one can accurately determine a model total drag for a more reliable comparison with the data actually includes the deceleration due to both density and winds.

8.2 DATABASE MIGRATION

The neutral thermosphere is an extremely complex system. Nevertheless, accurate and efficient modeling of the thermosphere is important for many applications. To assist in the development and evaluation of density models, PL has built an extensive database of thermospheric densities, based on satellite drag measurements in the thermosphere by on-board accelerometers [Marcos, 1985]. This database has been maintained on a CDC CYBER platform [Bass, *et. al.*, 1987, 1989], in which the data were stored on 2400 ft 9-track magnetic tapes residing at the PL central site. The replacement of the CYBER by UNIX-based work-stations required that the data be recast in a format suitable for these new platforms. This required not only reformatting the data itself, but also selecting an appropriate storage medium to replace the CYBER-based magnetic tapes. It was determined that the data would be written to Xabyte tapes readable on the SUN workstations. In addition a new software package has been written to duplicate the functionality of program STAT, which accessed the CYBER-based database to perform statistical analyses of measured vs model differences.

8.2.1 Description of the Cyber-based Database

The characteristics of the data base are summarized in Table 11. Note that the data for the first 4 satellites in the list do not sit separately, but exist only in a combined data set. The data set for this group, and for satellites S3-4 and SETA-1, were written in the standard CYBER FORTRAN unformatted unpacked. Due to the great size of the later data bases, for satellites SETA-2, SETA-3, and S85-1, the data for these are in a packed format.

Table 12 lists the identifiers of the tapes that resided in the library. They were written on the CYBER using the NOS operating system. Those with a "GE" next to their identifiers were written in 6250 bpi density, while the others were written in 1600 bpi. After the satellite name(s) is a list of density models whose values are included for each measurement point for comparison with the

data contained on the tape. The models are described briefly in Table 13, which includes references for further detail.

TABLE 11. Neutral Atmospheric Density Data Base Characteristics

SAT	PACKED/ UNPACKED	TIME/ALT	JULIAN DATE	SEASON	ALTITUDE RANGE (KM)	-AP- DAILY 6.7HR		INCL	MEAN F10.7	# FILES	# DATA RECS	# POINTS
AE-C		ALT	73353 74352	FWSS	135 245			68.4	86.9			62044
S3-1		ALT	74309 75120	FWS	135 245			97	76.3			27315
AE-D		ALT	75281 76029	FW	140 245			90	75.8			29762
AE-E		ALT	75325 76322	FWSS	135 245			20	73.3			35629
AE/S3-1	UNPACKED	ALT	73353 76322		135 245	Y	Y			23	12906	154750
S3-4	UNPACKED	TIME(MIX)	78089 78223	SS	162 285	N	Y	96*	145.8	161	4587	54073
SETA-1	UNPACKED	TIME(SEQ)	79079 79100	SPRING	168 250	Y	Y	96*	189.8	1	5221	62649
SETA-2	PACKED	TIME(MIX)	82137 82332	SSF	168 297	N	N	96*	170.0	114	37034	443805
SETA-3	PACKED	TIME(MIX)	83201 84075	SFWS	163 385	N	N	96*	116.0	150	24647 4	2956869
S85-1	PACKED	TIME(MIX)	84201 84283	SF	179 257	N	N	96*	80.6	72	28136	337219

* SUN SYNCHRONOUS ORBIT

TABLE 12. Neutral Atmospheric Density Data Base Tape Library

Tape #	Satellite	Models							
CC0271 GE	AE/S3-1	J71	J70T	MSIS86B	MSIS83B	US76			
CC0324 GE	AE/S3-1	MSIS77	MSIS78/79	MSIS83A	US62	US66	USSR		
CC0426 GE	AE/S3-1	J64	J70	J73	J77	L/N	USSR	DENSEL	JWB
CC0428 GE	AE/S3-1	J64	J70	J73	J77	L/N		DENSEL	JWB
CC2005	S3-4	J71	J70T	MSIS86B	MSIS83B	US76			
CC2133	S3-4	MSIS77	MSIS78/79	MSIS83A	US62	US66	USSR		
CC2171	S3-4	J64	J70	J73	J77	L/N	USSR	DENSEL	JWB
CC2177	S3-4	J64	J70	J73	J77	L/N		DENSEL	JWB
CC2424	SETA-1	J71	J70T	MSIS86B	MSIS83B	US76	J71KP=1		
CC2452	SETA-1	MSIS77	MSIS78/79	MSIS83A	US62	US66	USSR		
CC2516	SETA-1	J64	J70	J73	J77	L/N	USSR	DENSEL	JWB
CC2539	SETA-1	J64	J70	J73	J77	L/N		DENSEL	JWB
CC1371	SETA-2	J71	J70T	MSIS86B	MSIS83B	US76	J71KP=1		
CC1381	SETA-2	MSIS77	MSIS78/79	MSIS83A	US62	US66	USSR		
CC1444	SETA-2	J64	J70	J73	J77	L/N	USSR	DENSEL	JWB
CC1449	SETA-2	J64	J70	J73	J77	L/N		DENSEL	JWB
CC0361 GE	SETA-3	J71	J70T	MSIS86B	MSIS83B	US76			
CC0416 GE	SETA-3	MSIS77	MSIS78/79	MSIS83A	US62	US66	USSR		
CC0444 GE	SETA-3	J64	J70	J73	J77	L/N	USSR	DENSEL	JWB
CC1907 GE	SETA-3	J64	J70	J73	J77	L/N	MSIS77	DENSEL	JWB
CC0223	S85-1	J71	J70T	MSIS86B	MSIS83B	US76			
CC0179 GE	AE/S3-1	MASTER							
CC1838	S3-4	MASTER							
CC2375	SETA-1	MASTER							
CC1276	SETA-2	MASTER							
CC0318 GE	SETA-3	MASTER							
CC0123	S85-1	MASTER							
27 TAPES									

TABLE 13. Density Models

Table 12. Abbreviation	Full Name (Description)	Reference
DENSEL	DENSEL	Bramson, A. S., and Slowey, J. W., <u>Some Recent Innovations in Atmospheric Density Programs</u> , AFCRL-TR-74-0370 AD786414, 1974.
J64	Jacchia 1964	Jacchia, L. G., <u>Static Diffusion Models of the Upper Atmosphere with Empirical Temperature Profiles</u> , Smithsonian Astrophysical Observatory Special Report Number 170, 1964.
J70	Jacchia 1970	Jacchia, L. G., <u>New Static Models of the Thermosphere and Exosphere with Empirical Temperature Profiles</u> , Smithsonian Astrophysical Observatory Special Report Number 313, 1970.
J70T	Jacchia 1970 with improved L local time (tidal) model	Bass, J. N., and Robinson, E. C., <u>New Local Time Models for Jacchia Densities</u> , AFGL-TM-108, 1985.
J71	Jacchia 1971	Jacchia, L. G., <u>Revised Static Models of the Thermosphere and Exosphere with Empirical Temperature Profiles</u> , Smithsonian Astrophysical Observatory Special Report Number 332, 1971.
J71KP=1	Jacchia 1971 with $K_p = 1$	Same as J71
J73	Jacchia 1973	Bramson, A. S., and Slowey, J. W., <u>Some Recent Innovations in Atmospheric Density Programs</u> , AFCRL-TR-74-0370 AD786414, 1974.
J77	Jacchia 1977	Jacchia, L. G., <u>Thermospheric Temperature, Density, and Composition: New Models</u> , Smithsonian Astrophysical Observatory Special Report Number 375, 1977.
JWB	Jacchia-Walker-Bruce	Bramson, A. S., and Slowey, J. W., <u>Some Recent Innovations in Atmospheric Density Programs</u> , AFCRL-TR-74-0370 AD786414, 1974.
L/N	Lockheed/NASA	Butler, J. H., <u>A Preliminary Upper Atmosphere Density Model Derived from Satellite Drag Density Data</u> , Lockheed Missiles and Space Company, NASA Contractor Report Number 61298, 1969.
MSIS77	First MSIS model - longitude averaged	Hedin, A. E., et. al., "A Global Thermospheric Model Based on Mass Spectrometer and Incoherent Scatter Data", J. Geophys. Res., Vol. 82, No. 16, pp. 2139-2156, 1977.
MSIS78/79	MSIS77 plus longitude/UT variations	Hedin, A. E., et. al., "Global Model of Longitude/UT Variations in Thermospheric Composition and Temperature Based on Mass Spectrometer Data", J. Geophys. Res., Vol. 84, No. A1, pp. 1-9, 1979.
MSIS83A	MSIS 83 with daily average A_p	Hedin, A. E., "A Revised Thermospheric Model Based on Mass Spectrometer and Incoherent Scatter Data: MSIS-83", J. Geophys. Res., Vol. 88, No. A12, pp. 10170-10188, 1983.
MSIS83B	MSIS 83 with 3-hour a_p	Same as MSIS83A
MSIS86B	MSIS 86 with 3 hour a_p	Hedin, A. A., "MSIS-86 Thermospheric Model", J. Geophys. Res., Vol. 92, No. A5, pp. 4649-4662, 1987.
US66	U. S. Standard Atmosphere Supplements, 1966.	Environmental Science Services Administration, NASA, and USAF, 1966.
US76	U. S. Standard Atmosphere 1976	National Oceanic and Atmospheric Administration, NASA, and USAF, 1976.
USSR	USSR-COSMOS	Elyasberg, P. E., et. al., "Upper Atmospheric Density Determination from COSMOS Satellite Deceleration Results", Space Res., Vol. XII, pp. 727-731, 1972.

8.2.2 Migration to Sun Workstations

Access to the original data was possible only by running system conversion utilities on 'amber', a CDC UNIX machine located at the PL central cite. The utilities allowed the tape database to be read in as 32-bits IEEE standard data words. The process of getting the data off the tape consisted of three parts: issue a tape mount request for a specific "cc" tape number, run "ddcd" to read the data off the tape into an interim binary file on 'amber', and execute a special FORTRAN code bundled with the conversion utilities ("dcmigrate") to process the interim file for the final output.

The interim binary file created in the second step represents a byte-map of the CYBER formatted data files stored on the tape. To indicate this type of file in this report, a suffix ".conv" is added to its name. The intermediate file is actually the data written in original CYBER 60-bits machine word format but without the magnetic tape blocking/record structure as in the case for the magnetic tape. In the event that a magnetic tape is lost or destroyed, the original data is still available in this file as long as the 'amber' "ddcd" utility is available.

The final stage of the migration process creates two UNIX/IEEE versions of the original data files. One is the file, with the name-suffix ".org", maintains original data structure and all of its values. The other file, with the name-suffix ".bin", is rewritten with a new data structure format with most of the original values saved. All values within both of those files are written as 32-bit IEEE standard data words. For the original "packed" database on the CYBER, the information has been stored in the same fashion as the original except that the data have been unpacked and the second header specifying the offsets and word counts for unpacking purposes is no longer kept. The SETA-3 database, because of its immense size, has been broken up into its 150 constituent individual files. The statistics program has been modified to read in those individual files sequentially with the consequence that no loss of statistical binning capabilities will occur.

8.2.3 Exabyte Database Organization

The SUN Exabyte database occupies 16 Exabyte tapes:

A master archival storage set of two Exabyte tapes (5 GB each) which holds all of the satellite data. These tapes include the data originally stored on the magnetic tapes, data in an upgraded format, and data with new models added.

A working copy which occupies one tape for each of the 6 satellite groups similarly formatted as the master archival storage tapes.

A backup copy for each of the above tapes.

The master archival storage is the "bank-vault shelf" set that should be used sparingly, principally for emergency data retrieval. The working copy provides a more offline storage for files that are not

being processed. Any files needed would be read in on the workstations for processing, thereby freeing the hard disk space from long-term storage.

Before showing in detail how the database is organized, some simple explanation should be made to clarify the file names and the reasons for saving them. First, there are six satellite groups: SETA-1, SETA-2, SETA-3, AE/S3-1, S3-4, and S85-1. Save for S85-1, there were four "cc" tapes in the CYBER database associated with each satellite group. Each tape actually contained several files. SETA-3 had the most with 150 and SETA-1, the least with 1. Each file had one or two header records followed by data records with specific structure.

When files were pulled in from the CYBER magnetic tapes via the "ddcd" command, interim binary files were created, containing byte-maps of the datafiles as stored on the magnetic tapes. The decision was made to also save these files which represents the files as they are stored in the original CYBER binary format. By keeping these file, we can circumvent the need to keep the original magnetic tapes since the original information is preserved. As long as the "dcdd" and "dcmigrate" utilities are available on AMBER, these file can be read in without having to remount the magnetic tapes. These files are referred to as "tape(p)1.conv".

There are two different UNIX/IEEE versions of each CYBER magnetic tape: one with the original data structure (henceforth labeled with the suffix ".org") and the other redone in new data structure (suffixed with ".bin") as used by RADEX the past two years. The reason for saving the original structured file is that it still preserves all of the data and the layout of its CYBER counterpart but written in IEEE standard format. In case that "dcmigrate" procedures are no longer available, this is next closest thing to original data we have backed up. If the new format structure needs to be modified, the original formatted file with all of its original values can be read in without the use of "dcmigrate"-based codes on AMBER.

One tape from each satellite group contains values for new models (VSH quiet and storm models) along with values for the Jacchia 70, AND MSIS 90B, for convenient comparison.

To best describe the archival scheme, let us use a generic example. Let there be a satellite group with N "cc" tapes labeled CC0001, CC0002, ..., CC000N. Say that the first tape is the one with the new models. Then, the Exabyte will have the following tar files stored upon it:

1. For tape CC0001, there are two tar files as:
 - A) One for 'amber'-related original data from CYBER with three files:
 - 1) CC0001.tape(p)1.conv,
 - 2) CC0001.org, and
 - 3) CC0001.bin;
 - and B) One for NM0001_newmodel.bin (one single ".bin" with new models).
2. For tapes CC0002-CC000N, there will be one tar file as:
 - One for 'amber'-related original data from CYBER with three files:

- 1) CC000(2-N).tape(p)1.conv,
- 2) CC000(2-N).org, and
- 3) CC000(2-N).bin;

This will give us the grand total of $2 + 1*(N-1) = N + 1$ tar files.

By loading the maximum amount of data, one 5-GB Exabyte tape can hold SETA-3 database and another one 5-GB tape can hold the rest of the satellite data base. A backup copy of those two tapes give us four tapes. These four will serve as emergency master archival backup set for the density tapes. A pair of working copy tapes exists for each satellite so as to avoid using the emergency masters. This gives us 12 more tapes for the grand total of 16 tapes. This organization is summarized as follows:

FIRST MASTER TAPE ARCHIVAL FORMAT:

SETA-3_CC0361_ORIG/cc0361_tape(p)1.conv	150 MB
SETA-3_CC0361_ORIG/cc0361_org/cc0361_#(001-150).org	180 MB
SETA-3_CC0361_ORIG/cc0361_bin/cc0361_#(001-150).bin	300 MB
SETA-3_NM0361_NEWMODELS/nm0361_#(001-150).bin	770 MB
SETA-3_CC0416_ORIG/cc0416_tape(p)1.conv	150 MB
SETA-3_CC0416_ORIG/cc0416_org/cc0416_#(001-150).org	180 MB
SETA-3_CC0416_ORIG/cc0416_bin/cc0416_#(001-150).bin	300 MB
SETA-3_CC0444_ORIG/cc0444_tape(p)1.conv	150 MB
SETA-3_CC0444_ORIG/cc0444_org/cc0444_#(001-150).org	180 MB
SETA-3_CC0444_ORIG/cc0444_bin/cc0444_#(001-150).bin	300 MB
SETA-3_CC1907_ORIG/cc1907_tape(p)1.conv	150 MB
SETA-3_CC1907_ORIG/cc1907_org/cc1907_#(001-150).org	180 MB
SETA-3_CC1907_ORIG/cc1907_bin/cc1907_#(001-150).bin	300 MB
Total SETA-3 data storage for first master tape:	3.29 GB

SECOND MASTER TAPE ARCHIVAL FORMAT:

SETA-2_CC1371_ORIG/cc1371_tape(p)1.conv	23 MB
SETA-2_CC1371_ORIG/cc1371_org/cc1371.org	28 MB
SETA-2_CC1371_ORIG/cc1371_bin/cc1371.bin	45 MB
SETA-2_NM1371_NEWMODELS/nm1371.bin	120 MB

SETA-2_CC1381_ORIG/cc1381_tape(p)1.conv	25 MB
SETA-2_CC1381_ORIG/cc1381_org/cc1381.org	30 MB
SETA-2_CC1381_ORIG/cc1381_bin/cc1381.bin	47 MB

SETA-2_CC1444_ORIG/cc1444_tape(p)1.conv	26 MB
SETA-2_CC1444_ORIG/cc1444_org/cc1444.org	30 MB
SETA-2_CC1444_ORIG/cc1444_bin/cc1444.bin	51 MB

SETA-2_CC1449_ORIG/cc1449_tape(p)1.conv	26 MB
SETA-2_CC1449_ORIG/cc1449_org/cc1449.org	30 MB
SETA-2_CC1449_ORIG/cc1449_bin/cc1449.bin	51 MB

Total SETA-2 data storage for second master tape:	532 MB
---	--------

The rest of satellites data are formatted similarly and require approximately: 1.45 GB

Total for second master tape:	2 GB
-------------------------------	------

Note that this does not address the issue of the original CYBER master tapes (CC0179, CC1838, CC2375, CC1276, CC0318, and CC0123). They are stored two additional Exabyte tapes to augment the emergency master backup.

8.2.4 File Formats

Each tar file contains one or more files, each of which contains 1 or more “sections”. A section consists of a header record, one or more data records, and an end of section record. The records are in unformatted SUN(IEEE)-compatible binary. Each record begins with two 4-byte integers containing, respectively, the number of words in each group of the record, and the number of groups in the record. The header record always has only one group. A data record can have up to 12 groups, each of which pertains to one density measurement.

The header record contains $12 + 2n$ words, where n is the number of models. The first 5 words are actually strings of 10 characters. The first four of these contain satellite names that are in the database (usually only the first is non-blank, the exception being the AE/S3-1 database). The 5th character string contains the experiment name. The sixth word is a string of 20 characters containing the name of the CYBER tape from which the data originated. The next 6 words are 4-byte integers containing: the data of the data (YYDDD); the date of the database creation (YYDDD); the file ID; the altitude in km (meaningful only for the AE/S3-1 database, which is sorted by altitude); and the location, in each data group, of the satellite-experiment dependency data, as explained below, in the format $100 \cdot IG1 + IG2$, where $IG1$ is the first word, in a data group, of the subgroup containing these parameters, and $IG2$ is the first word after this subgroup. The header record is completed by one pair of words for each density model. The first is a 10-character string indicating the model name, and

the second is a 4-byte integer, in the form $100 \cdot M1 + M2$, where, where M1 and M2 are the first and last words of the model's subgroup within a data group, relative to the index IG2. The total size of the header group is thus $94 + 14 \cdot n$ bytes, where n is the number of models.

Each data record contains one or more groups, specified by the second word in the record. Each group contains 4-byte real numbers. The first 19 of these specify astrodynamical and space environmental parameters as follows:

- | | |
|--|----------------------------------|
| 1. Orbit Number (or -9999.0 if end of section) | 11. $3 \cdot Kp$ (6.7 hour lag) |
| 2. Date (YYDDD) | 12. a_p (3 hour value) |
| 3. UT (Seconds; 86400 = 1 day) | 13. F10.7 (Current daily value) |
| 4. Geographic Latitude (deg) | 14. F10.7 (1 day lag) |
| 5. Geographic Longitude (deg. east) | 15. F10.7 (81-day centered mean) |
| 6. Geographic local time (Hours) | 16. F10.7 (90-day centered mean) |
| 7. Geomagnetic Latitude (deg) | 17. Satellite X-velocity (m/sec) |
| 8. Geomagnetic Longitude (deg. east) | 18. Satellite Y velocity (m/sec) |
| 9. Geomagnetic local time (Hours) | 19. Satellite Z-velocity (m/sec) |
| 10. Altitude (km) | |

The last three quantities are in the earth-fixed, earth-centered coordinate system, x-axis pointing toward Greenwich, z axis toward the North geographic pole.

Table 14 shows the next group of parameters, satellite experiment-dependencies parameters, are meaningful for SETA-1 and AE/S3-1 only. These parameters begin in word IG1 of the data group:

TABLE 14. Satellite Experiment-dependencies Parameters		
Word #	SETA-1	AE/S3-1
IG1	X-Direction	Empirical Model Density
IG1+1	X Wind (m/sec)	Configuration
IG1+2	Y Wind (m/sec)	Satellite index (1-4)
IG1+3	Z wind (m/sec)	Invariant latitude (deg)

For AE/S3-1, the configuration is in the form $UP+2 \cdot DAY+4 \cdot SPUN$, where $UP=1$ if the satellite is in the upleg of its orbit or 0 if in the downleg, $DAY=1$ if the local time on in the dayside, 0 if at night, and $SPUN=1$ for spinning mode, 0 for dspun mode. The satellite index identifies the satellite in accordance with the order in which the names are given in the header, i. e., 1 identifies the first satellite in the header, etc.

Word IG2 gives the measured density (g/cc). This is followed for each model by either 1 or 7 values, determined by the value of m2-m1 for that model, supplied in the header (see above). Word IG2+m1 gives the ratio of the measured to model density for that model. If m2-m1 > 0, this is followed by six values for the wind: the first 3 are the zonal, meridional, and vertical components of the wind, in m/sec, and the last 3 are the x, y, and z Earth-fixed, Earth-centered Cartesian components in m/sec.

The end of section record, as can be seen from the above description, is just a single group data record, with the orbit number equal to -9999.0.

8.3 REENTRY BY DRAG VS REENTRY BY RETROBURN

The usual procedure for effecting the re-entry of a space vehicle is to decelerate the vehicle by firing a retro-burn (a rocket thrust in the negative velocity direction). It is conceivable that a cost savings, relative to this conventional approach, might be realized by deploying a balloon to increase the effective area to mass ration, thereby allowing the increased atmospheric drag to slow down the vehicle. This would decrease the fuel requirements, at a cost associated with continuing tracking of the vehicle over the additional time the vehicle remains in orbit until sufficiently slowed down by the drag. To assist in evaluation of this trade-off we performed a few computations relevant to this issue.

8.3.1 Retrofire Fuel Consumption

The thrust can be related to the rate of fuel expenditure by:

$$F = m \frac{dv}{dt} = I_{sp} g \frac{dm}{dt} \quad (87)$$

where I_{sp} is the specific impulse in sec, g is the acceleration of gravity, and dm/dt is the rate of mass expenditure. This yields the solution [Fleeter 1995, p. 14, "The Rocket Equation"]:

$$\Delta v = g I_{sp} \Delta \ln m \quad (88)$$

Then, for initial mass m_0 , and final (reentry) mass m_r , we find for the mass consumed:

$$\Delta m = m_0 - m_r = m_0 [1 - \exp(-\frac{\Delta v}{g I_{sp}})] \quad (89)$$

with $\Delta v = v_0 - v_r$. If we expand the exponential through first order, we get:

$$\Delta m = m_0 \frac{\Delta v}{g I_{sp}} \quad (90)$$

To calculate Δv , we note that the initial velocity, for a circular orbit of radius a_0 , is $\sqrt{\mu/a_0}$, where μ is the earth's gravity constant. After the burn, the velocity is obtained from the after-burn kinetic energy, which is the difference between the new total energy and the original potential energy, which hasn't been changed by the burn. The new total energy is $-\mu/(2a_r)$, where a_r is the target semimajor axis, while the potential energy remains $-\mu/a_0$. Thus:

$$\frac{1}{2} v_r^2 = -\frac{\mu}{2a_r} + \frac{\mu}{a_0} \quad (91)$$

solving this for the reentry velocity v_r , we find:

$$\Delta v = \sqrt{\frac{\mu}{a_0}} - \sqrt{\frac{2\mu}{a_0} - \frac{\mu}{a_r}} \quad (92)$$

Achievement of elliptical orbit from circular orbit

If the thruster is fired in the negative velocity direction on a vehicle in a circular orbit of radius r_0 ($=a_0$), the satellite will fall into an elliptical orbit with apogee at the burn point and perigee radius $r_p < r_0$. The semi-major axis a_r is then $(r_0 + r_p)/2$, and by substitution we obtain

$$\Delta v = \sqrt{\frac{\mu}{r_0}} - \sqrt{\frac{2\mu r_p}{r_0(r_0 + r_p)}} \quad (93)$$

where μ is the earth's gravitational constant, g is the acceleration of gravity at the surface of the earth, r_0 is the radius of the initial orbit and r_p is the distance of the perigee of the final orbit from the center of the earth.

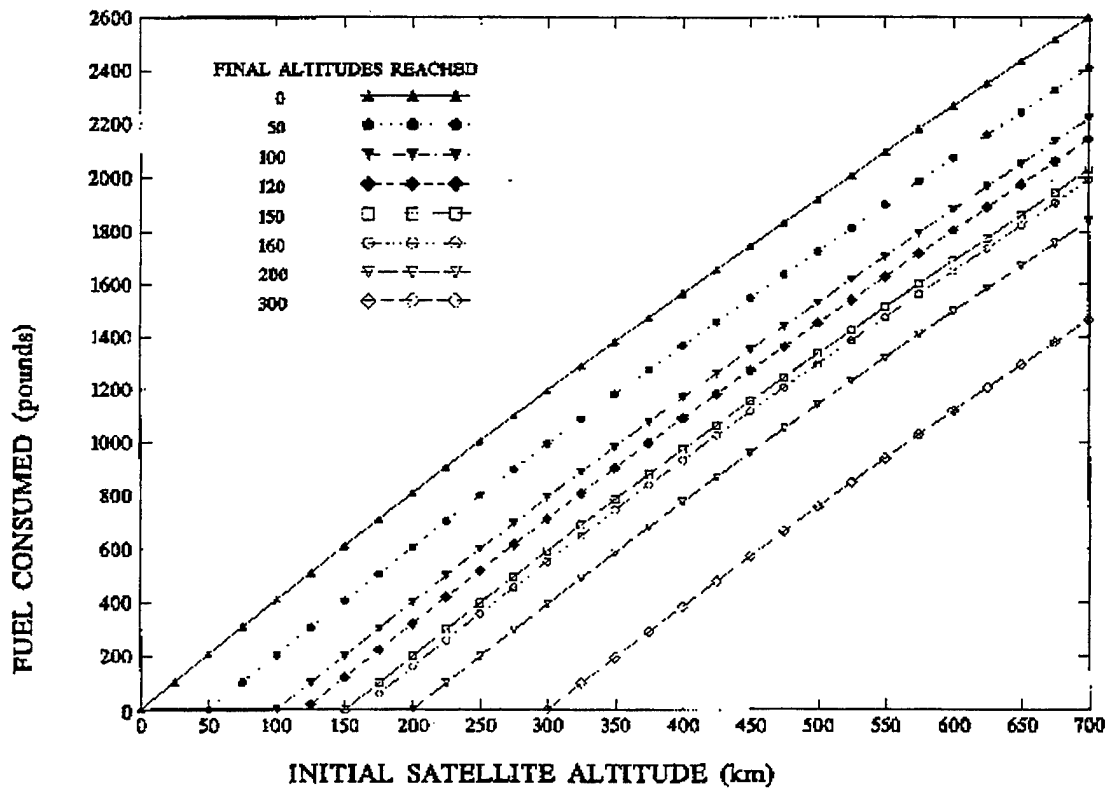
Table 15 shows Δv and Δm required to de-orbit from a circular orbit 300 km in altitude ($r = 6378.14 + h$) to elliptical orbits with perigee at 0 and 120 km. altitude, for an initial mass of 40000 pounds and specific impulse 300 sec. Figure 72 plots the fuel consumed to attain various perigee altitudes as functions of the initial circular altitude.

TABLE 15. Fuel Consumed and Δv Required from an Initial Circular Orbit at 300 km		
Initial mass = 40000 pounds Specific impulse = 300 sec		
Final perigee height (km)	Δv (m/sec)	Δm (pounds)
0	89.3	1196
120	53.0	713

FUEL CONSUMED (POUNDS) TO ACHIEVE A REQUIRED PERIGEE HEIGHT

INITIAL MASS = 40000 POUNDS ; $I_{sp} = 300$ SEC

NOTE: ZERO-ATMOSPHERE DENSITY SPHERICAL EARTH MODEL



06/24/96

Figure 72. Fuel requirement (pounds) to a specified perigee height from a circular orbit as a function of its altitude.

Achievement of new circular orbit

Previously we computed the fuel consumed in one retrofire burn to transfer from a circular orbit to an elliptical orbit whose apogee touches the circular orbit and whose perigee lies inside. A transfer from a circular orbit to a new circular orbit, inside the original, may be done with two burns:

- 1) Transfer from the outer circular orbit to the elliptical orbit whose perigee distance is equal to the radius of the desired inner circular orbit.
- 2) At perigee of the elliptical orbit, transfer to the inner circular orbit.

Let r_a and r_p be the radii of the two circles. These are also, respectively, the apogee and perigee distances in the elliptical orbit. Then, for the circular orbits the velocities are $[\mu/r_p]^{1/2}$ and $[\mu/r_a]^{1/2}$, while the velocities in the ellipse at apogee and perigee are given by:

$$\begin{aligned} v_a &= \sqrt{\frac{2\mu r_p}{r_a(r_a + r_p)}} \\ v_p &= \sqrt{\frac{2\mu r_a}{r_p(r_a + r_p)}} \end{aligned} \quad (94)$$

These equations allow us to determine the Δv of each burn. The fuel consumed in each burn is given by substituting this for Δv in Eq. (89).

The vehicle energy/mass ratio decrease in each burn is $v^2/2 - (v - \Delta v)^2/2$. Table 16 gives the appropriate quantities for a transfer from a 300 km altitude circular orbit (radius = 6378.14 km + 300 km) to a circular orbit at 120 km altitude. The Δv are in m/sec, the energy/mass loss is in MJ/pound, and the fuel consumed is in pounds.

TABLE 16. Transfer between Circular Orbits			
	Δv	$\Delta E/m$	Δm
Burn 1 (300 X 300 to 120 X 300)	53.0	0.900	713.5
Burn 2 (120 x 300 to 120 x 120)	53.3	0.924	705.5
Total	106.3	1.824	1419.0

The fuel consumed to transfer from a 300 x 300 orbit to a 0 x 300 orbit in one burn is only 1196 pounds, which is less than the total fuel consumed, 1419 pounds, in the two burns required to transfer from the 300 x 300 orbit to the 120 x 120. The total energy/mass loss agrees with what one obtains for the energy/mass difference for the two orbits, $\mu/(2 r_p) - \mu/(2 r_a)$.

Deceleration from apogee of an elliptical orbit

The velocity at apogee in an orbit (either the initial or the final orbit) is:

$$v_a = \sqrt{\frac{2\mu r_p}{r_a(r_a + r_p)}} \quad (95)$$

where μ is the earth's gravitational constant, g is the acceleration of gravity at the surface of the earth, r_a is the apogee distance and r_p is the perigee distance, both measured from the center of the earth. From Eq. (95) we may obtain Δv , and apply it to the mass consumption Eq. (89), as before. Table 17 tabulates the fuel (pounds) required for various transfers, for a vehicle of total mass 40000 pounds, with thruster of specific impulse 300 sec. The orbits are specified by altitude of perigee and apogee (km), and it is assumed that distance = altitude + 6378.14 km.

TABLE 17. Fuel Consumed (Pounds) in Orbit Transfer		
	Final Perigee Altitude (km)	
	0	50
Initial Orbit		
150 x 150	614	409
200 x 200	812	607
300 x 300	1196	994
500 x 500	1923	1727
700 x 700	2601	2410
150 x 200	613	408
150 x 300	611	406
150 x 500	606	403
150 x 700	601	400

8.4 DRAG-INDUCED ORBITAL LIFETIME STUDIES

For a near-Earth satellite experiencing atmospheric drag, a method of determining its orbital lifetime and assessing possible impact sites is strongly desired. Unfortunately, any orbit propagator is limited in accuracy largely to the density profile used in the drag component of the force model. In reality, there are density variations in the atmosphere due to the solar-terrestrial environmental effects. As such, any static earth atmosphere model such as the US 76 Standard Reference Atmosphere (US76) [NOAA, *et. al.*, 1976] obviously does not account for the dynamic behavior of the thermosphere caused by heating attributed to solar and geomagnetic sources. Even in cases of dynamic empirical density models such as Jacchia 70 and MSISE 90, the use of proxy indices to approximate the variability of the related components is not sufficiently adequate for providing a precise fix on the orbital lifetime, much less the impact site. This accuracy problem arises from the fact that unmodelled variations of the density profile will result in the actual orbital track to deviate from that of the projected trajectory for a satellite. If the long-term computed satellite motion is not corrected with frequent updates, the tracking errors between the observed and expected satellite positions will increase rapidly even for a short period of time.

Even if the neutral density variations are better modeled, the orbit propagator must also correct for effects of the thermospheric winds. A satellite resisting the winds will clearly experience a greater drag than if it is tracking the winds. Since the winds are variable in speed and direction, their effects on the satellite motion will also increase the uncertainties of the projected trajectory. In addition to winds, other effects such as gravity waves propagating from the lower atmosphere needs to be taken into account. At altitudes greater than 900 km, orbital perturbations are dominated by the effects of the luni-solar gravity forces and radiation pressure, but high-altitude satellites have not been considered. The scope of the investigation have been limited to lifetime studies of low-altitude satellites influenced by drag as being the principle perturbative effect on their orbital motion. Being preliminary, these lifetime studies have not incorporated the wind and gravity waves effects, and modeling of those effects have been postponed for later work.

The drag-induced orbital lifetime studies as such are also largely dependent on use of the satellite ballistic coefficient

$$B = C_d \frac{A}{m} \quad (96)$$

where C_d is the coefficient of drag, m is the satellite mass, and A is the cross-sectional area normal to the direction of the motion of the satellite. B is used in the expression for deceleration due to atmospheric drag,

$$\frac{d^2 \vec{r}}{dt^2} = -\frac{1}{2} B \rho(\vec{r}) V_d \vec{V}_d \quad (97)$$

where ρ is the total neutral mass density of the atmosphere and the velocity vector

$$\vec{V}_d = \vec{V} - (\omega_e \hat{z} \times \vec{r}) \quad (98)$$

is actually the satellite velocity relative to the rotating earth atmosphere with ω_e being the angular rotation of the earth. The expression for the velocity vector does not account for the presence of winds; a more exact definition and explanation exists elsewhere [Escobal, 1976].

Sources of the errors within the drag term are both the density model and B . As discussed above, the density profile variations imperfectly modeled would impose a certain amount of uncertainty upon any predicted orbital motions. Even more so would be the error bars associated with forecasting solar-terrestrial environment conditions in terms of probable proxy indices necessary for inputs to the density model. The uncertainties associated with B are also non-trivial. If the cross-sectional area varies (i.e., payload tumbling) or the mass changes (i.e., fuel being burned), the lifetime prediction is also limited to whether these effects are known to occur or how well they would be modeled. Worst yet, if the satellite B is an unknown quantity, the ability to perform lifetime predictions become even more tenuous since one must first derive a baseline value from performing a least-square fit over most if not all of the observed positions. The B value based on using the empirical data would be subjected to the errors in both the tracking data and the fitting processing.

These concerns lead to the realization that one would need to quantify the range of credible predicted decay lifetimes with a method which allow for continuously series of updates to the orbit propagator with most recent data in order to narrow down the errors. Reduction in errors can best be accomplished with the most suitable choice of a density model available and the corresponding rigorous iterative refinement of the baseline value for the ballistic coefficient. Because the variations in the drag term are time-dependent, the satellite motion must be computed from an orbit integration process. Whatever density model is used, the computational overhead must be ideally minimal since the integrator must perform multiple-sampling of the density profile about the local spatial coordinates within an optimal time step in order to derive the predicted trajectory.

The investigation into the topic of satellite orbital lifetime as affected by atmospheric drag have used both Jacchia 70E and MSISE 90 as primary choices for the dynamic neutral density models. The rationale have been that a dynamic neutral density model that exhibited modeled spatial and temporal variations would definitely provide a more realistic baseline profile in comparison to the static models. The advantages of static models are evident only in their minimal computational overhead in comparison to the dynamic models and may at best provide an order of magnitude check. The investigation also have been restricted to low-altitude satellite, particularly as being a passive vehicle, i.e., not capable of or performing maneuvers. If the spacecraft does tumble, the expectations have been that the rate of change to the area would be periodic and rapid enough that the effects would actually average out to a secular trend between successive observational data points.

One objection to the use of Jacchia 70 model for orbital lifetime studies was that the original version could only provide density values at the altitude of 90 km and higher [Lou, *et al.*, 1973]. To compensate, Radex had developed a companion low-altitude version, Jacchia 70E, where “E” signifying “extended”. Essentially, this version was Jacchia 70 model with an add-on algorithm that does density calculations from 90 km down to ground. This extension was accomplished by doing least-square fitting of the MSISE 90 density values with respect to the seasonal-latitudinal variations. Details of the MSISE 90 will not be given here save that it was a more commonly used dynamic model available that also provided density calculations down to the ground.

The key software component used for these lifetime studies have been ASAP, an orbit integration software package developed and distributed by the Jet Propulsion Laboratory (JPL) [Kwok, 1987]. This software package applies the Cowell’s method in the numerical integration of equations of motion using an 8th order Runge-Kutta integrator. ASAP also allows for perturbative effects such as non-central equipotential gravity field (up to order of 40X40), drag due to solar radiation pressure and atmospheric density, and luni-solar effects. The original program can either use the user-defined exponential density model or the US76. The standard issue code has been upgraded by Radex to also use the aforementioned dynamic density models, to read in the proxy indices as model inputs for solar and geomagnetic heating components of the thermosphere, and to convert the NORAD two-line element sets into Cartesian state vectors suitable for ASAP integration routines. The proxy indices to be used are the 3-hour planetary geomagnetic a_p and the 10.7 cm solar radio flux $F_{10.7}$ required by the models. SGP4-based routines have been incorporated into ASAP to enable the conversion of the NORAD element sets to Cartesian vectors [Hoots, *et al.*, 1980]. Additional features also have been added to assist the users in running the code, but they will not be discussed here save for specific points of clarity.

The studies conducted under this contract have primarily focused on four major stages in determining orbital lifetimes: calibrating the integrator, forecasting possible solar-terrestrial conditions, deriving a baseline ballistic coefficient, and obtaining a suitable range of dates of impact as determined by use of an array of possible density profile variations and a specific B value. The methodology to be described have been applied to real-case investigations to address specific questions related to orbital lifetimes.

8.4.1 Single-Satellite Case Study

The initial study of determining orbital lifetime predictions was motivated by an actual event in late 1995. A large Chinese military payload named FSW-1, which was launched in October of 1993 and assigned the international catalog ID 22870, failed to execute a return-to-Earth upon a ground command. Instead, the payload remained in space and began to eventually decay in orbit. Because it was nearly two-ton and was designed to survive re-entry for returning data after performing spaceborne surveillance, there were concerns as to when and where the satellite would likely impact. Radex was not tasked to provide any operational services for actually predicting the satellite lifetime; rather, the intent of the study was to validate the use of selected dynamic density models with an

orbit integrator for satellite lifetime determination. FSW-1 would provide a real-world scenario for the orbital simulations to be performed as a validation test.

With FSW-1 serving as a candidate satellite for the lifetime study, a methodology had to be proposed and developed in several stages. One stage required that the integrator would be calibrated to provide minimal tracking variances with respect to the order of the gravity equipotential model, time stepsize, and other runtime and modeled parameters. Another stage necessitated forecasting the solar-terrestrial proxy indices that must be reasonable for the time period of interest. The final stage involved finding the effective ballistic coefficient that satisfies the fitting criteria of the as-flown element sets. Once the integrator was calibrated and forecasted proxy indices were available, the simulated predictions for dates of impact were performed.

One of the steps in the calibration stage was to do a series of runs with the same initial conditions and a steady-state solar model (fixed a_p , solar radio flux) but with different orders of geopotential field. The studies were done for a fixed ballistic coefficient; the B value was then incremented and the runs were repeated. The intent then was to find the lowest order of geopotential desired that would minimize the change in the "predicted" crash dates due to changing the order of the gravity model but not impact upon the execution of the code by introducing undesired excess computational overhead in processing the higher-order geopotential terms. From extensive test runs, it was determined that a 8X8 satisfy these overlapping requirements for all range of ballistic coefficients.

Another step in calibration was the sensitivity study on impact dates with respect to the selection of the stepsize in the Artificial Satellite Analysis Program (ASAP). If large stepsize were used, the code would run quickly but it would have appeared not to pick up the short-term variations within the density profile. This was evident by the significant differences with the impact dates when the stepsize were changed from hours to fraction of minutes. If short stepsize were used, the code would take a considerably longer time to run. However, several minutes were found to satisfy the minimum execution time that also allowed for the density variations to be accounted for such that the difference in projected positions did not significantly change for the satellite in nominal orbits (orbits that do not precede immediately the reentry phase). However, the stepsize issue became more critical as the modeled satellite moved along its last few orbits. Because the density changes rapidly as the perigee height decreases and the orbit changes rapidly as drag increases, smaller step sizes were necessary to minimize the integration errors at the end of the deorbiting phase. This resulted in requiring one stepsize for nominal orbits and another for decaying portion of the satellite lifetime.

Clearly, the solution to the use of the desired time stepsizes was to develop a two-level algorithm where the integration processing for the nominal orbits was controlled by the initial user-input stepsize, but the deorbiting portion of the satellite lifetime was guided by an internal small-value stepsize. The automatic switchover to the smaller timestep was to occur upon detection of conditions leading to imminent reentry. The criteria for detecting the deorbiting phase of the satellite was based on both the perigee height dropping below a certain altitude and the orbit becoming circularized, i.e., its mean eccentricity approaches a near-zero value. The drawback encountered in implementing and testing the logic was that the detection must be made prior to the final orbit. As

it turned out, when the satellite was making its final orbit, the eccentricity and the perigee height became no longer physically meaningful. This was the result of one trying to fit an ellipse to the terminating leg of the actual spacecraft trajectory. The necessary fix was to switch to the smaller time steps at a slightly higher perigee height and check for a minimum-valued eccentricity; this fix usually increased the execution time at the end of the run because it spanned several of the last orbits instead of just at the reentry phase. The advantage gained was that the switchover does get invoked properly.

Other steps undertaken in the calibration stage involved settling minor issues and coding enhancements; these were not of major interest to this report. The end result was that the calibration stage enabled ASAP to execute with minimal computational overhead yet able to process sufficiently detailed physical models. That is, the execution parameters were chosen such that the dates of impact will not change significantly until the physical modeling criteria were substantially upgraded or the runtime tolerances were considerably tightened.

In illustrating effects of calibrating the integrator, Table 18 depicts a range of crash dates from a sample series of runs based on various fixed parameters of interest. The ASAP runs shown have used the 8X8 geopotential gravity field coupled with Jacchia 70E density model. As density model inputs, a range of fixed proxy indices were used. Each cell in the table contains two values; the first number gives the number of days relative to midnight of 96070, the second, number of orbits relative to 11800 revolutions. The date of 96070 is selected from the approximate deadline estimated by the midrange values in the majority of these runs. The reference orbit number is a roundoff value based on the sum of the initial mean motion times the relative number of days to the target date plus the initial orbit number in the element set. The tables list the dates of impact based on the initial conditions defined by the NORAD two-line element set whose epoch date was 96044 (13 Feb 1996) and are sorted by particular ballistic coefficient.

The next phase was forecasting the solar-terrestrial environment conditions. This involved creating a database of proxy indices to be used for forecasting density profile model variations. Since the sun was entering its solar minimum portion of the solar cycle in late 1995 to early 1996, it was initially decided that the forecasted values would be based on similarly-behaved values extracted from records of an earlier solar minimum. This was accomplished by selecting and comparing monthly-averaged $F_{10.7}$ trend of various solar minimums to the then known most recent values associated with the actual date. The most likely candidate was selected by using the values starting in June 1950 to be made coincidental with late Fall of 1995. The monthly solar flux values for early 1996 was expected to be at minimum 75 solar flux units (sfu) based on the older historical records.

TABLE 18. A Sample Set of Crash Dates and Final Orbits for Various Ballistic Coefficients

SATELLITE NAME: FSW-1	DENSITY MODEL: JACCHIA 70E		GRAVITY MODEL: 8 X 8	EPOCH OF INITIAL ELEMENTS: 96044.24410732
CRASH DATES RELATIVE TO TARGET DATE OF 96070 AND FINAL ORBIT NUMBERS RELATIVE TO REFERENCE ORBIT #11800 FOR CdA/m = .005m ² /kg				
$F_{10.7} = \underline{F_{10.7}}$	Ap = 0 (Kp = 0)		Ap = 7 (Kp = 2)	Ap = 27 (Kp = 4)
85	9.47 135		6.94 95	4.33 53
95	7.49 103		5.34 69	3.10 34
105	5.81 77		3.98 48	2.03 17

SATELLITE NAME: FSW-1	DENSITY MODEL: JACCHIA 70E		GRAVITY MODEL: 8 X 8	EPOCH OF INITIAL ELEMENTS: 96044.24410732
CRASH DATES RELATIVE TO TARGET DATE OF 96070 AND FINAL ORBIT NUMBERS RELATIVE TO REFERENCE ORBIT #11800 FOR CdA/m = .006m ² /kg				
$F_{10.7} = \underline{F_{10.7}}$	Ap = 0 (Kp = 0)		Ap = 7 (Kp = 2)	Ap = 27 (Kp = 4)
85	2.94 31		.93 -1	-1.14 -34
95	1.36 6		-.35 -21	-2.13 -49
105	.02 -15		-1.44 -38	-3.00 -63

SATELLITE NAME: FSW-1	DENSITY MODEL: JACCHIA 70E		GRAVITY MODEL: 8 X 8	EPOCH OF INITIAL ELEMENTS: 96044.24410732
CRASH DATES RELATIVE TO TARGET DATE OF 96070 AND FINAL ORBIT NUMBERS RELATIVE TO REFERENCE ORBIT #11800 FOR CdA/m = .007m ² /kg				
$F_{10.7} = \underline{E_{10.7}}$	Ap = 0 (Kp = 0)		Ap = 7 (Kp = 2)	Ap = 27 (Kp = 4)
85	-1.62 -41		-3.26 -67	-4.97 -94
95	-2.90 -61		-4.31 -84	-5.79 -107
105	-4.01 -79		-5.21 -98	-6.50 -118

Because the then-current daily solar flux values were judged to be more dynamic and frequent in their occurrences than their older counterpart in the historical database as was evident in the downturn portion of the latter part of 1995, the sliding 81-days centered mean flux value for the older solar minimum database was added 10 more sfu in an attempt to account for their effects. To minimize daily variations in fitting the ballistic coefficient to observed positions, the forecasted fluxes and geomagnetic indices were set to constant levels that best represent the probable baseline averaged solar-terrestrial conditions. To that end, the studies were conducted using both the daily and smoothed fluxes at 85 sfu; the 3-hr A_p at 7.

With a calibrated integrator and forecasted proxy indices available, the next phase of the study was critical: determining a baseline ballistic coefficient for the candidate satellite. Because exact details were not readily available about the shape, size, and mass of the test satellite, an empirical approach was needed. This requirement was fulfilled by a methodology that has been used in another orbit propagator package, Rapid Orbit Prediction Program (ROPP) designed for satellite experiencing drag-induced perturbations [Bass, *et. al.*, 1976]. Essentially, the technique was to use a trial B value in propagating the satellite from a known position to another known position several days later, keeping track of the relative number of revolutions the satellite has made and adjusting the B value to minimize the differences between the observed and expected number of orbits elapsed.

This test-tested approach was feasible since the standard NORAD element sets contain orbit numbers as part of its product. An enhanced version of the above methodology was developed and implemented into the ASAP code as an option for performing an iterative determination of B. Briefly, the process began with an user-defined trial B value and two similar values that were offset by a small amount. These values were then used for seeding multiple ASAP runs. A polynomial fit of the resulting orbit number errors versus the test B values was solved in a closed form to generate a new B value, which was to serve as the basis for the next iteration. Once the orbit number error was minimized, the final stage of the B determination process involved fine-tuning the value to minimize the intrack error. A pair of NORAD element sets, about ten to fourteen days apart, were used to provide end points for the integrated trajectory. Once the best possible B value was selected, the lifetime projection was then computed for the satellite using the first element set as its initial state vector. To update the baseline B value, a new pair of NORAD element sets were obtained for another round of iteration processing by ASAP.

Figure 73 shows a plot depicting the ballistic coefficients based on the various pairs of element sets as the investigation progressed. The bracketed line represents the given B value used in interpolating from the element set time-tagged at the beginning of the segment to the element set at end of the segment. The overall trend shows that the effective empirical B value swept through a minimum value, reached a secondary maximum, and was decreasing when the satellite actually deorbited on 12 March 1996 at 4:05 UT. Figure 74 shows the result of repeating for the same pairs of element sets used in the B determination cases, the density profile based on the actual proxy indices as provided by NOAA. There is a remarkable similarity between the trend of the values based on the runs using the forecasted baseline proxy indices and the trend of the values based on the runs using the actual proxy indices. The secular variation in the B values have been attributed to either the

density model deficiency with respect to the semiannual variation or the change of the satellite attitude. The differences between the two trends have been accredited to the disagreement between the forecasted and actual proxy indices.

With respect to the prediction of satellite lifetime as compared to the actual date of impact, the earliest recorded successful prediction was made within early February. The stability of the predicted date of impact being less than a day, and the difference between expected and actual date of impact being a day or less have given credence to the use of a dynamic density model within an integrator as being feasible for simulating and diagnosing orbital lifetimes for drag-induced decays.

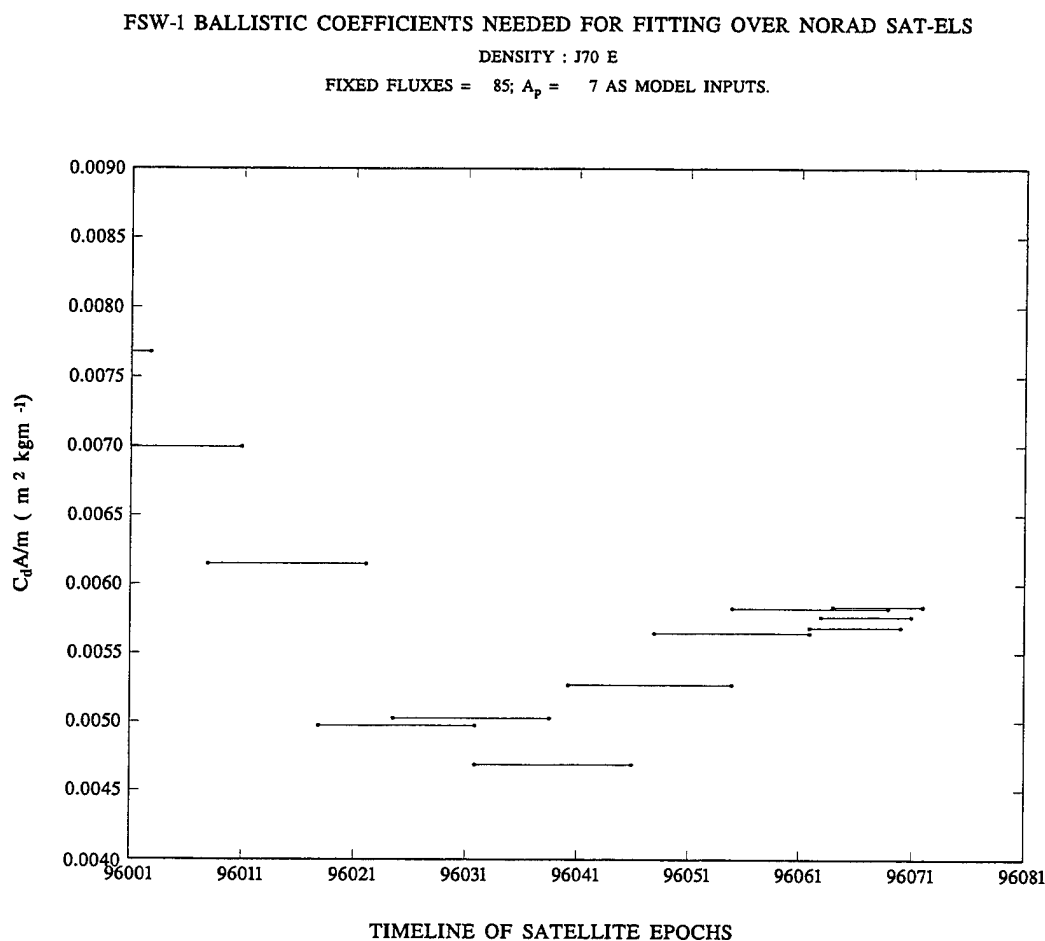


Figure 73. FSW-1 ballistic coefficients derived from fitting over pairs of NORAD element sets with the Jacchia 70E density model using fixed solar fluxes of 85, geomagnetic indices of 7.

FSW-1 BALLISTIC COEFFICIENTS NEEDED FOR FITTING OVER NORAD SAT-ELS

DENSITY : J70 E

ACTUAL FLUXES AND A_p INDICES USED.

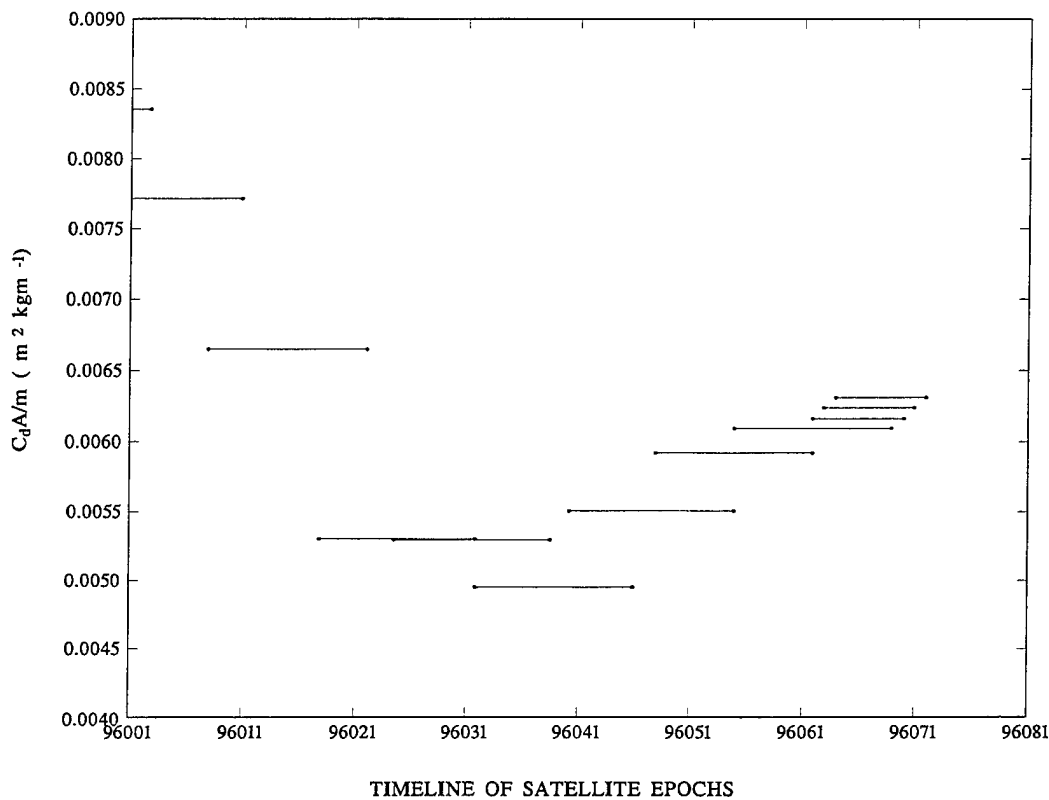


Figure 74. FSW-1 ballistic coefficients derived from fitting over pairs of NORAD element sets with the Jacchia 70E density model using actual solar fluxes and geomagnetic indices.

8.4.2 Controlled Drag-Induced Reentry Study

With the aforementioned tool for determining orbital lifetime, Radex was able to undertake the following study which was of great interest to the planners of a satellite program. The theme was that a spacecraft of a particular size and mass would be carrying a mounted balloon; upon deployment, the balloon would have effectively increased the surface area of the satellite, thereby also increasing the drag force on the vehicle. The goal of the study was to ascertain whether the increased drag generated by the inflated balloon would be a feasible alternative to using thrusters for initialing an earlier reentry. The attractive feature in successfully implementing the balloon-based method would be the saving in reduction of mass. The saving in mass would come from the satellite not carrying as much fuel in comparison to the mass of a hybrid system consisting of a balloon plus, perhaps, a minor thrusting apparatus. The benefit in reducing the fuel load would either translate to not having to launch with as much fuel onboard in favor of a lighter vehicle at lower cost. The planner might even have the option to increase the payload mass in compensation.

For these studies, it was assumed that the satellite would not have any capability for fuel-assisted maneuvers; all deorbital perturbations will be limited to the drag-induced effects. The studies will compute for a satellite of known ballistic coefficient, the relative lifetime span as a function of initial eccentricity, perigee height, and inclination. The computations were to be repeated for the same orbital conditions but with a substantial increase in the B value to simulate a deployed balloon. That is, the differences between the lifetime span for satellite with the balloon deployed and the lifetime span for the satellite experiencing nominal orbital decay have been characterized by types of orbit being considered.

One of the outstanding issues in lifetime span characterization was whether there are scaling of decay times for results based on the integrator using a dynamic model as opposed to the results based on the static model case. From previous experiences, it had been found for the use of static models in the integrator, the corresponding lifetime spans do scale to the ballistic coefficient. That is, a satellite of a particular B value would have decayed from orbit within a set number of days whereas a satellite whose ballistic coefficient is kB would have decayed within $(1/k)$ -th of the original timespan. Subsequent evaluations of results from cases involving dynamic models have established that this scaling law hold true only for short-term decay lifetimes or for cases of small density variations due to conditions of low-flux, low-geomagnetic activity. The scaling had clearly failed for situations where a satellite experienced density variations due to highly variable solar-terrestrial conditions or satellite remained in orbit for several months where seasonal effects manifest themselves by modulating the secular trend within the density profile to offset the dates of impact.

Table 19 shows some representative results from the scaling investigation. The two models used for comparison were Jacchia 70E and US76. The ballistic coefficients were selected such that the initial satellites would have remained in orbits for more than 5 months. To minimize the solar-terrestrial variations within Jacchia 70E runs, a low solar flux of 70 sfu was used. The comparison was to be restricted to cases where the spatial and temporal variations were independent of the solar-terrestrial conditions only; the results demonstrated the consequences of increasing the B values. As seen in the table, the US76 model have shown the scaling rule to be true for all values of k whereas the long-term orbit for Jacchia 70E failed the scaling test. The basic conclusion was that the scaling rule being applied to the dynamic models served only to approximate the lifetime span for long-term missions relative to the scaled multiple of the lifetime of the satellite that decayed much more rapidly with a higher B value.

TABLE 19a. Summary of the Decay Times for J70E Runs for a Satellite whose $C_d A/m = 0.005 \text{m}^2/\text{kg}$, and is set at an initial altitude of 300km. The decay times are relative to day 81 of 1996 and $F_{10.7} = 70$						
$k \times C_d A/m$	$i = 50^\circ$			$i = 83^\circ$		
	Δday	Δhours	ratio*	Δday	Δhours	ratio*
1	189	16.016 (189.667)	55.52	209	9.620 (209.401)	55.87
5	34	0.250 (34.010)	9.96	38	10.434 (38.435)	10.25
10	17	2.363 (17.098)	5.01	18	18.732 (18.781)	5.01
50	3	9.978 (3.416)	1.00	3	17.959 (3.748)	1.00
* ratio to $k = 50$ case for respective inclination investigation.						
TABLE 19b. Summary of the decay times for US76, $C_d A/m = 0.002 \text{m}^2/\text{kg}$ is used to get the same order of decay as for the $k=1$, J70E run.						
$k \times C_d A/m$	$i = 50^\circ$			$i = 83^\circ$		
	Δday	Δhours	ratio	Δday	Δhours	ratio
1	252	4.608 (252.192)	49.80	273	9.793 (273.408)	49.83
5	50	10.842 (50.452)	9.96	54	16.690 (54.695)	9.97
10	25	5.658 (25.236)	4.98	27	8.561 (27.357)	4.99
50	5	1.543 (5.064)	1.00	5	11.696 (5.487)	1.00

Given the abundance of the results generated from a considerable number of cases analyzed for this investigation, it is only best to present in Table 20 just a sample few of the runs to give a fair illustration of what was done. MSISE 90 was the density model of choice with fixed geomagnetic activity of 15 and both the daily and 81-days centered-average solar fluxes set to 165. The satellite was at 62 degree and the initial ascending node at noon local time. The initial date of the satellite timeline was for 96081 (96 Mar 21). For computing the ballistic coefficient, the value for C_d was 2.20. There were two different satellites being considered: one having an effective cross-sectional area of 330 sq. ft. with launch weight of 30,000 lb; the other was 430 sq. ft. and 40,000 lb. For the

case when the balloon was deployed, the increased effective cross-sectional area was 3300 sq. ft. Several types of orbits were presented; some were initially circular and others elliptic.

TABLE 20. Relative Orbital Lifetimes for Satellites With and Without Balloon Deployed According to MSISE90					
GEOPHYSICAL: $F_{10.7} = 165$ $A_p = 15$		INITIAL ORBIT: $i = 62^\circ$ $\Omega_0 = 0^\circ$		INITIAL TIMELINE: 96081 (96 Mar 21) 12:00 UT	
WEIGHT (lb)		40,000		30,000	
AREA (sq. ft)		430	3300	330	3300
BALLOON USED ?		no	yes	no	yes
INITIAL		Δ TIME DECAY		Δ TIME DECAY	
PERIGEE (km)	APOGEE (km)				
150	150	9.75 hr	1.8 hr	9.5 hr	1.5 hr
150	200	33 hr	5 hr	32 hr	4 hr
150	300	4.4 day	0.6 day	4.25 day	0.5 day
150	500	13.8 day	1.8 day	13.5 day	1.3 day
150	700	27 day	3.5 day	26.5 day	2.5 day
200	200	4.4 day	0.6 day	4.2 day	0.5 day
300	300	72 day	9 day	69 day	6.5 day
300	500			330 day	30 day

8.5 SPACECOM ORBIT DETERMINATION SUPPORT

Errors in neutral thermospheric density and wind modeling continue to limit satellite orbit determination accuracy. At least part of the cause of this problem is the inability to accurately specify in sufficient detail the energy and momentum inputs received by the thermosphere. Instead these are represented in the models by proxy indices: the 10.7 cm solar flux for the solar EUV input, and the geomagnetic activity index K_p for geomagnetic sources. In a recent SBIR study, showed that updating the density model in near real time has great potential for reducing the density and satellite tracking error. Although it may ultimately be possible to use a variety of other sources,

including in-situ measurements such as those discussed earlier in this section, the SBIR focussed on the use of tracking data of selected "star satellites" to estimate the current density. In the current contract, we briefly reviewed that work, deriving new information from the results.

8.5.1 Extension of SBIR Work

The SBIR focussed on the available tracking data from four satellites that had been studied earlier by *Snow and Liu* [1991]. These are listed in Table 21.

TABLE 21. Satellites in the Snow-Liu Study						
SCC no.	Int'l Desig	Common Name	Orbital Elements at beginning of data			
			Perigee Ht	Eccent	Inclin	Mean-mot
11703	80-14A	Solar Maximum Mission (SMM)	480 km	0.0008	28.5 deg	15.29 rev/day
12887	81-100A	Solar Mesospheric Explorer (SME)	500 km	0.0013	97.9 deg	15.22 rev/day
13138	82-33A	Salyut 7	470 km	0.0009	51.6 deg	15.33 rev/day
14898	84-34B	Long Duration Exper. Facil. (LDEF)	465 km	0.0003	28.5 deg	15.34 rev/day

Snow and Liu determined the trajectories of the four satellites, over an 18-month period, 1988 day 180 - 1989 day 365, by least-squares fits to a model which included a low-order geopotential and a drag force which used a density model and a ballistic coefficient. The parameters adjusted in the least squares process were the elements at epoch and the ballistic coefficient. Certain common trends were noted in the time behavior of the ballistic coefficients among the four satellites, which suggested, assuming that the real ballistic coefficients are constants, global variations in the density that were not predicted by the density models. In the SBIR, a more accurate orbit propagator was used, incorporating a higher order geopotential. The results differed little from the Snow-Liu results, indicating that geopotential and propagator methods were not responsible for the observed trends.

Subsequently, in the SBIR, methods were developed to correct the Jacchia 1970 model, based on the assumption that the variations observed in the ballistic coefficient originated from residuals between the actual density and the model. Two types of correction models were developed: corrections to the exospheric temperature, and density correction (multiplicative) factors. When the corrected Jacchia 1970 model was then used in the orbit determination process, the ballistic coefficient variations were reduced considerably from those seen when the original Jacchia 1970 model had been used (Figure 75).

8.5.2 New Results

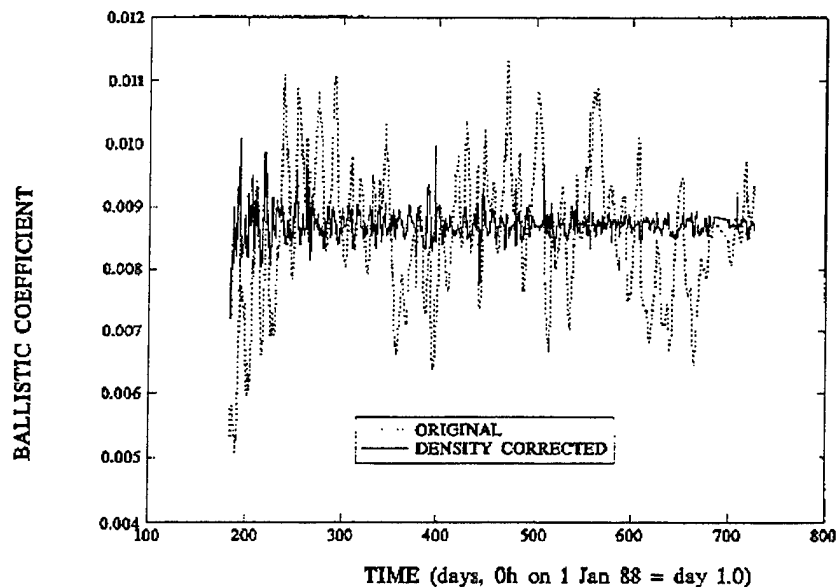
The work in this contract centered on preparation of two presentations [Marcos, *et al.*, 1997a, 1997b]. New insights resulting from this effort are discussed in the following paragraphs.

Commonality of Density Variations among Satellites

Figure 76 shows the time variations of the ballistic coefficients for the four satellites during the 18-month period of study. Common long-term trends, particularly the initial rise over the first 100 days, after averaging over the short-period, ~10-20 day oscillations, are seen for all four satellites. Figure 77 shows the ratios of the ballistic coefficients found for SOLAR MAX, SALYUT 7, and SME to the ballistic coefficient found for LDEF. With the exception of the SME/LDEF ratio, beginning with its rise in April-May, 1989, the long term variations in the ratios are nearly non-existent. Additionally, the short term variations are reduced considerably in amplitude relative to the variations in the ballistic coefficients of the individual satellites, showing that the satellites experience common short-term variations as well. The different behavior of the SME/LDEF ratio was initially thought to be caused by geomagnetic heating specific to high latitude, since SME was the only one of the four vehicles in an orbit of high enough inclination to reach the polar region. However recent information (Marcos, F. A., private communication) indicates that attitude control of SME terminated due to loss of contact on 13 April 1989, suggesting that the increases seen for SME is a real increase in the ballistic coefficient due to changing attitude. Large short-term variations seen for SALYUT 7 are probably caused by thrusting. Thus, in addition to emphasizing the general commonalities of the features in the data, the ratio plots are able to better highlight specific differences, that would signal anomalies in the data that should be re-assessed and/or rejected.

Exospheric Temperature

A scatter plot of the midnight minimum exospheric temperature, based on LDEF data, vs daily 10.7 cm solar flux ($F_{10.7}$) is shown in Figure 78. The exospheric temperature is obtained from the temperature correction model developed in the SBIR. Figure 79 shows exospheric temperature vs flux obtained by averaging over flux bins. A trend toward smaller rates of increase of exospheric temperature with increasing flux is seen at high flux values. This trend may be misleading, since the daily flux ranges to much higher values than the smoothed solar flux, as can be seen in Figure 80. The average temperature vs smooth flux bin, Figure 81, shows a more nearly constant rate of increase of exospheric temperature with flux.



	DAYS	MEAN	SD	PTS	
ORIGINAL	184 to 736	.008573	.001632	3616	
DENSITY CORRECTED	184 to 736	.008714	.000198	3605	07/24/97

Figure 75. The LDEF ballistic coefficient determined from orbit decay in the period 1988 day 180 - 1989 day 365. The solid line shows the ballistic coefficient associated with the original Jacchia 1970 model, while the dashed lines show the ballistic coefficient for the Jacchia 1970 model corrected by a density factor.

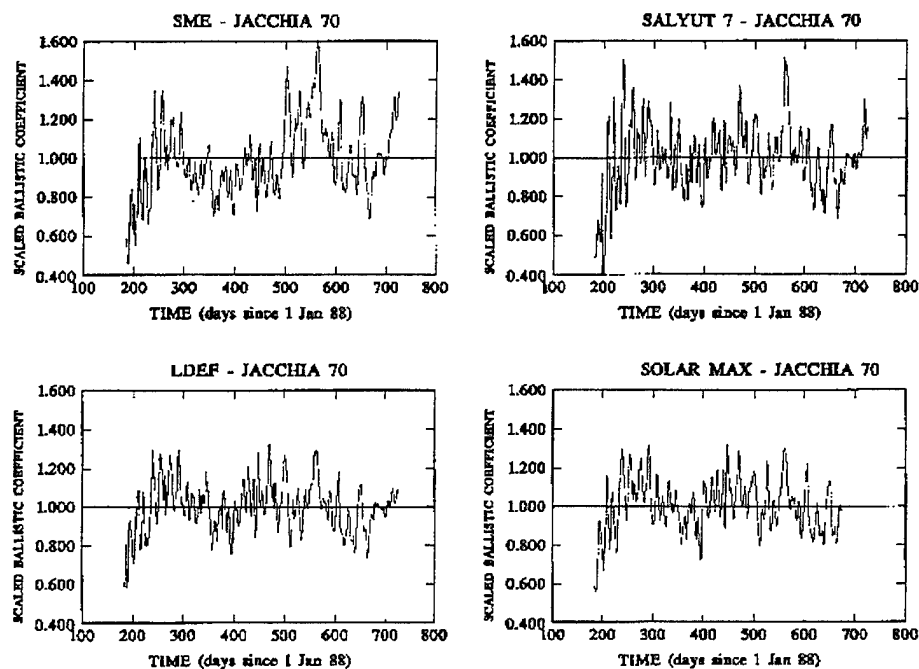


Figure 76. The scaled ballistic coefficients, associated with the original Jacchia 1970 model, for the four satellites, for the same period as in Figure 75.

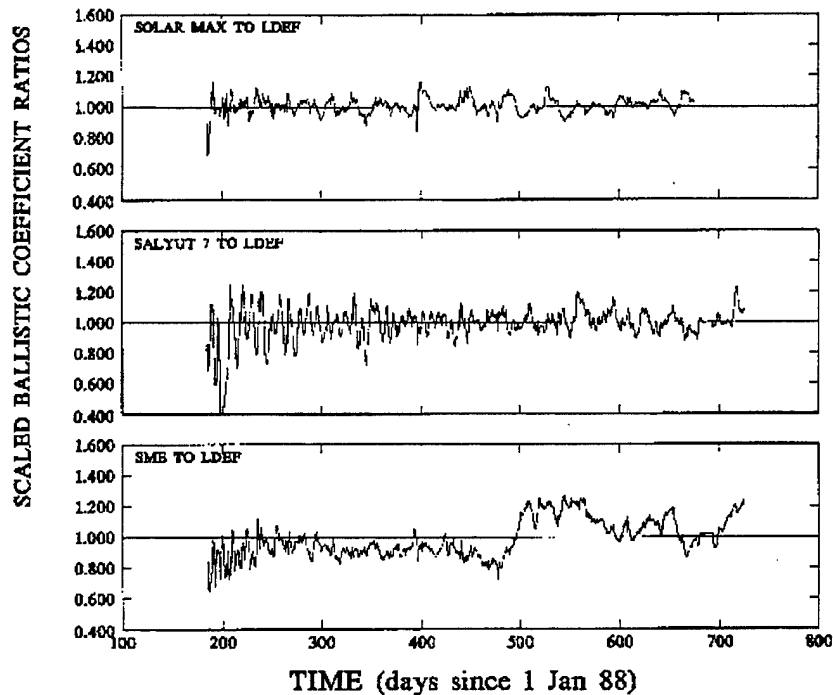


Figure 77. The ratio of the scaled ballistic coefficients of SALYUT 7, and SOLAR MAX to the scaled ballistic coefficient of LDEF, for the same period as Figures 75 and 76.

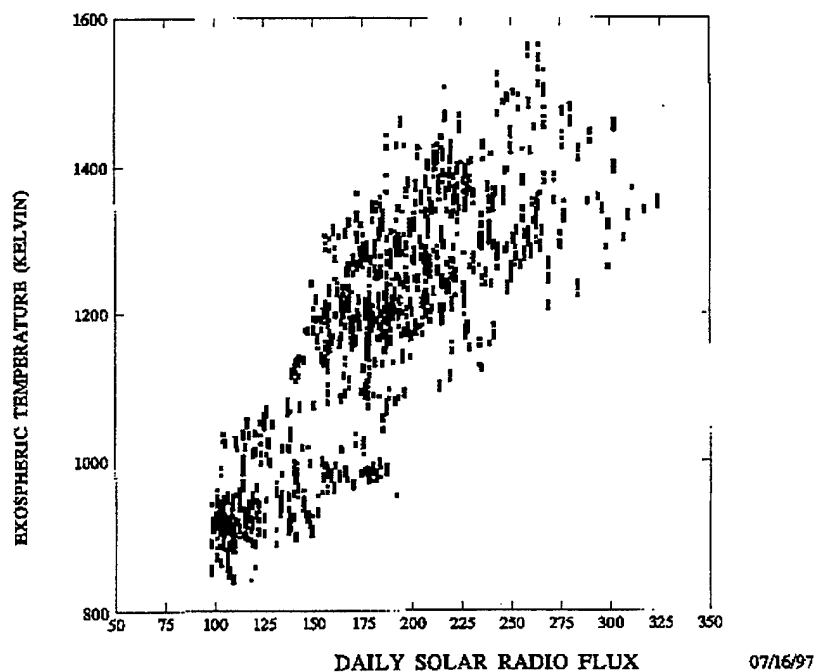


Figure 78. A scatter plot of corrected exospheric temperature vs daily 10.7 cm solar flux, based on LDEF data.

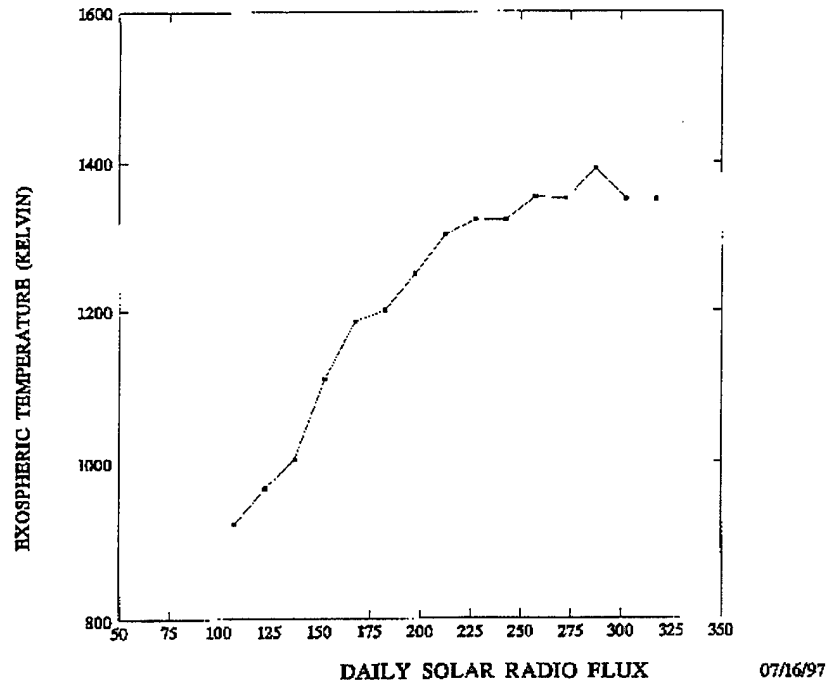


Figure 79. Bin averaged corrected exospheric temperature vs daily 10.7 cm solar flux.

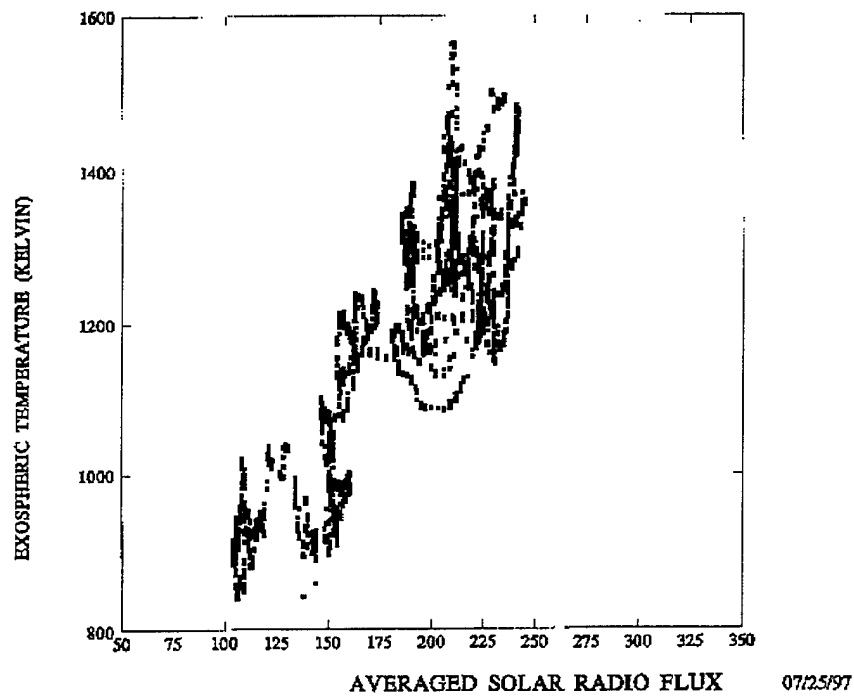


Figure 80. Scatter plot of corrected exospheric temperature vs 81 day mean 10.7 cm solar flux.

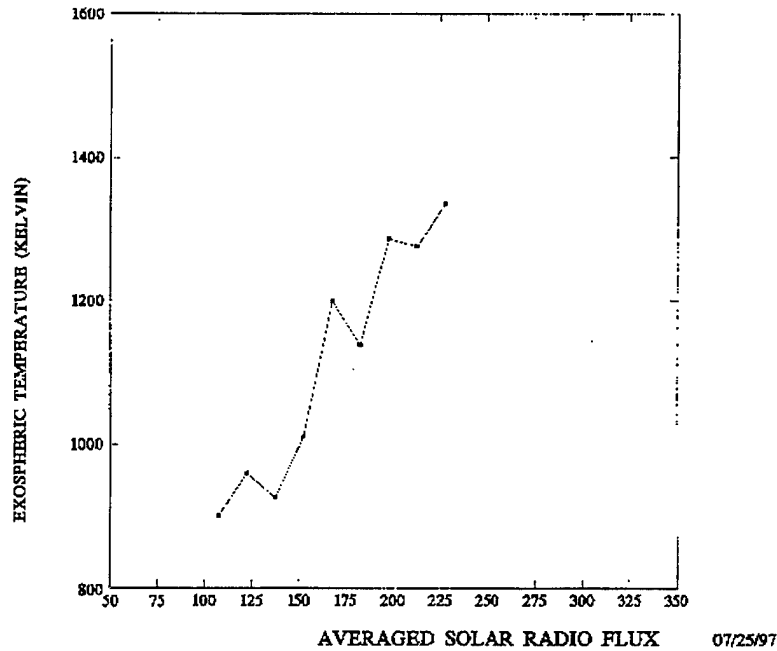


Figure 81. Bin averaged corrected exospheric temperature vs 81 day mean 10.7 cm solar flux.

New EUV Index

The exospheric temperature corrections were used to define an additive term to the solar flux to produce a new index which potentially better represents the EUV than the 10.7 cm flux alone. In the Jacchia 1970 model

$$T_c = 383^\circ + 3.32^\circ \bar{F}_{10.7} + 1.8^\circ (F_{10.7} - \bar{F}_{10.7}) \quad (99)$$

where T_c is the midnight minimum exospheric temperature. The 1.8° factor applied to the daily flux suggests the formula

$$EUV = F_{10.7} + \Delta T / 1.8^\circ \quad (100)$$

for estimation of an effective EUV index that would include the short-term variations found in the drag (ballistic coefficient) data but not in $F_{10.7}$. Here ΔT is the daily correction to the midnight minimum exospheric temperature. It is assumed here that the long term variations of EUV are correctly estimated by the $F_{10.7}$, and that the smoothing of the daily temperature corrections would contribute negligibly to the smooth (81-day) EUV index, leaving it approximately equal to the smoothed $F_{10.7}$. Figure 82 shows the new EUV index, "measured EUV flux" vs time for the period of study, 1988 day 180 - 1989 day 365. If another EUV data set can be found for this period, a comparison would allow determination of the validity of the new EUV index, which might then be used routinely to determine EUV in near-real time. Figure 83 shows a scatter plot of the new EUV index vs daily solar 10.7 cm flux.

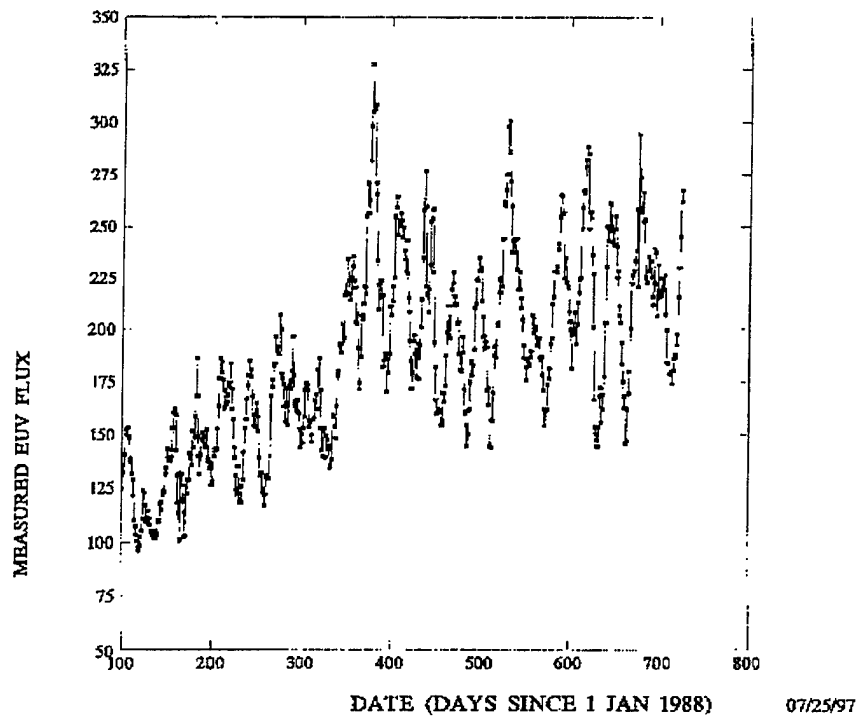


Figure 82. New EUV index ("measured EUV flux") vs time.

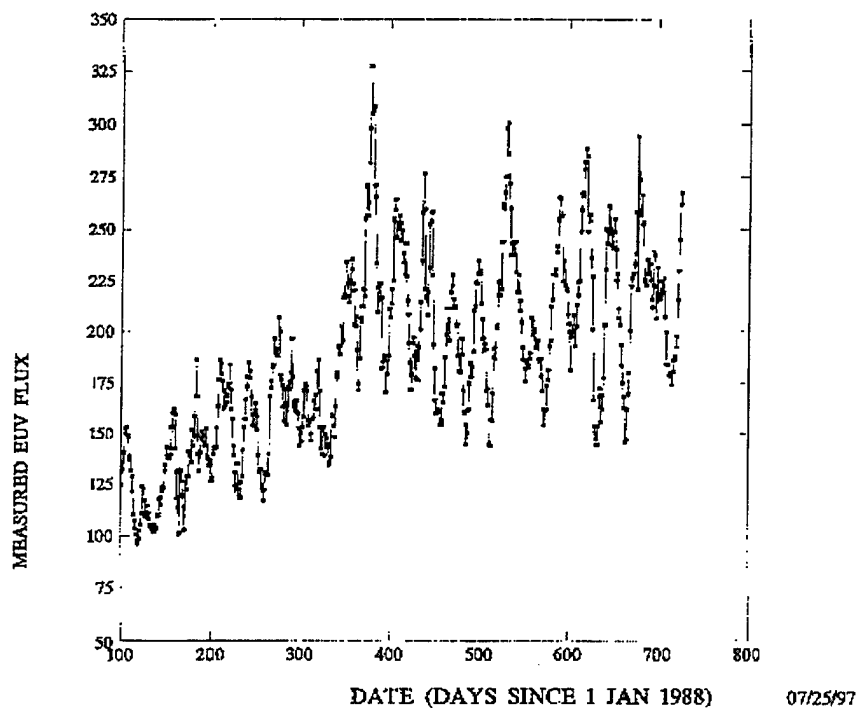


Figure 83. Scatter plot of new EUV index vs daily 10.7 cm solar flux.

8.5.3 Recommendations

The work should be repeated for current satellites, in near real time, so that an operational system can be developed and refined. In a real-time system, one does not know the future daily fluxes needed to compute the 81 day centered mean required by the models. Therefore, the previous 81 day mean is used instead. Figure 84 illustrates the difference between the centered and lagged mean flux. Satellites with orbits similar to those studied in the SBIR should be used first to verify whether the results are characteristically similar. Then other orbits, at different altitudes should be examined to determine to what extent the global properties in the density variations found so far are still present. This information is needed to determine the optimum number and distribution of "star satellites" to estimate the density for the various orbits that exist.

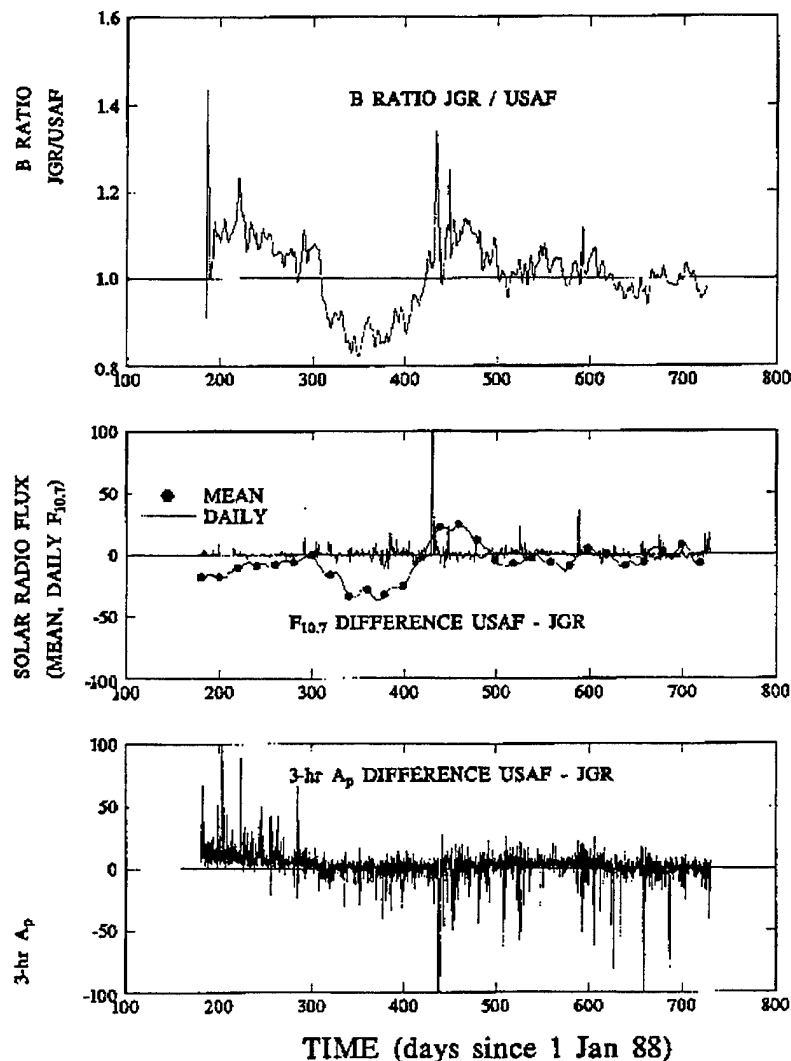


Figure 84. Comparison of LDEF ballistic coefficients, associated with the Jacchia 1970 model, obtained using the operation solar and geomagnetic indices ("USAF") with those obtained using the standard ("JGR") indices. The bottom two panel show index differences, USAF - JGR, while the top panel gives the ratio of ballistic coefficients, JGR/USAF.

In the determination of the new EUV index, it was assumed that the short-term density variations were attributed solely to EUV. A further examination of the data is needed to determine the contribution of unmodeled geomagnetic heating. A comparison with independent EUV data would be useful in this regard. The geomagnetic effect may have been hidden in the SBIR work by the use of 5-day orbit determination fit spans. Therefore, shorter time resolution in the orbit determination would be useful for separation of EUV and geomagnetic effects.

9. APEX - MSTI-II

9.1 ATTITUDE AND EPHEMERIS FOR THE APEX AND MSTI-II SATELLITES

As a follow-on to the CRRES project [Bass, *et al.*, 1989; McNeil, 1991; McNeil, 1993], Radex contributed support to in the areas of ephemeris, attitude and magnetic field data processing to two other satellite missions. These were the Advanced Photovoltaic and Electronics Experiment (APEX) satellite and the Miniature Sensor Technology Integration (MSTI-II) satellite. The APEX vehicle was launched on 3 August 1994 and was lost around 11 June 1996. The satellite carried three space radiation experiments; the PASP-Plus photovoltaic array of new generation solar cells along with a dosimeter, a cosmic ray upset experiment (CRUX) and a thin-film ferroelectric experiment (FERRO). MSTI-II was launched on 9 May 1994 and was lost on 28 August 1994. The satellite carried two narrow field infrared cameras and the mission was primarily for the purpose of testing the feasibility of targeting and tracking on-orbit.

As with the CRRES mission, the contributions made by Radex were diverse in nature, focusing generally on ephemeris, attitude and magnetic field data processing in support of the generation of quality controlled data sets for dissemination to the scientific community and interfacing with users of the data to aid in further processing efforts as well as to supply any further support required in these areas. The data processing program used for both these flights was based on the successful CRRES Orbital Data Processing System but with substantial modifications to meet the needs of these two very different missions. The processing begins with the receipt of analog tapes of spacecraft telemetry from ground recording stations around the world. These tapes are logged and digitized to create 100% telemetry data files on disk. When sufficient data has been accumulated to process one period (one day for APEX and one mission sequence for MSTI-II), the telemetry files are processed and data pertaining to each particular experiment is extracted and placed in separate files, called Agency Files, on a day-by-day or sequence-by-sequence basis. Post-processed satellite ephemeris files are generated independently from state vectors received electronically or *via* fax. The satellite position is supplemented with orbital parameters of specific interest, such as magnetic field related quantities and position in various coordinate systems. Attitude information is extracted along with the telemetry processing. This information is used to compute a post-flight attitude which is quality controlled by reference to satellite sensors and magnetic field models and used to generate a reference attitude file. The ephemeris and attitude information is then merged with the Agency Files to create an Agency Tape which can be easily accessed by the experimenters.

The duties performed by Radex in the processing of these data are many-fold. The primary objective is to ensure the quality of the ephemeris, attitude and magnetic field data. This quality is maintained on a day-to-day basis by survey plots, comparisons of measurements with model predictions, pre-launch modeling and estimation of expected precision, and more generally by a familiarity with satellite performance which is gained as the mission progresses. Another important function is to assist researchers in tracking down anomalies which inevitably arise in the data, for example alerting the user to the loss of attitude control or other anomalies in attitude which could give rise to misinterpretation of sensor data. Another function is to assist users with their further processing of the data by either supplying software for the computation of pointing information, producing detailed ephemeris for anomaly analysis, projections of upcoming eclipse durations needed to access power requirements, or even the complete regeneration of ephemeris sets using different models, as was recently done for APEX. Finally, support was provided in the diagnostics and solution of general telemetry processing problems, for example, characterization of bad data periods which can be recovered by more careful A/D conversion or the use of replacement analog tapes.

The development of software for these projects begins long before launch with simulations and studies into the expected characteristics and performance of the vehicles and definitions of the specific needs of particular experiments on board. Also, since these projects are done under MIL-STD-2167 guidelines, the requirements, performance, interfaces and testing of all software components must be carefully documented. We will begin with a description of these preliminary tasks for these missions and follow with highlights from the missions themselves.

9.1.1 Preliminary Investigations and Documentation

Work for the APEX mission began with a study of the expected accuracy of the ephemeris solutions to be generated with the LOKANGL program. This study was performed to define the requirements for frequency of state vectors received from the then Combined Space Test Center (CSTC). These vectors are derived from observations which are combined in a more intricate model than LOKANGL. The accuracy of the LOKANGL interpolation of these elements thus depends on the frequency with which they are received. The study used, as a reference, the ephemeris generated by the Artificial Satellite Analysis Program (ASAP) [Kwok, 1987] employing several geopotential terms, solar and lunar perturbations, and drag. By comparing solutions with LOKANGL predictions, it was determined that a frequency of once per two days was adequate for the generation of post-flight ephemeris.

A second study for APEX was initiated to answer the question of whether we could adequately assess the accuracy of the attitude post-flight. The basic problem here was that APEX had a relatively crude attitude control system based on a sun sensor and magnetometer only. We had only these models with which to evaluate the attitude and no secondary source of reference. The study included a relatively detailed simulation of the vehicle attitude control and included the simulation of magnetic field data and calibration of the magnetometer which later was to be used in the generation of the magnetic field data base for the satellite. The results indicated that attitude

verification should be possible to within a few tenths of a degree for pitch and yaw and about five degrees in the roll axis, which met mission requirements.

Similar studies were performed for the MSTI-II satellite which had an orbit quite different from APEX and used a sun sensor and horizon sensor and rate gyros for estimation of the attitude in the absence of sensor measurements. The MSTI-II attitude was quite critical in that the field-of-view of the cameras was limited to about a degree of solid angle. The ephemeris on-board was also limited to propagation by the on-board model. Therefore, errors in either of these led to problems in accurate pointing. One of the goals of the post-flight attitude and ephemeris analysis was to help in assessing the accuracy and the impact on pointing knowledge.

Both APEX and MSTI-II data processing systems were developed in the "spirit" of military standard MIL-STD-2167 which governs quite strictly the design, testing and documentation requirements for operational software. Because of this, the design and coding required extensive documentation including a Requirements Specification which outlines the basic inputs, operations, and outputs of a software component, a Design Specification which gives a rather detailed description of each subroutine along with its function, inputs, outputs, and internal data, a Software Test Plan which details a scenario through which all functions of the software component can be reasonably well tested, and a Software Test Report which documents the successful testing. The APEX software was subjected to formal testing before Space Division representatives. The MSTI-II software was not, due to the less formal nature of the program. However, documentation was written and reviewed for MSTI-II in the form of 2167 as well.

9.2 THE APEX SATELLITE

The APEX mission required a continuous and accurate ephemeris set for reduction of the scientific data. This was for the most part due to the dosimeter processing which required accurate values of L-shell, B and the magnetic equator along the field line. The CRRES ephemeris system was extensively revised to accommodate the 70-degree inclination of the satellite as well as its elliptical orbit. These modifications were required mainly in the field line tracing routines. APEX encountered much longer field lines than did CRRES which had only an approximately 17-degree inclination in spite of a higher perigee, about 35,000 km for CRRES but only about 2,500 km for APEX. The software was also extensively rewritten to improve functionality and ease of operation. One area that was revised was the routines for computing eclipses, which were problematic in the CRRES ephemeris processing.

The general philosophy for the APEX ephemeris processing was the same as for CRRES. Position and velocity vectors were received *via* fax and entered into a data base. For this purpose, a program was used to convert the position/velocity elements into mean elements using the general LOKANGL methods which include J_2 and J_3 terms of the geopotential. These mean elements are then displayed alongside prior elements as is shown in Figure 85 in order to assess the accuracy of the new element set proposed. The mean elements displayed in this figure are from late in the orbit and the "Day of

year” refers to day relative to 1994 when the satellite was launched. By comparing a proposed element to those already in the data base, one can assure that there has been no typographical errors in input and that the vectors are indeed from the desired reference epoch, here J2000.

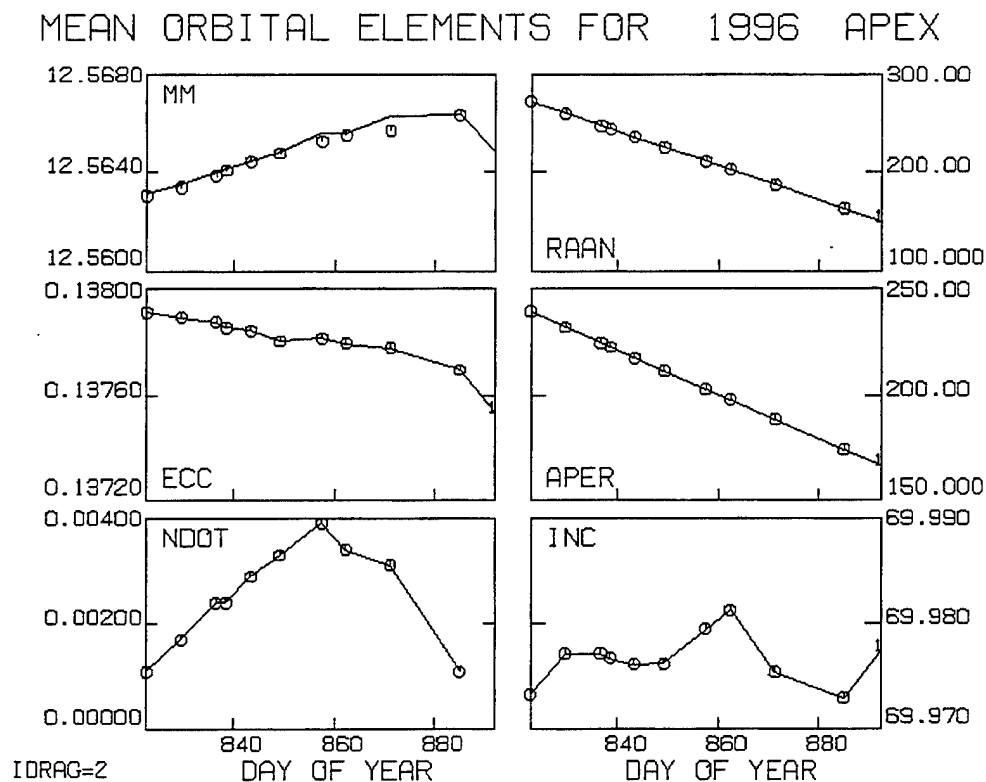


Figure 85. Orbital Elements derived from position/velocity vectors for the APEX satellite. Proposed element is indicated by a “1”.

One advance made in the APEX data processing was to derive the period decay from the change in mean motion from element to element. This allowed us to make use of a single element set from CSTC rather than the two sets used for CRRES. Period decay is not included on the standard position/velocity output from CSTC. Figure 86 gives an example of the anomalistic mean motion and a third-order polynomial fit to the data. Tests with the CRRES element set showed that the period decay derived in this way was equivalent to that provided by CSTC.

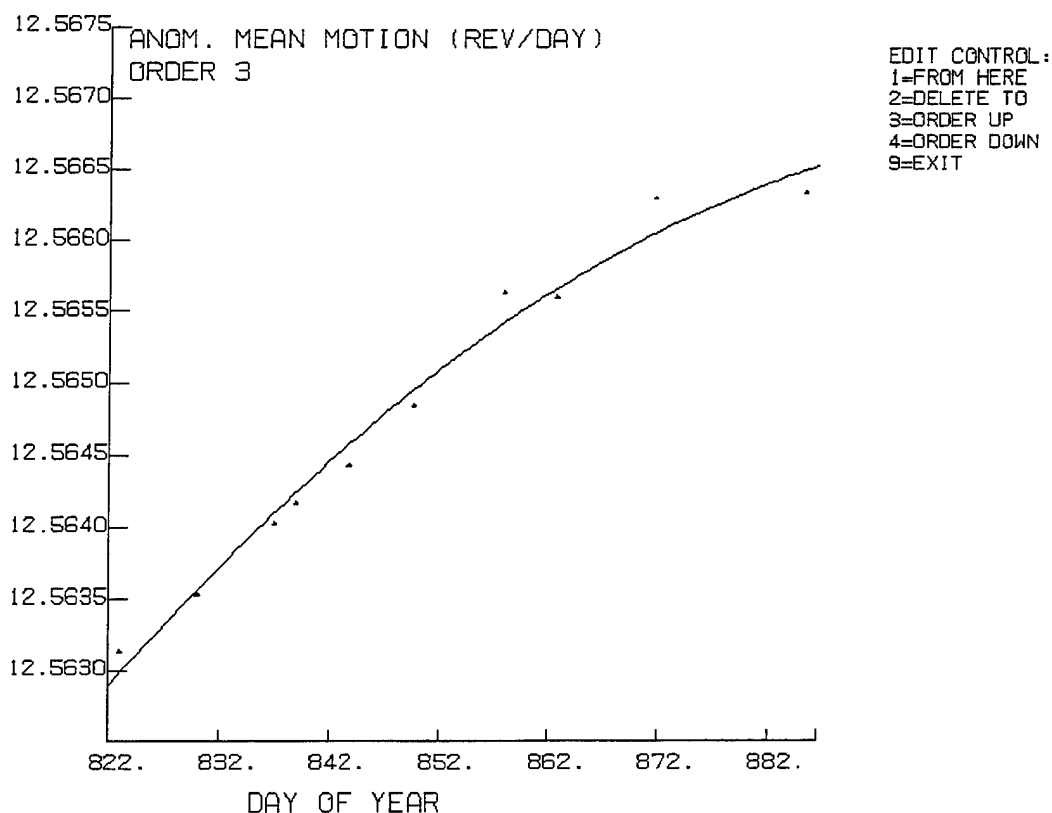


Figure 86. Illustration of the fitting of the anomalistic mean motion to arrive at the period decay.

Ephemeris for each APEX period was generated whenever sufficient vector sets were available to span the period and a summary plot was made for the purpose of quality control. An example is shown in Figure 87. The validity of the L-shell computation is judged by comparison with the Kane model which is a tabular representation of L-shell computed with a slightly different model, so that absolute agreement should not be expected. Since APEX L-shells can become very large, the comparison is made for three different magnitudes of L-shell. The average nodal period is computed from the calculated ephemeris data, as is the apogee and perigee, to assure that no major errors have been made. The presentation of the solar depression angle in the middle panel is given so that the correctness of the eclipse calculations can be judged. If eclipses had taken place in this orbit, they would have been indicated by dots in this panel. In the bottom panel, the latitude and longitude of the satellite, magnetic equator and conjugate point are shown in wrap-around style to assure that there are no serious aberrations in the field line tracing. The maximum and minimum geocentric and magnetic latitude is also shown.

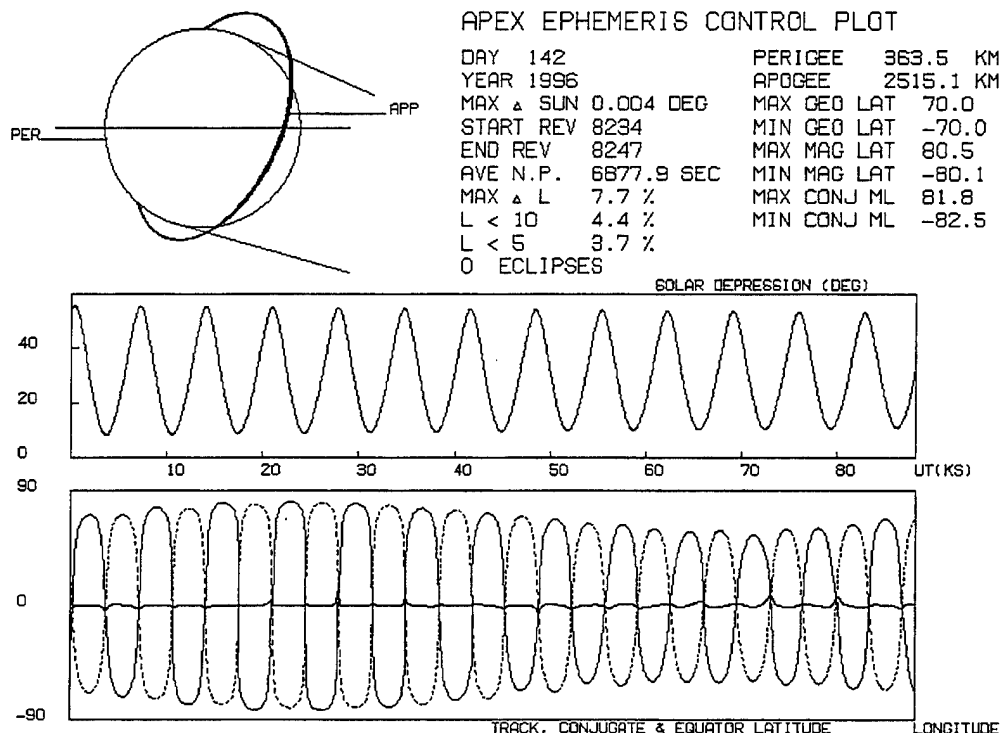


Figure 87. Sample quality control plot from a typical APEX orbit in which there are no eclipses.

The APEX attitude was defined as a pitch, yaw and roll referring to the sun direction (pitch and yaw) and the satellite x-axis in relation to the ecliptic plane (roll). Pointing information was not too essential to the post-flight data processing, however, attitude control was important in order to keep the electrostatic analyzer (ESA) pointing near the ecliptic. There were several periods of loss of attitude control which were flagged in the processed data and ignored in some of the further analyses. For this purpose, a post-flight attitude was always computed for quality control purposes and was occasionally substituted for the telemetered attitude when judged appropriate. The attitude computation is described fully in *McNeil* [1992]. Briefly, the attitude in sunlight was computed as a three-axis problem from sun and magnetic field vectors measured by the spacecraft. In eclipse, the attitude was estimated using a least-squares method best fit to the observed magnetic field.

In the plot shown in Figure 88 below, we see that the pitch and yaw calculated post-flight agree almost exactly with that computed on-board. The roll, which depends most strongly on the calibration of the magnetometer, is often in substantial error by as much as 10-degrees. This, however, is reasonably within the requirements for stability of the spacecraft x-axis. The calibration of the magnetometer was an integral part of post-flight attitude processing and it is believed that the post-flight roll is superior to the on-board version. Since the actual value was not used in any of the further processing of the data, however, post-flight attitude was substituted only when the on-board data was very much different due to known causes. The quantity of interest, that is, the direction of

the magnetic field in the body frame, was produced for further data analysis using the post-flight magnetometer calibration factors and, therefore, the post-flight results were included where important for ESA processing.

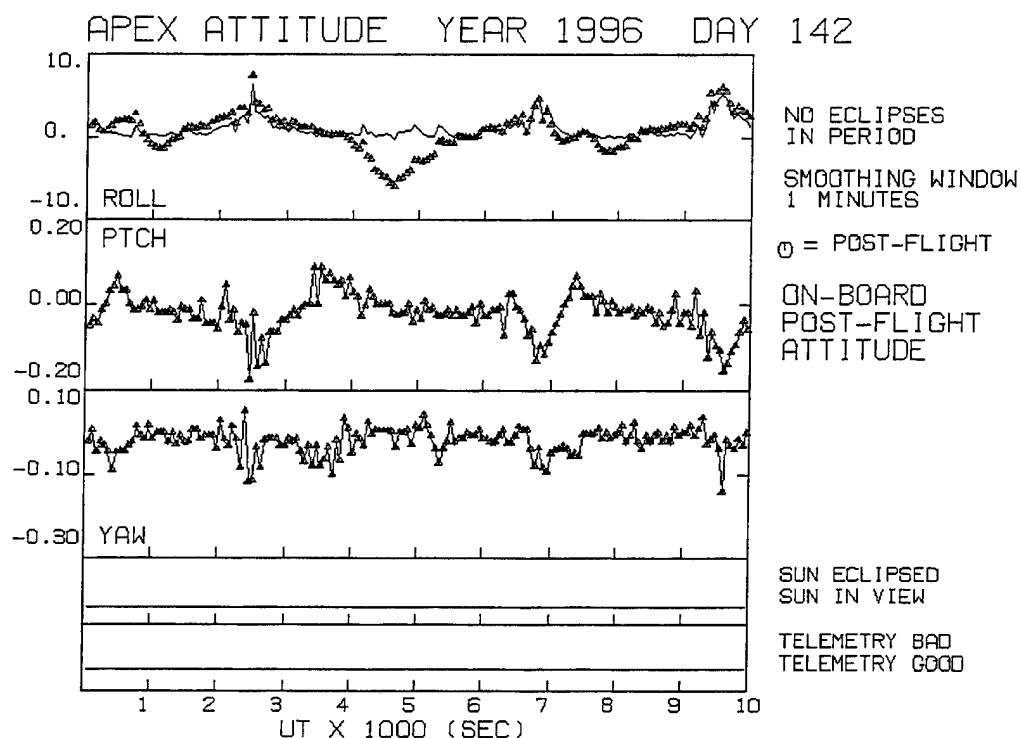


Figure 88. Sample APEX attitude quality control plot showing pitch and yaw and roll as well as flags for bad telemetry and eclipse conditions.

Summaries of the attitude behavior and of the current conditions of the orbit were made and included in the "Agency Bulletins" that were distributed along with the data tapes. Of special importance were the eclipse characteristics which were important in mission planning for the PASP-Plus experiment. Additional ephemeris computations of upcoming eclipse seasons and durations were made for mission planning and more detailed ephemeris was generated several times for anomaly analysis. The nearly three year APEX mission was quite a success leading to, among other things, a detailed model of the inner radiation belts.

9.3 THE MSTI-II SATELLITE

Processing requirements for MSTI-II were quite different from APEX in several ways. First, MSTI-II did not require continuous ephemeris generation but rather ephemeris was required only during mission events, those times when high rate imaging data was being collected. The only science data from MSTI-II was in the form of short and long wave infrared (SWIR and MWIR) images. Therefore, we decided that the most convenient way to generate ephemeris and attitude data was to produce it at the times of these images. This way, ephemeris and attitude data could be read along with the images record by record. Also, the MSTI-II cameras were controlled by a mirror which was steered to point to a chosen direction in the spacecraft body frame. Therefore, the look direction of the cameras was determined by both the gimbal angles and the spacecraft attitude. As with APEX, the attitude was contained in the telemetry, here in the form of quaternions.

The task of the attitude processing system was to perform a post-flight attitude computation where possible. Since data was available only during mission events and since in the absence of horizon sensor hits, a definitive attitude could not be computed post-flight, it was not always possible to perform the post-flight attitude. On-board, this attitude was computed by rate integrating gyros from the last full set of sun and horizon based attitude. A second task of the post-processing was to turn the attitude and gimbal data into a pointing direction, a latitude and longitude of the penetration point and/or a tangent height of the line-of-sight. These were then interpolated to the times of the images and quality control on all data points was carried out. This was accomplished mainly through the use of the images when recognizable geographic or astronomical features could be determined. Otherwise, quality control was limited to the general self-consistency of the data itself and familiarity with the satellite as the mission progressed.

The plot in Figure 89 is quite complicated and contains a substantial amount of information about the mission event in question, which is a stare at the Hawaiian Islands. In the upper left, the latitude and longitude of the sub-satellite point are presented throughout the pass overtop a world map. The lower left panel gives the attitude. The three quaternions are plotted in the top three panels, the fourth panel down labeled "TERPL" gives the time in milliseconds for which a data point had to be interpolated in order to correspond to each of the image times. The bottom panel of that figure gives the difference in degrees between the attitude of the spacecraft z-axis (along the horizon sensor) as computed post-flight and on-board. In this case, since the horizon sensor saw the Earth throughout the event, a post-flight attitude was possible throughout. Differences of a degree or less are due probably to primarily differences in the sensor alignments and were typical throughout the mission, but also might have been due in part to ephemeris errors. Ephemeris on-board was propagated from vectors uploaded shortly before an event began.

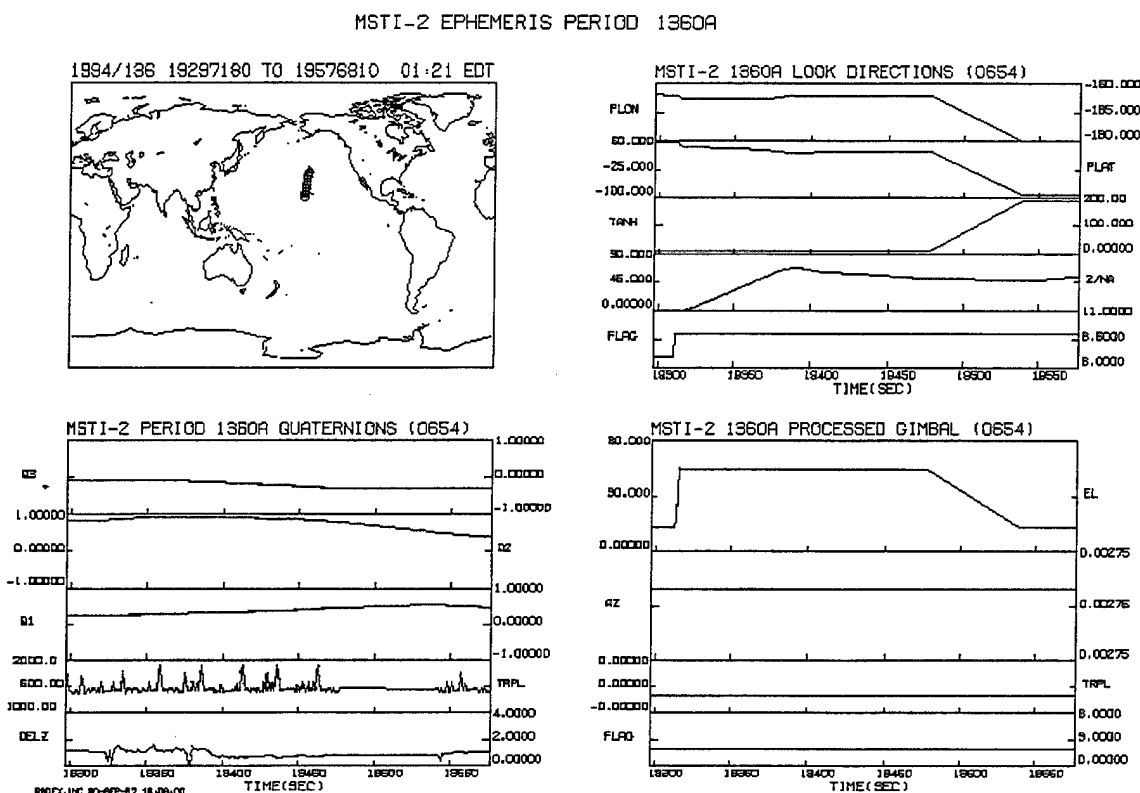


Figure 89. Sample of the ephemeris and attitude control plot for a MSTI-II stare at Hawaii. The beginning and end of the sequence includes stares at the calibration plate.

The post-flight processing of the ephemeris deserves some mention. Since ephemeris was generally available only before mission events and since mission events were sometimes separated by days, we encountered problems in vector availability. Eventually, we began to compute elements directly from the on-board recorded ephemeris by fitting the usual mean elements (*e.g.* Figure 85) to those computed from the on-board position vectors with a differential approximation for the velocity. This resulted in an ephemeris that was at least as good as the on-board solution during the mission event. Quality control of the attitude was also attempted, whenever possible, by a number of tools developed in either IDL or XView. One such tool is shown in Figure 90. The large diagonal box is the projection of the MWIR camera onto the celestial sphere. The small box shows the star that is selected by clicking on the screen near a chosen star. Other stars can be seen. In this case, MSTI-II missed the star. This tool also contained the moon and several of the planets and in stares at the moon and at Venus, it was possible to verify the correctness of the attitude and LOS computations to within perhaps one-half degree. This was generally accepted to be about the best that MSTI-II could do for various reasons. The button labeled PF/OB allowed the user to switch between the post-flight and on-board attitude solutions. It was generally true that both were of about the same accuracy except for a few cases where the uploaded vectors were clearly of low quality.

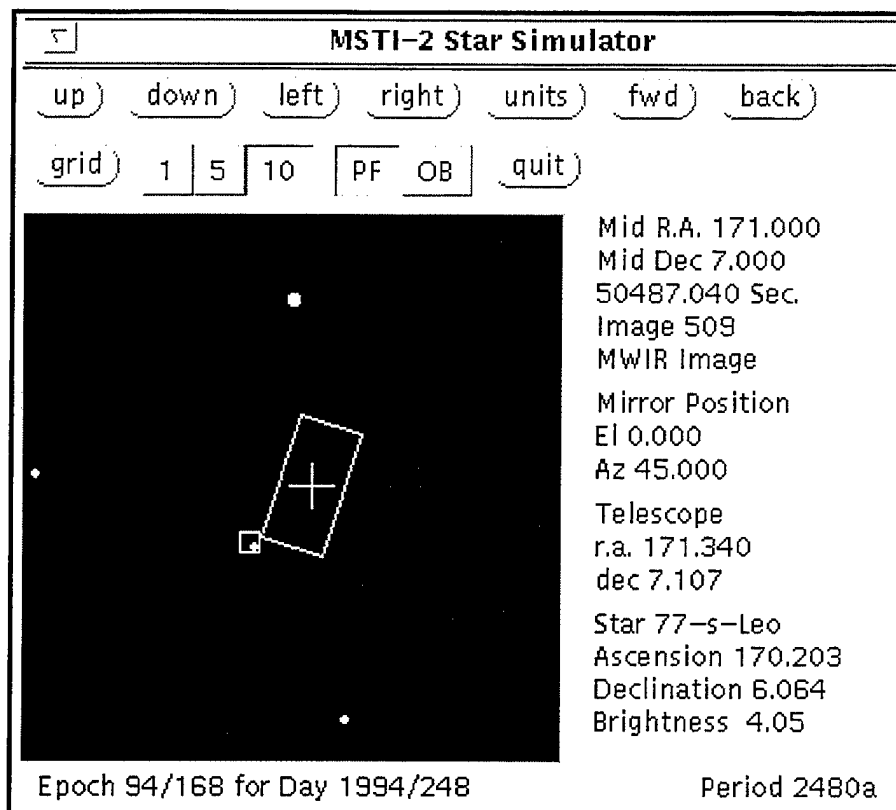


Figure 90. Sample of MSTI-II Q.C. tools for an attempted (and failed) star search.

Another tool that was quite useful in figuring out what the satellite was doing, and verifying that the data reflected this, is shown in Figure 91. This tool presents a three-dimensional rendering of the satellite track, the camera line-of-sight and the Earth. The scene can be advanced in time and the corresponding image can then be viewed in another window. The scene in Figure 91 is a stare at the Hawaiian Islands, the same mission event of Figure 89. The expanded image in the "zoom" box shows clearly the attempt to locate the islands, which did not seem to be successful in this case. The dawn/dusk terminator is also shown, indicating that the islands were in darkness at the time. Images corresponding to this event did not show anything recognizable.

In general, the effort to verify the pointing direction and to explore in a cursory fashion the image data from each event was useful in two ways. First, there was no other way to verify that the telemetry processing was being carried out correctly. For example, we noted early on that images from the SWIR camera appeared to be irregular on a line-by-line basis. This was traced to an incorrect interleaving of the readouts in the telemetry processing system and was then corrected. Also, when some difficulties arose in the decryption of telemetry for some especially important data, direct examination and reconstruction of the image data allowed us to produce some data from the event and satisfy quick look requirements until the decryption problems could be solved. Finally, we made up brief descriptions for each mission event which told the purpose of the event, the location of the target, the apparent success, and other items of note. These reports were disseminated along with the tapes so that users of the data could conveniently spot periods of particular interest.

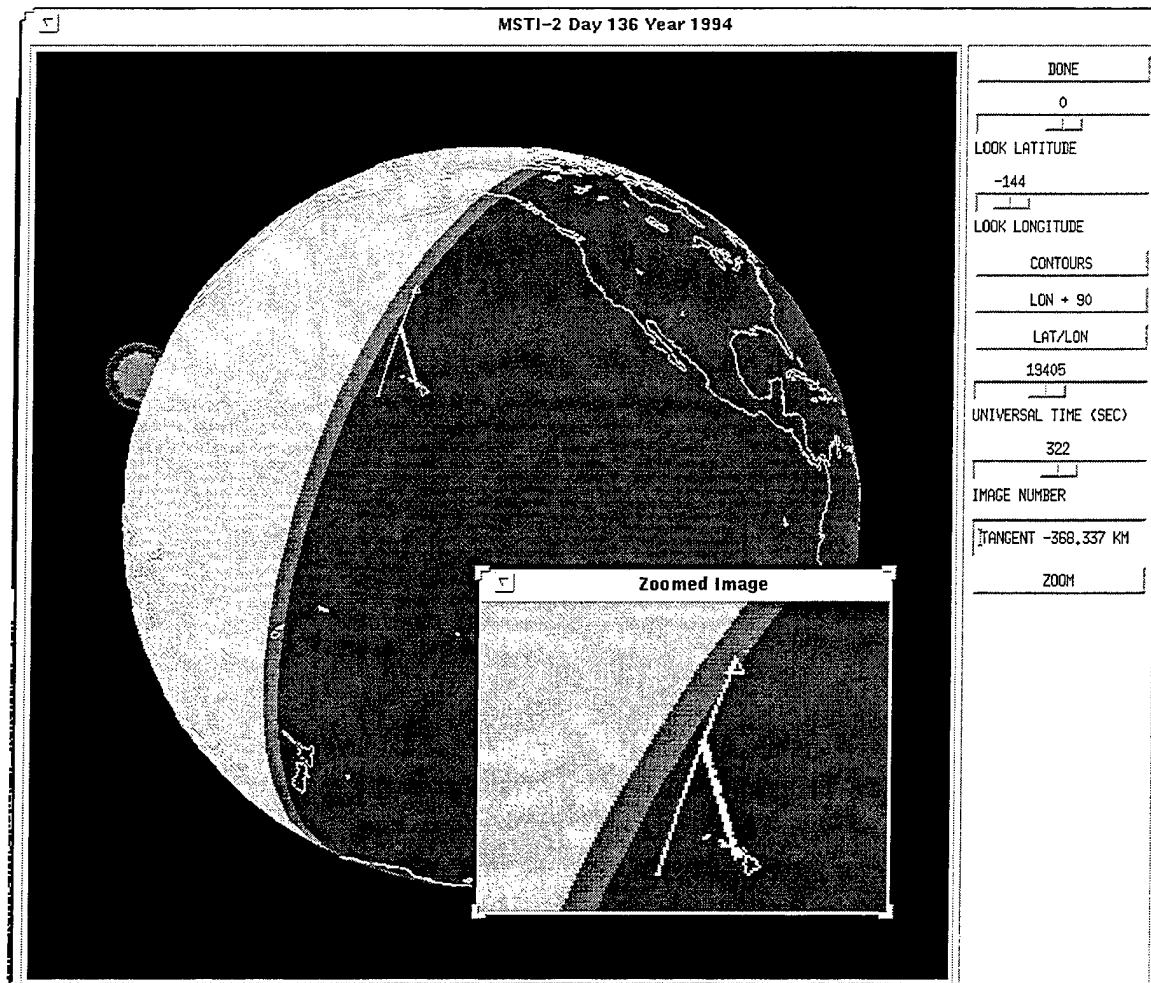


Figure 91. An example of the tool developed to locate the center point of the MSTI-II camera line-of-sight on the Earth's surface.

It seems appropriate to close out this section with a few images taken from the satellite. In all, tens of thousands of images were processed. The mission concentrated on trying to track and lock on emitters such as volcanos, stars, the moon and a few missiles. Shown in Figure 92 are two images taken from the ground.

The image on the left is, we believe, a river with a volcano (the hot spot in the upper right just above the scratch on the lens). To the right is a nice picture of brush fires taken north-west of Reno, Nevada. MSTI-II did a substantial amount of work in its short lifetime. The project was challenging as well as rewarding for us and we believe that the contributions made by Radex were significant.

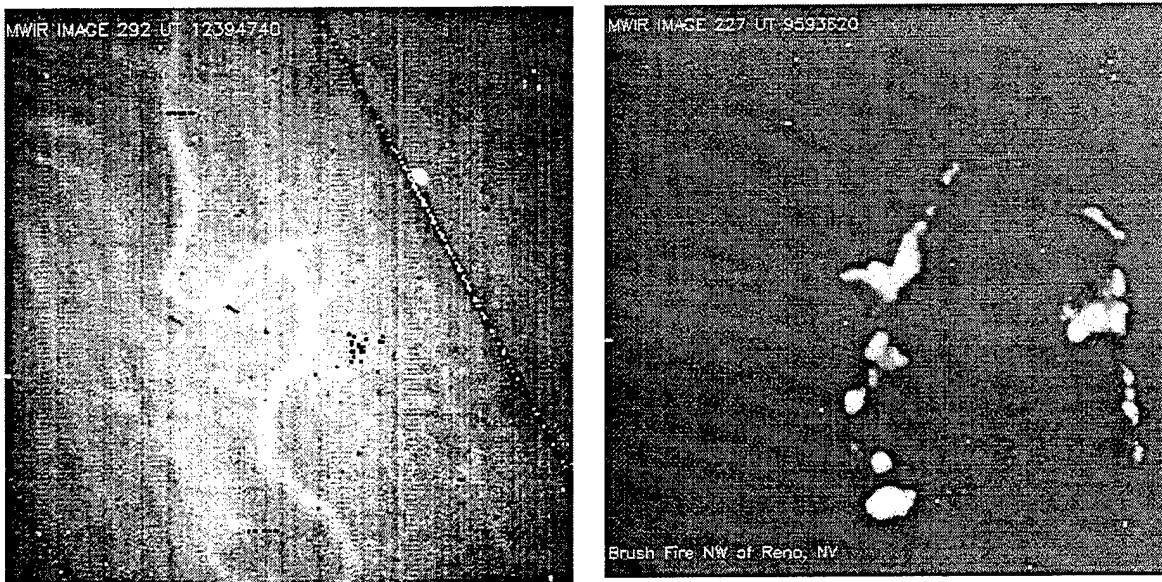


Figure 92. MSTI-II Images (left) of a river and volcano and (right) of a brush fire in Nevada. Diagonal line is a scratch on the lens of the camera, black dots are dead pixels.

10. DMSP MAGNETOMETER

The APHB code is the principal code for processing Defense Meteorological Satellite Program (DMSP) Magnetometer (SSM) data obtained from original digital telemetry data into geophysical parameters for use by the Space Forecast Center (SFC), Falcon AFB, CO. This brief report describes the modifications which were needed in order to properly process data for the DMSP 12 and DMSP 13 magnetometers at PL/GP. The effort described here is part of an effort to integrate the code into operational code base of the SFC.

10.1 BRIEF DESCRIPTION OF THE APHB CODE

10.1.1 History

The APHB code was written by Hughes Corp. for the SFC as a sub-task of the SSM/I work.. The Hughes version was adapted from a research-grade code written by PL/GP and Radex, Inc., based upon the experience of the DMSP F7 magnetometer. The Hughes version incorporated the known characteristics of the newer magnetometers onboard the DMSP F12-13 satellites, and pre-launch experience with these instruments in integration testing. The preliminary code was checked out using a dummy data file provided by PL/GP. At the time of completion of the effort described here, the input and output sections of the code had not been set up to use the SFC file systems.

Prior to the F12 flight, PL/GPS requested that efforts be made by Radex to correct any problems in the APHB code that were presented by the real data set but not apparent in the test data set. This report describes that effort. Additional efforts, such as documentation and delivery of the software to the SFC are underway as part of a follow-on contract.

10.1.2 Basic Operation of the F12 and Beyond Instruments

The SSM measures the magnetic field vector at the location of the sensor. The magnetic field measured is a combination of the Earth's internal magnetic field, the magnetic field created by electrical current flowing into and out of the ionosphere, and the magnetic fields created by the spacecraft electrical systems. The three components of the magnetic field vector are measured by three elements inside the sensor which are approximately orthogonal and approximately aligned with the spacecraft's axes, as described in Section 10.2.3.

Each element of the SSM sensor measures a component of the magnetic field in the range 0 to 8000 nT in steps of 2 nT. These measurements are referred to as the "fine" measurements. The total instrumental range of -64,000 nT to +64,000 nT is achieved by offsetting or biasing the measurement by one of 32 levels or bias steps. The instrument and telemetry data processing only permit the bias step to change once per second. The fine measurements are reported to the telemetry buffer 12 times per second. Only the first fine value of each second are put into the telemetry buffer. The 2nd to 12th values are reported as differences from the previous value to save bits in the telemetry buffer. In the case in which any of the differences exceeds bounds, an invalid data indicator ("DELTA EXCEED") is set in the telemetry for the affected data points.

10.1.3 SSM Data Input at PL/GP

The APHB code processes a "raw data" input file containing time tagged magnetic field data and ephemeris data for a user-defined time interval. The source of the APHB input at 50 WW will be "PREP" files from AFGWC. At the time of this effort the format of these "PREP" files had not been defined. Instead, PL/GP received "PREP" files from AFGWC. Each "PREP" file represents SSM data from one read-out of the flight record. One day of data is contained in 12 to 15 files from AFGWC. PL/GP re-formats the AFGWC files into one file per day with three minutes of data per record. The first step in using the APHB code at PL/GP was to modify the input section to accomodate the PL/GP data base format.

10.1.4 Converting from Telemetry Data to Magnetic Field Measurement

The raw SSM telemetry data consists tightly packed bits representing the one range and 12 measurements or "fine" values per second. After reading in a second of data, the code converts the "counts" or integers obtained from spacecraft telemetry into 12 X 3 sample points per second. The

range and “fine” values for each axis is converted to a measured field value in the x, y or z direction. Then each field vector is multiplied by a matrix to remove skew and misalignment in the sensor. If one of the error flags in the telemetry is set or the second of data is missing or corrupted, a dummy set of values replace the second of data. The second of data is written to a temporary file.

10.1.5 Measured Minus Model Geomagnetic Field

Since the magnetic field created by electrical currents into and out of the ionosphere is the only component of interest to the Air Force, the main magnetic field of the Earth must be removed or subtracted from the measurements. The ephemeris data is used to compute the model field. In the Hughes version, IGRF 85 (International Geomagnetic Reference Field, epoch 1985) is updated to current date using the IGRF secular terms. The Earth’s magnetic field is computed once per minute from the IGRF algorithm using the ephemeris information. The twelve values per second of the Earth’s field is computed by an interpolation scheme from the 1/minute values. After this step, the temporary file contains the difference vectors which should have a magnitude of 0 nT, ± 200 nT .

10.1.6 Jump Removal

Because of electric activity on the spacecraft (periodic switching on and off of satellite control and experimental instruments) “jumps” are present in the SSM data, as well as “noise”. “Jumps” are defined as abrupt changes in the SSM measured field vector. Typically a piece of onboard equipment is turned on which cause a “jump” in the measured field vector. Since the “jump” is related almost exclusively to the power being drawn, there is no change or variation in the measured field as the offending piece of equipment operates. When the offending piece of equipment is turned off, the SSM data “jumps” back to its original state. For computational convenience, jumps are classified as either “large” or “small.” “Large jumps” change the SSM magnetic field vector component by more than 1000 nT. “Small jumps” change the field vector components by 60 nT to < 1000 nT. Large jumps are caused by the torquing coil. Several items account for the small jumps. The jumps are removed in two steps; one for the large jumps and one for the small jumps, For each step, data are read, and a jump algorithm is applied, with the output written to the same data block in the scratch file. The jump logic algorithm tracks the history of the jumps, and creates a jump logic table. A maximum of seven jumps can be handled by the jump logic. Such jumps occur in a short time interval (a fraction of a second), and followed by a corresponding opposite jump as the electrical activity state is changed.

10.1.7 Noise Removal

Following the two-step jump removal, the resulting “observed minus model” field data is “filtered” or smoothed in order to remove high frequency variations attributed to noise. The problem that was of particular concern before the launch of F12 was the signature of the permanent magnets in the

SSM/I antenna. The antenna revolves at the rate of 1 rev per 1.89 seconds. The filter has been tuned to remove coherent variations with periods less than 2 seconds (or frequencies greater than 0.5 Hz).

10.1.8 Output

The last step is to read the temporary file from start to finish and to produce an ASCII output file of one second averages of the "measured minus model" vectors for further processing and analysis. It has always been understood that this will not be the output format in the operational version of APHB but no specification of the output format has been written prior to the completion of this effort.

10.1.9 Program Control

Most of the information that the APHB needs to get started is provided by the operator using the standard input unit (or console). The user specifies the name and location of input data file, and the time interval (start/stop times) to be processed. The raw data file name is used to construct the two output file names. This means that the output will be on the same disk unit as the input. During processing, data is stored in a scratch file which resides in the system default directory.

10.2 PROBLEMS AND MODIFICATIONS REQUIRED FOR DMSP F12, F13 AND BEYOND

As explained above, the first modification was to re-write the input section to accept real data. After that was done some real problems were found in the APHB code when actual F12 SSM data was used. To help with the analysis of the data, some existing graphics programs were modified to produce plots of the SSM data. These plots are intended only for internal usage and no attempt has been made to rewrite the plotting code to 50 WW software standards.

10.2.1 False Large Jumps

The first problem was that there were large jumps. Comparisons with the raw data indicated that many of these jumps did not correspond to any "glitches" in the raw data. Many of these jumps appeared near the end of a one minute data interval. At this point it was discovered that there was missing data within the minute interval, and these jumps were due to the changes in the manner in which missing data was stored in the new "raw" data files.

10.2.2 Slow Small Jumps

It was noticed that there seemed to be some small jumps that the code was not identifying and removing. Investigation of the problem showed that these changes in the spacecraft magnetic field due to electrical activity on the spacecraft were not really "jumps." A jump is an instantaneous change in the spacecraft magnetic field. These changes of approximately 150 nT (mostly in the X component) took 10 to 15 seconds. During pre-flight testing, no similar transition was observed. On a plot of data versus an hour or more of time, these transitions looked like jumps but did not satisfy the program logic for jumps. Since these transitions or "slow jumps" mostly affect the X component of the field which has little importance to the Air Force, the "slow jumps" have been left in the data.

10.2.3 Calibration Problem

The major problem encountered in this effort was a mis-match between the measured and model field of 1000 - 1500 nT per axis. When the difference between the measured and model component were plotted, there were large periodic residuals of approximately ± 1000 nT. The period of the residuals was approximately one orbit with a harmonic at 1/2 an orbit period. The first thought was that this large residual was due to a mis-alignment between the sensor axes and the spacecraft axes. It is known that the accuracy of the mechanical alignment is only 0.5 degree and the SSM is sensitive to mis-alignments of 0.05 degree. It was the task of NASA/Goddard Spaceflight Center to compute the mis-alignment angles. When they reported to PL that their solutions were of the order of 1.5 - 2.0 degrees per axes and changed from day to day by up to 1.0 degree, we knew that misalignment between the sensor's axes and the spacecraft's principal axes was not the problem. The spacecraft's principal axes are held to a tolerance of 0.01 degree and the spacecraft body between the SSM sensor and the principal axes location does not bend and twist by more than 0.05 degree.

Another potential source of the error was the ephemeris information supplied by AFGWC. If the time tag for the ephemeris were in error by 5 - 10 seconds and varied from day-to-day, we could account for most of the difference. Independent ephemeris computations were performed using LOKANGL (a local satellite ephemeris program) and NORAD orbit elements from both before and after the epoch of the ephemeris. The result was excellent agreement obtained between the ephemeris data computed by AFGWC and stored with the data and the LOKANGL computations. Similar comparisons of the field model calculations verified the accuracy of the model field calculation.

The next source of error that was investigated was the calibration. The conversion from counts to measured magnetic field is a three-step process. First, the counts are converted to a magnetic field observed by each of the three elements of the sensor:

$$B(i) = \text{Range}(\text{Bias}(i)) + K(i) * \text{Fine}(i) \quad (101)$$

where

i	=	index for one of the components of the SSM = x, y or z
Fine(i)	=	one of the 12 fine measurements per second in counts
K(i)	=	the conversion from fine counts to measured field
Range	=	one of 32 ranges of the sensor (determined from pre-flight calibration)
Bias(i)	=	the bias or range value reported in the SSM telemetry
B(i)	=	the component of field observed by one of the SSM sensor elements

Then the measured vector is multiplied by a matrix which accounts for the slight variation of the three sensor elements from perfect orthogonality and for some cross-talk between the elements. This matrix is almost a unit matrix and was computed as part of the pre-flight calibration.

$$B'(j) = M(j,i) * B(i) \quad (102)$$

where

B'(j)	=	the measured field at the SSM sensor in the orientation of the SSM sensor axes
M(j,i)	=	correction matrix determined by pre-flight calibration

The final step is to rotate the B' vector into the orientation of the spacecraft principal axes and to remove the d.c. (or permanent) magnetic field of the spacecraft. The rotation matrix is an Euler rotation matrix with three Euler angles which should be approximately 0.5 degree.

$$B''(k) = R(k,j) * B'(j) - \text{Off}(k) = R(k,j) * M(j,i) * B(i) - \text{Off}(k) \quad (103)$$

where

B''(k)	=	the measured field in the orientation of the spacecraft's principal axes
R(k,j)	=	the rotation matrix from the SSM sensor orientation to the spacecraft axes orientation
Off(k)	=	the permanent magnetic field of the spacecraft at the SSM sensor's location

It is possible to combine the two matrices into a single matrix which we call ORTHO.

$$B''(k) = \text{ORTHO}(k,i) * B(i) - \text{Off}(k) \quad (104)$$

A least squares linear fit program was used to calculate a new "ORTHO" matrix and offset. The residual error for a day of data was computed and minimized.

$$R = \text{Magnitude} ((M - B'')^2) \quad (105)$$

The measured field vectors (B") input to the least-squares fitting program is computed from the APHB program with the ORTHO matrix set to a unit matrix. Thus, all large and small jumps have been removed from the data. Geophysical variations are minimized by using only days when the activity (as measured by the Kp index) is very low. The model field vectors are the same ones computed in APHB for subtraction from the measured values. The results for F12 and F13 are:

F12

	0.98306978	0.01100111	0.00104030
ORTHO =	0.01084268	1.04327248	-0.00255244
	-0.01986832	-0.00789653	1.00009042
	-977.27		
Off =	-149.86		
	-52.69		

F13

	0.97855549	0.03463974	-0.01061612
ORTHO =	0.01094531	1.06662925	-0.02318646
	-0.02829291	0.02967541	1.00409263
	-11.24		
Off =	-798.00		
	189.39		

The minimization process was performed on several days of data from F12 and F13. The result was that the ORTHO matrix and Off vector were fairly uniform from one day to the next day. When these values are put back into APHB, there is a variation between the measured and model field by approximately 200 nT per axis with a period of approximately one orbit. Much of this is probably due to uncertainties in the model field, but some of this may be due to the fitting process not being optimal. In particular, even on very quiet days there is some variation in the magnetic field over the auroral zones. These auroral variations were left in the data. Also, after the fitting was done, a small error in the large jump removal routine was found which might affect the fitting results slightly. In addition, the F7 SSM showed a tendency to change its calibration over the lifetime of the spacecraft. The F7 change may have been due to a re-configuration of the power distribution on the spacecraft. As a result, the results of the minimization should be re-examined from time to time over the lifetime of each spacecraft.

10.2.4 Tweaking the Small Jump Logic

There were several problems found and corrected in the logic for finding small jumps. The most significant problem was that while a small jump offset should have a start and stop time some 10's of seconds to a few minutes apart, it sometimes happens that only the start or stop can be found and not the other. Since we are processing more than one orbit (102 minutes) at a time, such an error can become significant late in a run. In particular, the logic is written that no more than 7 small jumps will be tracked at any one time. While some progress was made in finding more starting and stopping points, the final solution was to clear the jump logic of any memory of past small jumps each time the spacecraft crossed the ascending node.

Data gaps are a fact of life in the real world but were not considered in the development of the code. There are problems in the jump logic when a jump starts or stops during a data gap. To handle data gaps, it was decided to reset the jump logic whenever there was a data gap more than 300 seconds.

10.2.5 Model Magnetic Field

The International Geomagnetic Reference Field at epoch 1985.0 (IGRF 85) model was used in the code during development because that was the best model available. It has been replaced by the IGRF 90 model. The replacement was done in such a manner as to make it easier to replace new releases of the IGRF models when they became available. The IGRF 90 model was replaced by the IGRF95 when it became available in early 1996. Also, the recomputation of the coefficients at the epoch of the data was eliminated because it consumed computing time without any noticeable effect.

11. EPHEMERIDES

11.1 SATELLITE ELEMENT ARCHIVAL SYSTEM

Standard NORAD two-line satellite orbital element sets have been used by PL scientists in support of a wide variety of studies. Satellite orbit prediction and analysis programs, such as LOKANGL [Hein and Robinson, April 1991] and Artificial Satellite Analysis Program (ASAP), require these element sets as input. In the past, satellite element listings were kept on paper in files and provided to PL on request. This method had several drawbacks. Access was inconvenient, files could easily be lost, and data was entered by hand, thus, it was a very cumbersome method. Since the satellite elements are obtained at PL through E-mail on the ESC VAX, a purely electronic system was seen as possible and it alleviates the previous problems.

The objectives of the work are focused on:

- developing a low maintenance procedure for archiving and retrieving satellite element sets,
- providing convenient access to the satellite element archives for the PL community.

11.1.1 Original Satellite Element Processing Procedure

The satellite elements are obtained through electronic mail on the ESC VAX, by running a package called All-in 1. The mail is saved in a file on the archive PC, using the "capture" feature of NCSA TELNET. The satellite elements are extracted from this file and sorted by satellite number. A merge procedure is then run to add the new element sets to the master databases. These databases are then sorted by date and time, and duplicate element sets are eliminated. Printouts of the updated database files are then generated. Finally, the master databases are transferred to the VAX 7000, where they are available for general access.

Originally, a four-phase procedure was in place and an early GSATEL program had been developed and incorporated in this procedure which is in four parts, namely, Element Capture, Element Extraction, PostScript Output Creation, and Transfer of Databases to the VAX 7000.

11.1.2 Processing Procedure Development

The GSATEL Program

GSATEL was written to process the captured electronic mail file. This file contains numerous binary control sequences, in addition to normal text. A variety of message headers and similar information must be distinguished from the element sets.

The GSATEL program operation may be divided into four specific tasks:

- 1) Extract all satellite elements from the electronic mail file.
- 2) Sort these elements by satellite number, and by date/time.
- 3) Merge the new elements into existing master databases.
- 4) Sort the master databases and eliminate duplicate elements.

The master database files created by GSATEL are simply a collection of two line elements sets in the conventional format.

Current Archiving

At present the satellite elements are obtained from the AFIT archive (archive.afit.af.mil) by an automated process on Radex's Sun workstation 'ziggy'. An automated anonymous FTP request is performed by 'ziggy' daily at 6:00AM and 6:00PM local time for the current update files for geosynchronous and other satellites. At approximately one week intervals, the data received by 'ziggy' are transferred to a PC, and processed using a revised version of GSATEL. The updated PC archive files are then transferred to the "erob" account on 'zircon'. Duplicate backups are stored on the PC, and the original AFIT update files are archived on 'ziggy'.

Satellite Element Data Access

Satellite data may be accessed by Phillips Lab personnel on the VAX 7000 (ZIRCON) in the directory USR\$DSK4:[ROB11]. NORAD file names have the form SATNNNNN.YY, where NNNNN is the 5-digit satellite designator, and YY is the 2-digit year. Data for the current year and the previous year will be maintained on-line on the VAX 7000. Older element sets will be archived

on floppy disk, and will remain available on request. Since the data will be stored on the floppies in the same format as on the VAX 7000, no special steps will be required to read these files.

11.2 GEOPHYSICAL MODELS LIBRARY

Work is being performed on an effort to construct a geophysical models library with an X-Windows graphical user interface. This system provides a user with easy access to any model in the system. The interface is currently being implemented with MOTIF widgets, which provide labeled boxes for user input of the parameters required by a model, and a scrolled text box for display of the output. At present, prototypes have been completed for the Jacchia 70 and MSIS90 density models, and the IGRF 85 + Olsen-Pfitzer 77 magnetic field model. For each of these models, the inputs are date, UT, geographic latitude, geographic longitude, and a range of altitudes. The density models also require daily and mean $F_{10.7}$, and a_p . The outputs consists of total density or magnetic field magnitude vs. altitude. Error checking of the input parameters is implemented. For each of these models, a brief writeup has been completed to assist the user. Interface development was worked on for the NASA radiation belt models and ephemeris program LOKANGL. The radiation belt model package puts integrated flux as a function of L shell for specified energy, and B/B_0 for the AP8 and AE8 models. It was planned to include CRRES models. The LOKANGL interface is more challenging because of the many inputs and outputs involved.

A demonstration of the interface was given to the initiator with 18 completed writeups. An X-Windows interface was completed for NASA radiation belt models AP8MIN, AP8MAX, AE8MIN, and AE8MAX. Writeups were completed for these models, the CRRES radiation belt dose model, and for the Hilmer-Voigt magnetic field model. For the CRRES dose model, a FORTRAN routine was built which uses tables acquired from PL's CRRESRAD, since the CRRESRAD package had been written in PASCAL. These tables supply mean dose in bins specified by L and B/B_0 . The FORTRAN routines for the radiation belt models and for the Hilmer-Voigt model were timed, and sample results generated, for inclusion in the writeups.

The IGRF95 magnetic field model was added to the geophysical models data library. Code to run the model was imported from NSSDC. This code uses the fast Kluge method to compute magnetic field parameters, including L-shell. Test cases were run for the IGRF95 model and results were inserted into the writeup, including time statistics.

11.3 SSJ4/5

Radex has developed improved codes for the computation of Corrected Geomagnetic (CGM) Coordinates for use by the Space Forecasting Center, and for the research community. Particular improvements were made in codes for Altitude Dependent Corrected Geomagnetic Coordinates. The codes in question were CGLALO, CGLALO_INVERSE and SFC_CONVERT_GEO_COORD.

The CGLALO and CGLALO_INVERSE codes are used for low altitudes, and are table lookup and interpolation codes which are efficient routines for the computation of CGM coordinates and their inverses for 0 km altitude. These two codes also form the basis for the Altitude Dependent Corrected Geomagnetic Coordinates (and their inverses) routine SFC_CONVERT_GEO_COORD in the sense that they provide the “boundary” conditions for the latter at 0 km altitude.

The need for these coordinates is based upon the fact that ionospheric processes and the motion of charged particles, both in the ionosphere and the radiation belts, are determined by Earth’s magnetic field. In the early period of space exploration, the use of Geomagnetic Coordinates, a spherical coordinate system aligned with a earth centered dipole field, was suitable for the analysis of rocket and satellite based observations of the motion of charged particles and ionospheric phenomena.

As improvements in observational techniques were developed, and more precise measurements became possible, it became necessary to develop coordinate systems which more closely reflected the actual magnetic field of the Earth. These *Corrected* Geomagnetic Coordinate (CGM) systems were based upon magnetic field line tracing using magnetic field models, in which the magnetic field is represented by the negative gradient of a magnetic scalar potential.

The original procedure to compute CGM coordinates was as follows: A real field line from Earth’s surface is traced to the centered dipole equator. This point is defined to be equivalent to a line trace along a centered dipole field. The latitude and longitude of the landing point in centered dipole coordinates are the desired “corrected” geomagnetic coordinates.

CGM coordinates, unlike geographic coordinates or centered magnetic dipole coordinates, are distorted, the distortion being a reflection of the deviation of the Earth’s magnetic field from a centered dipole. An Earth globe based upon CGM coordinates will distort distances and angles between pairs of points compared to one based upon geographic coordinates. This distortion will be particularly evident in the South Atlantic Magnetic Anomaly (SAA), where the actual (offset location) of the dipole component of Earth’s magnetic field is closest to Earth’s surface.

The CGM coordinates for a given magnetic field model were provided to users in the form of a table for a uniform geographic coordinate grid (uniform spacing in latitude and longitude). Some of these tables were incomplete, and excluded low (CGM) latitudes. The CGLALO routine incorporates such a table, and uses four point interpolation to compute the CGM coordinates except for the immediate vicinity of the CGM poles. For the latter a three-point interpolation is used, with the pole being one of the three points. CGLALO_INVERSE routine computes the geographic coordinates from CGM by using a search routine, and then performing a Newton-Ralphson procedure using the CGLALO routine. The current versions of these two routines CGLALO95 and CGL95INV are based upon the IGRF 1995 Magnetic Field Model. To alleviate (and smooth) distortions in the vicinity of the magnetic equator, the IGRF 1990 and 1995 tables used to generate CGLALO were modified as follows:

The magnetic dip equator is the set of points on the Earth reference sphere at which the actual

magnetic field lines (as defined by the magnetic field model) are tangent to the sphere. Note that the dip equator does not actually lie in a plane, but is taken as the reference plane (equator) for CGM coordinates. From the original tables, the entries within a band of ~15 degrees around the magnetic dip equator were deleted, and replaced by values obtained using a spline fit, with the added constraint that the spline curve passes through the coordinates of the dip equator.

The `SFC_CONVERT_GEO_COORD` routine computes Altitude Adjusted Corrected Geomagnetic Coordinates from Geographic Coordinates and altitude, and, where they exist, the inverse from CGM coordinates and altitude. In this enhancement of the CGM coordinate system concept, the CGM coordinates of an actual field line are constant for the portion of the field line north or south of the dip equator (at 0 km altitude), and differ only in the sign of CGM latitude. The CGM coordinates are the landing points of the field line as defined by the `CGLALO95` routine. The altitude range for the current version is 0 - 7200 km; previous versions had an altitude range from 0 - 2000 km.

The original version was developed by *Baker and Wing* [1989]. In their method, the corrected geomagnetic coordinates (and the corresponding inverses) are computed by evaluation of functions for the X, Y, and Z components of a unit vector obtained from a fourth order spherical harmonic expansion. They first computed the coefficients for the X, Y, Z components of a unit vector in the magnetic dipole coordinates for both the forward and inverse transformations for altitudes 0, 150, 300 and 450 km. They developed an interpolation/extrapolation scheme for computing the spherical harmonic coefficients for altitudes from 0 to 2000 km altitude. Since they were primarily concerned with representing higher CGM latitudes, the South Atlantic Anomaly/equatorial problem described above, and the equatorial discontinuity problem (described below) were not taken into account. As a result, the features of the South Atlantic Anomaly and the equatorial region are not well represented in the Baker and Wing computation.

Subsequent versions are based upon an improved method described in *Bhavnani and Hein* [1994], with the current version based on additional improvements described in *Hein and Bhavnani* [1996]. These versions alleviated the equatorial discontinuity problem which arises as follows: For increasing altitude, field lines above the dip equator have landing points further away from the equator, resulting in a discontinuity in the altitude adjusted CGM coordinates at the dip equator. For mathematical reasons, it is not practical to use a ground-based dipole coordinate system for either computing the spherical harmonic coefficients or the spherical harmonic expansion. Instead, it was found that the use of dipole coordinates at altitude and the use of an altitude dependent latitude adjustment algorithm alleviated the discontinuity.

This approach provides an improved representation of the South Atlantic Anomaly region, and a solution to the equatorial discontinuity problem. For the 0 - 2000 km altitude versions, spherical harmonic fits to the direct and inverse transformations were performed for altitudes 0, 300 and 1200 km, and the altitude dependence of the spherical harmonic coefficients was expressed as a quadratic interpolation and extrapolation to the individual coefficients. For the 0 - 7200 km version, spherical harmonic fits to the direct and inverse transformations were performed for 24 altitudes between 0 and 7200 km, and a 5th order (4th degree) weighted polynomial fit was performed for each of the

spherical harmonic coefficients.

Since the altitude adjusted CGM coordinates along a field line trace are (by definition) constant on a CGM hemisphere, and differ only by the sign of the CGM latitude as they cross hemispheres, it is possible to use the current version (and, with less accuracy, the two previous versions) for field line tracing. A description of the field line trace application and comparisons of the results with precise field line tracing routines are presented in *Hein and Bhavnani* [1996]. Overall, with the exception of the region in the vicinity of the South Atlantic Anomaly, agreement is better than a few tenths of a degree of arc. A comparison is provided in the following graphs. Figure 93 is a graph of the "landing points" for a field line trace from 850 km to ground using an initial grid of 2 degrees in latitude (88, 86, ..., 2, 0, -2, ..., -88) and 10 degrees in longitude (0, 10, ..., 350). Figure 94 is a similar graph using the SFC_CONVERT code.

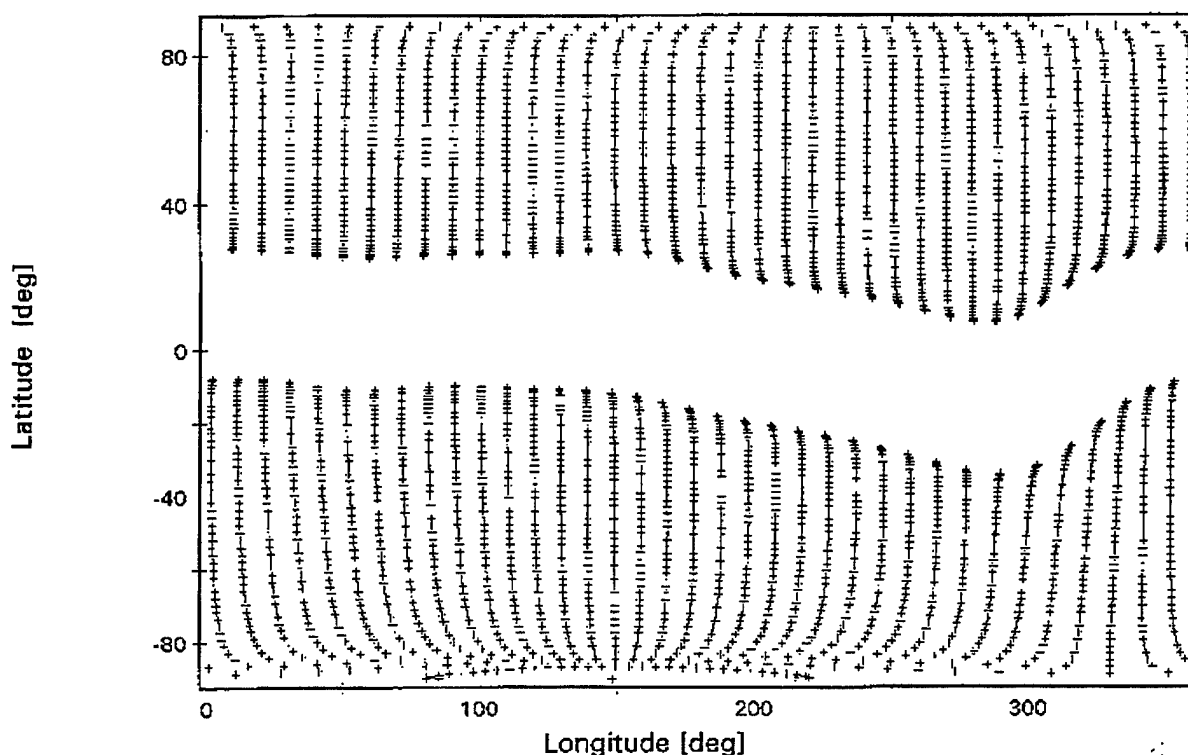


Figure 93. Magnetic field line trace from altitude to ground, using the IGRF 1995 model, altitude 850 km.

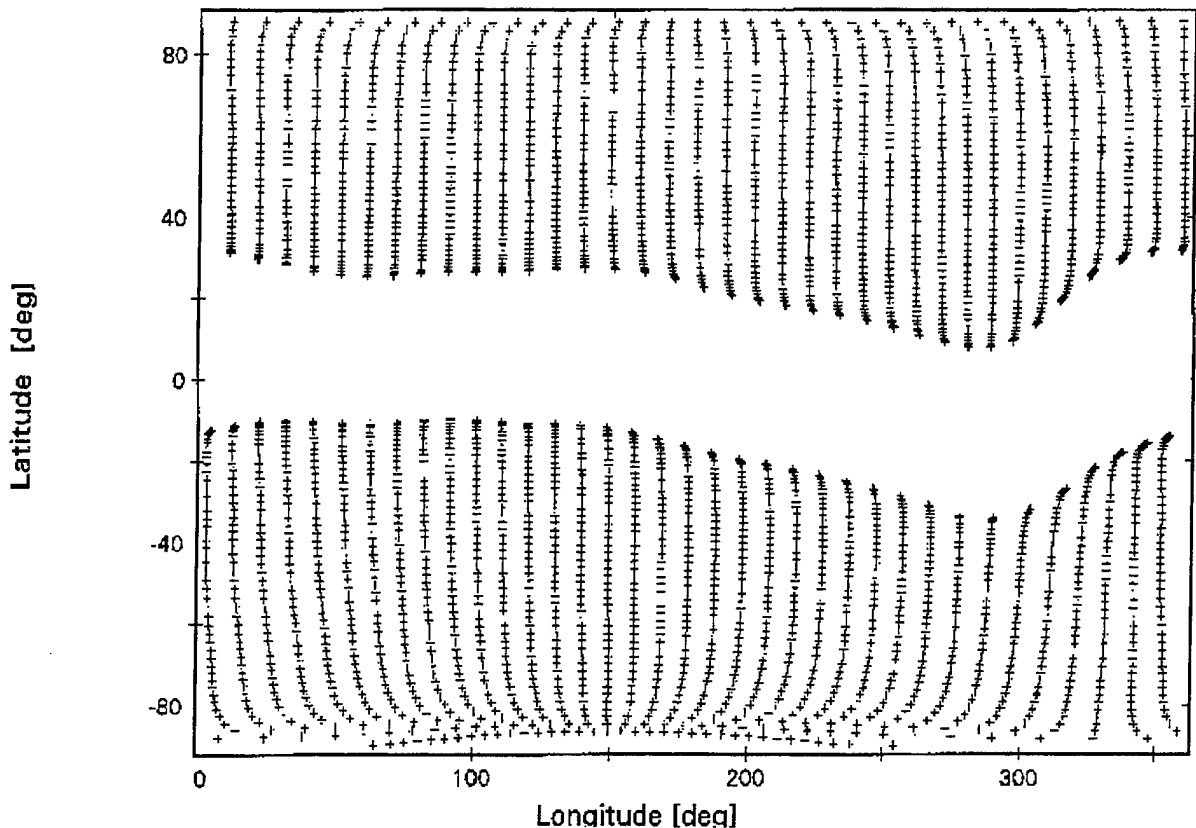


Figure 94. Magnetic field line trace from altitude to ground using the SFC CONVERT_GEO_COORD routine for 1995.

Versions of the SFC_CONVERT_GEO_COORD routine (which differ only in the Spherical Harmonic Coefficients) were prepared for earlier IGRF models: 1975, 1980, 1985 and 1990 at the request of the sponsor for the research community to facilitate the analysis of existing observational data.

11.4 COMPARISON OF LOKANGL AND SPACETRACK CODES FOR ORBIT PREDICTION

The SPACETRACK code implements five different analytic perturbation schemes compatible with the NORAD satellite elements distributed by SPACECOM. The NORAD elements are mean elements which differ significantly from osculating (instantaneous position and velocity, or equivalent Keplerean elements) by modeling perturbations due to deviations of Earth's gravitational field from spherical symmetry, and the effect of Earth's atmosphere upon satellite orbits. There is no "standard" definition of mean elements; each particular definition is characterized by the perturbations which are taken into account (modeled) and those which are ignored. The SPACETRACK codes enable users to make Position and Velocity predictions using the NORAD elements. The SPACETRACK code is described in the NORAD document "SPACETRACK

REPORT #3 - Models for Propagation of NORAD Element Sets", December 1980.

According to the SPACETRACK report, the models recommended for element prediction are the SGP4 for near-earth satellites (orbital periods < 225 minutes) and SDP4 for longer period satellites. The latter model takes into account certain "resonance" terms in Earth's gravitational field for synchronous satellites, and for 12-hour period satellites, as well as perturbations due to the sun and moon. In addition to SGP, SGP4 and SDP4 models, two additional models are available in SPACETRACK, SGP8 and SDP8, which are improved versions of SGP4 and SDP4, which, according to the document, had not yet been adopted.

We have adapted the SPACETRACK code to convert the predicted position and velocity vectors into spherical coordinates: Altitude (above the Earth reference ellipsoid), latitude (geocentric and geodetic) and geographic longitude. The selection of these models, unless overridden by the user, is automatic. We have compared the results of the SPACETRACK code predictions with LOKANGL, a standard PL satellite ephemeris code.

LOKANGL and the five SPACETRACK prediction models differ in the manner in which the perturbations described above are taken into account (or ignored). LOKANGL is primarily intended for post-mission processing, and not for prediction. For any satellite ephemeris prediction code, it should be expected that the predictions will degrade in accuracy with time. Three satellites with significantly different orbital characteristics were chosen to evaluate the performances of these codes in orbital prediction mode. The Mir satellite was chosen for the study because it is in a relatively high drag environment due to its low altitude. DMSP F7 was chosen because it is relatively free of atmospheric drag effects because of its ~800 km altitude circular orbit. CRRES was chosen because of its high eccentricity and long period, where it is affected both by drag and by lunar-solar perturbations. LOKANGL does not treat the latter.

The results of this comparison are presented in Figures 95 - 101 and are described below. The figures provide a comparison of the in-track (position along the orbit) difference, and in the predictions of LOKANGL and the SGP4, SDP4, and SGP models. We obtained the best agreement between LOKANGL and the SPACETRACK SGP model, undoubtedly because they used similar prediction algorithms. These graphs provide the worst cases encountered from a sample of three runs for each satellite. DMSP F7 is in a near-circular 800 km altitude orbit. Mir is in a near circular ~400 km orbit, and CRRES is in an eccentric orbit (eccentricity ~0.72) with perigee at ~300 km.

Note that the SGP and (SGP4/SDP4) models use different input variables for modeling of drag. For SGP the input variable \dot{N} (derivative of mean motion) is used; for SGP4/SDP4 a drag coefficient B^* is used. If the values supplied in the NORAD elements are inconsistent (a situation which can occur with shuttle missions, or if either \dot{N} or B^* are absent), the differences over a ten day interval can be substantial.

The results of this study show that the predictions of LOKANGL and the SPACETRACK models are comparable, so that in-track differences over a few days rarely exceed 10 km. In Figures 101 -

104 a separate investigation of the SPACETRACK code predictions shows that propagated orbits from one element set tend to differ in-track at the next element set by similar amounts. Prediction using SPACETRACK models is therefore unnecessary unless required by other user agencies.

In Figures 98-101, a subset of elements issued by SPACECOM is randomly selected over an interval of approximately 100 days. The orbit is propagated from each element set to the next element set, where the in-track error is evaluated. The vertical displacement exhibits the in-track error associated with the interval between the epochs of the selected elements. The symbol is placed at the predicted in-track error at the time of the subsequent element set. The vertical component of the line length reflects the in-track prediction accuracy of the model used as compared with the following element set. These graphs illustrate the limitations of both the predictions of these models, and of the orbital fitting process which produce the element sets (which, of course are based upon observations of variable accuracy).

In comparing Figures 100 and 101 it should be noted that SGP4 exhibits a biased predictive error not seen with SDP4, so that SDP4 is indeed superior for "deep space" orbits.

For interpolation use between element sets (post-mission), and when Cartesian state vector element sets are provided, LOKANGL is currently the only choice available. In the interpolation mode the performance of LOKANGL for various satellites was reported in *Hein and Robinson* [September 1991].

Comparison: Ephemeris Predictions for SGP4 and LOKANGL

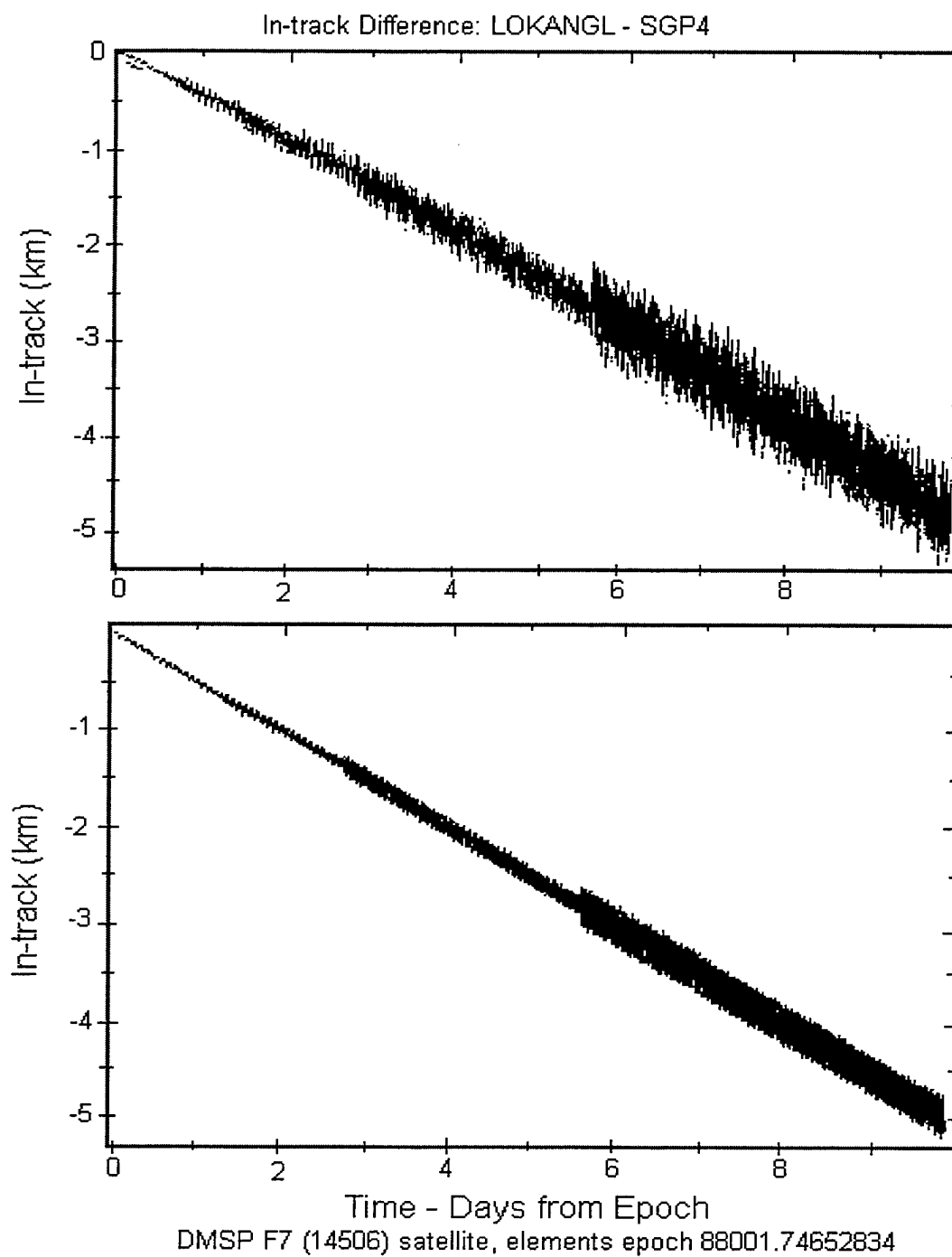
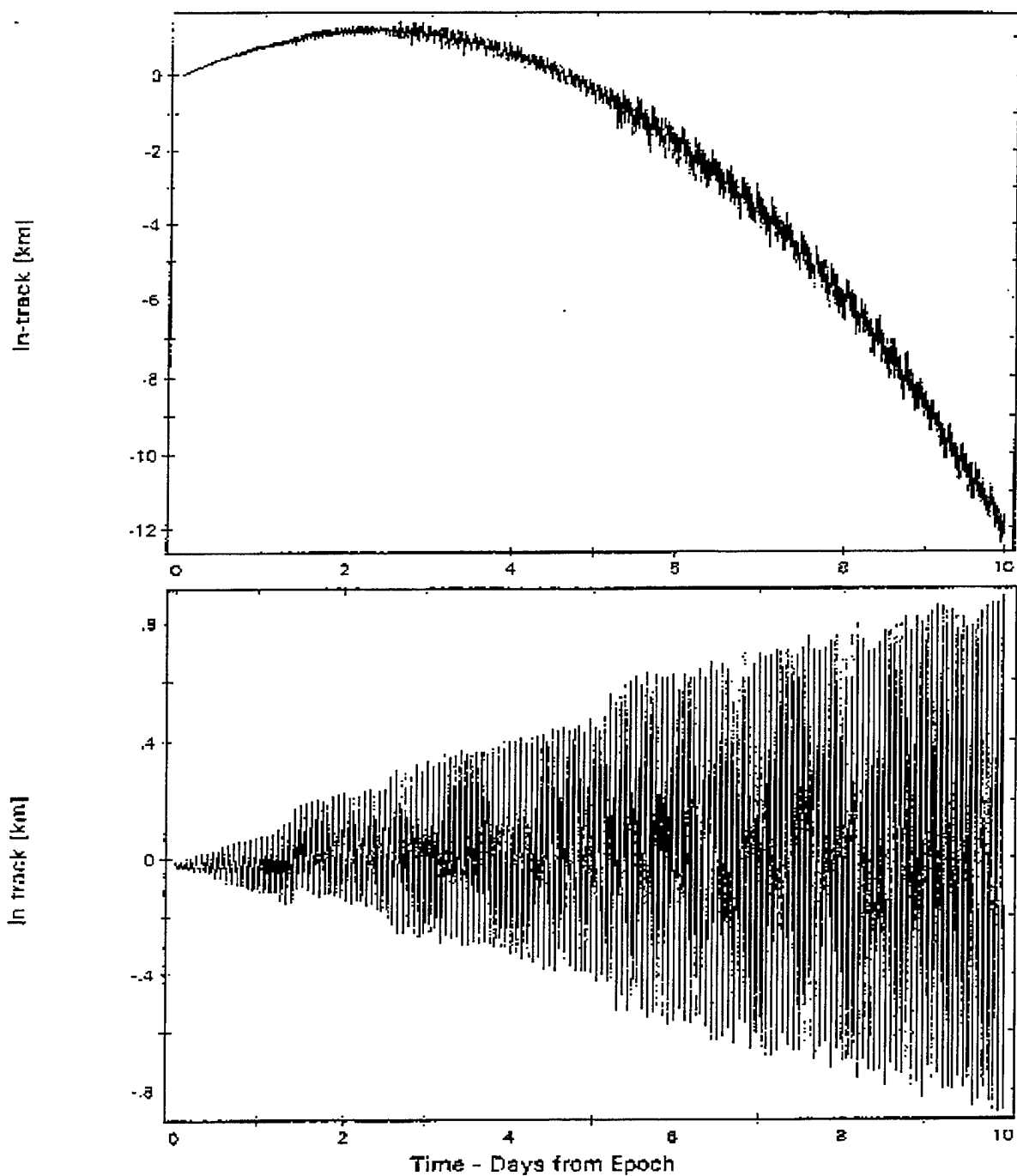


Figure 95. In-track differences between the predictions of LOKANGL and SGP4 (top) and LOKANGL and SGP (bottom), for DMSP F7 (14506).

Comparison: Ephemeris Predictions for SGP4 and LOKANGL

In-track Difference: LOKANGL - SGP4



Mir : 16609, elements epoch 84332.37130088

DATE RUN: 26 May 96

Figure 96. In-track differences between the predictions of LOKANGL and SGP4 (top) and LOKANGL and SGP (bottom), for the Mir satellite (16609).

Comparison: Ephemeris Predictions for SDP4 and LOKANGL In-track Difference: LOKANGL - SDP4

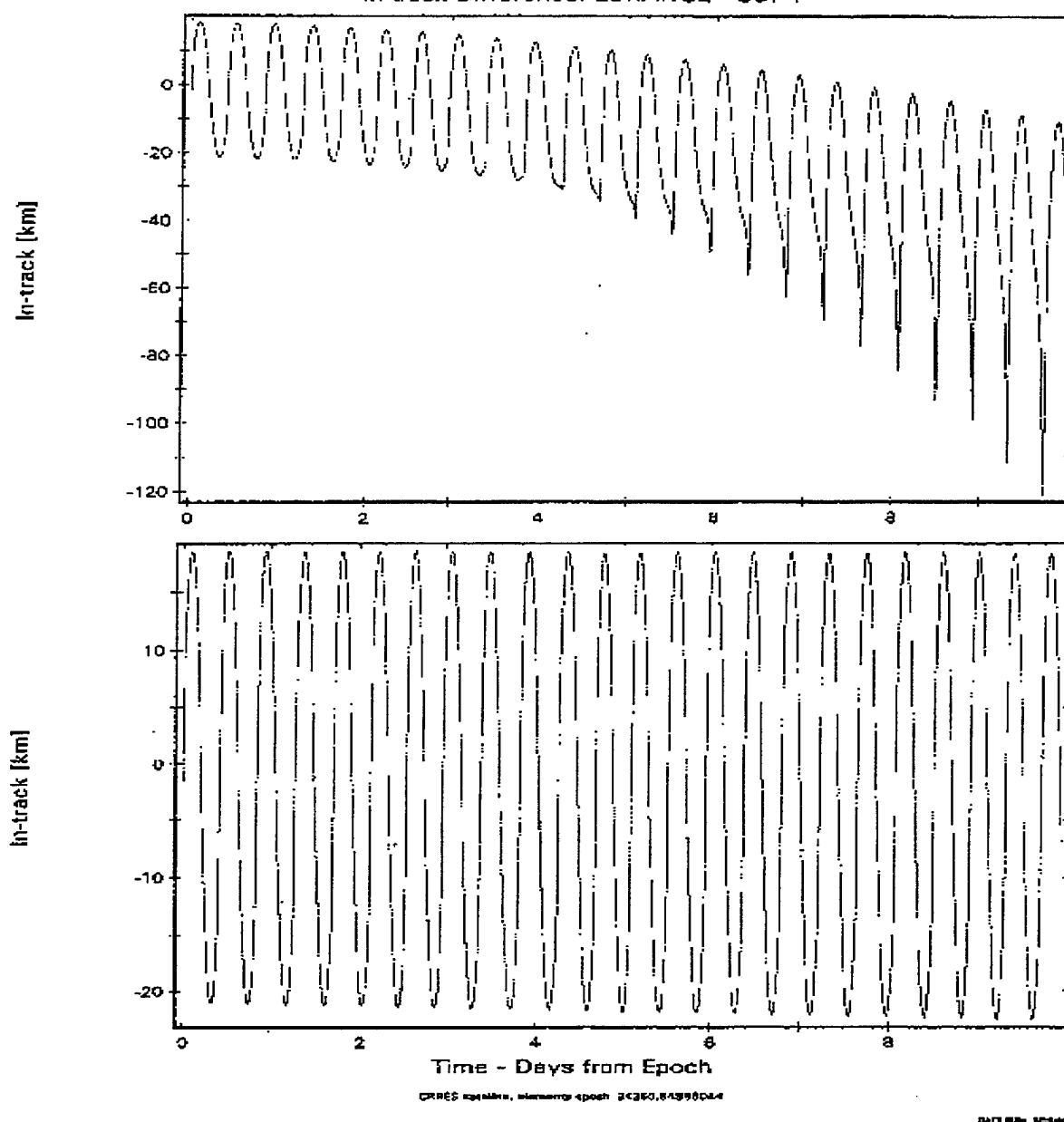


Figure 97. In-track differences between the predictions of LOKANGL and SDP4 (top) and LOKANGL and SGP (bottom), for the CRRES satellite (20712). The oscillation period evident in these figures is the same as the orbital period (~ 2.3 rev/day).

SGP4 PROPAGATOR IN-TRACK DEVIATIONS FOR DMSPF7
SATELLITE ELEMENT SETS SPANNING 87077 TO 87352

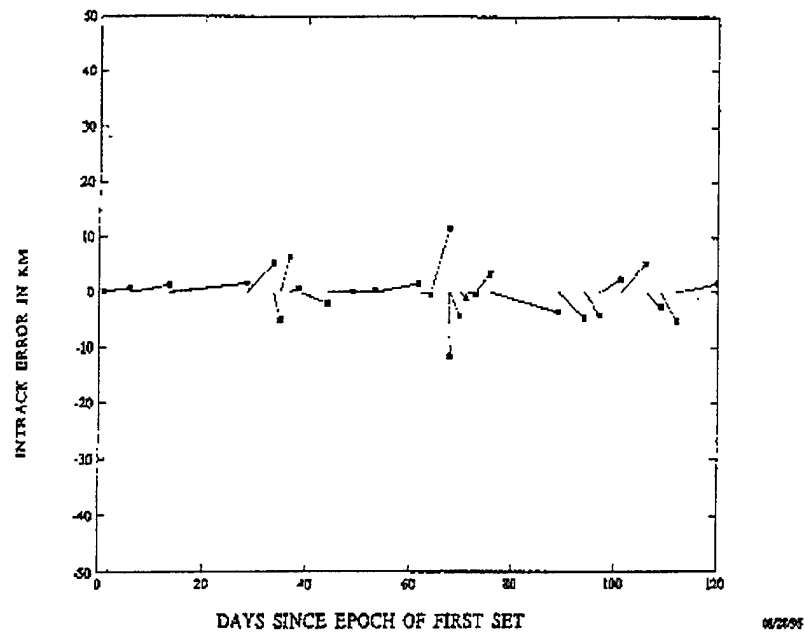


Figure 98. In-track prediction accuracy of SGP4 for DMSP F7.

SGP4 PROPAGATOR IN-TRACK DEVIATIONS FOR MIR
SATELLITE ELEMENT SETS SPANNING 95025 TO 95136

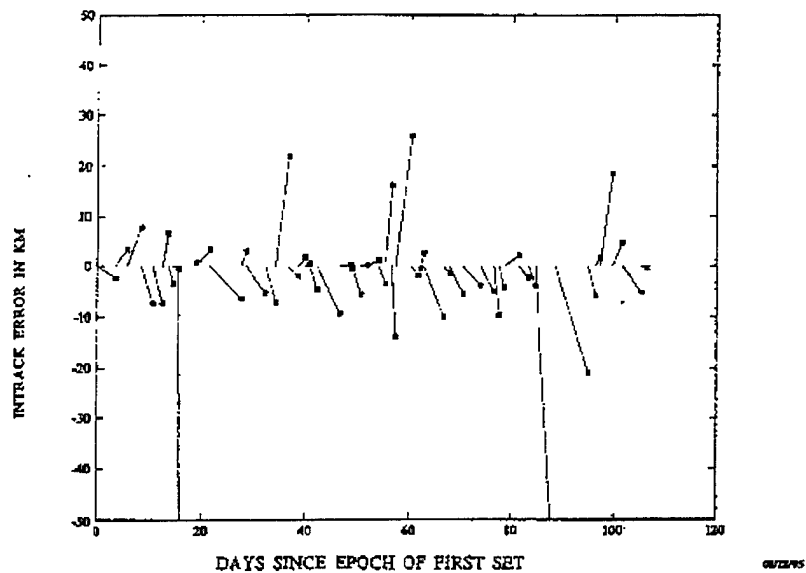


Figure 99. In-track prediction accuracy of SGP4 for Mir.

SDP4 PROPAGATOR IN-TRACK DEVIATIONS FOR CRRES
SATELLITE ELEMENT SETS SPANNING 95002 TO 95136

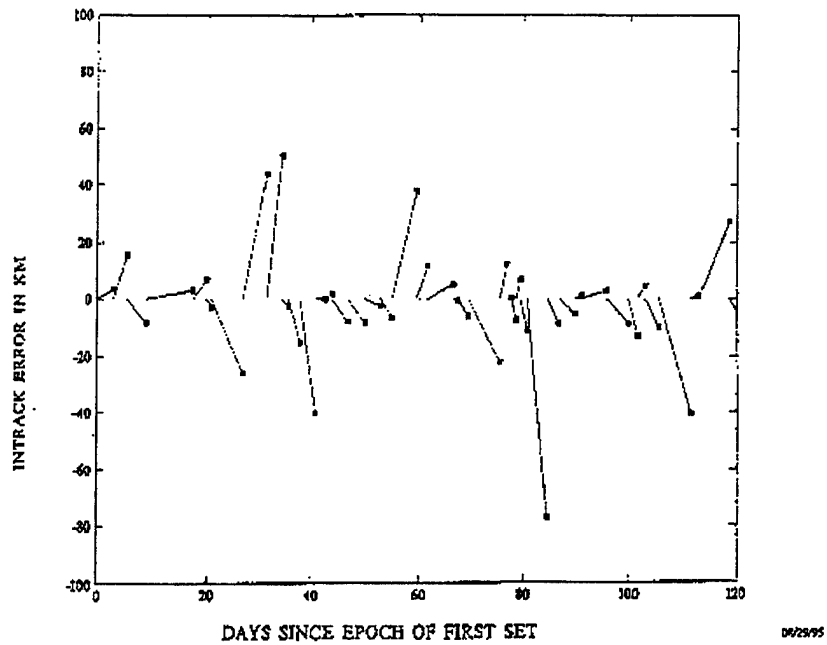


Figure 100. In-track prediction accuracy of SDP4 for CRRES.

SGP4 PROPAGATOR IN-TRACK DEVIATIONS FOR CRRES
SATELLITE ELEMENT SETS SPANNING 95002 TO 95136

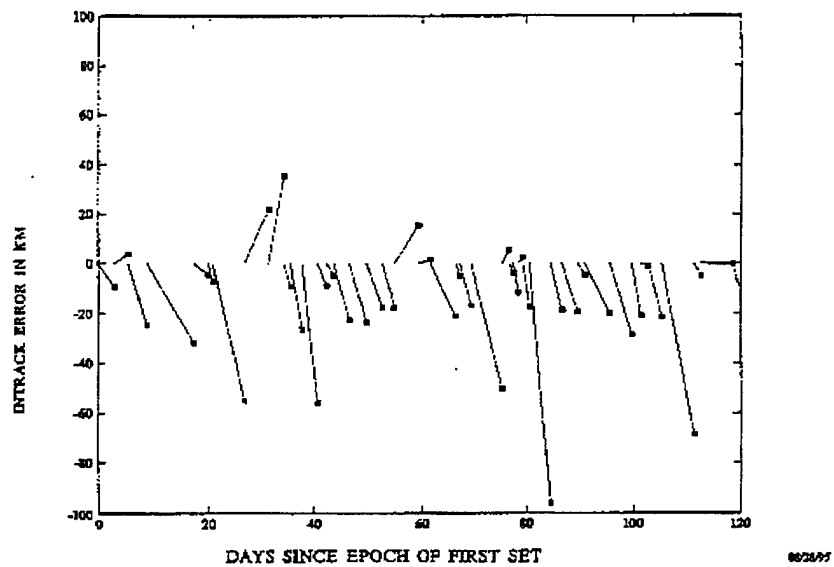


Figure 101. In-track prediction accuracy of SGP4 for CRRES.

REFERENCES

- Aarons, J. and S. Basu, "Scintillation on Transionospheric Radio Signals", Handbook of Geophysics and the Space Environment, A. S. Jursa, ed., AFGL/AFSC/USAF, 1985, ADA167000.
- Alishouse, J. C., J. B. Snider, E. R. Westwater, C. T. Swift, C. S. Ruf, S.A. Snyder, J. Vongsathorn, and R. R. Ferraro, "Determination of cloud liquid water content using the SSM/T", *IEEE Trans. Geosci. Remote Sensing*, Vol. 28, Pp. 817-821, 1990.
- Arfken, G., "Mathematical Methods for Physicists", Academic Press, New York, 1985.
- The Astronomical Almanac*, National Almanac Office, U. S. Naval Observatory, and Her Majesty's Nautical Almanac Office, Royal Greenwich Observatory, U. S. Government Printing Office, Washington, and Her Majesty's Stationery Office, London, 1984.
- Baker, K. B. and S. Wing, "A new magnetic coordinate system for conjugate studies at high latitudes", *J. Geophys. Res.*, 94, 9139, 1989.
- Bass, J. N., Hein, C. A., Jordan, C. E., and Vancour, R. P., "Analysis and Modeling of the CRRES Satellite Data", PL-TR-92-2086, 1992, ADA254349.
- Bass, J. N., N. A. Bonito, C. A. Hein, W. J. McNeil, D. S. Reynolds, C. J. Roth, M. F. Tautz, K. H. Bhavnani, K. Bounar, C. J. Jordan, M. M. Pratt, F. R. Roberts, D. A. Sannerud, and R. P. Vancour, "Integrated Analytical Evaluation and Optimization of Model Parameters Against Preprocessed Measured Data", GL-TR-89-0163, Geophysics Laboratory, Hanscom AFB, MA, 23 June 1989, ADA215518.
- Bass, J. N., K. H. Bhavnani, N. A. Bonito, C. M. Bryant, Jr., W. J. McNeil, F. R. Roberts, D. A. Sannerud, and A. J. Kantor, "Integrated Systems with Applications to the Multi-Phases of the Ephemerides, Physics, and Mathematics of the Upper Atmosphere", AFGL-TR-87-0064, February, 1987, ADA185748.
- Bass, J. N., K. H. Bhavnani, B. J. Guz, R. R. Hayes, P. N. Houle, S. T. Lai, and L. A. Whelan, "Analysis and Programming for Research in Physics of the Upper Atmosphere", AFGL-TR-76-0231, September 1976, ADA034066.
- Basu, S., E. Kudeki, Su. Basu, C. E. Valladares, E. J. Weber, "Scintillations, Plasma Drifts, and Neutral Winds in the Equatorial Ionosphere After Sunset", PL-TR-97-2035, Dec 96, ADA323542.

- Basu, S., Su. Basu, J. J. Sojka, R. W. Schunk, E. MacKenzie, "Macroscale modeling and mesoscale observations of plasma density structures in the polar cap", *Geophys. Res. Lett.*, 22, 8, p881-884, April 1995.
- Basu, S. and Su. Basu, "Equatorial Scintillations: Advances Since ISEA-6", AFGL-TR-86-0027, 1985, ADA164801.
- Bauer, P. and N. C. Grody, "The potential of combining SSM/I and SSM/T measurements to improve the identification of snowcover and precipitation", *IEEE Trans. Geosci. Remote Sensing*, Vol. 33, p. 252, 1995.
- Bhavnani, K., C. A. Hein, "An Algorithm for Computing Altitude Dependent Corrected Geomagnetic Coordinates", Phillips Laboratory Technical Report PL-TR-94-2310, 1994, ADA293967.
- Bhavnani, K. H., and R. P. Vancour, "Coordinate Systems for Space and Geophysical Applications", PL-TR-91-2296, 1991, ADA247550.
- Bohren, C. F., D. R. Huffman, "Absorption and Scattering of Light by Small Particles", New York: John Wiley & Sons, 1983.
- Boriakoff, V., K. H. Bounar, and E. W. Cliver, "Power spectra of the geomagnetic aa index: Simulation of observed differences between even- and odd-numbered solar cycles", *J. Geophys. Res.* (in preparation), 1997.
- Bounar, K. H., E. W. Cliver, and V. Boriakoff, "A prediction of the peak sunspot number for solar cycle 23", *Nature* (in preparation), 1997.
- Brautigam, D. H., M. S. Gussenhoven, and E. G. Mullen, "Quasi-static model of outer zone electrons", *IEEE Trans. Nucl. Sci.*, 39, 1797 (1992)
- Chapman, S., and J. Bartels, *Geomagnetism*, Oxford at the Clarendon Press, London, 1940.
- Chapront-Touze, M. and J. Chapront, *Astron. Astrophys.* 124, 50, 1983.
- Chernosky, E. J., "Double sunspot-cycle variation in terrestrial magnetic activity, 1884-1963", *J. Geophys. Res.*, 71, 965, 1966.
- Cliver, E. W., K. H. Bounar, and V. Boriakoff, "The solar wind during Maunder minimum", *Nature* (in preparation), 1997.
- Cliver, E. W., V. Boriakoff, and K. H. Bounar, "The 22-year cycle of geomagnetic and solar wind activity", *J. Geophys. Res.* 101, 27091, December 1, 1996.

- Daniell, R. E. and D. N. Anderson, "Realtime operational ionospheric specification and forecast models (WBMOD V.13)", paper 95-0549, presented at AIAA Meeting, Reno NV, 1995.
- Dickinson, R. E., E. C. Ridley, and R. G. Roble, "A three-dimensional general circulation model of the thermosphere", *J. Geophys. Res.*, Vol. 86, Pp. 1499-1512, 1981.
- Dickinson, R. E., E. C. Ridley, and R. G. Roble, "Thermospheric general circulation with coupled dynamics and composition", *J. Atmos. Sci.*, Vol. 41, Pp. 205-219, 1984.
- Eddy, J. A., "Maunder minimum", *Science*, 192, 1189-1203 (1976).
- Escobal, P. R., *Methods of Orbit Determination*, Robert E Krieger Publishing Company, Malabar, FL, 1965.
- Escobal, P. R., *Methods of Orbit Determination*, 2nd edition, Robert E. Krieger Publishing Company, Malabar, FL, 1976.
- Eversole, W. L., and R. E. Nasberg, "Maximum Likelihood Estimation for Image Registration", SPIE Proceedings, Volume 432, August, 1983.
- Explanatory Supplement to the Astronomical Almanac*, Siedelman, P. K., editor, University Science Books, Mill Valley CA, 1992.
- Falcone, V. J. Jr., L. W. Abrev, and E. P. Shettle, "Atmospheric Attenuation of Millimeter and Submillimeter Waves: Models and Computer Code", Air Force Geophysics Laboratory, Hanscom AFB, MA, AFGL-TR-79-0253, 15 Oct 1979, ADA084485.
- Fegley, B., Jr., and A. G. W. Cameron, "A vaporization model for iron/silicate fractionation in the Mercury protoplanet, *Earth Planet. Sci. Lett.*, 82, 207, 1987.
- Feynman, J. and N. U. Crooker, "Solar wind at the turn of the century", *Nature* 275, 626-627 (1978).
- Fleeter, R., Micro Space Craft, p. 14, The Edge City Press, Reston, VA, 1995.
- Fremouw, E. J. and J. F. Bates, "Worldwide behavior of average UHF-UHF scintillation", *Radio Sci.*, 6, 863, 1971.
- Fuller-Rowell, T. J., M. V. Codrescu, R. J. Moffett, and S. Quegan, "Response of the thermosphere and ionosphere to geomagnetic storms", *J. Geophys. Res.*, Vol. 99, Pp. 3893-3914, 1994.
- Gonzalez, W. D., B. T. Tsurutani, A. L. C. Gonzalez, E. J. Smith, F. Tang, and S-I. Akasofu, "Solar wind-magnetosphere coupling during intense magnetic storms,(1978-1979)", *J. Geophys. Res.*, 94, 8835, 1989

- Granier, C. P., J. P. Jegou, and G. Megie, "Atomic and ionic calcium in the upper atmosphere", *J. Geophys. Res.*, **94**, 9917, 1989.
- Griffin, J. M., and Bass, J. N., "Programmer and End User Guide for Processing LEPA Data Files", PL-TR-95-2083, 1995, ADA301063.
- Gussenhoven, M. S., E. G. Mullen, M. D. Violet, C. Hein, J. Bass, and D. Madden, "CRRES high energy proton flux maps", *IEEE, Trans. Nucl. Sci.*, **40**, 1450-1457 (1993).
- Haerendel, G., "Theory of equatorial spread-F", preprint, Max-Planck-Institut für Extraterrestr. Phys., Garching bei München, Germany, 1973.
- Hapgood, M. A., "A double solar cycle in the 27-day recurrence of geomagnetic activity", *Ann. Geophys.*, **11**, 248, 1993.
- Hardy, D. A., Walton, D. M., Johnstone, A. D., Smith, M. F., Gough, M. P., Huber, A., Pantazis, J., and Burkhardt, R., "Low Energy Plasma Analyzer", *IEEE Trans. Nucl. Sci.*, Vol. 40, No. 2, pp. 246-251, 1993a.
- Hardy, D. A., Walton, D. M., Johnstone, A. D., Smith, M. F., Gough, M. P., Huber, A., Pantazis, J., and Burkhardt, R., "The All New, Improved, Revised and Expanded Story of L", unpublished, 1993b.
- Hardy, D. A., M. S. Gussenhoven, and E. Holeman, "A statistical study of auroral electron precipitation", *J. Geophys. Res.*, **90**, A5, 4229-4248, 1985.
- Hardy, D. A., M. S. Gussenhoven, and D. Brautigam, "A statistical study of ion precipitation", *J. Geophys. Res.*, **94**, A1, 370-392, 1989.
- Hedin, A. E., "Correlations between the thermospheric density, temperature, solar EUV flux, and 10.7 cm flux variations", *J. Geophys. Res.*, Vol. 89, p. 9828, 1984.
- Hedin, A. E., "MSIS-86 thermosphere model", *J. Geophys. Res.*, Vol. 92, Pp. 4649-4662, 1987.
- Hedin, A. E., "Extension of the MSIS thermosphere model into the middle and lower atmosphere", *J. Geophys. Res.*, Vol. 96, Pp. 1159-1172, 1991.
- Hedin, A. E., M. A. Biondi, R. G. Burnside, G. Hernandez, R. M. Johnson, T. L. Killeen, C. Mazaudier, J. M. Meriwether, J. E. Salah, R. J. Sica, R. W. Smith, N. W. Spencer, V. B. Wickar, and T. S. Viridi, "Revised model of thermosphere winds using satellite and ground-based observations", *J. Geophys. Res.*, Vol. 96, Pp. 7657-7688, 1991.

- Hein, C. A., and K. Bhavnani, "An Expanded Algorithm for Computing Altitude-Dependent Corrected Geomagnetic Coordinates", Phillips Laboratory, PL-TR-96-2274, 1996, ADA324654.
- Hein, C. and J. Bass, "Modeling the DMSP and CRRES dosimeters using the Path Length Distribution Method.", Phillips Laboratory, PL-TR-93-2120, 1993, ADA269898.
- Hein, C. A. and E. C. Robinson, *Private Communication*, September 1991.
- Hein, C. A. and E. C. Robinson, *Private Communication*, April, 1991.
- Heinemann, M. A., T. Totten, A. G. Rubin, and K. H. Bounar, "The Solar Wind From L1 Through the Magnetopause", ISTP Workshop, Hitachi, Japan, 1996.
- Hilmer, R. V. and G. H. Voigt, "A magnetostatic magnetic field model with flexible current systems driven by independent physical parameters", *J. Geophys. Res.*, 100, 5613, 1995.
- Hoffleit, D. and W. H. Warren, Jr. "The Bright Star Catalogue, Astronomical Data Center", NSSDC/GSFC, 1991.
- Hogg, D. C., F. O. Guiravo, J. B. Snider, M. T. Decker, and E. R. Westwater, "A steerable dual-channel microwave radiometer for measurement of water vapor and liquid in the troposphere", *J. Climate Appl. Meteor.*, Vol. 22., Pp. 789-806, 1983.
- Hollinger, J. P., J. L. Pierce, and G. A. Poe, "SSM/I instrument evaluation", *IEEE Trans. Geosci. Remote Sensing*, Vol. 28, Pp. 781-790, 1990.
- Hoots, F. R. and R. L. Roehrich, "Spacetrack Report No. 3: Models For Propagation of NORAD Element Sets", Department of Commerce, National Technical Information Service, Springfield, VA, 1980, (also available from FTP site archive.afit.af.mil as /pub/space/spacetrk.doc (SPACETRK)).
- Hughes, D. W., "The meteorite flux", *Space Science Reviews*, **61**, 275, 1992.
- Hughes, D. W., "Cosmic Dust Influx to the Earth", *Space Science XV*, Akademie-Verlag, Berlin, 1975.
- Hunten, D. M., R. P. Turco, O. B. Toon, "Smoke and dust particles of meteoric origin in the mesosphere and stratosphere", *J. Atmos. Sci.*, **37**, 1342, 1980.
- IGA Division I, Working Group 1, "International Geomagnetic Reference Field Revision 1985", EOS, Vol. 67, No. 24, 1986.

- Jacchia, L. G., "New Static Models of the Thermosphere and Exosphere with Empirical Temperature Profiles", SAO Special Report No. 313, 1970.
- Jaspersen, W. H., D. E. Venne, M. R. Peterson, "A Single-Station Forecasting Model", PL-TR-92-2097, Phillips Lab, Hanscom AFB, MA, 1992, ADA256403.
- Kelly, M. C., "The Earth's Ionosphere", Int. Geophys. Ser., vol. 43, p. 71, Academic, San Diego, Calif., 1989.
- Kerns, K. J. and M. S. Gussenhoven, "CRRESRAD Documentation", PL-TR-92-2201, Phillips Lab, Hanscom AFB, MA, 1992, ADA256673.
- Kerns, K. J., "Programmer's Guide to LEPA", *Private Communication*, 1993.
- Killeen, T. L., and R. G. Roble, "Development of a Vector Spherical Harmonic (VSH) Neutral Thermosphere Model", PL-TR-93-2225, 1994, ADA282039.
- Kohn, D. J., "Refinement of a Semi-Empirical Model for the Microwave Emissivity of the Sea Surface as a Function of Wind Speed", Texas A&M Univ., Master's Thesis, Dec. 1995.
- Kwok, J. H., "The Artificial Satellite Analysis Program (ASAP) Version 2.0", JPL EM 312/87-153, Jet Propulsion Laboratory, Pasadena, CA, 1987.
- Liebe, H. J., G. A. Hufford, and T. Manabe, "A model for the complex permittivity of water at frequencies below 1 THz", *Int. J. Infrared Millimeter Waves*, Vol. 12, Pp. 659-674, 1991.
- Liebe, H. J., T. Manabe, and G. A. Hufford, "Millimeter-wave attenuation and delay rates due to fog/cloud conditions", *IEEE Trans. Ant. Prop.*, Vol. 37, p 1617, 1989.
- Lo, T. K., and G. Gerson, "Guidance System Position Updated by Multiple Subarea Correlation", SPIE Proceedings, Volume 186, May, 1979.
- Lou, G. Y., S. A. Mills, R. E. Smith, R. L. King, and W. W. Youngblood, "Models of Earth's Atmosphere (90 to 2500 KM)", National Aeronautics and Space Administration Space Vehicle Design Criteria Monographs: NASA SP-8021, National Technical Information Service, Springfield, VA, 1973.
- Love, S. G., and D. E. Brownlee, Heating and thermal transformation of micrometeoroids entering the Earth's atmosphere, *Icarus*, **89**, 26, 1991.
- Marcos, F. A., "Requirements for Improved Thermospheric Neutral Density Models", AAS Paper No. 85-312, AAS/AAIA Astrodynamics Specialist Conference, AAS Publications, San Diego, CA, 1985.

Marcos, F. A., *Private Communication*, 1995.

Marcos, F. A., J. N. Bass, D. Larson, J. J. Liu, and E. C. Robinson, "Satellite Drag Model Calibration and Feedback for Precision Low Earth Orbit Determination", Proceedings of the 1997 Space Control Conference, MIT Lincoln Laboratory, L. B. Spence, ed., Lexington, MA, 1997a.

Marcos, F. A., M. J. Kendra, J. M. Griffin, J. N. Bass, D. R. Larson, and J. J. Liu, "Precision Low Earth Orbit Determination Using Atmospheric Density Calibration", AAS Paper 97-631, 1997b.

Mayaud, P. N., "The aa indices: A 100 year series characterizing the magnetic activity", *J. Geophys. Res.*, 77, 6870, 1972.

McClure, J. P., W. B. Hanson, and J. H. Hoffman, "Plasma bubbles and irregularities in the equatorial ionosphere", *J. Geophys. Res.*, 82, 2650, 1977.

McIlwain, C. E., "Coordinates for mapping the distribution of magnetically trapped particles", *J. Geophys. Res.*, 66, No. 11, Pp. 3681-3691, 1961.

McKinnon, J. A., "Sunspot Numbers: 1610-1985", Rep. UAG-95, World Data Cent. A for Sol.-Terr. Phys., Boulder, Colo., 1987.

McNeil, W. J., "Differential Ablation of Cosmic Dust and Implications for the Relative Abundances of Atmospheric Metals, PL-TR-97-2134, Hanscom AFB, MA, September 1997, ADA339130.

McNeil, W. J., A. R. Long, M. J. Kendra, "Detection and Characterization of Equatorial Scintillation for Real-Time Operational Support", PL-TR-97-2059, April 1997, ADA329175.

McNeil, W. J., "A model for meteoric magnesium in the ionosphere", *J. Geophys. Res.*, 101, A3, 5251, 1996.

McNeil, W. J., E. Murad, and S. T. Lai, "Comprehensive model for the atmospheric sodium layer", *J. Geophys. Res.*, 100, D8, 16,847, 1995.

McNeil, W. J., "Simulation and Calculation of the APEX Attitude", PL-TR-92-2209, Hanscom AFB, Mass., 29 July 1992, ADA258716

McNeil, W. J., "Calculation and Modeling of the Attitude for the Combined Release and Radiation Effects Satellite", PL-TR-91-2239, Phillips Laboratory, Hanscom AFB, Mass., 26 September 1991, ADA243950.

- McNeil, W. J., "Aspects of the Calibration and Processing of the CRRES Fluxgate Magnetometer Data, PL-TR-93-2124, Phillips Laboratory, Hanscom AFB, Mass., 21 May 1993, ADA270127.
- Meffert, J. D. and M. S. Gussenhoven, "CRRESPRO Documentation", PL-TR-94-2218, 1994, ADA284578.
- Meffert, J. D., J. Bell, and M. S. Gussenhoven, *Private Communication*, 1996.
- Minka, K., "Orbit Determination and Analysis by the Minimum Variance Method", AFCRL 65-579, 1965.
- Montenbruck, O., T. Pfleger, "Astronomy on the Personal Computer", Springer-Verlag, 1991.
- Mullen, E. G., "The DMSP SSJ4 Electron Contamination Display: Technical User's Guide", Phillips Laboratory, 1996.
- National Ocean and Atmospheric Administration, National Aeronautics and Space Administration, United States Air Force, "U.S. Standard Atmosphere, 1976", NOAA-S/T76-1562, U.S. Government Printing Office, Washington, D.C., 1976.
- Nevanlinna, H., and E. Kataja, "An extension of the geomagnetic activity index series aa for two solar cycles (1844-1968)", *Geophys. Res. Lett.*, 20, 2703, 1993.
- Olson, W. P., and K. A. Pfitzer, Magnetospheric Magnetic Field Modeling, Annual Scientific Report, AFOSR Contract No. F44620-75-C-0033, McDonnell-Douglas Astronautics Company, Huntington Beach, CA, 1977.
- Olson, W. P. and K. A. Pfitzer, "A qualitative model of the magnetospheric magnetic field", *J. Geophys. Res.*, 79, 3739, 1974.
- Ossakov, S. L., "Spread-F theories - a review", *J. Atmos. Terr. Phys.*, 43,437,1981.
- Pfitzer, K. A., "Improved Models of the Inner and Outer Radiation Belts", Interim Technical Report DI-MISC-8071/T, McDonnell Douglas Space Systems Company, Huntington Beach, CA, 1991.
- Plane, J. M. C. and M. Helmer, "Laboratory studies of the chemistry of meteoric metals", *Res. Chem. Kinet.*, 2, 313, 1994.
- Plane, J. M. C., "The chemistry of meteoric metals in the Earth's upper atmosphere", *International Reviews in Physical Chemistry*, 10, 55, 1991.

- Pratt, W. K., "Digital Image Processing", New York, John Wiley and Sons, 1978.
- Ray, P. S., "Broadband complex refractive indices of ice and water", *Appl. Op.*, Vol. 11, Pp. 1836-1844, 1972.
- Reynolds, D. S., and E. C. Robinson, *Private Communication*, 1994.
- Rino, C. L., "A power law phase screen model for ionospheric scintillation", *Radio Sci.*, 14, 1135, 1979.
- Roberts, C. S., "On the relationship between the unidirectional and omnidirectional flux of trapped particles on a magnetic line of force", *J. Geophys. Res.*, **70**, No. 11, 2517-2527, 1965.
- Roble, R. G., R. E. Dickinson, and E. C. Ridley, Global circulation and temperature structure of thermosphere with high-latitude plasma convection, *J. Geophys. Res.*, **87**, 1599-1614, 1982.
- Roble, R. G., E. C. Ridley, and R. E. Dickinson, On the global mean structure of the thermosphere, *J. Geophys. Res.*, **92**, 8745-8758, 1987.
- Roble, R. G., E. C. Ridley, A. D. Richmond, and R. E. Dickinson, "A coupled thermosphere/ionosphere general circulation model", *Geophys. Res. Lett.*, **15**, 1325-1328, 1988.
- Rosenberg, R. L., and P. J. Coleman, "Heliographic latitude dependence of the dominant polarity of the interplanetary magnetic field", *J. Geophys. Res.*, **74**, 5611, 1969.
- Rossi, B., and Olbert, S., Introduction to the Physics of Space, McGraw-Hill, New York/St. Louis/San Francisco/London/Sydney/Toronto/Mexico/Panama, 454 pp, 1970.
- Rubin, A. G., M. A. Heinemann, E. W. Cliver, K. H. Bounar, and T. R. Detman, "The Interplanetary Shock Detector", Boulder, 1996.
- Russell, C. T., and R. L. McPherron, "Semiannual variation of geomagnetic activity", *J. Geophys. Res.*, 78, 92, 1973.
- Sargent, H. H., III, "The 27-day recurrence index, in Solar Wind Magnetosphere Coupling", edited by Y. Kamide and J. A. Slavin, p. 143, Terra Sci., Tokyo, 1986.
- Scannapieco, A. J. and S. L. Ossakov, "Nonlinear equatorial spread-F", *Geophys. Res. Lett.*, 3, 451, 1976.
- Schowengerdt, R. A., "Techniques for Image Processing and Classification in Remote Sensing", Orlando, Academic Press, pp. 249, 1983.

- Secan, J. A., R. M. Bussey, and E. J. Fremouw, "An improved model of equatorial scintillation", *Radio Sci.*, 30,607,1995.
- Secan, J. A. and R. M. Bussey, "An Improved Model of High-Latitude F-Region Scintillation", PL-TR-94-2254, 1994, ADA288558.
- Setayesh, A. A., "The Integration of the PSU/NCAR Mesoscale Model (MM5) with the PL Cloud Scene Simulation Model (CSSM), PL-TR-96-2098, 1996, ADA319529.
- Simon, J. L., P. Bretagnon, J. Chapront, M. Chapront-Touze, G. Francou, J. Laskar, *Astron. Astrophys.*, 282, 663, 1994.
- Singer, H. J., Sullivan, W. P., Anderson, P., Mozer, F., Harvy, P., Wygant, J., and McNeil, W., "The Fluxgate Magnetometer Instrument on the Combined Release and Radiation Effects Satellite", *J. Space Roc.*, Vol. 29, p. 599, 1992.
- Snell, H. E., J. H. Chetwynd, J.-L. Moncet, J. Wang, and G. P. Anderson, *Private Communication*, 1996.
- Snow, D. E., and J. J. F. Liu, J. J. F., "Atmospheric Variations Observed in Orbit Determination", AAS Paper 91-492, 1991.
- Steel, D. L., and W. G. Elford, "The height distribution of radio meteors: Comparison of observations at different frequencies on the basis of standard echo theory", *J. Atmos. Terr. Phys.*, 53, 409, 1991.
- Tsunoda, R. T., "Time evolution and dynamics of equatorial backscatter plumes, I, Growth phase", *J. Geophys. Res.*, 86,139,1981.
- Tsunoda, R. T., R. C. Livingston, J. P. McClure, and W. B. Hanson, "Equatorial plasma bubbles: vertically elongated wedges from the bottomside F-layer", *J. Geophys. Res.*, 87,9171,1982.
- Tsyganenko, N. A., "A magnetospheric magnetic field model with a warped tail current sheet, *Planet. Space Sci.*, 37, 5-20, 1989.
- Valladares, C. E., W. B. Hanson, J. P. McClure, and B. L. Cragin, "Bottomside sinusoidal irregularities in the equatorial F-region", *J. Geophys. Res.*, 88,8025,1983.
- Vandev, D., K. Danov, P. Mateev, P. Petrov, M. Kartalev, N. Trendafilov, Z. K. Smith, and M. Dryer, "Detection of solar wind discontinuities", *Astrophys. and Space Sci.*, 120, 211, 1986
- Vette, J. I., "Models of the Trapped Radiation Environment Volume I: Inner Zone Protons and Electrons", NASA SP-3024, 1966.

- Viereck, R. A., E. Murad, S. T. Lai, D. Knecht, C. P. Pike, "Mg(+) and Other Metallic Emissions Observed in the Thermosphere", PL-TR-96-2065, 1996, ADA305809.
- Weber, E. J., Sa Basu, T. W. Bullett, C. Valladares, G. Bishop, K. Groves, H. Kuenzler, P. Ning, P. J. Sultan, R. E. Sheehan, and J. Araya, "Equatorial plasma depletion precursor signatures and onset observed at 11 degrees South of the magnetic equator", *J. Geophys. Res.*, 101, 16829, 1996.
- Wilson, R. M., D. H. Hathaway, and E. J. Reichmann, *NASA Tech. Paper 3648*, NASA Marshall, Huntsville, AL, 1996.
- Woodman, R. F., and C. LaHoz, "Radar observations of F-region equatorial irregularities", *J. Geophys. Res.*, 81, 5447, 1976.
- Zwickl, R., *Private Communication*, 1994.